



Title	Studies on Monte Carlo Particle Transport in Irregularly Distributed Fuel Elements for High Temperature Gas-Cooled Reactors
Author(s)	村田, 勲
Citation	大阪大学, 1999, 博士論文
Version Type	VoR
URL	<a href="https://doi.org/10.11501/3155641">https://doi.org/10.11501/3155641</a>
rights	
Note	

*The University of Osaka Institutional Knowledge Archive : OUKA*

<https://ir.library.osaka-u.ac.jp/>

The University of Osaka

**Studies on Monte Carlo Particle Transport  
in Irregularly Distributed Fuel Elements  
for High Temperature Gas-Cooled Reactors**

1999

Isao MURATA

**Studies on Monte Carlo Particle Transport  
in Irregularly Distributed Fuel Elements  
for High Temperature Gas-Cooled Reactors**

(高温ガス炉における不規則配列燃料要素中の  
モンテカルロ粒子輸送に関する研究)

1999

Isao MURATA

## ABSTRACT

In high temperature gas-cooled reactors (HTGR) as represented by the high temperature engineering test reactor (HTTR) under construction in Japan Atomic Energy Research Institute (JAERI) and the Arbeitsgemeinschaft Versuchsreaktor (AVR) in Germany, which utilize high-temperature coolant gas for various applications, coated fuel-particles manufactured by coating uranium fuel kernel with several ceramic layers or fuel pebbles made by sintering a number of coated fuel particles are used. These spherical fuel elements are usually loaded or packed irregularly to constitute a fuel compact or a pebble-bed reactor core. So far such a system was dealt with by a conventional approximate method. In the present study, an investigation of method to treat irregularly distributed fuel elements in a continuous energy Monte Carlo simulation was carried out aiming at the development of a new method giving the reference solution for the particle (neutron and/or photon) transport problem.

The basic technique for solution is sampling of a fuel element ("base geometry" in the following) itself instead of modeling all the irregularly distributed base geometries: Along a particle flight path, the location of a base geometry to be arranged is sampled probabilistically and modeled at a certain forward place being distant from the current particle position. Consequently, the modeled base geometry moves continuously according to the flight of the particle. The most critical issues to realize this sampling method are the evaluation of probability distribution by which the sampling of the base geometry location to be arranged should be done and the development of the sampling procedure of the base geometry to reproduce the prescribed inventory of the irregularly distributed base geometries. For the former probability distribution, a three dimensional hard sphere packing simulation code MCRDF, based on a newly proposed random vector synthesis method, was developed to evaluate the probability of finding the nearest neighbor spherical geometry in a spherical shell at distance  $r$  from the reference point (nearest neighbor distribution (NND)), which was necessary for the sampling. The obtained results with MCRDF were compared with the experimentally obtained radial distribution function (RDF) by the X-ray diffraction analysis of alloy, the RDF derived from the Percus-Yevick equation which is well known as equation of state for liquids, and the mathematically estimated NND using a simple assumption. From the result of the comparisons, it was confirmed that the present method was superior to others by ascertaining the fact that the present results agreed with the experimental results better than the other two methods. Also, it was confirmed at the same time that the NNDs prepared by the



present method could excellently reproduce the inventory of base geometries. And for the latter sampling procedure, there were some problems to be solved especially in the process of sampling in points near the boundary surface. By developing two Monte Carlo codes in which the present sampling process was implemented, it was successfully applied to practical use having a generalized function.

The originality of the present method is the realization of the probabilistic treatment (namely, sampling) of geometry in a Monte Carlo particle transport in a system having an irregular arrangement of a lot of base geometries. Such a treatment method has been established for the first time in the world. Also, the sampling procedure developed to reproduce the inventory of base geometries in any container having any shape must be regarded as an essential and universal method to be utilized for future Monte Carlo applications.

The method was implemented in the general purpose Monte Carlo code MCNP to develop the revised codes MCNP-CFP and MCNP-BALL. After the codes were validated basically through two confirmation calculations of inventory reproduction of base geometries and reactor-criticality problems for ordered packed geometries, their applicabilities to a real system were confirmed by the analyses of criticality experiments at critical fission reactor assemblies like VHTRC and PROTEUS. Also, a heavy concrete irradiation experiment using DT neutron source and its analysis were conducted. Heavy concrete is expected to be used as a shielding material for fusion reactor. The results indicated firstly that not a conventional method but the developed codes had to be utilized for an accurate treatment of heavy concrete in a design work of fusion reactor, and secondly that unexpectedly depending upon the dimensions the shielding performance of heterogeneous shield was greater than the homogeneous one especially in higher energy region.

Since the random arrangement system possesses many advantages if the base geometry is sphere, such an arrangement is under planning to be widely applied to fusion blanket, minor actinide incineration reactors and so on. In such cases, the present method can predict the particle transport behavior very accurately and is expected to give the most probable or reference solution.

# 高温ガス炉における不規則配列燃料要素中の モンテカルロ粒子輸送に関する研究

## 概要

原子炉のうちHTTRやAVRに代表される高温ガス炉では高温の冷却材を利用するために、ウラン燃料をセラミックで被覆した被覆粒子燃料もしくはそれらを球状に焼結したペブル燃料が用いられる。これらの球状燃料体は通常不規則に充填され、燃料コンパクトあるいはペブル炉心を構成する形で使用される。本研究では、従来、近似的に取り扱われていたこれらの体系中の粒子輸送問題に対し、参照解が求められるような新しい手法の確立を目指した。そして、連続エネルギーモンテカルロ法を用いた不規則配列燃料要素の取扱手法の開発を行った。

基本的な不規則配列燃料要素（以下幾何形状と呼ぶ）の取扱は、多数の不規則に存在する幾何形状全てをモデル化する代わりに、粒子輸送に沿って1つの幾何形状の設置位置を確率的にサンプリングし、粒子の少し前方にモデル化する手法を用いている。従って、モデル化される幾何形状は常に1つだけであり、結果的に飛行粒子の移動に沿って幾何形状も次々に移動することになる。そして、この手法実現のための重要なキーポイントは、サンプリングに使用する確率分布の評価と、体系内のインベントリを正確に再現するためのサンプリングスキームの確立である。前者、すなわち幾何形状のサンプリング時に必要となる空間分布については、新たに提案したランダムベクトル合成法に基づく3次元剛体球充填模擬コード（MCRDF）を開発し、飛行粒子が他の幾何形状に初めて入射する確率（最近接粒子分布）を計算で求めた。この分布は、合金のX線回折実験から得られた径方向分布関数と液体の状態方程式として知られるPercus-Yevick方程式から得られた結果及び数学的な理論計算から得られた空間分布と比較され、より実験値に近い結果を示すことを確かめることで、他の手法よりすぐれていることを確認した。また、この分布を用いることで正確にインベントリが再現されることも併せて確認した。後者のサンプリングスキームについては、特に壁際の処理で様々な解決すべき問題が生じることが明らかになったが、開発するモンテカルロコードを2つに分離することで、汎用性を持たせながら実用化することに成功した。

本手法の独創的な点は、幾何形状をこのように確率的に取り扱う（サンプリングする）ことで、幾何形状が不規則に配置している体系における粒子輸送計算を模擬できることであり、モンテカルロコードでは世界で初めてのことである。また、インベントリを正確に再現するための幾何形状のサンプリング手順は、まさにモンテカルロ法によりそのような系を取り扱う場合の純粹に普遍的な手法となりえるといえる。

この手法を、汎用モンテカルロコードMCNPに組み込み、新しいコード（MCNP-CFP, MCNP-BALL）を開発した。これらのコードは、幾何形状のインベントリ保存の確認計算と規則配列体系における臨界計算を通じて、その精度の妥当性検討を完了した後、VHTRCとPROTEUS原子炉の実験結果の解析を行い、実機への応用性が確認された。また、DT核融合炉の遮へいとして期待される重コンクリートの非均質効果を測定する実験とその解析から、DT炉の遮へい評価で非均質効果を正確に取り扱うためには、本研究により開発した手法を用いることが非常に有効であることが分かった。また、遮へい体の大きさによっては予想に反して、特に高エネルギー側で均質遮へい体よりも非均質遮へい体の遮へい効果が大きいことが明らかになった。

不規則配列は、特に球状形状の場合有利な点が多いことから、高温ガス炉だけではなく、将来的にも核融合炉のブランケットや消滅処理炉等色々な応用に使用されることが検討されている。本研究で述べている手法は、これらの場合についても正確に粒子輸送を予測し、参照解を与えることを可能にする優れた手法であるといえる。

# CONTENTS

<b>CHAPTER I INTRODUCTION</b> .....	1
I.1 Background .....	1
I.2 Motivation of the study .....	2
I.3 Continuous energy Monte Carlo method in nuclear engineering field .....	5
I.4 Applications of irregularly distributed geometries .....	12
I.4.1 Minor Actinide annihilation reactor .....	14
I.4.2 HTGRs with CFPs .....	15
I.4.2.1 Compact type HTGRs .....	19
I.4.2.2 Pebble bed type HTGRs .....	19
I.4.3 Fusion blanket .....	22
I.4.4 Radiation shield with heterogeneous absorbers for high energy neutrons ...	23
I.5 Conventional neutron transport method in irregularly distributed geometries ...	26
I.5.1 Diffusion and $S_N$ methods .....	27
I.5.2 Continuous energy Monte Carlo method .....	30
I.6 Purpose of the study .....	31
References .....	33
 <b>CHAPTER II THEORY</b> .....	 38
II.1 Introduction .....	38
II.2 Tracking method of irregularly distributed geometries .....	39
II.2.1 Monte Carlo sampling of the Boltzmann equation .....	39
II.2.2 Basic tracking concept and method .....	48
II.2.3 Random sampling with probability distribution .....	52
II.3 Probability distribution necessary for geometry sampling .....	54
II.3.1 Evaluation of nearest neighbor distribution (NND) .....	56
II.3.1.1 Numerical packing simulation .....	57
II.3.1.2 Equation of state for liquids .....	57
II.3.1.3 Statistically uniform distribution .....	59
II.3.2 Computer simulation of random packing .....	64
II.3.2.1 Random packing of equal hard spheres .....	64

II.3.2.2 Packing algorithm of MCRDF .....	66
II.3.2.2.1 Random vector synthesis method .....	68
II.3.2.3 Calculated results by MCRDF .....	72
II.3.2.3.1 Packing fraction of RCP .....	72
II.3.2.3.2 Radial distribution function (RDF) and two dimensional RDF ...	74
II.3.2.3.3 NND .....	82
II.3.2.3.4 Entering angle distribution into sphere .....	87
II.3.2.3.5 Distribution of faces with N edges .....	87
II.3.2.4 Validation of MCRDF .....	90
II.3.3 Determination of method to calculate NNDs .....	92
II.4 Application to Monte Carlo code .....	95
II.4.1 Sampling method of irregularly distributed geometries .....	95
II.4.1.1 Basic principle of sampling .....	95
II.4.1.2 Essential sampling timing and necessary NNDs .....	99
II.4.1.3 Sampling method at boundary surface .....	105
II.4.1.3.1 Low packing fraction mode .....	105
II.4.1.3.2 High packing fraction mode .....	109
II.4.2 Developed codes .....	114
II.4.2.1 MCNP-CFP code .....	114
II.4.2.2 MCNP-BALL code .....	118
II.5 Summary .....	124
References .....	126

<b>CHAPTER III VALIDATION OF THE METHOD .....</b>	<b>128</b>
III.1 Introduction .....	128
III.2 Inventory calculations of irregularly distributed geometries .....	128
III.2.1 Inventory evaluation method .....	128
III.2.2 Inventory checking for MCNP-CFP .....	133
III.2.3 Inventory checking for MCNP-BALL .....	133
III.3 Criticality calculations of ordered packing models .....	135
III.3.1 Criticality calculation by MCNP-CFP .....	138
III.3.2 Criticality calculation by MCNP-BALL .....	138

III.4 Summarized discussion of the validation .....	144
References .....	145
<b>CHAPTER IV APPLICATIONS .....</b>	<b>146</b>
IV.1 Introduction .....	146
IV.2 Analyses of critical assembly experiments .....	147
IV.2.1 NND evaluation for CFP .....	147
IV.2.2 Analysis of critical assembly experiment at VHTRC .....	152
IV.2.2.1 VHTRC experiment .....	152
IV.2.2.2 Analysis method and conditions .....	156
IV.2.2.3 Results and discussion .....	158
IV.2.3 Analysis of critical assembly experiment at PROTEUS .....	161
IV.2.3.1 PROTEUS experiment .....	161
IV.2.3.2 Analysis method and conditions .....	161
IV.2.3.3 Results and discussion .....	165
IV.3 Heterogeneity effect of heavy concrete by fusion neutrons .....	170
IV.3.1 Experimental .....	171
IV.3.1.1 Heavy concrete sample .....	171
IV.3.1.2 Method to measure heterogeneity effect .....	175
IV.3.1.3 14 MeV neutron source .....	180
IV.3.2 Analysis method .....	180
IV.3.3 Results and discussion .....	182
IV.3.3.1 Comparison of measured and calculated heterogeneity effects .....	182
IV.3.3.2 Heterogeneity effect of heavy concrete .....	191
IV.4 Summary .....	196
References .....	197
<b>CHAPTER V CONCLUSIONS .....</b>	<b>200</b>
V.1 Summary of the study .....	200
V.2 Proposal for the future work .....	204
References .....	208

<b>APPENDIX A EVALUATION METHOD OF 2-DIMENSIONAL RDF FROM THE CROSS SECTION PHOTOGRAPHS OF REAL FUEL COMPACTS .....</b>	<b>209</b>
<b>ACKNOWLEDGEMENT .....</b>	<b>218</b>
<b>LIST OF PUBLICATIONS .....</b>	<b>220</b>

# I. INTRODUCTION

## I.1 Background

In Japan, nuclear energy by fission reactors have been covering national electric power demand by several tens percentages. Gradually, it becomes the dominant and key energy resources in Japan. As is well known, we need not be anxious about that fossil fuel will be consumed very soon. However, taking into account the facts that nuclear fuel lasts long as energy material compared to fossil fuel and that the amount of exhaust carbon dioxide gas, which is thought to be a serious cause of green house effect<sup>(1)</sup>, can be suppressed by the use of nuclear plants, it is an undoubted truth that the nuclear energy should be one of the most desirable energy in the future. Also one can analogize the perspective and position of future nuclear energy circumstances from Marchetti's report<sup>(2)</sup> as shown in Fig. 1.1 which examines and predicts the energy share of the world as a function of time. He contended that only nuclear energy could supply the increasing energy demand in the future and for that purpose we had to positively develop nuclear related energy resources.

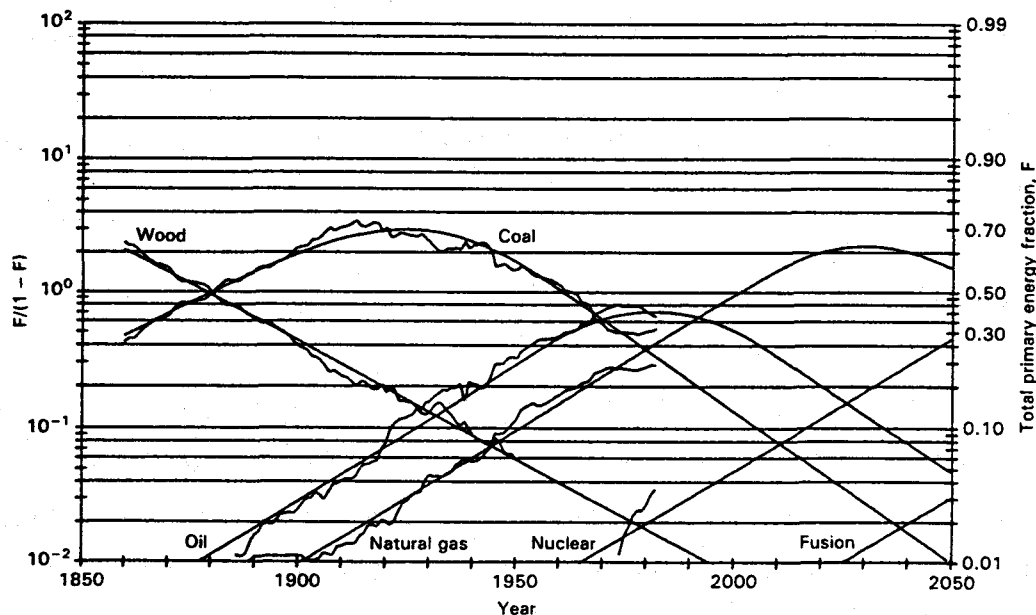


Fig. 1.1 Historical trends in energy substitution. The amount of primary energy (in coal-tons equivalent) from each primary source is plotted as fraction  $F$  of the total energy market with the ordinates expressing  $\log(F/(1-F))$ . This makes logistics appear as straight lines; the fitting set of the equation is given by the smooth curve.



Although definitely nuclear energy has an excellent potential to give us stable energy as electric power continuously for an extra-long term, in return for the benefit, nuclear power station generates nuclear waste having inherent poison, that is radioactivity. This problem is critically important for nuclear engineers and at the same time this fact drives some people opposing to the Japanese nuclear energy policy. Of course, we, especially researchers participating in nuclear engineering, have to recognize that it is a critical problem to control the radioactivity. Practically, we have to design a nuclear reactor so as to prevent an accident, then construct it carefully, operate it safely, decommission it and transmute the nuclear waste of it completely. In this situation, much effort has been made continuously for the various issues mentioned above by many nuclear engineers. Japan Atomic Energy Research Institute (JAERI), a representative research facility with respect to nuclear engineering in Japan, energetically investigates reactor safety<sup>(3)</sup> including behaviors of nuclear reactor and nuclear fuel in accidents and abnormal operating occurrences, radiation protection including nuclear waste incineration<sup>(4)</sup>, research and development of fusion reactor<sup>(5)</sup> and new concept and more safe reactors<sup>(6)</sup>. Also scientists in universities continue new researches concerning nuclear energy from the standpoint of fundamental physics. A lot of results from the above effort have been actually obtained and effectively applied to practical problems. Nevertheless we should continuously give a lot of effort to an extra-long term stable-energy resources problem regarded as the first priority subject to be solved.

One of the results obtained through such effort made by the author is introduced in the present thesis.

## **I.2 Motivation of the study**

It is expected actually that nuclear energy especially by light water reactor (LWR) can cover our electric power demand for the time being. We believe that currently this way is the best selection for the human-being and the planet earth. As mentioned above, many researchers participating in nuclear engineering continuously perform research and development on new power generators based on nuclear energy. Fast breeder reactor (FBR) is regarded as one of the most promising nuclear power resources in the next century. However, we face the disgrace of accidents in Power Reactor and Nuclear Fuel Development Corporation (PNC)<sup>(7)</sup> in Japan and an unfavorable wind against nuclear engineering society. We nevertheless have to go on examining

the development of FBR, because it can utilize nuclear fuel about two orders of magnitude more efficiently than LWR since uranium-238 being obstructive uranium isotope in LWR can be used in FBR as an available fuel. The key point is that abundance ratio of uranium-235 used as fuel in LWR is only 0.7% in natural uranium ore, conversely 99.3% is uranium-238. We believe firmly that FBR must be put to practical use for procurement of energy for over several hundred years.

Also development of fusion power reactor is being done energetically. Fusion reactor is thought to be an ideal energy resources because fusion reaction occurs in the sun and we can secure its raw materials, that is abundant deuterium, from the Oceans almost eternally. The practical leading research is based on the international thermonuclear experimental reactor (ITER)<sup>(8)</sup> which directs the future of fusion reactor application. Many scientists emphasize its importance from the stand point of energy supply for over thousands years.

For the procurement of necessary energy for next several tens years, we think we have to do improvement of current LWRs or preparation of other types of fission reactors, because at present we cannot utilize plutonium fuel in FBR for the reasons mentioned above, and uranium-235 fuel may be exhausted within 100 years if the fuel is used at the current pace. An example of answers to solve the difficulty is MOX fuel<sup>(9)</sup> which is a metal oxide plutonium fuel designed to be applied to LWRs. Recently, May 8, 1998, according to a newspaper, Mr. Kurita, Governor of Fukui Prefecture admitted use of MOX fuel in LWR, for the first time in Japan. It is planning to start the project next spring by Kansai Electric Power Company.

As another candidate fission reactor for the next several tens years, JAERI proposed, over 20 years ago, a high temperature gas-cooled reactor (HTGR). HTGR is a graphite moderated and helium gas-cooled thermal reactor with low enriched  $\text{UO}_2$  fuel to achieve high outlet coolant temperature of about 1000°C. This type reactor has been constantly developed from the earliest period, i.e., since the research and development on fission reactor started, because not only a very high thermal efficiency can be obtained, but also it has inherent safety because of the large heat capacity of graphite and the negative power coefficient. It means that even in an abnormal reactivity insertion accident such as abnormal control rod withdrawal from a subcritical condition the reactor response is slow and a runaway never happens. Research scientists in Department of HTGR Project in JAERI (the author was one of them in 1988~1994) thought that it must be a promising fission reactor supporting the next generation. In Oarai Research Establishment of JAERI, a critical approach experiment is now in progress to achieve its first criticality of a new HTGR named high temperature engineering test reactor (HTTR)<sup>(10)</sup>. The most unique feature of

this type of reactor is the usage of a coated fuel particle (CFP) as a fuel element which is a small ceramic-coated spherical fuel element developed for HTGR. Actually the CFP is employed in most HTGRs of the world because it can suppress fission product (FP) release by the ceramic layers even if the fuel temperature rises beyond 1000°C.

As well known, one of the most important physical quantities in nuclear reactors is an effective multiplication factor, that is namely estimation of burnup of uranium fuel. This is normally obtained by calculation with a neutron transport code which is detailed in the next section. It is a little complicated to calculate it for the HTGRs because CFPs are distributed irregularly in a fuel compact. In LWRs, the core consists of fuel, moderator and coolant regions, each one of which can be regarded as a homogeneous part in some cases. Therefore by modeling their regions precisely we can accurately estimate the effective multiplication factor in principle. Even when we cannot calculate it since there is a heterogeneous structure for example in the fuel region, usually we can obtain the result using group constants having the specific characteristics of the local heterogeneous region. However, in HTGR a CFP itself has a heterogeneous structure caused by several layers and fuel kernel. And a lot of CFPs, normally over 10000, are packed in a fuel compact. Moreover, as their arrangement is completely irregular, the locations of all CFPs cannot be determined. Therefore, the accurate modeling of all of them is impossible, and the method to make group constants by extracting the local heterogeneous region is approximately available because some CFPs are in contact with each other and some are isolated. Conventional methods to cope with such a situation are described in Sec. I.5 in detail. The design work of such reactors has proceeded with such conventional approximate methods which are made in consideration of their spatial distribution approximately or entirely neglecting the configuration of them. In Japan, some available methods were developed and energetically validated by the semi-homogeneous experimental critical assembly (SHE)<sup>(11)</sup> and very high temperature reactor critical assembly (VHTRC)<sup>(12)</sup>.

The nuclear design code system for the HTTR is one of such available methods developed at JAERI. The system consists of the computer codes DELIGHT<sup>(13)</sup>, TWOTRAN-2<sup>(14)</sup> and CITATION-1000VP<sup>(15)</sup>. The validation work was conducted mainly by the analyses of experiments at VHTRC<sup>(16,17)</sup>. The results indicated that the system is available for the VHTRC-1 type reactor which can be recognized as a small and simple core. Because many staffs thought that it was questionable whether or not the nuclear design code system could give a correct calculation results even for larger and more complicated structure than VHTRC, from the early phase of the

HTTR core design, it was pointed out that studies on a new evaluation method to give a reference transport solution were necessary. In this situation, the present study has started. In fact, according to the recent reports, VHTRC experimental results can be pretty well reproduced through the Monte Carlo analysis with MVP<sup>(18)</sup> by adding the reactivity effect of CFPs evaluated by other method as precisely described in Sec. I.5.2. Examples of the result are shown in Tables 1.1 and 1.2<sup>(19)</sup>. Also, it is found from the preliminary analyses for HTTR's start-up physics tests using the nuclear design code system for HTTR and the reference Monte Carlo code MVP that various corrections such as calculation mesh effect, radiation streaming and so on cannot be avoided to obtain acceptable results by using the nuclear design code system as the reliable prediction for the start-up test. The comparison results of burnable poison and streaming reactivities in HTTR are shown in Tables 1.3 and 1.4<sup>(20)</sup>. These evidences indicate that the present study is valuable for application to HTGR design works such as HTTR.

### **I.3 Continuous energy Monte Carlo method in nuclear engineering field**

In the present study, an investigation is focused on how the reference solution mentioned in the previous section can be obtained. In this section, many excellent characteristics of the Monte Carlo method are described to answer the question; why the Monte Carlo method must be utilized.

The systems, e.g., nuclear power station, that generate energy through nuclear reactions are obliged to release radiation or radioactivity. Radiation is an extremely small particle, sometimes acting like wave, therefore normally it is invisible and it is an ultimate constituent of matter. In addition, radiation as a particle having a mass can be energy carrier. On the other side, much amount of radiation exposure is bad for the human health. In the nuclear engineering field, therefore, evaluation of the various radiation-related characteristics of the nuclear power station by the transport calculation has to be regarded as an essential research activity. Actually, a major research objective of many scientists participating in nuclear engineering is to study a behavior of radiation emitted from nuclear fuel, FP, nuclear wastes and so on.

The behavior of radiation is fundamentally governed by the nuclear reaction. Due to nuclear reaction, radiation is generated. The theoretical calculation based on nuclear reaction can explain the mechanism of phenomena in fission and fusion reactors. A particle transport calculation

Table 1.1 Effective multiplication factors of VHTRC analyzed with MVP compared with the experiments.

(a) Using JENDL-3.1

Core	Fuel rods	BP rods	$k_{\text{eff}}$ (Exp.)	$k_{\text{eff}}$ (Cal.) <sup>1)</sup>	Calculated $k_{\text{eff}}$ corrected with heterogeneity effect of CFPs	Error (1 $\sigma$ )	C/E-1(%)
VHTRC-1	282(B-4)	0	1.0079	0.99669	1.005	0.0018	-0.29
VHTRC-4	284(B-2,B-4,T-6)	0	1.0077	1.00006	1.008	0.0008	0.03
VHTRC-6	572(B-2,B-4,T-6)	34	1.0073	0.99636	1.004	0.0014	-0.13

1) 1920000 histories (48000 particles/batch, 40 batches)

(b) Using JENDL-3.2

Core	Fuel rods	BP rods	$k_{\text{eff}}$ (Exp.)	$k_{\text{eff}}$ (Cal.) <sup>1)</sup>	Calculated $k_{\text{eff}}$ corrected with heterogeneity effect of CFPs	Error (1 $\sigma$ )	C/E-1(%)
VHTRC-1	282(B-4)	0	1.0079	1.00534	1.013	0.0018	0.51
VHTRC-4	284(B-2,B-4,T-6)	0	1.0077	1.00809	1.016	0.0007	0.82
VHTRC-6	572(B-2,B-4,T-6)	34	1.0073	1.00552	1.014	0.0024	0.67

1) 1920000 histories (48000 particles/batch, 40 batches)

Table 1.2 Reactivities of burnable poison (BP) rods of VHTRC analyzed with MVP compared with the experiments.

Core	Fuel rods	BP rods	$k_{\text{eff}}(\text{Cal.})^{1)}$	BP reactivity (% $\Delta$ k/k)		Analysis error (%)	C/E-1 (%)
				Cal.	Exp.		
VHTRC-4(0)	276	0	0.995086 $\pm$ 0.00077	—	—	—	—
VHTRC-4(1)	276	12	0.930102 $\pm$ 0.00126	-7.021	-7.09	3.3	-0.97
VHTRC-4(2)	276	24	0.910097 $\pm$ 0.00134	-9.385	-10.07	2.6	-6.81
VHTRC-4(3)	276	36	0.833601 $\pm$ 0.00082	-19.468	-18.29	1.1	5.8
VHTRC-4(4)	276	24	0.882315 $\pm$ 0.00111	-12.844	-13.31	1.8	-3.5
VHTRC-4(5)	276	36	0.841989 $\pm$ 0.00104	-18.273	-18.4	1.3	-0.1

1) 1920000 histories (48000 particles/batch, 40 batches)  
Used nuclear data file : JENDL-3.1

Table 1.3 Comparison of BP reactivities estimated for the HTTR's start-up physics tests with MVP and the nuclear design code system for HTTR.

Number of column	BP reactivity (% $\Delta$ k/k)		
	6 mesh model <sup>1)</sup>	24 mesh model <sup>1)</sup>	MVP
30	9.07	10.54	11.68
24	8.60	10.17	11.35
18	8.69	10.16	11.63

1) Calculated by the nuclear design code system for HTTR.

Table 1.4 Comparison of reactivity effect due to radiation streaming.<sup>1)</sup>

Number of column	Reactivity effect (% $\Delta$ k/k)			
	Control rod column		Control rod colum+ upper and lower replaceable reflector	Upper and lower replaceable reflector
	Diffusion cal.	MVP		
30	1.03	1.3	1.12	0.086
24	1.12	—	1.21	0.088
18	1.33	2.3	1.42	0.095

1) Details about the calculation conditions are given in Ref. (20).

code known as a theoretical calculation program is often used for a reactor design work. Using a transport code, one can discuss various physical features such as fuel burnup, radiation shielding performance, activation of devices and so on. Typical transport code is based on diffusion approximation<sup>(21)</sup>,  $S_N$  transport approximation<sup>(14,22,23)</sup> and Monte Carlo method<sup>(24,25)</sup>.

Currently operated nuclear reactors were designed by one of the transport codes above. However, since most reactors were constructed in an early stage of the development of nuclear engineering, the design was often done by the simplest method, e.g., diffusion approximation codes, partly because the method had been established first of the three methods and mainly because the code greatly save time compared with other two methods. In the diffusion method, behavior of neutron in matter is approximately treated by the same manner as the diffusion phenomenon in gas. In addition, group constants are used to represent the characteristics of fuel assembly even normally having complicated geometry, because to precisely model the whole structure is not valid due to the violation of assumption employed in the diffusion method, i.e., the limit of diffusion approximation. For this reason, to design a nuclear reactor, various cell burnup codes were developed for calculating the group constants and the fuel burnup, resulting in establishing the nuclear design code system for each kind of nuclear reactor<sup>(26,27)</sup>. However, in the early stage the nuclear reactor designers had to calculate with one-dimensional code for a simplified core model. With progress of the computation performance of computer so as to realize an  $S_N$  transport calculation, two or three dimensional diffusion calculations could be available. The  $S_N$  transport calculation method is based on a numerical simulation of the Boltzmann equation governing the neutron transport behavior in matter. It has various advantages in comparison with the diffusion method: Even distorted neutron flux distribution in a complicated structure having strong absorber such as control rod can be predicted by preparing the fine calculation meshes. Also neutron scattering anisotropy can be taken into account. Therefore, in general the diffusion method was often and mainly used for the parametric analysis of the reactor core design, while the  $S_N$  transport method was utilized for a precise evaluation of the neutronic characteristics in such a reactivity control element. For saving the calculation cost in a practical reactor design, a more simplified and conservative model was adopted. The conservatism is consequently a cause of existence of safety margin and is leading to an irrational design. Recently the computer has been remarkably improved. However, reactor design with three-dimensional model by the  $S_N$  method was not yet made because of the difficulty in three dimensional modeling and lack of memory in the computer to cover the array to be prepared for the calculation model.



More recently aiming at rational reactor design by modeling the reactor as precisely as possible, detailed design was begun to be performed. Such a detailed design consequently requires an additional analysis of neutron streaming and so on caused by the local fine structure of the reactor. In that case, a Monte Carlo code instead of the conventional methods based on the diffusion and  $S_N$  approximations was started to be used in practical application<sup>(28)</sup>. The principle of the Monte Carlo method has been developed since a long time ago<sup>(29)</sup>. It is based on precise tracking of a particle in a calculation model exactly considering its nuclear interaction with a material atom. Therefore, it was not of practical use to conduct Monte Carlo simulation by computer because of a very long computation time required. However, the Monte Carlo method has many advantages that compensate the weak point: There is no approximated process in tracking simulation. Hence it can become a reference transport calculation code. An exact three-dimensional modeling is possible since generally the Monte Carlo code allows a geometry modeling by some equation expressions. Especially for a continuous energy Monte Carlo method<sup>(24)</sup>, a more precise calculation can be realized because it employs an exact form cross section data considerably reproducing the expression of the evaluated nuclear data. With progresses of the computer performance, various variance reduction techniques<sup>(30-34)</sup> and vectorization<sup>(35-37)</sup> and parallelization<sup>(38)</sup> of the code, three-dimensional precise calculation with the Monte Carlo code is likely to fall into our hands.

At present, Monte Carlo code is mainly utilized for various shielding analyses focusing on a locally complicated structure to supplement the deterministic method<sup>(28,39,40)</sup>. They are thus carried out with a three dimensional precise model to obtain the most probable result. However, it is gradually applied to criticality and shielding calculations for a whole reactor model. Actually an example of such calculations using a large-scale three dimensional model was reported<sup>(41)</sup> for recently constructed reactor, HTTR, which is planned to reach the first criticality soon. Also, criticality calculations for LWRs and critical assemblies such as VHTRC in JAERI were done with the whole core model<sup>(42-44)</sup>.

Monte Carlo code possessing an excellent applicability to reactor analysis has, on the other side, some problems, e.g., (1)it requires a long computation time, (2)it does not deal with fuel burnup calculation and (3)it does not calculate adjoint flux especially for a continuous energy Monte Carlo method. These problems are critical for the use of the code as a design tool and to be solved for the future. Recent progresses for that matters are briefly given in the following.

As mentioned earlier about (1), it is one of the severest cause that disturbs the

application of Monte Carlo code to the design work. The shortest cut to the solution is to improve the computation performance. In fact the computer development is outstandingly rapid. Also, development of vector and parallel processors enhances vectorization and parallelization of computer programs. However, no matter how efficiently the performance of the computer and code are improved, practical calculation for very thick shield wall becomes difficult. The issue is how variance of calculation can be reduced. In Monte Carlo code, there are usually many variance reduction techniques attached<sup>(45)</sup>, they generally require much trial and error. No authorized method to satisfy all the users is not established so far. Although excellent methods such as weight window generator (WWG)<sup>(30)</sup> were proposed to facilitate the trial and error, this problem is not solved completely.

As for the problem (2), the burnup calculation is also an important function when applying Monte Carlo method to design of nuclear reactor. Many scientists have been continuously examining a practical method and procedure to calculate fuel burnup by Monte Carlo method. Basically, the calculation is divided into two steps, i.e., transport calculation and burnup calculation using time steps. It is thought that use of Monte Carlo method is superior to deterministic method, because the former method can estimate propagation of error between time steps. As recent examples, a Monte Carlo / deterministic hybrid method was proposed with coarse and fine time steps<sup>(46)</sup>. Atomic densities at the end of a fine time step calculated by collision probability method is corrected by the correction factors evaluated at the coarse time step including the above fine time step using both Monte Carlo and collision probability methods. In JAERI, a fuel assembly burnup code by Monte Carlo method named MKENO-BURN was developed by combining the three dimensional Monte Carlo neutron transport code MULTI-KENO and the routine for burnup calculation of the one dimensional burnup code UNITBURN<sup>(47)</sup>. However, a general purpose Monte Carlo burnup calculation code is not released so far to apply to a practical design work.

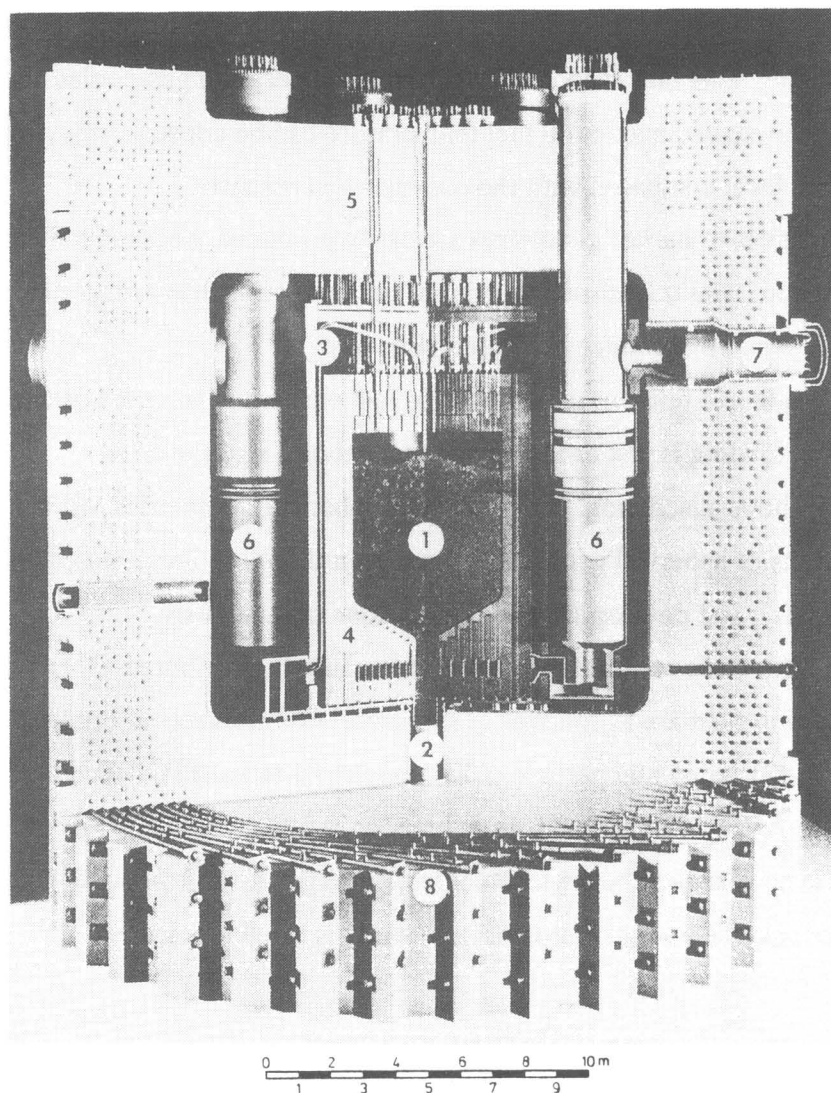
The problem (3) is very famous for its difficulty. Some basic methods were proposed to solve the adjoint Boltzmann equation with the continuous energy Monte Carlo method<sup>(48-50)</sup>. Their essential concept is appropriation of the method developed for the same problem in case of using deterministic method or group-wise Monte Carlo method<sup>(51)</sup>. As well known, adjoint neutron spectrum can be calculated by group-wise Monte Carlo code, diffusion code and so on which use the group constants. The practical method is to transform the adjoint Boltzmann equation to yield the same form as the forward equation. It is therefore required to remake the cross section library

according to the transformation procedure of the adjoint Boltzmann equation: The cross section kernel should be transposed. However, it is not so easy to transpose the kernel because the continuous energy Monte Carlo code treats continuous energy (point wise) cross section data. In principle rewriting of the cross section kernel is formally possible. But the calculational result with the deformed kernel has consequently a large variance. Recently the research is focused on how to reduce the variance of the calculation with the transposed continuous energy cross section data.

Overcoming the problems described above must enhance recognition of Monte Carlo code as a design tool of a reactor. However, in case of applying Monte Carlo code to HTTR, for example, and obtaining the reference solution in the eigenvalue estimation of the reactor, there is a severer problem to be solved: Monte Carlo code cannot deal with the configuration of CFPs distributed irregularly in a fuel compact. This thesis' main purpose is to give the exact solution of this problem. But, as a matter of fact, there are many applications with use of irregularly distributed spheres in nuclear engineering field. This research can commit not only HTGR technology but also various new applications, as is described in the following sections with several examples.

## **I.4 Applications of irregularly distributed geometries**

In the present thesis, the irregularly distributed geometries are defined as a state in which a lot of base equal elements are distributed or packed in a container, as shown in the following examples. The first application employing irregularly distributed geometries in nuclear engineering field was Arbeitsgemeinschaft Versuchsreaktor (AVR)<sup>(52)</sup> in Germany in 1969, which adopted spherical fuel element named fuel pebble. After AVR, the second pebble bed reactor THTR achieved its criticality in 1985. The schematic cross sectional arrangement of THTR is illustrated in Fig. 1.2<sup>(53)</sup>. As shown in the figure, a large number of fuel pebbles are piled up irregularly in the core. This is a quite unique idea compared with conventional LWRs or critical assemblies which have a core with not-spherical-shape fuel elements loaded strictly and regularly, though we cannot know how the excellent concept came out exactly, because such kind of research started a long time ago; in about 1956<sup>(53)</sup>. We instantly notice that this idea is quite new and very interesting, and it is probably difficult to analyze a reactor core having irregularly distributed geometries, because they are distributed irregularly. However, this type of core has many advantages in comparison with a regularly piled-up core:



- |                           |  |
|---------------------------|--|
| 1 Core (675 000 Elements) | 5 Absorber Rods                        |
| 2 Discharge Tube          | 6 Heat Exchanger                       |
| 3 Charge Tube             | 7 Blower                               |
| 4 Graphite Reflector      | 8 Prestressed Concrete Pressure Vessel |

Fig. 1.2 Sectional view of THTR pressure vessel.

- (a) Because a pile of spheres act like fluid, the fuel exchange can be done continuously during the operation.
- (b) Fuel pebbles in the core generate heat by fission reaction. The heat can be removed more efficiently than conventional core in which not-spherical-shape fuel elements are loaded regularly, because the pressure loss of gas coolant in the pebble bed core is smaller. This fact is so critical for high temperature gas-cooled reactor (HTGR), i.e., the evaluated maximum fuel temperature can be consequently suppressed within a lower level compared with the conventional reactors.
- (c) Fuel pebbles (spherical geometry) are easily produced, because they are just piled up in the core, and therefore a loose production tolerance is acceptable.
- (d) Spheres are strong since no projections exist.
- (e) Fuel loading is quite easy because the fuel element is sphere. For example, in AVR, the fuel loading is just dropping the fuel pebbles into the core.

As shown in the above discussion, by employing spherical geometries we can receive many benefits. Applications of spherical geometries have been therefore investigated energetically and at present the research and development are being done continuously.

Currently, studies related to the use of irregularly distributed spherical geometries in the nuclear engineering field are as follows: (1)Spherical fuel elements adopted in minor actinide incineration reactor, (2)coated fuel particle (CFP) employed as an HTGR fuel element, (3)pebble bed reactor such as AVR, (4)spherical tritium breeder in fusion blanket, (5)heavy concrete used as a strong shield in nuclear facilities, which contains heavy ores or iron punchings, and so on. In the following sections, the present status of each study is briefly reviewed.

### **I.4.1 Minor actinide annihilation reactor**

Since the early stage of the research and development of nuclear engineering, disposal, including transmutation (incineration), of high level nuclear wastes unexpectedly yielded in the nuclear reactor is a serious problem. Nevertheless, we can expect that, in the future, utilization of the nuclear energy will be more progressed even slowly. Also we have to consider the fact that actually a large amount of high level nuclear wastes are stored now. We need to recognize that the issue is quite difficult and critical for us. These nuclear wastes are planned to be treated by shallow land burial for an extra long period of time. We also need to recognize that there is a deep

anxiety for the shallow land burial for over  $10^9$  years. In this situation, studies on incineration of troublesome radioisotopes having an extra long half life have been started.

Nuclear waste incineration is a new disposal technology described as follows: Partitioning the fission products (FPs) and minor actinides (MAs) contained in the high level nuclear wastes, they are transmuted into short-half-life radioisotopes or stable nuclides through nuclear reactions by accelerator, fission reactor and so on. Potential hazard index for high level nuclear waste from PWR spent fuel is shown in Fig. 1.3<sup>(54)</sup>. As is understood in the figure, almost all MAs have a long half life, i.e., strong potential hazard and as a result they are basically incinerated after converting them into FPs by fission reaction<sup>(55)</sup>.

As a new idea for the incineration, nuclear reactors using irregularly distributed spherical fuel elements was proposed recently. The basic concept is that a high power density can be achieved because heat removal is efficiently done in the core in which spherical fuel elements are piled up irregularly. For instance, a small nitride MA fuel was designed for efficient incineration of MAs<sup>(56)</sup>. Good heat removal characteristics of the spherical fuel elements suppresses the fuel temperature. The coated layer thickness can be therefore diminished to realize harder neutron spectrum resulting in improvement of incineration efficiency. The structure of the nitride MA fuel is shown in Fig. 1.4. Also a unique idea was proposed for destruction of excess plutonium prepared for nuclear weapons<sup>(57)</sup>. Basically two kinds of spherical fuel element are used that include fertile material such as thorium (breeder ball fuel) and fissile material as object of transmutation such as plutonium (burner ball fuel), respectively. In the proposed pebble bed reactor, the fertile material continuously burns up as a driver fuel and on the other hand the fissile material can be transmuted until it is exhausted almost completely. Also since continuously fuel unloading is possible, constantly inspecting the level of fuel burnup after retrieving the fuel element, we can exchange the fuel element at any time when it attains the prescribed burnup. The conceptual arrangement of the reactor is described in Fig. 1.5.

## **I.4.2 HTGRs with CFPs**

HTGRs surely proved availability of irregularly distributed geometries. There exist two kinds of reactors with a lot of spherical fuel elements distributed irregularly, i.e., compact type HTGR and pebble bed type HTGR as shown in Fig. 1.6. As shown in the figure, in the compact type HTGR, fuel compacts packed with CFPs irregularly are loaded regularly in the core<sup>(10,58)</sup>. On

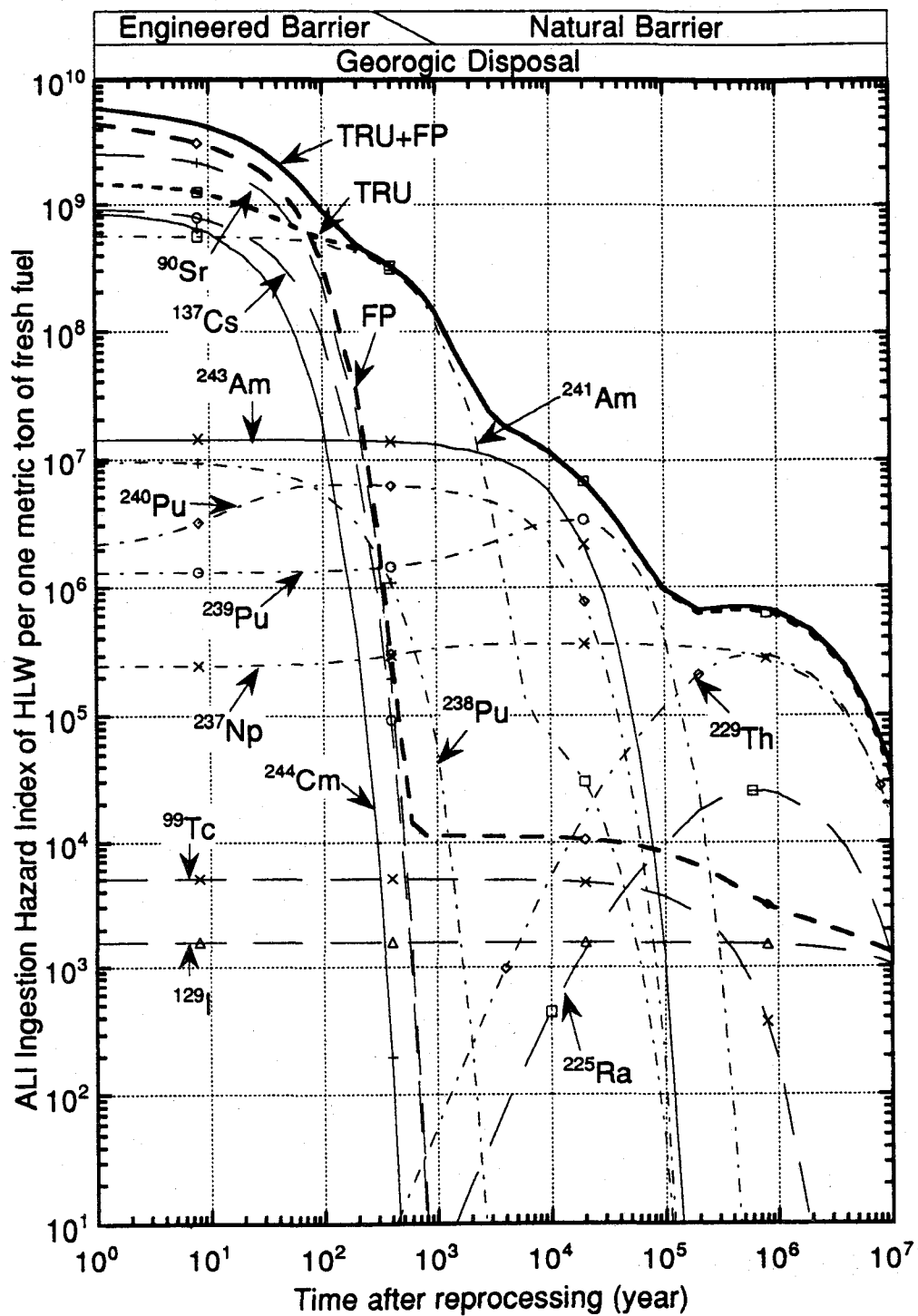


Fig. 1.3 Potential hazard index vs time for HLW from PWR spent fuel. ALI ingestion hazard index is defined as the ratio of the amount (in Bq unit) of a nuclide to ALI value of the nuclide. HLW is recovered from the reprocessing of PWR spent fuel (burnup of 33 GWD/MT, 3 years cooling). U and Pu recovery is 95 %.

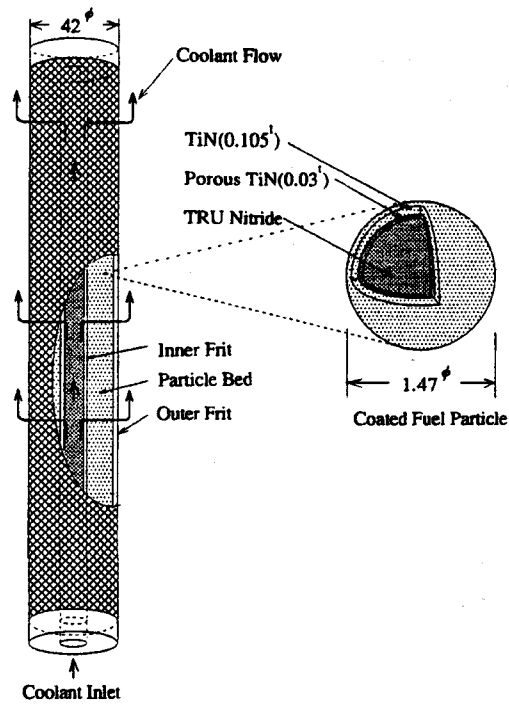


Fig. 1.4 Fuel element with TRU nitride in MA burner reactor.

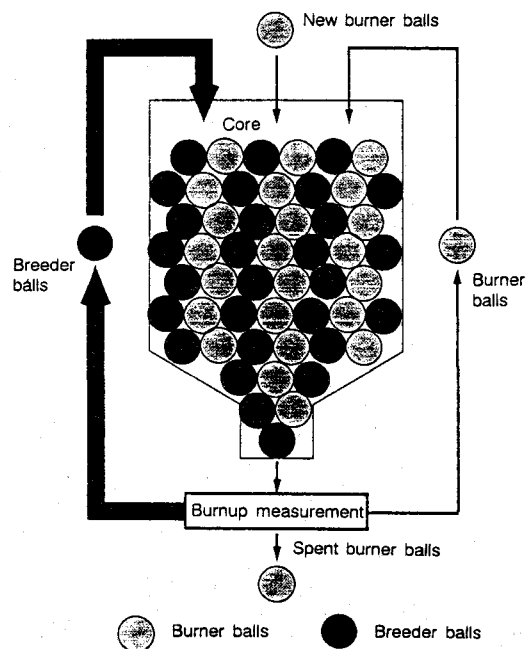
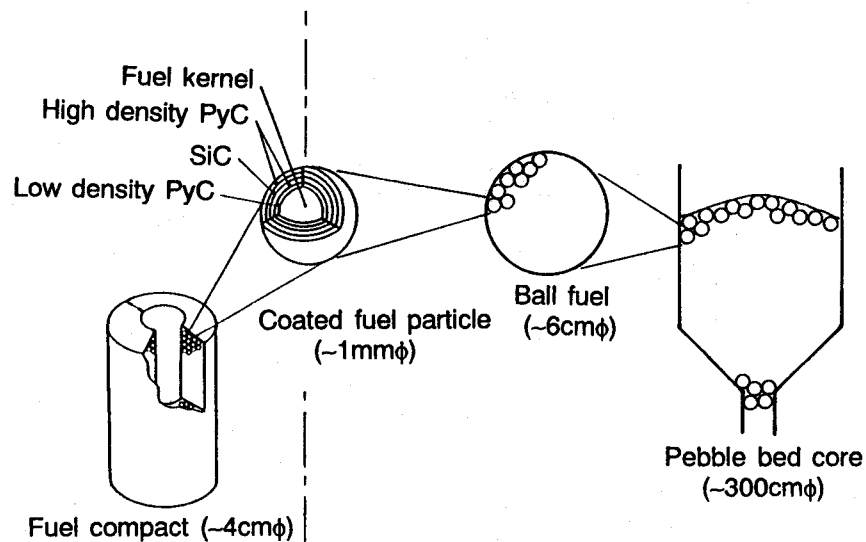


Fig. 1.5 Conceptual arrangement of Pu burner reactor with breeder balls and burner balls.





(a) Compact type fuel element employed in VHTRC, HTTR and so on

(b) Pebble-bed type fuel element employed in AVR, PROTEUS and so on.

Fig. 1.6 Spherical fuel elements employed in HTGRs.

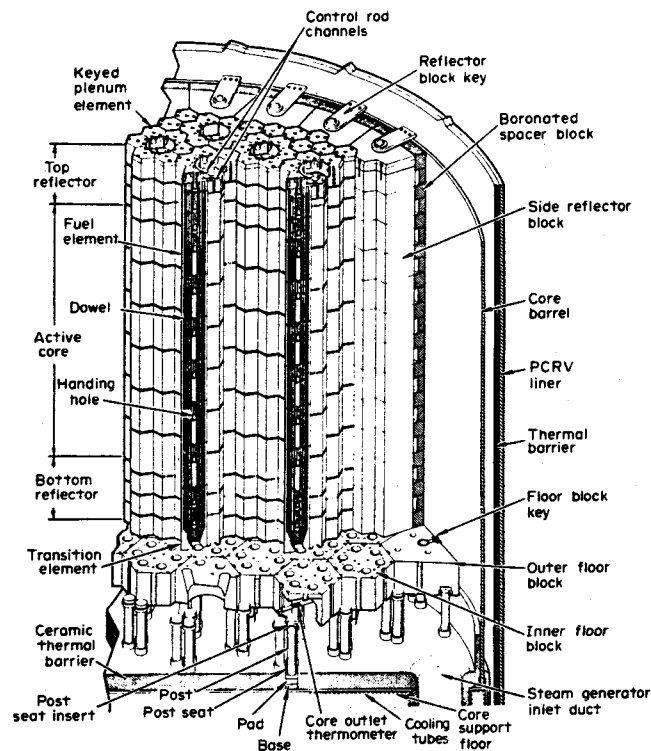


Fig. 1.7 Reactor core arrangement. Design features of the core support structures for the Fort St. Vrain nuclear generating station.

the other hand, in the pebble bed reactor spherical fuel elements, fuel pebbles, in which CFPs are packed irregularly, are piled up also irregularly in the core<sup>(59)</sup>. Both reactors have double heterogeneity. However, the former has a heterogeneous structure caused by irregular and regular arrangements, while the latter has that of two irregular arrangements.

#### **I.4.2.1 Compact type HTGRs**

As an example of a compact type HTGR, the high-temperature engineering test reactor (HTTR)<sup>(10)</sup>, which aims at the highest outlet coolant temperature of 950°C in the world, is under construction to achieve its criticality this autumn in Japan. One of the previous compact type HTGRs is Fort St. Vrain (FSV)<sup>(60)</sup> which has already been shut down in the US. The reactor core arrangement of FSV is illustrated in Fig. 1.7<sup>(53)</sup>. Since the detailed description is given about a general HTGR in Sec. I.2, the feature of HTTR is briefly introduced in the following<sup>(10)</sup>: The schematic arrangement of HTTR is illustrated in Fig. 1.8. HTTR is a graphite moderated and helium gas-cooled reactor with low enriched (3~10wt%) UO<sub>2</sub>. In order to suppress the maximum fuel temperature as much as possible, the spatial fuel temperature distribution has to be made uniform in the core. This was achieved by loading higher enriched fuel element at upper and outer regions of the core. Table 1.5 shows the description of 12 fuel elements having different enrichment. Also, to keep the fuel kernel temperature as low as possible, CFPs were packed irregularly with binder graphite in as acceptably low packing fraction as possible to form a fuel compact. However, the fuel temperature inevitably rises up to over 1000°C because we are planning to utilize extremely high-temperature (~1000°C) coolant for various applications. To restrain FP release below 1600°C, the fuel kernel is coated with several ceramic layers. The schematic configuration of the fuel element of HTTR is shown in Fig. 1.9. The fuel rod, which is composed of fuel compacts in which the CFPs are packed irregularly, is contained within a vertical hole of a graphite block. The core is constituted by the graphite blocks piled up regularly as shown in Fig. 1.8.

#### **I.4.2.2 Pebble bed type HTGRs**

At first, countries developing the pebble bed type HTGRs were England and Federal Republic of Germany. Especially in Germany, the most famous pebble bed type reactor,

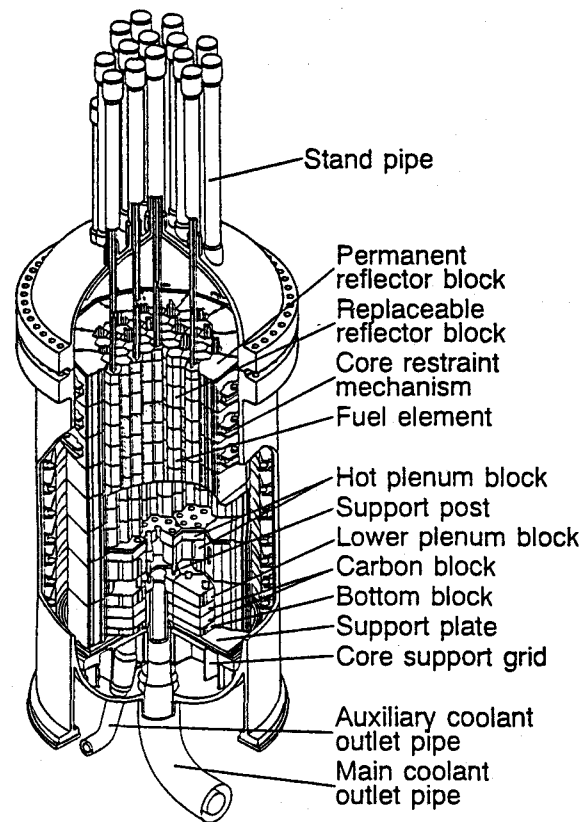


Fig. 1.8 Bird's-eye view of HTTR reactor vessel and core.

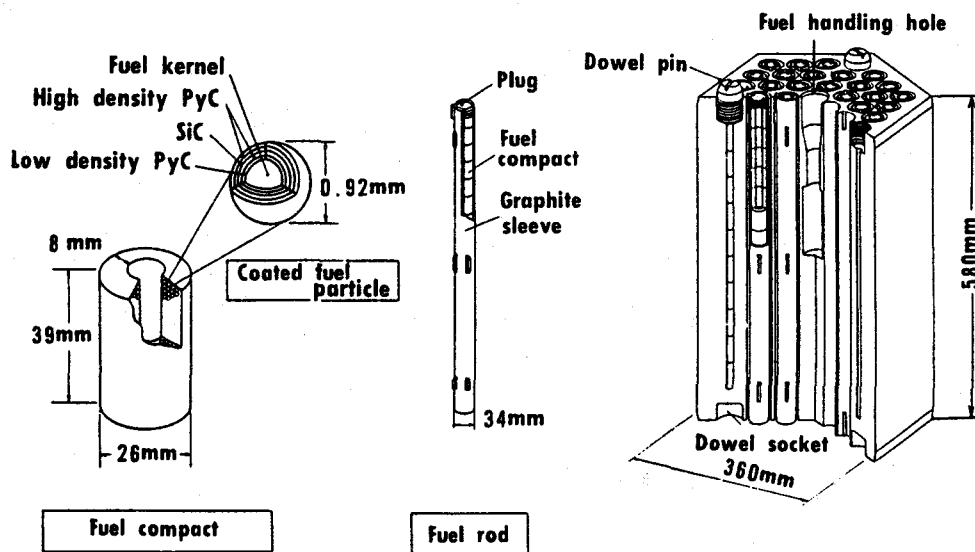
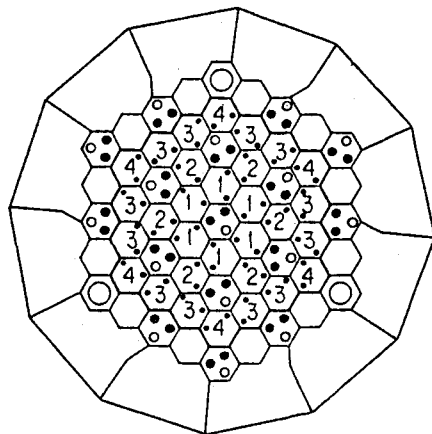


Fig. 1.9 Configuration of HTTR fuel element.

Table 1.5 Fuel and BP zoning plan of HTTR.



Layer <sup>*3</sup>	Fuel zone number <sup>*1</sup>				BP <sup>*2</sup>
	1	2	3	4	
1	6.7	7.9	9.4	9.9	2.0
2	5.2	6.3	7.2	7.9	2.5
3	4.3	5.2	5.9	6.3	2.5
4	3.4	3.9	4.3	4.8	2.0
5	3.4	3.9	4.3	4.8	2.0

\*1 <sup>235</sup>U enrichment(wt%)

\*2 Natural boron concentration(wt%)

\*3 The number indicates the layer number from the top fuel block.

- ⬢ : Fuel column
- N : Zone number
- : Burnable poison
- ⬢ : Control rod guide column
- : Control rod
- : Reserve shut down system
- ⬢ : Replaceable reflector
- ⬢ : Irradiation column

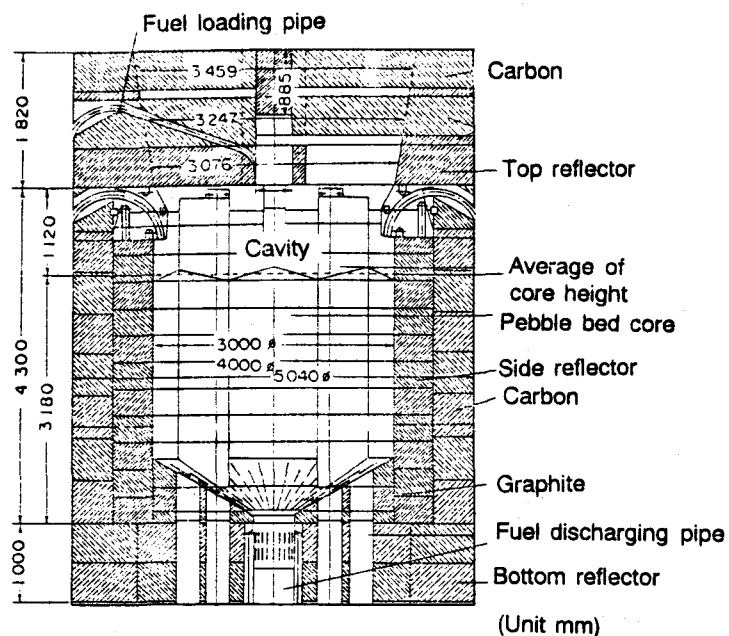


Fig. 1.10 Vertical cross section of AVR core.

Arbeitsgemeinschaft Versuchsreaktor (AVR)<sup>(52)</sup>, was constructed, which has been operated for about 20 years since 1969. AVR has been shut down and there is no commercial reactors in operation now. However, most nuclear engineers know that the pebble bed type reactor is superior to others. Recently, to find out a new meaning in the pebble bed type reactor, Paul Sherrer Institute (PSI) constructed a pebble bed type reactor critical assembly (PROTEUS)<sup>(61)</sup> in 1992.

Since AVR is an HTGR, it properly employed CFP, to suppress FP release and the maximum fuel temperature, as well as fuel pebble, containing CFPs, piled up irregularly in order to eliminate time loss due to batch refueling from the stand point of electricity generation efficiency. In AVR, a continuous refueling of fuel pebbles was employed during reactor operation. This refueling scheme achieves the best generation efficiency because of the following quantitative reason: As well known, by adopting several time reloadings of fuel during the fuel lifetime, the achieved burnup can be increased. The estimated attainable burnup can be approximately given by<sup>(53,62)</sup>

$$B_n = \frac{2n}{n+1} B_1, \quad (1.1)$$

where  $B_n$  is the burnup of the spent fuel for  $n$ -times batch refueling,  $B_1$  the burnup of the spent fuel for one batch refueling and  $n$  the number of batch refueling during the fuel lifetime. The continuous refueling for AVR corresponds to  $B_\infty$ , i.e.,  $B_n$  when  $n$  is extrapolated to infinity. In this case, a twice larger burnup of  $B_1$  can be accomplished. Fig. 1.10 shows the sectional view of AVR core<sup>(63)</sup>. The refueling was conducted by retrieving fuel pebble from the bottom funnel-exit during operation, examining the burnup to remove ones attaining the prescribed burnup and reloading the rest ones in the core immediately after the examination. Moreover, as discussed in Sec. I.4, the coolant flowing between pebbles effectively removes the heat generated in the fuel pebbles, resulting in suppression of the maximum fuel temperature. The pebble bed type reactor is a typical example that well puts the excellent characteristics of irregularly distributed spherical geometries to a practical application.

### I.4.3 Fusion blanket

Irregularly distributed geometries are utilized in a blanket of fusion reactor as a

spherical tritium breeder material. The basic and important factor in the blanket structure design is determination of the breeder material form and how to cool the breeder. In the design work so far, breeder configurations of pebble, pellet, plate and block were mainly investigated<sup>(64)</sup>. Cracking of the breeder due to thermal stress can be easily prevented by the use of small spherical breeders compared with other configurations. Also spherical breeders can be easily produced and loaded in the container. For these reasons, the research was focused on the pebble type breeder.

Two ways to cool the breeder region are proposed, i.e., breeder outside tube (BOT) type and breeder inside tube (BIT) type. The BOT type consists of cooling tube and breeder existing outside the tube, while in the BIT type the breeder is packed in the cooling tube. A typical conceptual arrangement of the BOT type is shown in Fig. 1.11. This blanket was designed as a solid breeder blanket for the next European torus (NET)<sup>(65)</sup>. A 0.5mm-diameter small spherical breeder is used to restrain decrease of the packing fraction due to the wall effect, detailed in Sec. II.3.2.1, since the coolant does not flow between spherical breeders. A BOT type blanket is also examined for the FER<sup>(66)</sup>. A typical example of the BIT type blanket design is one of the candidate blankets for power nuclear plant proposed by JAERI<sup>(64)</sup>. The conceptual blanket design is illustrated in Fig. 1.12. Spherical breeders are packed in a pressure tube and helium gas flowing between the spherical breeders removes heat and tritium generated in the breeder simultaneously. The breeder sphere diameter is set to be 3mm to facilitate the loading into the pressure tube, to avoid cracking of the spherical breeder caused by thermal stress and to reduce the pressure loss of the coolant. A BIT type blanket is proposed as a candidate for the INTOR<sup>(67)</sup>.

Recently, as an idea concerning the nuclear waste incineration, a hybrid fusion reactor is designed to transmute the weapons-grade excess plutonium with  $\text{PuO}_2$  fuel pebbles and to create tritium from lithium, at the same time converting the kinetic energy of fusion neutrons and the energy released in the fission of plutonium to heat, which is removed for the production of electricity<sup>(68)</sup>.

#### **I.4.4 Radiation shield with heterogeneous absorbers for high energy neutrons**

Radiation generated in nuclear reactor, fusion reactor and so on is shielded by using mixture of various shielding materials, in which ordinary concrete is very much often used, because it is one of the most effective, reliable and cheap shields. In nuclear reactor, ordinary concrete is

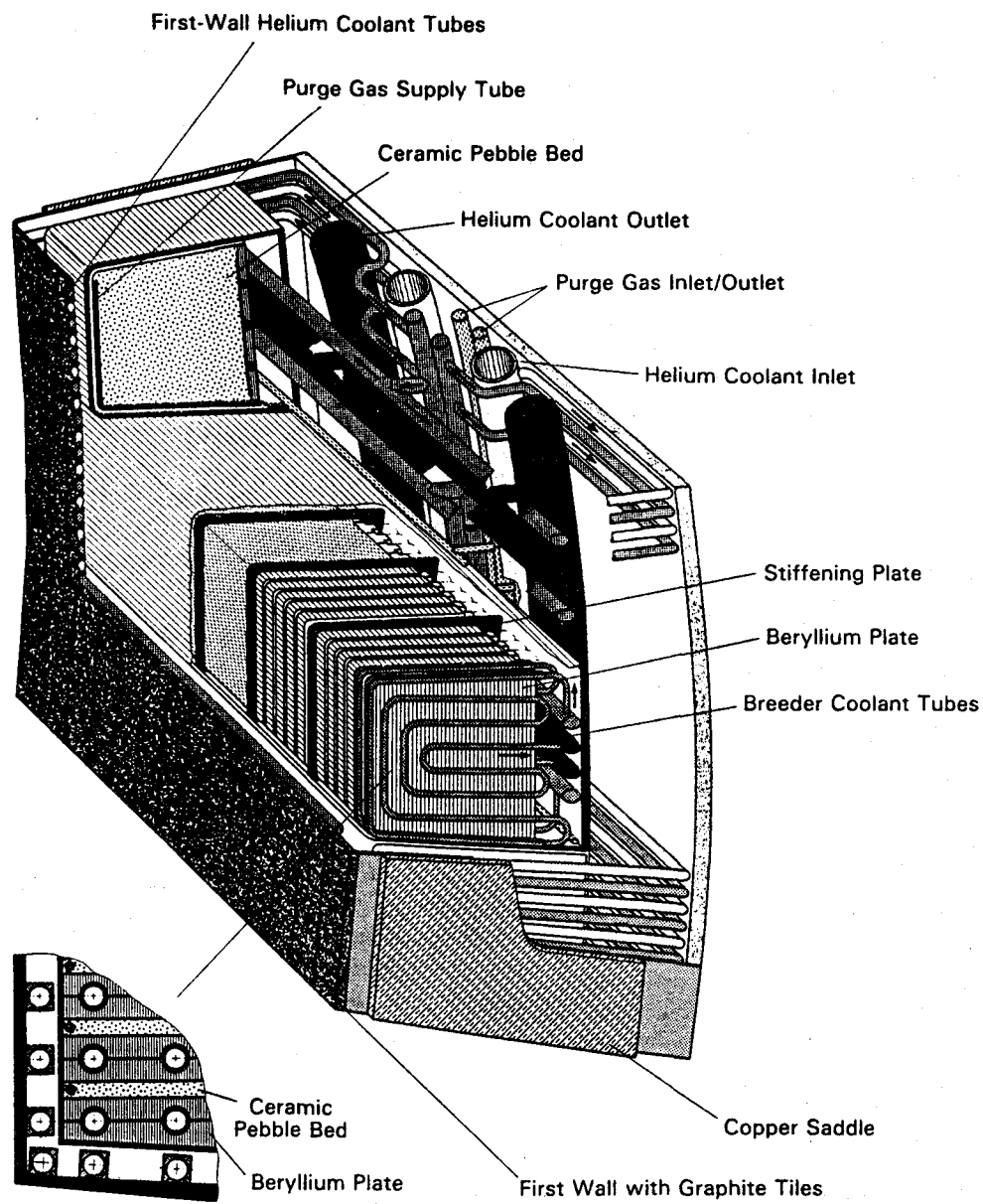


Fig. 1.11 Typical arrangement of the BOT type blanket.

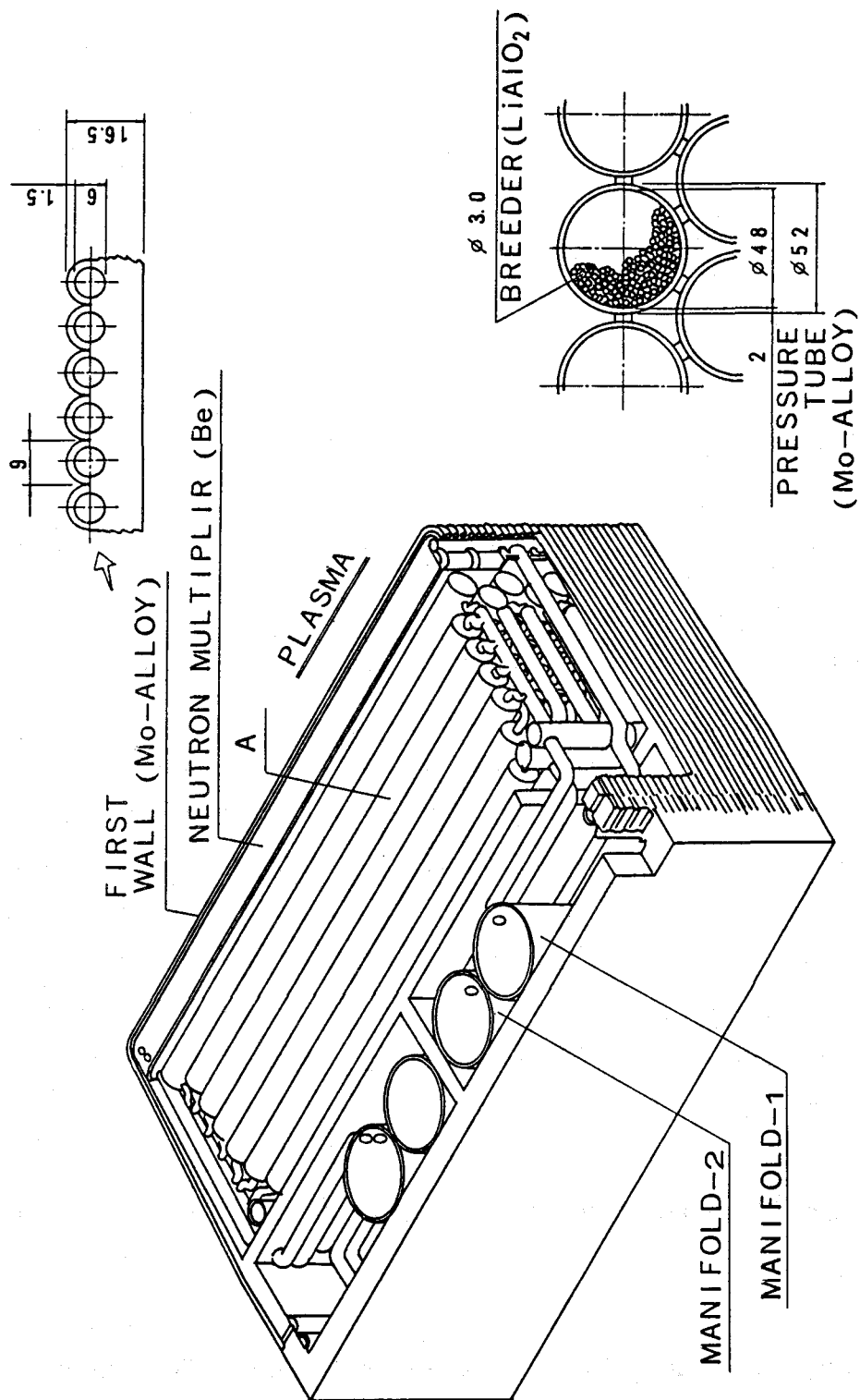


Fig. 1.12 An example of the BIT type blanket (Mo-alloy/LiAlO<sub>2</sub>/He/Be blanket).



usually utilized as a shielding material, since the neutron energy is not so high. However, there sometimes exists a particular region requiring a strong shield locally. Heavy concrete can be available in that case. On the other hand, in fusion reactor, it is expected that heavy concrete can be employed as biological shield in order to attenuate high energy neutrons and gamma-rays leaking from the first wall region via non-elastic neutron scatterings with heavy or medium heavy nuclides, because metal material like stainless steel is thought to be a promising candidate as a structural material for fusion reactor.

In case of a shielding analysis of an experimental result for ordinary concrete, in general the experimental and analysis results often disagree with each other, since the estimate of water content in the ordinary concrete is difficult<sup>(69)</sup>. Heavy concrete contains, in addition, heavy aggregates such as high density ores, iron punchings and so on. It has therefore heterogeneous structure to make the shielding analysis more complicated. The addition of aggregates can certainly improve the shielding performance. However, depending upon the dimensions the estimation of the shielding performance including the effect of the heavy aggregates becomes difficult. In the shielding design, to avoid this difficulty a conservative modeling is usually employed assuming that the concrete has a minimum density allowed in law and there exist no heavy aggregates in it.

From the stand point of shielding performance, we know that the best way is to use powder iron as an absorber instead of aggregates to remove the heterogeneity. But this is not a practical method because the necessary cost is getting extremely high. Consequently, in this application, the usefulness of the irregular arrangement is not reflected, but as an available and low-cost shielding method heavy concrete with heavy aggregates is quite effective. To aim at more rational core shielding design, it should be examined how much heterogeneity effect the heavy concrete has and how large the dimensions of the heavy aggregates are available not to deteriorate the shielding performance.

## **I.5 Conventional neutron transport method in irregularly distributed geometries**

The shape of irregularly distributed geometries discussed so far is mostly sphere. Of course, the shape available for the developed method is not always sphere. However, in practical applications, spherical elements are generally utilized because they have various advantages.

Moreover, it does not matter significantly whether a treated element is spherical or not. It is a problem how they are distributed in phase space. The direction of the geometry arranged is not a serious issue. Therefore in the following discussion, we treat spherical element unless pointed out.

In the following two sections, the conventional transport methods to deal with irregularly distributed geometries are described for diffusion,  $S_N$  and Monte Carlo theories.

### **I.5.1 Diffusion and $S_N$ methods**

Over 20 years ago, an idea of using a spherical fuel element in thermal reactor was proposed. Various contrivances were considered for simulating the neutron transport in a system having irregularly distributed spherical fuel elements. Tsuchihashi and Gotoh<sup>(70)</sup> had studied the effective resonance absorption of irregularly distributed CFPs in a graphite matrix using a radial distribution function (RDF) derived from the Percus-Yevick (P-Y) equation<sup>(71)</sup>. Their method was implemented in the SRAC code system<sup>(26)</sup> which was used for cross check calculations of the design method of HTTR. Lieberoth and Stojadinovic<sup>(72)</sup> investigated the problem of neutron diffusion in a pebble-bed reactor core. They obtained a theoretical expression of  $D/D_H$  ( $D$ : diffusion constant,  $D_H$ : homogeneous diffusion constant) and compared it with the result of spherical-fuels mock-up experiment. Segev and Caner<sup>(73)</sup> added the function to the WIMS code which was capable of calculating the homogeneous-collapsed cross section of pebble bed fuels possessing a double heterogeneity structure, by modifying the cluster option of WIMS, originally developed for Canada deuterium uranium (CANDU)-type clusters. This method is capable of treating resonance absorption in a double heterogenous lattice.

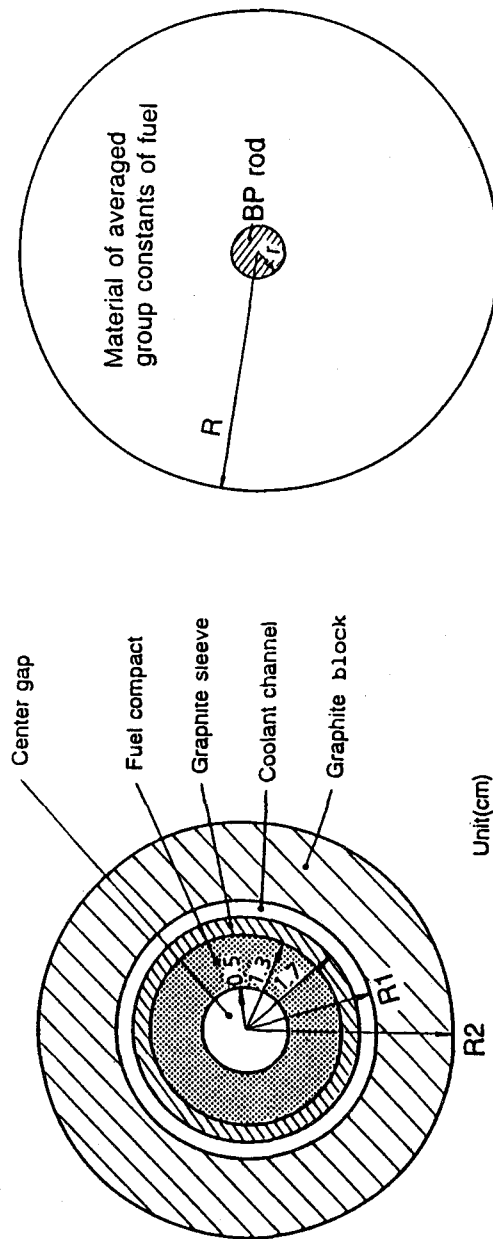
As mentioned above, such physical quantities as group constants, diffusion coefficient and so on for cores having spherical fuels could be calculated with some approximate methods. However, no transport codes to treat irregularly distributed spherical fuels directly exist today.

In addition, several studies on core design analyses of reactors with CFPs have been performed. In the AVR, the reactor core analysis was performed using a diffusion code with the group constants of the homogenized core<sup>(74)</sup>. It means that the design ignored the irregular arrangement of fuel pebbles. Also the nuclear design of HTTR was performed with the 3-dimensional diffusion code CITATION-1000VP after preparing the group constants by a 1-dimensional cell burnup code DELIGHT<sup>(75)</sup>. In this case, the irregular arrangement of CFPs was

considered approximately with the collision probability method.

Summarizing the discussion, generally when we intend to analyze irregularly distributed geometries such as HTGRs, because all the locations of spherical fuel elements cannot be specified, and in addition even if we have the whole data, it is not a practical method to model all the spherical fuel elements, we usually have to apply a conventional calculation method like the diffusion or  $S_N$  methods to the neutron transport evaluation, as follows: First we have to prepare the group constants specifically for the fuel region after calculating the neutron spectrum around there approximately. The full core calculation can be conducted with the model smearing the fuel region using the group constants. The model used for the preparation of group constants is called super cell model. For example, in the nuclear design of the HTTR core the group constants were calculated by the collision probability method with the model described in Fig. 1.13<sup>(75)</sup>, and in the case of AVR a whole smeared model was utilized in the design<sup>(13)</sup>. These procedures were practically being applied to other-type nuclear reactor designs. However, we could not exclude the inherent error due to the approximation contained in the neutron spectrum calculation of the fuel element. In case of analyzing HTGR cores, the effect of the local configuration of spherical fuel elements, i.e., some are in contact with each other while some are not, therefore they are arranged probabilistically in a certain spatial probability distribution, cannot be exactly taken into consideration with the conventional methods. Also in these cases, it is impossible to ascertain whether or not the calculations can exactly reproduce the reactivity effect of spherical fuel elements by either experiment or calculation (of course, this is really realized by the developed method in the present study). Moreover, as discussed in Sec. I.2, for the critical approach analysis of HTTR, the MVP calculations fairly revised the results obtained by the nuclear design code system. In advance, we confirmed that the analyses of the VHTRC core with MVP well reproduce the experimental ones.

As for other applications of irregularly distributed geometries described in detail in Sec. I.3, such as high energy particle accelerator, fusion blanket, hybrid reactor for nuclear waste incineration and so on, particles (mainly neutrons) transport not always in a criticality system. It means that neutron anisotropic scattering becomes dominant compared with thermal reactor because the neutron energy is high enough to distort angular distribution of the emitted neutrons. Neutrons, as a result, strongly flow outward in the biological shield, and the neutron spectrum varies depending on the transmitting length in the shield. For this reason, we cannot prepare appropriate group constants using the super cell model. A simple smeared model thus should be



R1: Outer radius of coolant channel

R2: Outer radius of fuel cell

(a) Fuel cell model.

R: Outer radius of BP cell

r: Outer radius of BP rod

(b) BP cell model.

Fig. 1.13 One-dimensional cylindrical calculation models for DELIGHT.

used in that case. Nevertheless, if no strong absorber exists in the region of interest, the simple smeared model calculation may give a fairly good approximated result. However, a serious problem is still left that an accurate analysis, like a reference solution, considering even an surrounding radiation shield such as a biological shield cannot be done with the simple smeared model.

In addition, we have to mention the treatment of irregularly distributed geometries by the group-wise Monte Carlo method. The basic cross section preparation is exactly the same as the conventional diffusion and  $S_N$  methods. As a general purpose three dimensional Monte Carlo code, the group-wise Monte Carlo code has a little advantage of them from the stand point of modeling. Nevertheless, the continuous energy Monte Carlo code finally defeats the group-wise Monte Carlo code completely when we consider the fact that the point-wise cross section data is superior to the group-wise data.

### **1.5.2 Continuous energy Monte Carlo method**

Except application of irregularly distributed spherical geometry, the continuous energy Monte Carlo code has been used for years as a reference calculation method to confirm availability of various methods, because as is well known there is no approximation in the calculation procedure (Of course, as recognized in general, strictly speaking, some approximated processes cannot be avoided). However, there was no trial of applying it to the analysis of irregularly distributed spherical geometry, because a great number of spherical elements distributed irregularly cannot be modeled exactly. Moreover, there is a severe issue that it requires an extreme long CPU time to obtain a solution with an acceptable good statistics, although many scientists admit the inherent potential with respect to the fundamental calculation performance. For this reason, the study about this matter has not been progressed strongly so far, though the HTGR research and development started. However, recently, combined with improvement of the computation performance, the continuous energy Monte Carlo code has been gradually applied to various analyses in order to exhibit its ability to give a reference answer. Recently, the calculation by explicit representation of the individual fuel particle distributed irregularly for VHTRC core analysis was reported by Difilippo<sup>(76)</sup>. In his study, heterogeneous precise calculations were carried out assuming that the fuel particles in fuel compact were arranged in a cubic lattice, the cell size of which is given by the average number of fuel particles per unit volume. More recently, Nojiri<sup>(19)</sup>

in JAERI adopted a method to separate reactivity effects of irregularly distributed spherical fuel elements and the other region. He evaluated beforehand the reactivity effect of irregularly distributed spherical fuel elements of VHTRC fuel compact by the SRAC system. And the effect was added to the Monte Carlo calculated reactivity for the core model in which the fuel compact is just smeared. These methods are last resorts of applying continuous energy Monte Carlo method to the analysis of irregularly distributed spherical elements. However, it is indistinct that if their methods can reproduce the real configuration properly. Especially for the former method, it is easily expected that it requires a lot of time and effort to prepare the calculation model and conduct the complete computation. Actually, it is impossible to prefer this method in order to carry out the parameter survey analyses for the neutronic design work of HTGRs such as HTTR, because as mentioned earlier there are about 13000 CFPs in the HTTR fuel compact and several tens-thousands of fuel compacts are loaded in the core<sup>(58)</sup>.

In the existing circumstances, the continuous energy Monte Carlo code having a lot of advantages in neutron transport problem, is not always an available method for the analysis of irregularly distributed spherical geometries in view of the discussion above.

## **I.6 Purpose of the study**

A calculation route for the analysis of HTGRs with irregularly distributed spherical fuel elements having various merits exists at present, that is to utilize the group constants prepared through the cell calculation with a super cell model. However, the method never gives the reference solution and it is not confirmed how the reactivity effect is reproduced appropriately through experiment. Also as described in Sec. I.2, in case of analyzing a little complicated core configuration for such as a temporary core during a critical approach, the agreement of the calculated results using the conventional methods with the experimental results is not satisfied. Moreover, as mentioned in Sec. I.4, in the future world in which the fusion reactor is put to practical use for electricity supply and the large-scale high energy proton linac will be constructed for basic study of nuclear waste incineration, extra-high energy neutrons generated in their facilities are scattered anisotropically with material atoms through inelastic nuclear reactions and therefore the scattered neutrons strongly flow outward. To simulate such circumstances specifically for a system having irregularly distributed spherical elements and evaluate an acceptable reference solution with a good statistics for the whole region of interest are critically

difficult by the conventional methods even with some approximate methods.

On the other hand, as shown in Sec. I.3, continuous energy Monte Carlo code is a powerful tool to obtain a direct exact solution with no approximation. Since it can deal with an anisotropic scattering strictly, it is regarded as an ideal method to apply to the problem to be solved in the future facility design work above. But the advantage of not utilizing group constants leads to the disadvantage that it could not cope with irregularly distributed spherical geometry such as HTGR core. In such a difficult situation, improvement of computation technology enables a Monte Carlo code to do every complicated analysis, i.e., such as an extreme precise analysis for various nuclear facilities with the complete full facility model as they are constructed. However, as pointed out in Sec. I.3, it is true that there remain several functions to be investigated in the near future in order to use it for practical design work. The issue of how to treat irregularly distributed spherical elements taken up in the thesis is one of such problems. And when they are completely solved, more rational designs for nuclear reactors, future high energy particle accelerators and so on are successfully realized.

The purpose of the present study is to establish a basic method of sampling a geometry itself during particle transport calculation with continuous energy Monte Carlo method for the system having a lot of irregularly distributed spherical fuel elements such as HTGRs, in order to achieve highly accurate calculation for them which becomes equivalent to a reference solution. The developed method in this study is very unique and has for the first time enabled us to analyze such geometries with almost no approximation. Also, it is exactly a fundamental and universal procedure to treat irregularly distributed elements by continuous energy Monte Carlo method. It is thus expected to contribute to design studies of various future applications with irregularly distributed elements in such as high energy accelerators and fusion blankets as well as HTGRs.

## REFERENCES

- (1) K. Ott, *Prog. Nucl. Energy*, **29**, 81 (1995).
- (2) C. Marchetti, *Nucl. Sci. Eng.*, **90**, 521 (1985).
- (3) "Present Situation of Research on Nuclear Safety, 1990," Japan Atomic Energy Research Institute (1990).
- (4) "Present Status of Transmutation Research and Development - Breakthrough Possibility in Nuclear Technology," Atomic Energy Society of Japan (1994).
- (5) Y. Iso, "Present Status of Fusion Research and Development at Japan Atomic Energy Research Institute," *Proc. 10th Symp. Fusion Eng.*, **34** (1983).
- (6) S. Saito, "Present Status of HTGR Development Program in Japan," *Energy, Oxford*, **16**, 129 (1991).
- (7) K. Itoh et al., "Technical Report on Monju's Sodium Leak Incident," *J. Atomic Energy Soc. Japan*, **39**, 704 (1997).
- (8) R. Aymer, *Fusion Eng. Des.*, **36**, 9 (1997).
- (9) M. Yamamoto and K. Matsumoto, *Nucl. Technol.*, **89**, 194 (1990).
- (10) S. Saito et al., "Design of High Temperature Engineering Test Reactor," *JAERI-1332*, Japan Atomic Energy Research Institute (1994).
- (11) Y. Kaneko et al., "Critical Experiments on Enriched Uranium Graphite Moderated Cores," *JAERI-1257*, Japan Atomic Energy Research Institute (1978).
- (12) H. Yasuda et al., "Construction of VHTRC (Very High Temperature Reactor Critical Assembly)," *JAERI-1305*, Japan Atomic Energy Research Institute (1986).
- (13) R. Shindo, K. Yamashita and I. Murata, "DELIGHT-7; One Dimensional Fuel Cell Burnup Analysis Code for High Temperature Gas-cooled Reactors (HTGR)," *JAERI-M 90-048*, Japan Atomic Energy Research Institute (1990).
- (14) L. D. Latherop and F. W. Brinkley, "TWOTRAN-2: An Interfaced Exportable Version of the TWOTRAN Code for Two-Dimensional Transport," *LA-4848-MS*, Los Alamos National Laboratory (1973).
- (15) H. Harada and K. Yamashita, "The Reactor Core Analysis Code CITATION-1000VP for High Temperature Engineering Test Reactor," *JAERI-M 89-135*, Japan Atomic Energy Research Institute (1989).
- (16) K. Yamashita et al., "Accuracy Investigation of Nuclear Design Method for High



- Temperature Engineering Test Reactor (HTTR) Based on VHTRC Experimental Data," *JAERI-M 88-245*, Japan Atomic Energy Research Institute (1988).
- (17) F. Akino et al., "Critical Experiment on Initial Loading Core of Very High Temperature Reactor Critical Assembly (VHTRC)," *J. Atomic Energy Soc. Japan*, **31**, 682 (1989).
  - (18) T. Mori and M. Nakagawa, "MVP/GMVP: General Purpose Monte Carlo Codes for Neutron and Photon Transport Calculations Based on Continuous Energy and Multigroup Methods," *JAERI-Data/Code 94-007*, Japan Atomic Energy Research Institute (1994).
  - (19) N. Nojiri et al., "Evaluation of Accuracy of Monte Carlo Code MVP with VHTRC Experiments -Multiplicaiton Factor at Criticality, Burnable Poison Worth and Void Worth-," *JAERI-Tech 97-060*, Japan Atomic Energy Research Institute (1997).
  - (20) N. Fujimoto et al., "Preliminary Analyses for HTTR's Start-up Physics Tests by HTTR Nuclear Characteristics Evaluation Code System," *JAERI-Tech 98-021*, Japan Atomic Energy Research Institute (1998).
  - (21) T. B. Fowler, D. R. Vondy, and G. W. Cunningham, "Nuclear Reactor Core Analysis Code: CITATION," *ORNL-TM-2496*, Oak Ridge National Laboratory (1971).
  - (22) W. W. Engle, Jr., "A Users Manual for ANISN; A One Dimensional Discrete Ordinates Transport Code with Anisotropic Scattering," *K-1693*, Union Carbide Corporation (1967).
  - (23) F. R. Mynatt et al., "The DOT III Two-dimensional Discrete Ordinates Transport Code," *ORNL-TM-4280*, Oak Ridge National Laboratory (1971).
  - (24) J. F. Briesmeister, "MCNP-A General Monte Carlo Code for Neutron and Photon Transport, Version 3A," *LA-7396-M, Rev.2*, Los Alamos National Laboratory (1990).
  - (25) E. A. Straker et al., "The MORSE Code- A Multigroup Neutron and Gamma-Ray Monte Carlo Transport Code," *ORNL-4585*, Oak Ridge National Laboratory (1970).
  - (26) K. Tsuchihashi et al., "Revised SRAC Code System," *JAERI-1302*, Japan Atomic Energy Research Institute (1986).
  - (27) U. Hansen and E. Teuchert, "The V.S.O.P. reactor code system," *Joint Dragon-KFA Report* (1975).
  - (28) I. Murata et al., "Reactor Shielding Design of the High Temperature Engineering Test Reactor - Analysis of Radiation Streaming through the Standpipes by Monte Carlo Code MCNP -," *Proc. 8th Int. Conf. on Radiation Shielding*, Arlington, 359 (1994).
  - (29) J. Spanier and E. M. Gelbard, "Monte Carlo Principles and Neutron Transport Problems," Addison-Wesley Publishing Company.

- (30) T. E. Booth and J. S. Hendricks, *Nucl. Technol./Fusion*, **5**,90 (1984).
- (31) A. Dubi, A. Goldfeld, and K. Burn, *Nucl. Sci. Eng.*, **93**,204 (1986).
- (32) T. E. Booth, *Nucl. Sci. Eng.*, **104**,374 (1990).
- (33) R. S. Baker and E. W. Larsen, "A 'Local' Exponential Transform Method for Global Variance Reduction in Monte Carlo Transport Problems," *LA-UR-92-2349*, Los Alamos National Laboratory (1992).
- (34) I. Murata, R. Shindo and S. Shiozawa, *J. Nucl. Sci. Technol.*, **32**, 971 (1995).
- (35) D. F. Hollenbach, L. M. Petrie, and H. L. Dodds, *Nucl. Sci. Eng.*, **116**,147(1994).
- (36) F. Brown, "Present Status of Vectorized Monte Carlo," *Trans. Am. Nucl. Soc.*, **55**,323 (1987).
- (37) M. Takano et al., "Parallelization of Monte Carlo Shielding Code MCACE and Monte Carlo Criticality Code KENO-IV," *J. Atomic Energy Soc. Japan*, **34**, 533 (1992).
- (38) F. Masukawa et al., "Parallelization of MCNP4, a Monte Carlo Neutron and Photon Transport Code System, in Highly Parallel Distributed Memory Type Computer," *JAERI-M 93-210*, Japan Atomic Energy Research Institute (1993).
- (39) M. L. Williams and W. W. Engle, Jr., *Nucl. Sci. Eng.*, **62**, 92 (1977).
- (40) L. B. Levitt, "The Application of Monte Carlo Methods to the Design of Invessel Shielding in a Large LMFBR," *Trans. Am. Nucl. Soc.*, **39**, 768 (1981).
- (41) I. Murata, R. Shindo, and S. Shiozawa, "Reactor Shielding Design of the High Temperature Engineering Test Reactor - Application of 3-dimensional Monte Carlo Code MCNP to Shielding Analysis for Thick and Complicated Structure -," *Proc. 8th Int. Conf. on Radiation Shielding*, Arlington, 365 (1994).
- (42) T. M. Flanders and M. H. Sparks, *Nucl. Sci. Eng.*, **103**, 265 (1989).
- (43) I. Murata, T. Mori, and M. Nakagawa, *Nucl. Sci. Eng.*, **123**, 96 (1996).
- (44) M. Nakagawa and T. Mori, *J. Nucl. Sci. Technol.*, **30**, 692 (1993).
- (45) J. S. Hendricks and T. E. Booth, "MCNP Variance Reduction Overview," *LA-UR-85-1173*, Los Alamos National Laboratory (1985).
- (46) T. Kitada, T. Takeda and E. Saji, *J. Nucl. Sci. Technol.*, **32**, 683 (1995).
- (47) Y. Naito et al., "Burnup Code for Fuel Assembly by Monte Carlo Code, MKENO-BURN," *JAERI-Data/Code 96-37*, Japan Atomic Energy Research Institute (1996).
- (48) J. E. Hoogenboom, "FOCUS: A Non-Multigroup Adjoint Monte Carlo Code with Improved Variance Reduction," *ANL-75-2*,243 (1974).
- (49) A. D. Matteis and R. Simonini, *Nucl. Sci. Eng.*, **65**, 93 (1978).

- (50) R. J. Brissenden, "Continuous Energy Adjoint Monte Carlo," *Prog. Nucl. Energy*, **24**, 129 (1990).
- (51) B. Eriksson et al., *Nucl. Sci. Eng.*, **37**, 410 (1969).
- (52) R. Schulten, *Atomwirtschaft Atomtechnik*, **11**, 218 (1966).
- (53) L. Massimo, "Physics of High Temperature Reactors," Pergamon Press, Oxford (1976).
- (54) M. Kawai and Y. Matoba (Eds.), "Challenge to Time Axis," *J. Atomic Energy Soc. Japan*, **33**, 818 (1991).
- (55) H. Sekimoto and T. Osawa (Eds.), "Research and Development of Transmutation of High Level Radioactive Waste," *J. Atomic Energy Soc. Japan*, **37**, 159 (1995).
- (56) T. Ogawa, T. Mukaiyama, H. Takano, T. Takizuka, Y. Suzuki and M. Osakabe, "Fuel Elements and Fuel Cycle Concepts of Actinide Burner Reactors -Conceptual Study of Actinide Burner Reactors (IV)-," JAERI-M 89-123, Japan Atomic Energy Research Insititute (1989).
- (57) K. Yamashita et al., "Destruction of Weapons-Grade Plutonium with Pebble Bed Type HTGRs Using Burner Balls and Breeder Balls," *J. At. Energy Soc. Japan*, **36**, 865 (1994).
- (58) K. Fukuda et al., "Research and Development of HTGR Fuels," JAERI-M 89-007, Japan Atomic Energy Research Institute (1989).
- (59) I. Murata and A. Takahashi, "Analysis of Critical Assembly Experiments by Continuous Energy Monte Carlo Method with Statistical Geometry Model," *Technol. Repts. Osaka Univ.*, **48**, 19 (1998).
- (60) "Fort St. Vrain Nuclear Generation Station Final Safety Analysis Report," Docket-50267, Public Service Company of Colorado (1970).
- (61) R. Brogli et al., *Energy, Oxford*, **16**, 507 (1991).
- (62) H. W. Graves, "Nuclear Fuel Management," John Wiley & Sons, Inc. (1979).
- (63) K. Yamashita et al., *J. Nucl. Sci. Technol.*, **31**, 470 (1994).
- (64) T. Tone et al., "Technical Evaluation of Major Candidate Blanket Systems for Fusion Power Reactor," JAERI-M 87-017, Japan Atomic Energy Research Institute (1987).
- (65) M. D. Donne et al., *Fusion Technol.*, **14**, 1357 (1988).
- (66) "Conceptual Design of Fusion Experimental Reactor (FER)(FY 1983 Report)," JAERI-M 84-212, Japan Atomic Energy Research Institute (1984).
- (67) INTOR Group, "INTOR: Phase Two A Part I," IAEA, Vienna (1983).
- (68) W. M. Stacey et al., *Fusion Technol.*, **27**, 326 (1995).
- (69) V. M. Raghunath et al., *Nucl. Instr. and Meth.*, **206**, 303 (1983).

- (70) K. Tsuchihashi and Y. Gotoh, *Nucl. Sci. Eng.*, **58**, 213 (1975).
- (71) J. K. Percus and G. J. Yevick, *Phys. Rev.*, **110**, 1 (1957).
- (72) J. Lieberoth and A. Stojadinovic, *Nucl. Sci. Eng.*, **76**, 336 (1980).
- (73) M. Segev and M. Caner, *Nucl. Sci. Eng.*, **112**, 43 (1992).
- (74) W. Drechsel, G. Ivens and A. Schatz, *Atomwirtschaft Atomtechnik*, **11**, 265 (1966).
- (75) K. Yamashita et al., *Nucl. Sci. Eng.*, **122**, 212 (1996).
- (76) F. C. Difilippo, "Applications of Monte Carlo Methods for the Analysis of MHTGR Case of the VHTRC Benchmark," *ORNL/TM-12698*, Oak Ridge National Laboratory (1994).

## II. THEORY

### II.1 Introduction

In this chapter, a new method developed in this study to deal with irregularly distributed geometries by Monte Carlo method is presented in detail<sup>(1-4)</sup>. First, the theoretical approach of the sampling method is described. The theoretical expression is based on the famous Monte Carlo text written by Spanier and Gelbard<sup>(5)</sup>, and Irving's report<sup>(6,7)</sup> having been referred when developing the Monte Carlo code MORSE<sup>(8)</sup>. However, maybe we can understand the present theory easier by examining a practical transport process in a Monte Carlo simulation. Such explanation is also tried to help reader to understand the theory. As for sampling theory, after introducing and investigating three candidates, the packing simulation method was chosen. This is also well known as the molecular dynamics (MD) method. The selection story is discussed in the present paper. Another feature is that probability density or probability distribution function necessary is used for the developed sampling process. The probability distribution is calculated with a newly developed computer code. Various statistical quantities with respect to the simulated packing state can be calculated with the code and are used for the validation of the method. The practical method of sampling and arranging geometry in a Monte Carlo simulation is successfully developed by precisely analyzing the algorithm of Monte Carlo transport process. Since the developed method includes a basic and universal sampling process to treat irregularly distributed geometries as explained in the later sections, this method is expected to be used in various applications in the future. The most difficult issue in the newly modified Monte Carlo code in which the developed sampling method was implemented is interference effect of arranged geometries with the boundary of the container, which made the sampling algorithm very complicated. It requires two codes corresponding to high and low packing fractions of irregularly distributed geometries, since the packing fraction of three dimensional random packing has an upper limit value as clarified later in detail. The code for low packing fraction can simulate a real arrangement more accurately. The code for high packing fraction includes a slight approximate process in geometry sampling near the boundary of the container. The above-mentioned developing process is described precisely in the following sections and this is the essence of the present study.

## II.2 Tracking method of irregularly distributed geometries

In this section, how to simulate irregularly distributed geometries by Monte Carlo method in a particle transport simulation is presented. In Sec. II.2.1, for preparation of understanding the essential Monte Carlo sampling, treatment of the Boltzmann equation for particle transport by Monte Carlo method is given. In this paper, neutrons, photons and so on which move in the system are called 'particle'. Practical procedure to simulate irregularly distributed geometries is detailed in Sec. II.2.2 from both stand points of theoretical and phenomenological approaches to clarify the developed method.

### II.2.1 Monte Carlo sampling of the Boltzmann equation

Neutron transport phenomenon is expressed strictly with the integro-differential Boltzmann equation for particle neutron transport as shown in the next equation,

$$\vec{\Omega} \cdot \nabla \phi(\vec{r}, \vec{E}) + \Sigma_t(\vec{r}, E) \phi(\vec{r}, \vec{E}) = S(\vec{r}, \vec{E}) + \int d\vec{E}' \Sigma_s(\vec{r}, \vec{E}' \rightarrow \vec{E}) \phi(\vec{r}, \vec{E}') \quad (2.1)$$

where  $\phi(\vec{r}, \vec{E})$  is the flux of particles,  $\Sigma_t(\vec{r}, E)$  and  $\Sigma_s(\vec{r}, E' \rightarrow E)$  are the total and scattering macroscopic cross sections and  $S(\vec{r}, \vec{E})$  is the external source density. Also  $\vec{E}$  is used as  $(E, \vec{\Omega})$ . We use  $\vec{r} = \vec{r}' - R\vec{\Omega}$ , where  $R$  and  $\vec{r}'$  are variables, to convert Eq.(2.1) to its integral form. The relation of  $\vec{r}$ ,  $\vec{r}'$  and so on is shown in Fig. 2.1. As well known, the first term in Eq.(2.1) will be transformed as the next equations (see Fig. 2.2):

$$\begin{aligned} \vec{\Omega} \cdot \nabla \phi(\vec{r}', \vec{E}) &= \Omega_x' \frac{\partial \phi}{\partial x'} + \Omega_y' \frac{\partial \phi}{\partial y'} + \Omega_z' \frac{\partial \phi}{\partial z'} \\ &= - \frac{dx'}{dR} \frac{\partial \phi}{\partial x'} - \frac{dy'}{dR} \frac{\partial \phi}{\partial y'} - \frac{dz'}{dR} \frac{\partial \phi}{\partial z'} \\ &= - \frac{d\phi(\vec{r}', \vec{E})}{dR} \end{aligned} \quad (2.2)$$

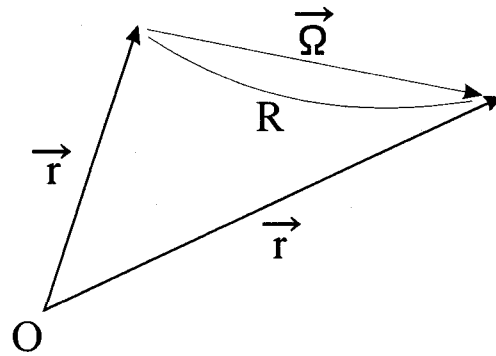


Fig. 2.1 Relation of  $\vec{r}$  and  $\vec{r}'$ .

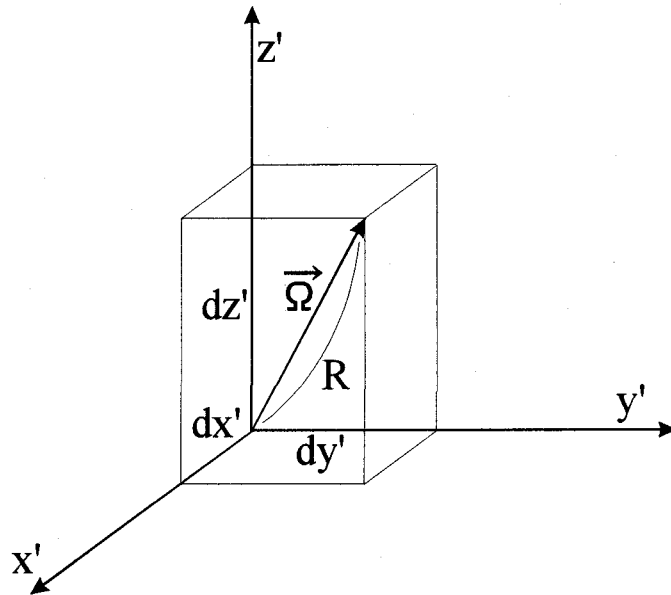


Fig. 2.2 Description of vector  $\vec{R}$  in  $(x', y', z')$  coordinates.

Then we obtain

$$-\frac{d\phi(\vec{r}',\vec{E})}{dR} + \Sigma_t(\vec{r}',E)\phi(\vec{r}',\vec{E}) = S(\vec{r}',\vec{E}) + \int d\vec{E}' \Sigma_s(\vec{r}',\vec{E}' \rightarrow \vec{E})\phi(\vec{r}',\vec{E}') \quad (2.3)$$

Introducing the factor

$$\begin{aligned} & \exp\left(-\int_0^R \Sigma_t(\vec{r}-R'\vec{\Omega},E)dR'\right), \\ & -\frac{d}{dR}\left[\phi(\vec{r}',\vec{E})\exp\left(-\int_0^R \Sigma_t(\vec{r}-R'\vec{\Omega},E)dR'\right)\right] = \exp\left(-\int_0^R \Sigma_t(\vec{r}-R'\vec{\Omega},E)dR'\right) \\ & \times \left[S(\vec{r}',\vec{E}) + \int d\vec{E}' \Sigma_s(\vec{r}',\vec{E}' \rightarrow \vec{E})\phi(\vec{r}',\vec{E}')\right] \end{aligned} \quad (2.4)$$

Thus Eq.(2.4) can be easily integrated from  $R=0$  to  $\infty$ , then

$$\begin{aligned} \phi(\vec{r},\vec{E}) &= \int_0^\infty dR \cdot \exp\left(-\int_0^R \Sigma_t(\vec{r}-R'\vec{\Omega},E)dR'\right) [S(\vec{r}-R\vec{\Omega},\vec{E}) \\ & + \int d\vec{E}' \Sigma_s(\vec{r}-R\vec{\Omega},\vec{E}' \rightarrow \vec{E})\phi(\vec{r}-R\vec{\Omega},\vec{E}')] \end{aligned} \quad (2.5)$$

because  $\phi$  converges to zero if  $R \rightarrow \infty$ . This is called the integral form of the Boltzmann equation.

Next we introduce two kinds of collision densities. This is the key to a solution of the Boltzmann equation by the Monte Carlo method. One is defined as;

$$\psi(\vec{r},\vec{E}) = \Sigma_t(\vec{r},E)\phi(\vec{r},\vec{E}) \quad (2.6)$$

which is the density of particles entering a collision at  $\vec{r}$ . This is usually called simply the collision



density. And the other is defined as;

$$\chi(\vec{r}, \vec{E}) = S(\vec{r}, \vec{E}) + \int d\vec{E}' \Sigma_s(\vec{r}, \vec{E}' \rightarrow \vec{E}) \Phi(\vec{r}, \vec{E}') \quad (2.7)$$

which is the density of particles leaving a real collision point or a source at  $\vec{r}$ .

From Eqs. (2.5) and (2.6), the integral equation for the collision density is derived:

$$\begin{aligned} \Psi(\vec{r}, \vec{E}) = & \int_0^R dR \Sigma_t(\vec{r}, E) \exp \left( - \int_0^R \Sigma_t(\vec{r} - R' \vec{\Omega}, E) dR' \right) \\ & \times \left[ S(\vec{r} - R \vec{\Omega}, \vec{E}) + \int d\vec{E}' \frac{\Sigma_s(\vec{r} - R \vec{\Omega}, \vec{E}' \rightarrow \vec{E})}{\Sigma_t(\vec{r} - R \vec{\Omega}, E')} \Psi(\vec{r} - R \vec{\Omega}, \vec{E}') \right] \end{aligned} \quad (2.8)$$

To facilitate to understand the Monte Carlo transport simulation process, the integral equation is converted to a kernel form. For this purpose, first the equation is transformed into a three dimensional form:

$$\begin{aligned} \Psi(\vec{r}, \vec{E}) = & \int d\vec{\Omega}' \int_0^R R'^2 dR' \frac{\delta(\vec{\Omega}' \cdot \vec{\Omega} - 1)}{R'^2} \Sigma_t(\vec{r}, E) \exp \left( - \int_0^R \Sigma_t(\vec{r} - R' \vec{\Omega}', E) dR' \right) \\ & \times \left[ S(\vec{r} - R \vec{\Omega}', \vec{E}) + \int d\vec{E}' \frac{\Sigma_s(\vec{r} - R \vec{\Omega}', \vec{E}' \rightarrow \vec{E})}{\Sigma_t(\vec{r} - R \vec{\Omega}', E')} \Psi(\vec{r} - R \vec{\Omega}', \vec{E}') \right] \end{aligned} \quad (2.9)$$

where  $d\vec{E}$  is read explicitly as  $dE d\vec{\Omega}$ , and  $\vec{\Omega}' \cdot \vec{\Omega} = (\vec{r} - \vec{r}') / |\vec{r} - \vec{r}'| \cdot \vec{\Omega}$  since setting  $\vec{r}' = \vec{r} - R \vec{\Omega}'$ . Also  $d\vec{r}' = R^2 dR d\vec{\Omega}'$ . Thus we have

$$\Psi(\vec{r}, \vec{E}) = \int d\vec{r}' \Sigma_t(\vec{r}, E) \exp \left( - \int_{\vec{r}' \rightarrow \vec{r}} \Sigma_t(\vec{r}'', E) ds \right) \frac{\delta \left( \frac{\vec{\Omega}' \cdot \vec{r} - \vec{r}'}{|\vec{r} - \vec{r}'|} - 1 \right)}{|\vec{r} - \vec{r}'|^2}$$

$$\times \left[ S(\vec{r}-R\vec{\Omega}', \vec{E}) + \int d\vec{E}' \frac{\Sigma_s(\vec{r}-R\vec{\Omega}', \vec{E}' \rightarrow \vec{E})}{\Sigma_t(\vec{r}-R\vec{\Omega}', E')} \Psi(\vec{r}-R\vec{\Omega}', \vec{E}') \right] \quad (2.10)$$

where

$$\int_{\vec{r}' \rightarrow \vec{r}} \Sigma_t(\vec{r}'', E) ds$$

is the integral of  $\Sigma_t$  along the line from  $\vec{r}'$  to  $\vec{r}$ .

Next we introduce the transport kernel,

$$T(\vec{r}', \vec{r} | \vec{E}) = \Sigma_t(\vec{r}, E) \exp \left( - \int_{\vec{r}' \rightarrow \vec{r}} \Sigma_t(\vec{r}'', E) ds \right) \frac{\delta \left( \frac{\vec{\Omega}' \cdot \vec{r} - \vec{r}'}{|\vec{r} - \vec{r}'|} - 1 \right)}{|\vec{r} - \vec{r}'|^2} \quad (2.11)$$

and the collision kernel:

$$C(\vec{E}', \vec{E} | \vec{r}) = \frac{\Sigma_s(\vec{r}, \vec{E}' \rightarrow \vec{E})}{\Sigma_t(\vec{r}, E')} = \frac{\Sigma_s(\vec{r}, E')}{\Sigma_t(\vec{r}, E')} \cdot \frac{\Sigma_s(\vec{r}, \vec{E}' \rightarrow \vec{E} | \vec{r})}{\Sigma_s(\vec{r}, E')} \equiv P_s \cdot C_s \quad (2.12)$$

Consequently, the collision density equation is

$$\Psi(\vec{r}, \vec{E}) = \int d\vec{r}' \cdot T(\vec{r}', \vec{r} | \vec{E}) \left[ S(\vec{r}', \vec{E}) + \int d\vec{E}' \cdot C(\vec{E}', \vec{E} | \vec{r}') \Psi(\vec{r}', \vec{E}') \right] \quad (2.13)$$

Summarizing the above, we can obtain the next two important equations:

$$\Psi(\vec{r}, \vec{E}) = \int d\vec{r}' \cdot T(\vec{r}', \vec{r} | \vec{E}) \chi(\vec{r}', \vec{E}) \quad (2.14)$$

$$\chi(\vec{r}, \vec{E}) = S(\vec{r}, \vec{E}) + \int d\vec{E}' \cdot C(\vec{E}', \vec{E} | \vec{r}) \Psi(\vec{r}, \vec{E}') \quad (2.15)$$

Using these equations, the transport simulation process by Monte Carlo is interpreted as follows: By Eq.(2.14) the collision density  $\Psi(\vec{r}, \vec{E})$  at the next collision position  $\vec{r}$  is determined from  $\chi(\vec{r}, \vec{E})$  and transport kernel, i.e., the reaction place can be determined, then the density leaving collision  $\chi(\vec{r}, \vec{E})$  can be obtained from  $\Psi(\vec{r}, \vec{E})$  and collision kernel, i.e., the energy and scattering angle are fixed. A particle transport is made up of a lot of this basic process using Eqs.(2.14) and (2.15). More practically, the following steps are taken into consideration in a transport simulation process in Monte Carlo code (See Fig. 2.3):

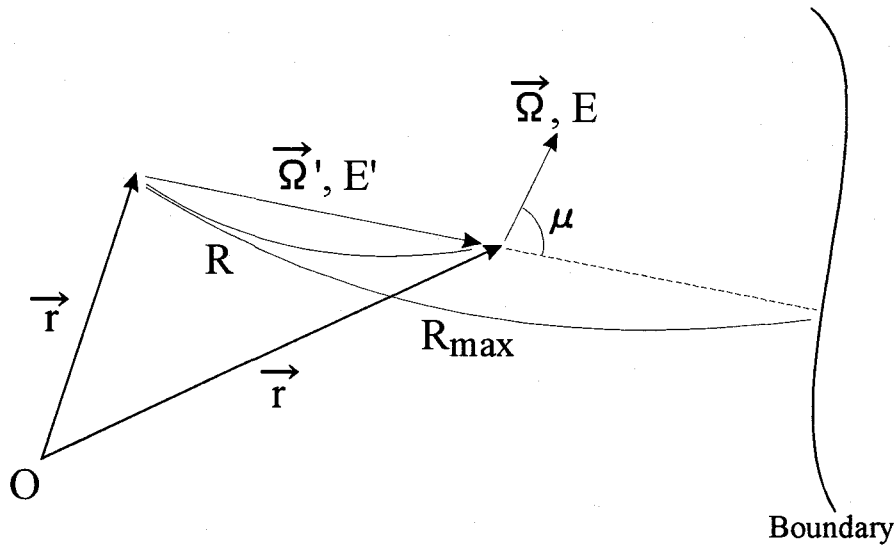


Fig. 2.3 Description of a particle transport process in Monte Carlo simulation.

Step 1: An initial position and energy are chosen from the external source  $S(r, E)$ . The weight and time are appropriately assigned by the user or the default value.

Step 2:  $R_{max}$  is calculated which is defined as the distance from the current particle position to the boundary beyond which the composition is not the same as the current region. The distance R from the current particle position to the next collision position is determined from the transport kernel:

$$\Sigma_s(\vec{r}' + R\vec{\Omega}', E') \cdot \exp\left(-\int_0^R \Sigma_s(\vec{r}' + R'\vec{\Omega}', E') dR'\right) \quad (2.16)$$

The particle position  $\vec{r}$  is set to  $\vec{r}' + R\vec{\Omega}$ . If  $\vec{r}$  is outside the system of interest, the particle has escaped and the history is terminated. If  $R$  is larger than  $R_{\max}$ , the particle has reached the boundary,  $\vec{r}$  is set to  $\vec{r}' + R_{\max}\vec{\Omega}$  and go back to the head of Step 2.

Step 3: Usually in non-analog Monte Carlo code, to realize an efficient calculation particle absorption reaction is prohibited. To compensate the weight effect, at the new collision point  $\vec{r}$  the particle weight  $W$  is adjusted according to the following equation:

$$W = W_{\text{prev}} \cdot P_s(\vec{r}, E') \quad (2.17)$$

where  $W_{\text{prev}}$  is the previous particle weight before collision and  $P_s(\vec{r}, E')$  is the correction factor for absorption:

$$P_s(\vec{r}, E') = \frac{\Sigma_s(\vec{r}, E')}{\Sigma_t(\vec{r}, E')} \quad (2.18)$$

Then weight cut-off check is done, i.e., if the particle weight is below the weight range of interest, the history is terminated.

Step 4: Finally a new energy and direction of the particle are determined from the collision kernel:

$$\begin{aligned} C_s(E', \vec{\Omega}' \rightarrow E, \vec{\Omega} | \vec{r}) &= \frac{\Sigma_s(E', \vec{\Omega}' \rightarrow E, \vec{\Omega} | \vec{r})}{\Sigma_s(\vec{r}, E')} \\ &= \frac{N_A(\vec{r}) \cdot \sum_j \sigma_{Aj}(E')}{\Sigma_s(\vec{r}, E')} \cdot \frac{\sigma_{Aj}(E')}{\sum_j \sigma_{Aj}(E')} f_{Aj}(E', \vec{\Omega}' \rightarrow E, \vec{\Omega}) \end{aligned} \quad (2.19)$$

where  $N_A$  is the atomic number density for nuclide A,

$$\frac{N_A(\vec{r}) \cdot \sum_j \sigma_{Aj}(E')}{\Sigma_s(\vec{r}, E')}$$

is used for sampling of nuclide to be reacted with the incident particle,

$$\frac{\sigma_{Aj}(E')}{\sum_j \sigma_{Aj}(E')}$$

is used for the determination of the reaction type, j, and  $f_{Aj}$  is a normalized function called the scattering kernel. From the scattering kernel, first the  $\mu$  in Fig. 2.3 is sampled from the energy integrated angular distribution, the particle energy E is determined from  $E=E(\mu, E')$  then  $\vec{\Omega}$  is given so as to keep the relation of  $\vec{\Omega} \cdot \vec{\Omega}' = \mu$ .

Step 5: If the new energy, E, is below the energy range of interest, the history is terminated, otherwise we set  $\vec{r}' = \vec{r}$  and  $E' = E$  and go back to Step 2.

This iteration calculation corresponds to estimates using the Von Neumann series for the transport equation. The calculation starts with a source term:

$$\chi_0(\vec{r}', \vec{E}') = S(\vec{r}', \vec{E}') \quad (2.20)$$

Then in Step 2,

$$\psi_0(\vec{r}, \vec{E}') = \int d\vec{r}' \cdot T(\vec{r}', \vec{r} | \vec{E}') \chi_0(\vec{r}', \vec{E}') \quad (2.21)$$

And Steps 3 and 4 produce

$$\chi_1(\vec{r}, \vec{E}) = \int d\vec{E}' \cdot C(\vec{E}', \vec{E} | \vec{r}) \psi_0(\vec{r}, \vec{E}') \quad (2.22)$$

After that, return Step 2 iteratively to calculate

$$\psi_n(\vec{r}, \vec{E}') = \int d\vec{r}' \cdot T(\vec{r}', \vec{r} | \vec{E}') \chi_n(\vec{r}', \vec{E}') \quad (2.23)$$

And by Steps 3 and 4

$$\chi_{n+1}(\vec{r}, \vec{E}) = \int d\vec{E}' \cdot C(\vec{E}', \vec{E} | \vec{r}) \psi_n(\vec{r}, \vec{E}') \quad (2.24)$$

At the termination of all the histories we sum the Von Neumann series to obtain the collision densities:

$$\chi(\vec{r}, \vec{E}) = \sum_{n=0}^{\infty} \chi_n(\vec{r}, \vec{E}) \quad (2.25)$$

This can be estimated by summing all particle weights at the beginning of Step 2, and

$$\psi(\vec{r}, \vec{E}) = \sum_{n=0}^{\infty} \psi_n(\vec{r}, \vec{E}) \quad (2.26)$$

which is also estimated by summing all particle weights at the beginning of Step 3. The flux may be obtained by

$$\phi(\vec{r}, \vec{E}) = \frac{\psi(\vec{r}, \vec{E})}{\Sigma_t(\vec{r}, E)} \quad (2.27)$$

## II.2.2 Basic tracking concept and method

The issue focused on in the present study is how we treat the transport behavior of a particle by the Monte Carlo method in a region where a lot of equal geometries (called base geometry in the following) are distributed irregularly. Of course, we do not prefer the method to model all the base geometries as already described in Chap. 1, because such a method, which is thought to be feasible in principle, cannot be applied to a practical design work. In the following, a base geometry is normally regarded as a sphere to help or facilitate understanding the theory though actually a geometry with an any shape is available in principle.

First we try to explain the essential method from the theoretical point of view. As shown in the previous section, in a Monte Carlo transport simulation iterative processes with Eqs. (2.14) and (2.15) constitute a particle transport history. Practically, the sampling with the transport kernel moves the particle to the next collision site. After sampling from the collision kernel, the particle having a new energy and direction moves by sampling the next transport kernel. Each sampling process with both kernels is independent of other one. Therefore at the beginning of each process, it is just necessary to know the location of the base geometry which the particle is likely to enter next as shown in Fig. 2.4. This fact enables us to move a base geometry to the next

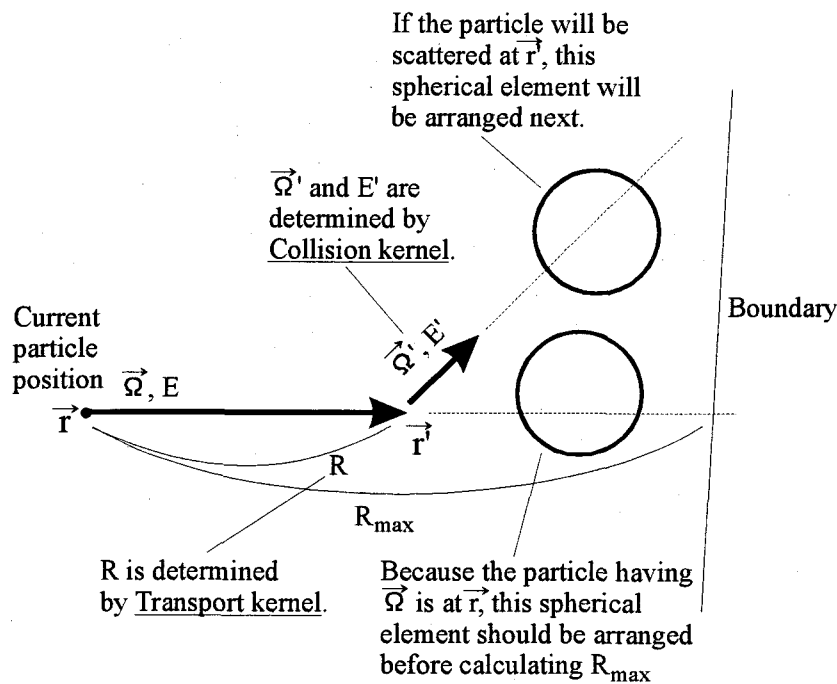


Fig. 2.4 Sampling method with Transport and Collision kernels.

position along the particle transport before every transport kernel sampling. By this method we can avoid modeling all the equal geometries distributed irregularly. Just one base geometry should be modeled. If only arranging the geometry at a proper location along the particle flight path, we can obtain the accurate solution as if all the equal geometries are exactly modeled. As for the practical algorithm in Monte Carlo simulation, if the region which an incident particle enters next is a region where base geometries are packed irregularly, before calculating  $R_{\max}$  at the beginning of Step 2, a process of arranging a base geometry properly should be added. The flow of the sampling is shown in Fig. 2.5. If the particle is scattered with a material atom, after sampling a new energy and direction in Steps 3~5, the arrangement of a base geometry should be done.

A qualitative interpretation of the developed method from the phenomenological point of view is also tried. Similar to the above discussion, we start with a Monte Carlo particle transport simulation in a region containing a lot of base geometries distributed irregularly. In a physical phenomenon occurring in a real particle transport, there exists a basic process that the particle enters a base geometry, then penetrates it, leaves it and enters the next base geometry; as shown in Fig. 2.6. The complete particle transport history in the region consists of many basic processes. Therefore it means that it is not necessary to know the locations of all base geometries at the same time in the calculation. It also means that the transport simulation can be continued only if the location of the base geometry which the particle is likely to enter next is determined when the particle gets out of the previous base geometry or the particle enters a container in which base geometries are distributed irregularly. Considering this fact, we established the method of arranging a base geometry one after another along the particle flight path at a certain place determined probabilistically during a random walk of each particle. Practically, as shown in Fig. 2.6, when the particle reaches point P, a base geometry (sphere in this case) is arranged beforehand at the place where the particle is likely to enter at the next time.

It can be confirmed clearly that the phenomenological explanation is easy to understand rather than the theoretical one. The procedure mentioned above is a new and original method developed in the present study to deal with irregularly distributed geometries in a particle transport simulation by Monte Carlo method.

One of the most difficult issues is how to determine the place where the particle is likely to enter the next base geometry. We have to sample the position of the next base geometry from a proper spatial probability distribution of base geometry. It means that next we need to discuss what kinds of probability distribution to be used and how to sample location of a base



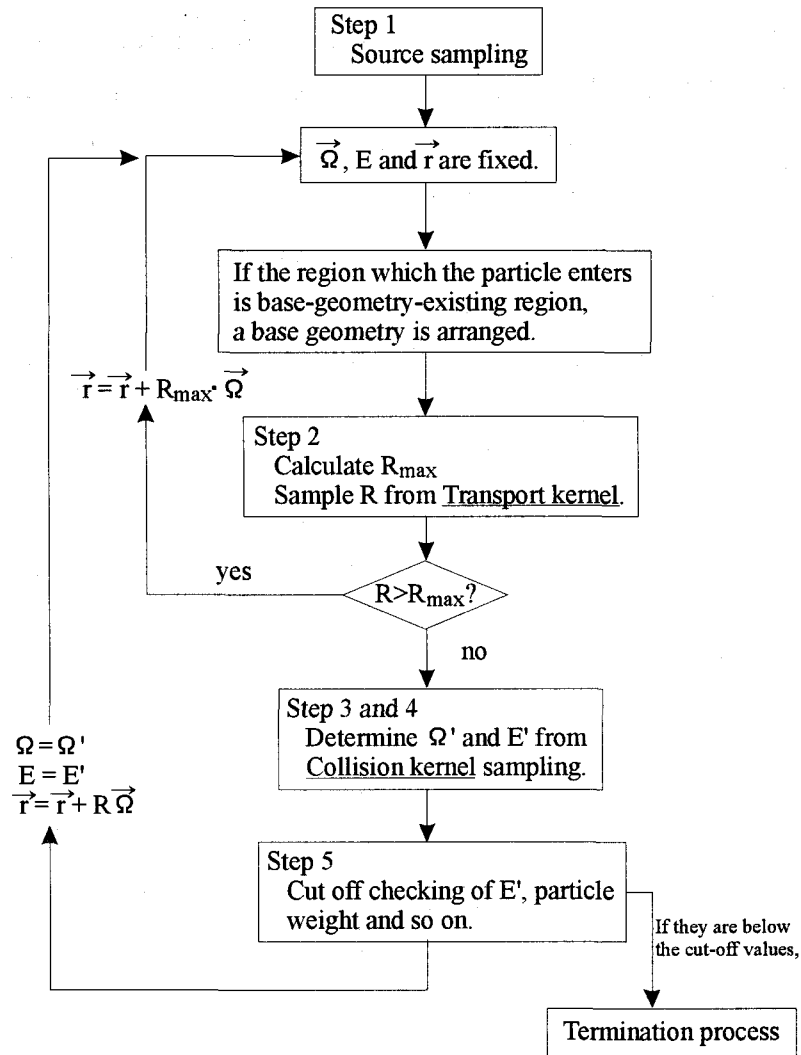


Fig. 2.5 Simplified base geometry sampling flow.

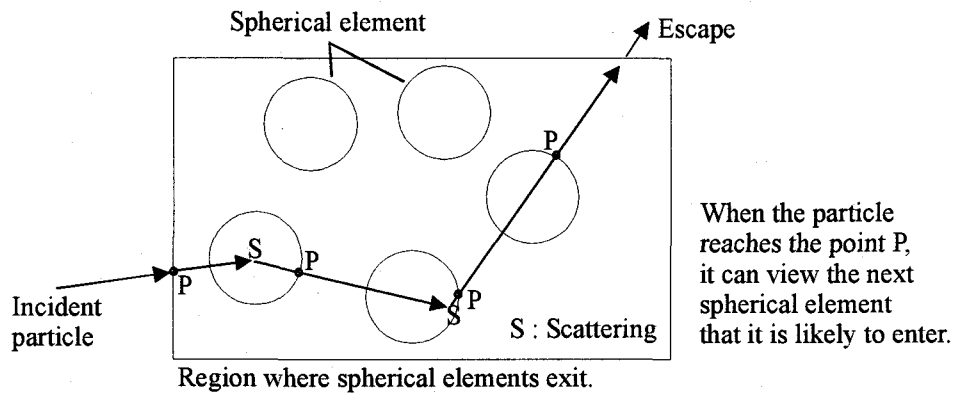


Fig. 2.6 Behavior of transport particle in the region in which irregularly distributed spherical elements exist.

geometry from the probability distribution. We discuss here only the important conditions of the distribution required. Other details to be discussed are given in the following sections.

The necessary probability distribution should give the location of a base geometry to be placed next. The location of the next base geometry can be determined from the particle entering location and the entering angle. Fig. 2.7 illustrates the basic method to determine the location of the next base geometry to be arranged. The essential procedure to arrange a base geometry is understood as the following two steps: (1) Sample the location of an incident particle entering into a base geometry using the probability distribution. (2) Sample the incident angle of the particle entering into the base geometry from an appropriate angular distribution. Therefore, we prepared the probability distribution of the entering location of a particle into the base geometry as a function of the distance from the current particle location and the angular distribution of entering the base geometry. It should be noted that the sampling result from the calculated probability and angular distribution should reproduce the prescribed packing fraction and the real arrangement of base geometries.

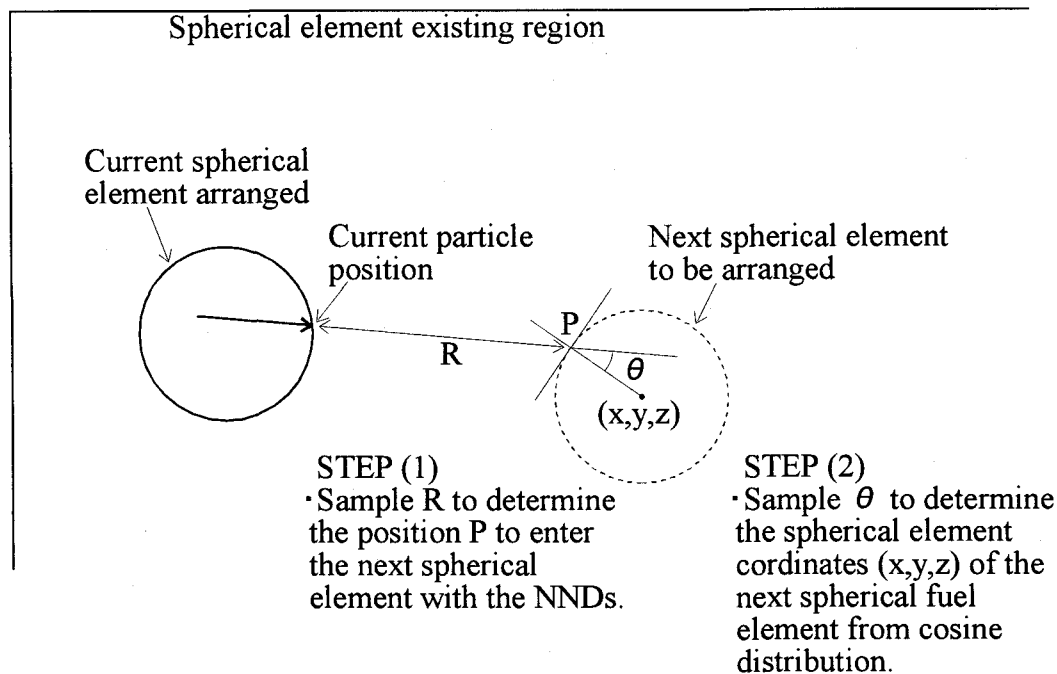


Fig. 2.7 Basic method to determine the location of spherical element to be arranged next.

## II.2.3 Random sampling with probability distribution

In this section, how to sample from the given probability distribution is shown. A more practical expression and procedure will be presented in the following sections. The probability density distribution of which a certain event occurs is expressed in two patterns, i.e., a continuous probability process and a discrete probability process. The former is expressed as

$$p(x)dx = (\text{probability of which } x \text{ can be found between } x \text{ and } x+dx) \quad (2.28)$$

where  $\int p(x)dx=1$ . And for the discrete probability process

$$p(i)=P_i \quad (i=1, \dots, n) \quad (2.29)$$

where the probability of which event  $i$  occurs is  $P_i$  and  $P_1+P_2+\dots+P_n=1$ .

In the present case, the base geometry is normally sphere. The required angular distribution is thus estimated to be cosine distribution theoretically as shown later in the next section. Also, the probability distribution of the entering location of a particle into a base geometry is given by a histogram. The angular distribution is

$$f_{\text{ang}}(\mu)d\mu = 2\mu d\mu, \quad (2.30)$$

where  $\mu = \cos(\theta)$  and  $\theta$  is the incident angle of the particle into sphere. Also the entering location distribution is

$$f_{\text{ent}}(i)=F_i \quad (2.31)$$

where  $i$  is the bin number corresponding to the distance from the current particle location and  $F_i$  is the probability density of which the particle is likely to enter the next base geometry at  $x=x_i \sim x_{i+1}$ . To sample an angle  $\mu$  and a position  $i$ , a random number  $r$  ( $0 < r_i < 1$ ) is prepared. From the next equations,

$$r_1 = \int_1^{\mu} f_{avg}(\mu) d\mu = \mu^2 \quad (2.32)$$

$$r_2 = F_1 + F_2 + \dots + F_i \quad (2.33)$$

$\mu$  (=sqrt( $r_1$ )) and  $i$  can be determined.

## II.3 Probability distribution necessary for geometry sampling

In this section, two probability distributions, introduced in Sec. II.2.2, required for sampling geometry in a Monte Carlo particle transport simulation treating irregularly distributed geometries are described. One is the probability distribution of the particle entering location into a base geometry as a function of the distance from the current particle location assuming that the particle go straight without scattering. The other is the angular distribution of the particle entering the base geometry. The next base geometry is fixed by sequential two samplings with these probability distributions.

The angular distribution is easily expressed theoretically if the base geometries are spheres and distributed statistically at random: Because the geometry of which one can see from the outside of the sphere is a circle, random insertion of particle into the sphere can be regarded as a uniform broad parallel beam as shown in Fig. 2.8. As a result, the angular distribution  $P(r)dr$  is

$$P(r)dr = 2\pi r \cdot dr \quad (2.34)$$

where  $r=R\sin \theta$ , and we set  $\mu = \cos \theta$ , thus

$$dr = R \cdot \cos \theta, \quad d\mu = -\sin \theta \cdot d\theta \quad (2.35)$$

Then

$$P(r)dr = 2\pi r R \cdot \cos \theta d\theta = -2\pi R^2 \mu d\mu \quad (2.36)$$

We integrate  $P(\mu)d\mu$  from  $\mu=0$  to  $\mu=1$ :

$$\int_0^1 P(\mu)d\mu = \pi R^2 \quad (2.37)$$

To normalize the integral of the probability density,  $\pi R^2=1$ , therefore

$$P(\mu)=2\mu \quad (2.38)$$

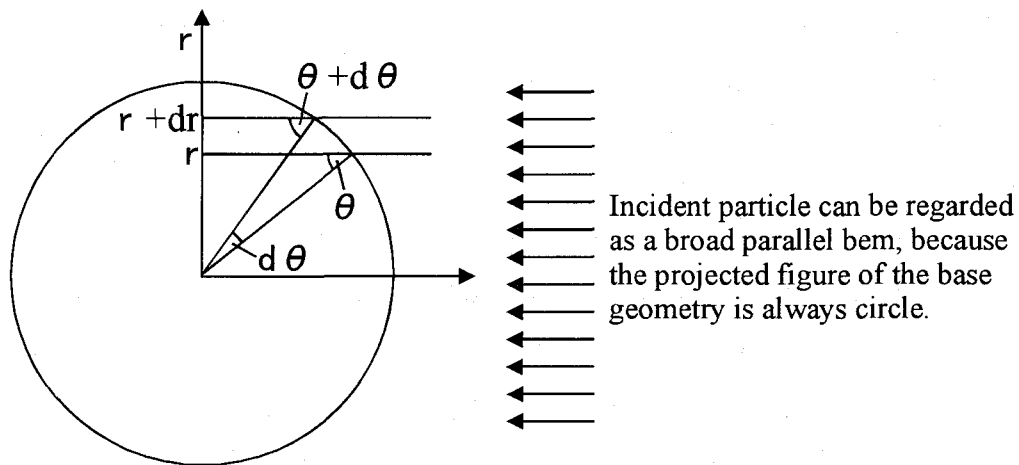


Fig. 2.8 Calculation of angular distribution of particle entering a base geometry.

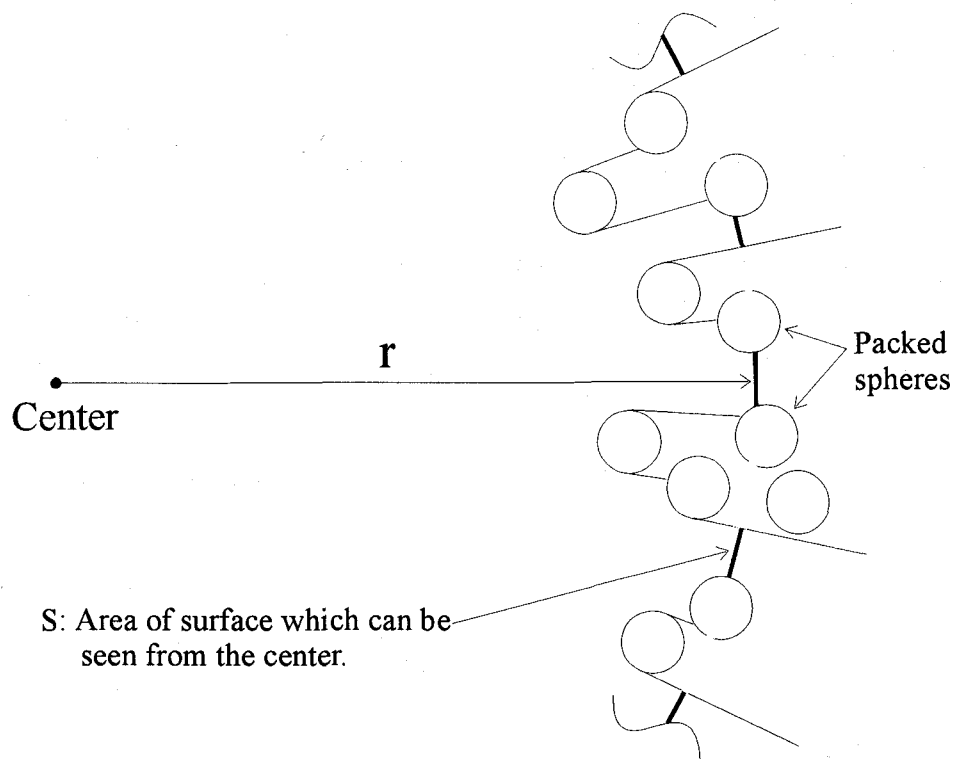


Fig. 2.9 Nearest neighbor distribution (NND).  
Formal definition of NND is  $1 - S/(4\pi r^2)$ .

It is found that the distribution is so-called cosine distribution. The practical sampling method is very simple as shown in the previous section, that is just taking  $\sqrt{r}$  where  $r$  is random number of  $0 \sim 1$ . However, the distribution is not strictly cosine distribution depending upon the packing fraction of the base geometries, as detailed in Sec. II.3.2.3.4.

The other distribution is called nearest neighbor distribution (NND). The NND is defined as the probability of finding the nearest neighbor base geometry in a spherical shell at a distance  $r$  as shown in Fig. 2.9. By the sampling method of a histogram distribution described in the previous section, at the beginning of Step 2 in Sec. II.2.1, the location where the particle is likely to enter the next base geometry can be determined when the particle gets into the region in which a lot of base geometries are distributed irregularly. However, we cannot find an example of study of applying spatial distribution of irregularly distributed geometries as well as the NND to a particle transport problem except utilization of radial distribution function (RDF) to be introduced in the later section for the analysis of HTGR core. In the following sections in Chap. 2, evaluation methods of NND are precisely examined with three candidates, i.e., packing simulation of geometries similar to molecular dynamics (MD) calculation, classical Percus-Yevick equation and mathematical theory with physical consideration.

### **II.3.1 Evaluation of nearest neighbor distribution (NND)**

In the system that we are interested in, a lot of spherical base geometries (of course we can deal with geometry with any shape in principle) are distributed or rather packed irregularly. As candidates to express such a system and to evaluate the NND, the following three methods were investigated:

1. numerical packing simulation used as an approximation to the atomic structure of amorphous materials (see Refs. (10) through (14))
2. equation of state for liquids which is well known as Percus-Yevick equation, to study molecular nature of fluids (see Refs. (15) through (19))
3. theoretical calculation assuming statistically uniform distribution of geometries in phase space<sup>(1)</sup>.

The first method determines the NND distribution by numerically simulating packing of equal hard spheres without interaction force among them. The second method gives an RDF of packing spheres using the equation of state in liquids, which is well known as the P-Y equation,

representing a proper interaction among molecules. The RDF is defined as the radial distribution of the average number of sphere centers per unit area in a spherical shell as detailed in Sec. II.3.2.3.2. Although it becomes easy to evaluate NNDs in an analytical expression with the second or third method, consequently the first method was finally adopted in this study. The critical reason to prefer the first method and the details about three methods are given in the following sections.

### **II.3.1.1 Numerical packing simulation**

By regarding molecules and atoms constituting crystal and so on as hard spheres, the real packing of them can be simulated under several simple assumptions. After the packing simulation, various physical values can be evaluated from the simulated system. Especially studies on packing of equal hard spheres were strongly performed for years. Micro-characterizations of gas, liquid and amorphous<sup>(10,20-22)</sup> and macro-granular features of powder and porous material<sup>(23-25)</sup> were studied with such a simulation method which is known as molecular dynamics (MD) method in the material science field. For example of application, it was found that the ratio of the densities of regular close packing and random close packing is close to the ratio of solid and liquid densities at the triple points of neon, argon, krypton and xenon<sup>(26)</sup>. Also, the radial distribution function for dense random packing was similar to that of the rare-gas liquids<sup>(16,27)</sup>. Recently, two kinds of hard spheres having a different radius are used to investigate the characteristics of alloy metal<sup>(14)</sup>. In addition, some scientists research the upper limit of packing fraction of three dimensional random packing of hard spheres<sup>(12,13)</sup>.

The feature of this method is to simulate directly a real packing, resulting in achievement of packing exactly similar to the real one compared with other two methods. In the present study, this method was thus selected to make NND from the various analyses. The precise description of the method and the reason why the method was selected are given in detail in Sec. II.3.2.

### **II.3.1.2 Equation of state for liquids**

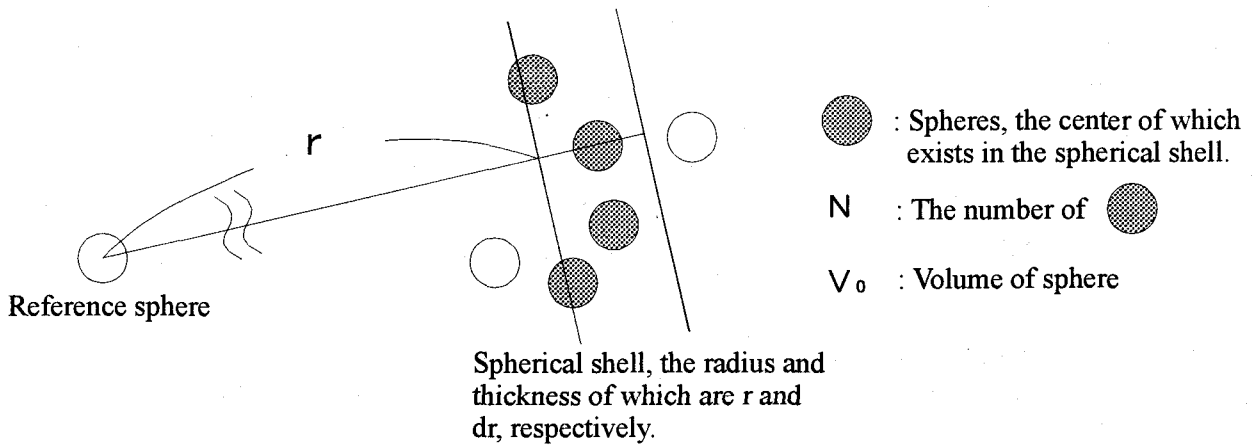
The Percus-Yevick equation<sup>(28)</sup> is well known as equation of state for liquids to give the radial distribution function (RDF) of a classical fluid of hard spheres. The RDF is defined as the radial distribution of the average number of sphere centers per unit area in a spherical shell as



shown in Fig. 2.10. There is a relation in the next equation between the RDF and  $NND^{(29)}$ :

$$NND_L(R) = \int_{r_0}^R RDF(r) \cdot 4\pi r^2 \cdot \rho \cdot (1 - NND_L(r)) dr \quad (2.39)$$

where  $r_0$  is the radius of sphere, and  $\rho$  the number density and the  $NND_L(R)$  the rigorous lower bound on  $NND(R)$ . This is due to finite dimensions of spheres. We need some further modifications of the equation to obtain the correct form<sup>(29)</sup>. The P-Y equation was solved exactly by Wertheim<sup>(30)</sup> and Thiele<sup>(15)</sup>. The RDF can be calculated by other approximate methods as well as an exact molecular dynamics simulation. Wehner<sup>(19)</sup> discussed various approaches of the RDF through the comparison of their results. In the nuclear engineering field, Tsuchihashi<sup>(9)</sup> studied the effective resonance absorption of irregularly distributed spherical fuel elements in a graphite matrix by using the result of the solution of the P-Y equation. Throop and Bearman<sup>(31)</sup> performed the inversion of the Laplace transform of the P-Y equation in the region  $r_0 < r < 4r_0$  to give the numerical tables of RDF at several densities. According to Wertheim, the expression for the RDF is



$$RDF(r) = \frac{N \cdot V_0}{4\pi r^2 dr} \quad (\text{packing fraction})$$

Fig. 2.10 Geometrical description of radial distribution function (RDF).  
(Details of RDF are described in Sec. II.3.2.3.2.)

$$rRDF(r) = \frac{1}{2\pi i} \int_{\delta-i\infty}^{\delta+i\infty} \frac{tL(t)e^{rt}dt}{12\eta(L(t)+S(t)e^{-t})} \quad (2.40)$$

where  $S(t) = (1-\eta)^2 t^3 + 6\eta(1-\eta)t^2 + 18\eta^2 t - 12\eta(1+2\eta)$ ,  $L(t) = 12\eta((1+0.5\eta)t + (1+2\eta))$ ,  $\eta = \pi r_0^3 \rho / 6$ , and  $\rho$  is the number density. The integration can be conducted by a little complicated mathematical technique. And the final solutions are as follows: For  $r < r_0$ ,  $RDF(r) = 0$ . For  $r_0 < r < 2r_0$ ,  $RDF(r) = RDF_1(r)$ ,

$$RDF_1(r) = \frac{1}{12\eta r} \sum_{i=1}^3 \lim_{t \rightarrow t_i} \left[ (t-t_i) \frac{tL(t)\exp(t(r-r_0))}{S(t)} \right] \quad (2.41)$$

For  $2r_0 < r < 3r_0$ ,  $RDF(r) = RDF_1(r) + RDF_2(r)$ ,

$$RDF_2(r) = \frac{1}{12\eta r} \sum_{i=1}^3 \lim_{t \rightarrow t_i} \frac{d}{dt} \left[ (t-t_i)^2 t \left( \frac{L(t)}{S(t)} \right)^2 \exp(t(r-2r_0)) \right] \quad (2.42)$$

For  $3r_0 < r < 4r_0$ ,  $RDF(r) = RDF_1(r) + RDF_2(r) + RDF_3(r)$ ,

$$RDF_3(r) = \frac{1}{24\eta r} \sum_{i=1}^3 \lim_{t \rightarrow t_i} \frac{d^2}{dt^2} \left[ (t-t_i)^3 t \left( \frac{L(t)}{S(t)} \right)^3 \exp(t(r-3r_0)) \right] \quad (2.43)$$

The obtained  $RDF(r)$  is shown in Fig. 2.11. From the comparison result of  $RDF$  done by Wehner<sup>(19)</sup> as shown in Fig. 2.12, the solution of P-Y equation produces results more accurate than other approaches and seems to be as accurate as the exact molecular dynamics results. Therefore, it seems that the P-Y equation can supply an appropriate NND. However we have to study how the assumption of including inter-molecular forces in the P-Y equation affects the final results, though Tsuchihashi utilized it very effectively in a neutron transport problem.

### II.3.1.3 Statistical uniform distribution<sup>(1)</sup>

The probability of finding the nearest neighbor of a base geometry in a spherical shell between  $r$  and  $r+dr$ , called nearest neighbor distribution(NND), is derived mathematically by

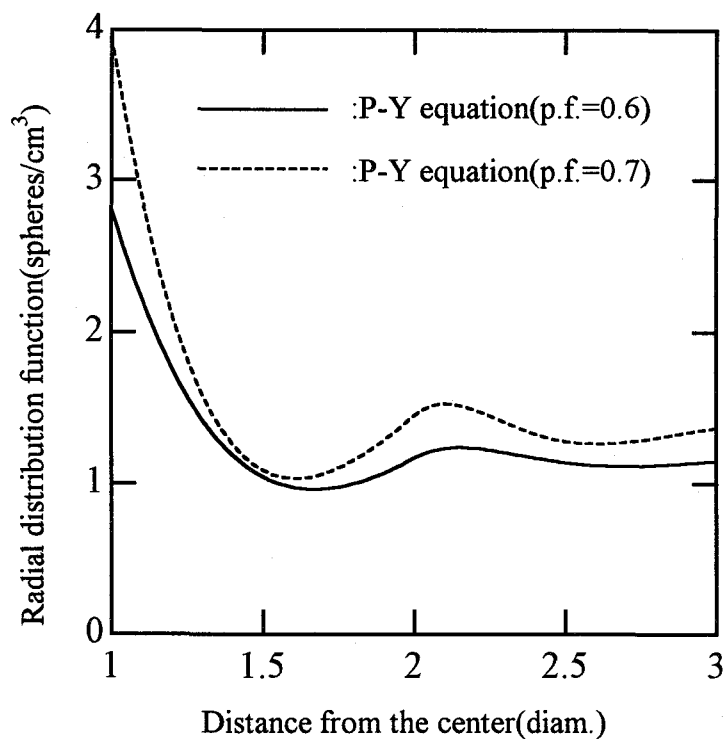


Fig. 2.11 RDFs made from the P-Y equation<sup>(30)</sup>.

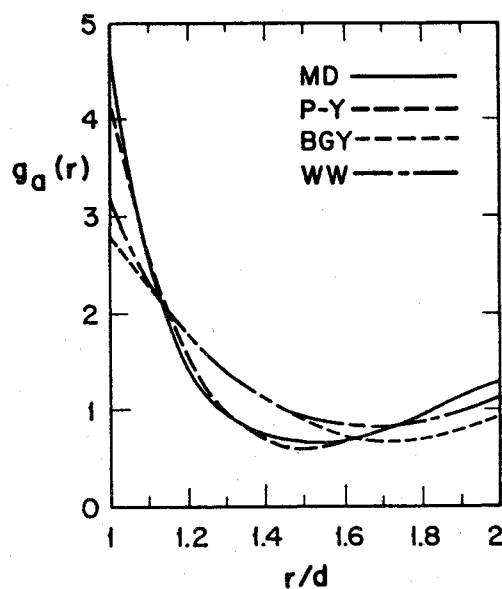


Fig. 2.12 A graphical comparison of some of the various hard-sphere radial distribution function at the packing fraction of 0.463. MD is the molecular dynamics results of Alder and Hecht. PY is the Wertheim-Thiele solution of the Percus-Yevick equation. BGY is the numerical solution of the Born-Green-Yvon equation. WW is the third-order perturbation solution.

assuming that base geometries are distributed in a statistical uniform way.

The derivation is done according to the following procedure:

The NND at distance  $r$  from the center clearly meets the next proportion relation:

$$dNND(r) \propto (1 - NND(r)) \cdot dr \quad (2.44)$$

Equation (2.44) indicates this problem is physically similar to the transport problem of neutrons through material. In other words, the interaction of neutrons with material atoms is equivalent, in this problem, to absorption of a virtual particle started at the center by a base geometry. Thus, we obtain the next equation easily, assuming the proportion constant of Eq.(2.44) does not contain the variable  $r$ :

$$NND(r) = 1 + C \cdot \exp(-\Sigma \cdot r), \quad (2.45)$$

where  $\Sigma$  is the physical value to be determined, which corresponds to the macroscopic cross section in case of the neutron transport problem. Employing the boundary condition,  $NND=0$  at  $r=0$ :

$$NND(r) = 1 - \exp(-\Sigma \cdot r) \quad (2.46)$$

From Eq.(2.46), the value  $D$  corresponding to the mean free path is expressed as follows:

$$D = \frac{1}{\Sigma} \quad (2.47)$$

The problem is focused on clarifying the mean free path  $D$  in this problem.

Supposing the system containing hollow spheres packed randomly having an equal radius  $r_0$ , the average transmitting length of a virtual particle through a sphere becomes the representative length of the sphere,  $L$ , which is estimated to be  $4r_0/3$ . Now introducing the value  $D_0$ , which is the average transmitting length between spheres, that is like a matrix region in a fuel compact, the following expression applies:

$$\frac{L}{L + D_0} = f_p \quad (2.48)$$

where,  $f_p$  is the packing fraction. The value  $D_0$  mentioned earlier has exactly the same definition as the mean free path  $D$ . Employing the diameter unit for  $D$ ,

$$D = \frac{2}{3} \cdot \left( \frac{1}{f_p} - 1 \right) \quad (2.49)$$

Consequently, we obtain the solution:

$$NND(r) = 1 - \exp\left(-\frac{3}{2} \cdot \frac{f_p}{1-f_p} \cdot r\right) \quad (2.50)$$

Differentiating Eq.(2.50),

$$\frac{dNND(r)}{dr} = \frac{3}{2} \cdot \frac{f_p}{1-f_p} \cdot r \cdot \exp\left(-\frac{3}{2} \cdot \frac{f_p}{1-f_p} \cdot r\right) \quad (2.51)$$

The probability density of NND calculated with Eq.(2.51) is shown in Fig. 2.13. The probability density decreases more rapidly with increase of the packing fraction. Also, each curve is exactly an exponential function, therefore sampling of Eq.(2.50) becomes quite easy in transport calculation. However, near the reference center we have to examine how much the local effect due to several base geometries around the reference appears, because most transport particles get into base geometries near the reference after getting out of it. The details about this problem are described in Sec. II.3.3.

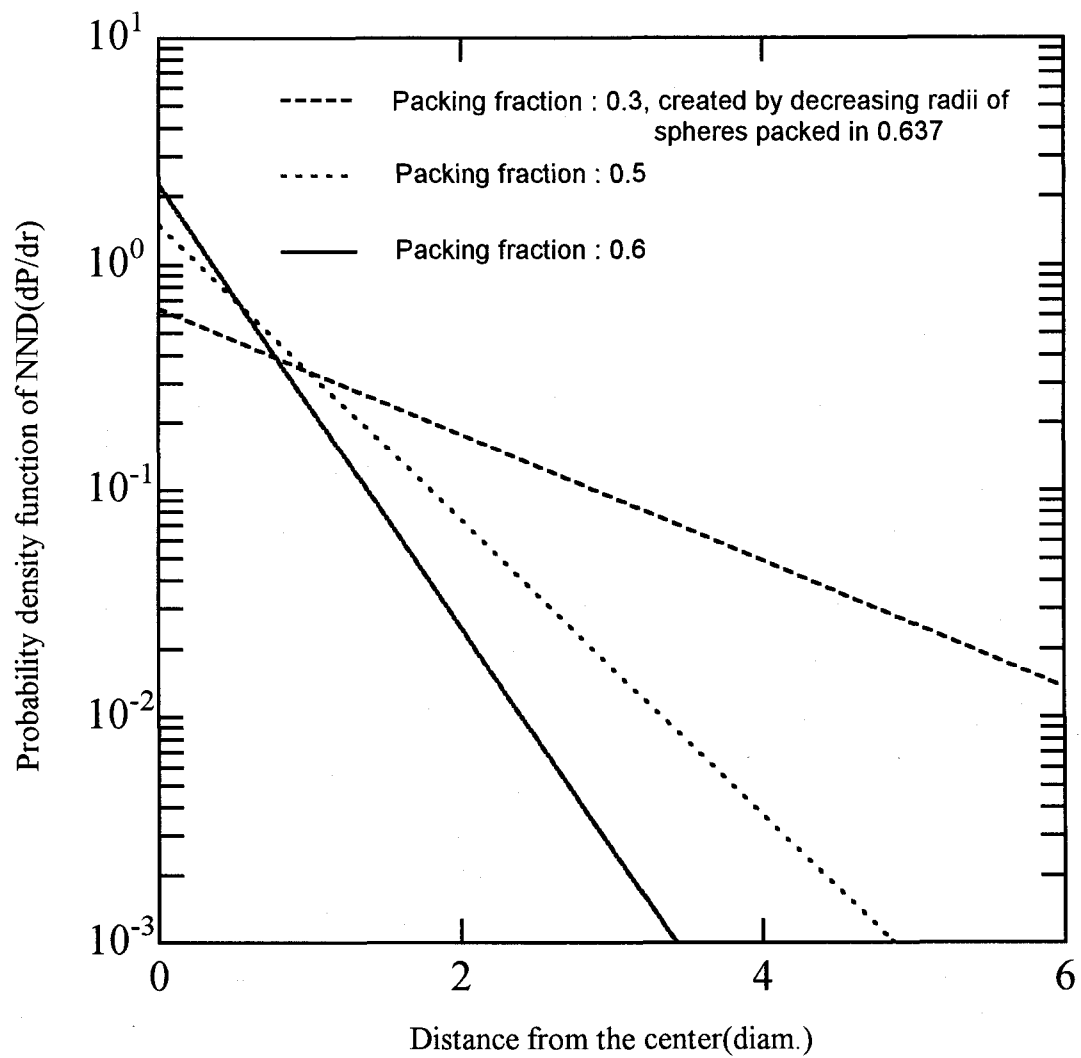


Fig. 2.13 Probability density function of NND produced by equation (2.51).

## II.3.2 Computer simulation of random packing

In this section, the packing simulation of equal hard spheres employed in the present study to give NND is precisely described (Even if a base geometry is not a sphere, this packing simulation method is still applicable by regarding the geometry as a volume equivalent sphere.). The reason why the packing simulation method was selected is summarized in Sec. II.3.3. The NND can be evaluated by a ray-trace method after the packing state is prepared. The evaluated NND was first applied to a practical transport simulation in this study. The most critical difficulty was that there was no general purpose codes of simulating packing of hard spheres. Therefore we had to develop a new code. However a simple packing code with just collective rearrangement could not achieve a packing state in a high packing fraction larger than 0.6. We had to prepare that of the highest packing fraction. An original algorithm was thus required to overcome the limitation of packing fraction. From the mathematical point of view, vigorous researches with respect to multi-dimensional random packing are now being done to clarify the packing theory. In this study, a new packing simulation algorithm named random vector synthesis method was studied to develop a three dimensional packing simulation code MCRDF. The details about the code as well as its practical calculation results are given in the following sections.

### II.3.2.1 Random packing of equal hard spheres

First the random packing is introduced. The three dimensional packing problem is generally equal to a study to examine the attainable packing fraction of equal hard spheres packed in a container. Usually, to remove the effect of the finite dimensions of the container, which normally underestimate the packing fraction, the highest packing fraction is estimated by extrapolating the container dimensions:

$$\lim_{r \rightarrow \infty} [(\text{Total volume of spheres packed in the container}) / (\text{Volume of the container})] \quad (2.52)$$

where  $r$  is the dimensions of the container. This problem is energetically discussed by expanding the N-dimensions problem<sup>(32)</sup>. According to Rogers<sup>(33)</sup>, for three dimensional sphere packing, "While many mathematicians believe, and all physicists know, that the density of packed spheres cannot exceed  $\pi/18^{0.5}$ ." In 1958, he proved that, if some packing more dense than ordered close

packing (FCC, for example) should ever be achieved, this would certainly have density less than  $18^{0.5}(\cos 1/3 - \pi/3)=0.7797\dots^{(34)}$ . Recently, this value has been modified gradually. In 1986, Lindsey improved the value of  $0.7736^{(35)}$ .

As for the random packing, the upper packing fraction is continuously investigated because the theoretical discussion is very difficult. From some experimental approaches<sup>(26,36)</sup>, this was estimated to be 0.6366. Many physicists believed that this is the upper value. However, several simulation calculation results show packing fractions exceeding 0.6366 occur. The issue discussed is that there exists a local packing state, only made by simulation calculations, which may be packed in packing fraction beyond the experimentally expected upper packing fraction. Such a packing state may already lose randomness, therefore the packing fraction attained by that way may not be a real upper limit packing fraction of three dimensional random packing. At present, it is thought that the real upper limit packing state is predicted to occur for the packing fraction of  $0.64 \pm 0.02^{(29)}$ .

The ordered packing such as FCC, BCC and so on introduced earlier is called ordered close packing (OCP). Random packing is divided into two states, i.e., the operation of shaking is performed or not. The packing obtained with the operation is random close packing (RCP). This is experimentally made by shaking containers full of hard spheres and extrapolating the measured packing fractions to eliminate finite-size effects. If not shaking, the packing is, difficult to be defined, named random loose packing (RLP), which is observed by dumping hard spheres into a container without shaking and measuring the resulting packing fraction at  $r \rightarrow \infty$ . The best estimate of the packing fraction for RLP is probably  $0.60 \pm 0.02^{(29)}$ . The summary of three packings of hard spheres is shown in Table 2.1.

Table 2.1 Packings of equal hard spheres in three dimensions.

Name	Packing fraction	Physical definition
Random close packing (RCP)	$\sim 63.7\%$	Hard spheres are poured into a container. Then shaking the container, the packing of RCP is obtained by extrapolating the container's dimensions; $r \rightarrow \infty$
Random loose packing (RLP)	$60 \sim 62\%$	The same as above except shaking is not done.
Ordered close packing (OCP)	$74\%$	Hard spheres are packed regularly. The maximum packing fraction is obtained at FCC.



### II.3.2.2 Packing algorithm of MCRDF

In the present study, we have developed a new code to simulate a packing of equal hard spheres in as high packing fraction as possible. The reason why aiming at such a high packing fraction, detailed in Sec. IV.2.1, is briefly given in the following: The packing fraction of fuel pebbles in pebble bed type HTGRs is nearly  $0.60 \sim 0.62$ . Also in other applications, spherical elements are generally packed in a container in packing fractions of  $\sim 0.60$ , which is corresponding to RLP. However, we had to prepare a higher packing fraction, because it was confirmed that NND made by using a packing in as high packing fraction as RCP could simulate excellently CFPs packed in a fuel compact used in compact type HTGRs like HTTR. As for the packing fraction of RCP used in the present study, as shown in the previous section, the experimentally obtained upper packing fraction of RCP is  $\sim 0.637$ . Also we know that some calculated results exceed the experimentally obtained upper packing fraction. Finally, because we judged that their artificial packings are not homogeneous, not isotropic and are not performed randomly<sup>(11)</sup>, consequently, we aimed at development of random packing simulation code which could reproduce the experimentally obtained random packing state, within an appropriate and acceptable short computation time.

The basic concept of the newly developed three dimensional Monte Carlo packing simulation code MCRDF is quite simple: In a simulation of a packing, hard spheres, the number of which is determined by the packing fraction, are packed in a container, i.e., points are arranged randomly inside the container, and we assign radii to the points to define spheres. To simulate an infinite system, periodic boundary conditions are used as shown in Fig. 2.14. After the initial packing, in general there are overlaps among the spheres. We have to reduce the overlaps by moving the spheres using collective rearrangement<sup>(4,14)</sup>: The overlapped spheres are moved along the vector sum of the overlaps as in Fig. 2.15. By iterating this procedure, overlaps can be reduced or eliminated. However, it should be noticed that to attain a high density random packing various counteractions are required. MCRDF employed the random vector synthesis method developed newly for that purpose. The detail is presented in the next section.

Besides the method above, other numerical simulations have been done extensively with various algorithms. Bennett<sup>(10)</sup> proposed the new method of packing of hard spheres that is mathematically analogous to vapor deposition. Supposing a seed cluster of spheres at first, each additional sphere, one by one, is placed at a certain surface of the cluster where it can be in a hard

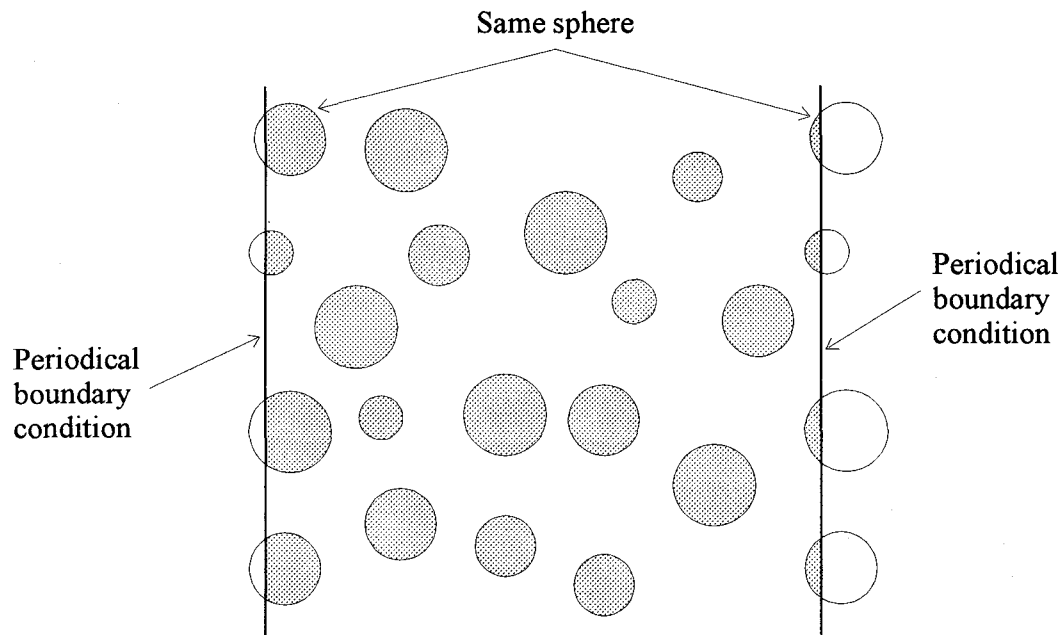


Fig. 2.14 Periodical boundary conditions in packing simulation of MCRDF.

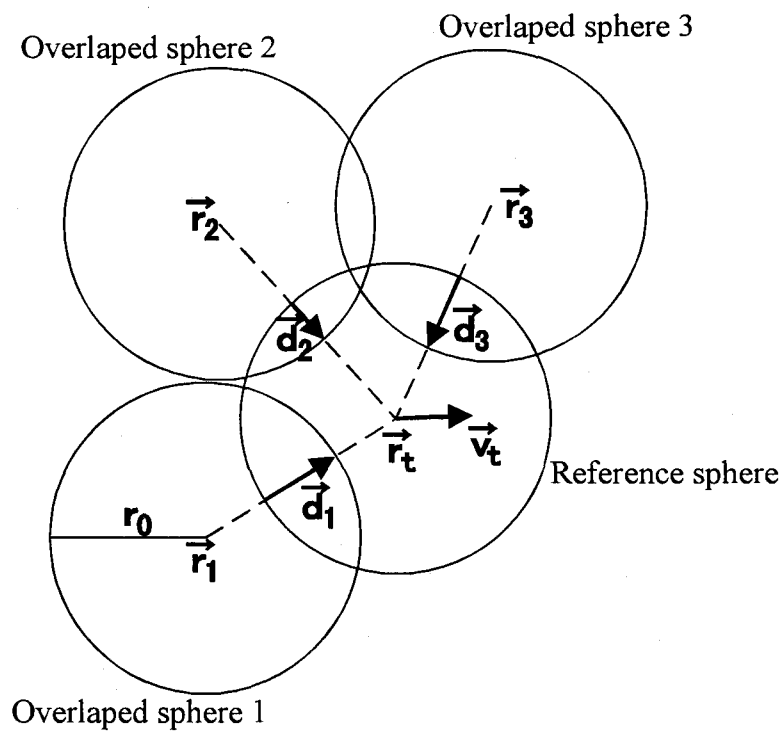


Fig. 2.15 Simple collective rearrangement to remove or eliminate overlaps.

contact with three spheres in the cluster. However, it is pointed out that the packing becomes inhomogeneous with this method because the algorithm does not employ the collective rearrangement<sup>(11)</sup>. Recently, numerical simulations were performed to realize homogeneous and isotropic packing of hard spheres by various algorithms<sup>(11,13,14)</sup>, for example, doing away with any boundary constraint in corrective rearrangement<sup>(11)</sup> or assuming hypothetical spheres having dual structure whose inner diameter defines the true density and the outer one a nominal density<sup>(13)</sup>.

### II.3.2.2.1 Random vector synthesis method

In MCRDF, the random vector synthesis method was developed to reduce overlaps especially aiming at packing in high packing fraction near the RCP state. As already introduced, the easiest and most reliable adjustment to reduce overlaps of spheres, i.e., collective rearrangement, is to move the spheres along the vector sum of overlaps: The vector proportional to the difference of position vectors of the reference sphere and the overlapped sphere is summed and averaged, as shown in Fig. 2.15. The reference sphere is moved by the next vector:

$$\vec{v} = \frac{1}{n} \sum_{i=1}^n \vec{d}_i \quad (2.53)$$

where  $n$  is the number of overlaps and  $\vec{d}_i$  is the overlap vector for the overlapped sphere  $i$ . Only with this method, a packing fraction of  $\sim 0.6$  can be attained in a reasonable computation time. However, we cannot obtain easily packing state in higher packing fraction than 0.6 with this simple collective rearrangement method. It means that moving a sphere reduces some overlaps but creates or increases others. In the course of simulation calculation, this occurs repeatedly or periodically. During the iteration calculation, a certain position of sphere thus appears repeatedly. As a result, the simulation calculation is not converged and the spheres become finally locked up. To overcome this problem and at the same time to be homogeneous and isotropic in packing of hard spheres, randomization in reducing overlaps was introduced. It was found that this is very important and indispensable for achievement of higher packing fraction. Practically, adjustment of sphere position and preparation of the vector to be moved are done considering a little randomness. The former is to move the position of the reference sphere randomly irrespective of the position of spheres around the reference sphere. The latter means that determination of the

Table 2.2 Relation of convergence rate and randomness of adjuster vectors in MCRDF.

Randomness (%)	Calculation result	Convergence index <sup>1)</sup>
2.5	Not converged	$1.401 \times 10^{-3}$
5.0	Converged	$1.000 \times 10^{-3}$
10.0	CPU time over	$1.063 \times 10^{-3}$
33.3	CPU time over	$1.032 \times 10^{-3}$

1) Average overlap ratio per cycle.

direction and absolute length of the adjustment vector is done a little randomly. In a low packing fraction,  $<0.6$ , the randomness in moving spheres does not take effect. On the other hand, it was confirmed that the randomness in the adjustment vector has a significant effect. Table 2.2 shows the randomness dependency for the effect observed. Setting the randomness over 10%, the calculation never converges; while at  $<5\%$ , convergence becomes slow. We confirmed that 5% is almost the optimum value to obtain the fastest convergence. However, in a higher packing fraction of  $\sim 0.63$ , even if the random adjustment is taken into account, the spheres are obliged to be locked up. In this case, there are some regions, the packing fraction of which is as high as that of RCP, while there also exist regions, the packing fraction of which is around that of RLP. As a counteraction, we developed a new packing method named the random vector synthesis method: When there is a large overlap, coarse adjustment to reduce it properly is done to decrease the high packing fraction in a local region, because a lot of overlaps means the packing fraction is high around there. Of course, if there is a small overlap, fine adjustment to attain high packing fraction is required.

Practically, by the random vector synthesis method, each sphere  $t$  having overlaps is moved by the vector  $\vec{v}_t$  in Eq.(1) to reduce or eliminate overlaps.

$$\vec{v}_t = C_t \vec{e}_t \quad (2.54)$$

where  $C_t$  is the absolute length to be moved along the vector  $\vec{e}_t$ .  $\vec{e}_t$  and  $C_t$  are defined as follows:

$$\vec{e}_t = \left( \sum_{i=1}^n \vec{d}_i \right) / \left| \sum_{i=1}^n \vec{d}_i \right|, \quad (2.55)$$

$$C_i = \frac{1}{2} \max \left[ \left| \vec{d}_1 \right|, \left| \vec{d}_2 \right|, \dots, \left| \vec{d}_n \right| \right] \cdot \eta, \quad (2.56)$$

where,  $\vec{d}_i$  is the vector between overlapped sphere centers,  $\eta$  the random factor, determined empirically, of the absolute length to be moved ( $=0.95$  or  $1.05$ ) and  $n$  the number of overlapped spheres, and

$$\vec{d}_i = \left[ 2r_0 - \left| \vec{r}_i - \vec{r}_i \right| \right] \cdot \frac{\vec{r}_i - \vec{r}_i}{\left| \vec{r}_i - \vec{r}_i \right|}, \quad (2.57)$$

where,  $\vec{r}_i$  is the position vector of the target sphere,  $\vec{r}_i$  the position vector of the overlapped sphere  $i$  and  $r_0$  the radius of sphere.

The unique feature of this algorithm is the introduction of the  $C_i$  factor which is given as a half of the maximum among absolute lengths of the vectors  $\vec{d}_i$  times a random factor  $\eta$ . With this method, the reference sphere is surely moved by a half of the maximum overlap among those of the spheres overlapping the reference sphere. It seems that the packing simulation is hard to converge seemingly. As a matter of fact, this algorithm possesses the function of adjusting spheres' coordinates as a whole during an early stage of overlap reduction, i.e., while the average overlap length is still large. At the same time it also has the function of reducing local overlaps as the average overlap length decreases. In addition, the process of moving the spheres randomly, which does not take effect in a low packing fraction, was applied to the algorithm. This is more effective especially in a high packing fraction,  $>0.63$ .

Iterating the adjustment process, gradually the number of overlaps and the absolute length decrease. However, this procedure cannot remove overlaps completely, because by using this algorithm the half of the overlap is always left. In MCRDF, when the maximum overlap length is below a certain tolerance, a complete overlap-free packing is attained by reducing the radii of all the spheres. In a packing simulation calculation of a system having 500 spheres, it takes about 10 minutes to accomplish the RCP state with the FACOM VP-2600 vector processor of JAERI. The algorithm of MCRDF is shown in Fig. 2.16.

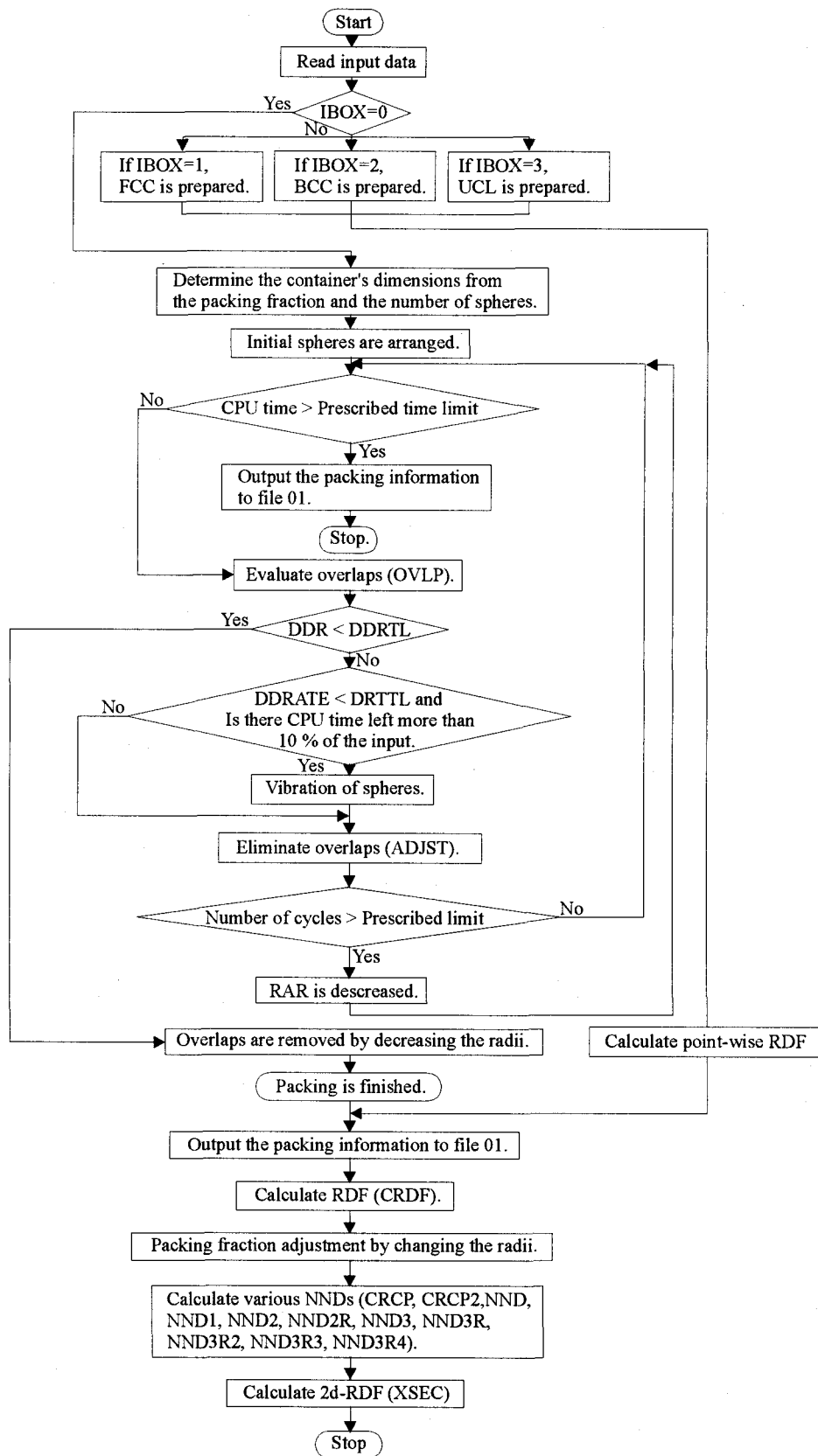


Fig. 2.16 Calculation flow of MCRDF.

### II.3.2.3 Calculated results by MCRDF

The MCRDF can realize not only a packing state in high packing fraction, but also evaluation of various statistical quantities from the packing, such as RDF, NND, Voronoi-cell statistics and so on. In the following sections, the details of them as well as the maximum packing fraction attainable by MCRDF are presented.

#### II.3.2.3.1 Packing fraction of RCP

As shown in Sec. II.3.2.1, the experimentally obtained maximum packing fraction of three dimensional random packing, i.e., the packing fraction of RCP, is believed to be  $0.6366^{(26,36)}$ . In the simulation calculation of random packing, results beyond the experimental upper value are observed as listed in Table 2.3. Berryman said from the results that the RCP is predicted to occur for  $0.62 \pm 0.02$  in three dimensions<sup>(29)</sup>. But it is still unclear what the packing fraction of RCP is. It is doubtful that a high-packing-fraction state beyond the experimental limit of 0.6366 exists. Maybe in such a case a complete homogeneous packing is impossible and there may be a denser region than RCP locally. This must be seriously dependent of the algorithm of packing. In MCRDF the packing algorithm to create a uniform distribution of spheres as much as possible is an important goal in order to reproduce the experimentally obtained packing fraction of RCP, because non-uniform packing can supply NND not reproducing the real spatial distribution of the hard spheres. In the development of MCRDF code, the algorithm was iteratively and carefully modified by watching the local packing fraction to realize an uniform packing.

We examined whether MCRDF can reproduce the RCP packing or not by comparing the calculated packing fraction of RCP with the experimental value. It requires skill in use of MCRDF to obtain packing fraction over 0.635, i.e., input of initial packing fraction, setting of internal calculation option in the code and so on. With an equal calculation condition, the change of the packing fraction as a function of reciprocal of computation time is illustrated in Fig. 2.17. By extrapolating the computation time up to infinite, namely reading the packing fraction at  $x(1/\text{time})=0$ , the packing fraction of RCP is estimated to be 0.6386. Though this is slightly larger than the experimentally obtained upper value of 0.6366, and comparing it with recently calculated results which mostly show larger values than 0.64, it can be concluded that our result well reproduces the experimental result for RCP, and the packing state obtained by MCRDF is

confirmed to be enough random and isotropic.

Table 2.3 Packing fractions of RCP state,  $f_{RCP}$ , in three dimensions.

$f_{RCP}$	Year	Reference	Ref. No.
0.62 ~ 0.64	1966	Haughey and Beveridge	24
$0.6366 \pm 0.0005^{1)}$	1969	Scott and Kilgour	36
$0.6366 \pm 0.0004$	1970	Finney	16
0.62	1972	Bennet	10
0.64	1972	LeFerve	37
0.610 ~ 0.647	1974	Gotoh and Finney	38
$0.637 \pm 0.002$	1976	Woodcock	39
0.6436, 0.6537	1976	Gordon et al	22
0.665	1976	Finney	11
0.654	1981	Woodcock and Angell	40
0.6366	1981	Jodrey and Tory	12
$0.638 \sim 0.647$	1982	Anguilera-Navarro et al	41
$0.64 \pm 0.02$	1983	Berryman	29
$0.642 \sim 0.649$	1985	Jodrey and Tory	13
0.637, 0.645	1987	Clarke and Wiley	14
0.6386	1995	Present work	2

1) This was obtained experimentally.

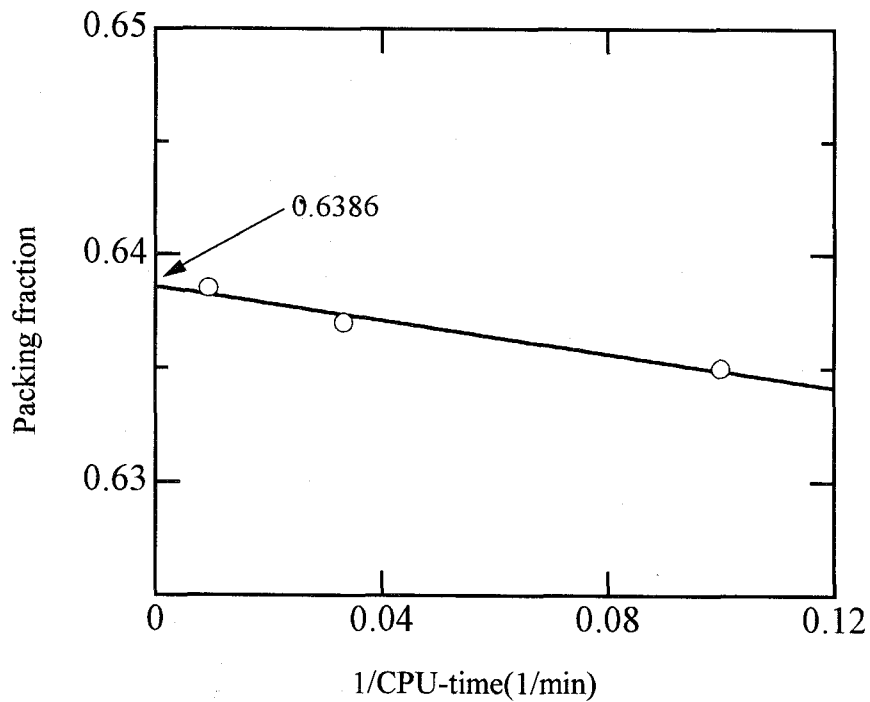


Fig. 2.17 Estimated maximum packing fraction of RCP with MCRDF.



### II.3.2.3.2 Radial distribution function (RDF) and two dimensional RDF

Radial distribution function (RDF) is a quite important quantity to study physical nature of materials, and it is well known that RDF can be evaluated directly from the P-Y equation. In MCRDF, after packing spheres, the RDF is calculated as follows: Now supposing that packing of N spheres is done, by taking into account the periodic boundary conditions in the calculation of the distance between spheres, N-1 distances from one of the N reference spheres can be tabulated to make the frequency curve. Therefore, normally several hundreds spheres are enough large to evaluate the RDF with a high accuracy.

The RDF is defined as the radial distribution of the average number of sphere centers per unit area in a spherical shell (See Fig. 2.10). Practically,

$$RDF(r) = \frac{\left[ \begin{array}{c} \text{The number of spheres, } N, \\ \text{contained in } r \sim r+dr \end{array} \right]}{4\pi r^2 dr} \quad [n/cm^3] \quad (2.58)$$

Also, this equation is deformed into the next equation, if necessary:

$$RDF_p(r) = \frac{N \cdot V_0}{4\pi r^2 dr} \quad [\text{Packing fraction}] \quad (2.59)$$

where  $V_0$  is the volume of the sphere. Moreover, this can be transformed into the next equation:

$$RDF_r(r) = \frac{N \cdot V_0}{4\pi r^2 dr \cdot f_p} \quad [\text{Relative packing fraction}] \quad (2.60)$$

where  $f_p$  is the packing fraction.

Figure 2.18 shows the RDF in packing fraction of 0.635 calculated by MCRDF compared with other simulation calculation results. From the figure, instantly we can find the following: The peak locations in our RDF are in good agreement with others. The shape of our curve is also in fairly good agreement with Bennett's result<sup>(10)</sup> calculated by the sphere addition method except a slight discrepancies in the absolute values of the first and second peaks. It is thought that this difference is caused by the fact that his method do not employ the collective

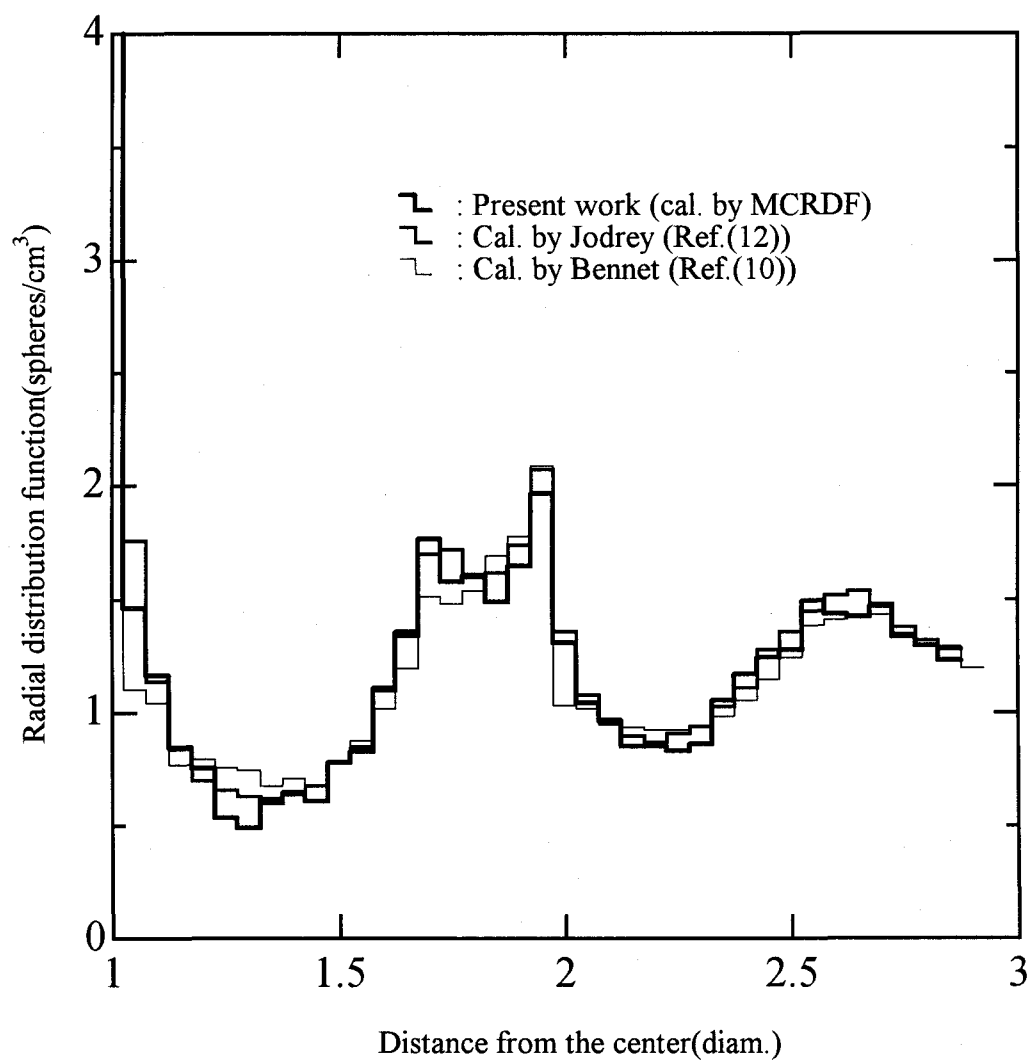


Fig. 2.18 Comparison of calculated radial distribution functions of RCP.

rearrangement and his packing fraction is a little smaller than ours. Jodrey's result<sup>(12)</sup> agrees well with our result because his method and attained packing fraction is similar to ours.

We discuss next the locations of the observed peaks, namely; why the peaks can be observed at 1-diameter, 2-diameter and so on. The largest peak can be found at 1-diameter from the reference sphere. This corresponds to neighboring spheres in contact with each other. The second and third peaks are seen at 1.73-diameter and 2-diameter, respectively, as shown in Fig. 2.19. Another peak is expected to be seen at the vertex of a regular hexahedron composed of 5 spheres on its maximum diagonal line, 1.63-diameter. In fact, from the distribution of faces with N edges in Fig. 2.20 introduced in Sec. II.3.2.3.5, regular hexahedrons seem to be made by the packing simulation. However, the MCRDF calculation result shows that the probability that 4 spheres are in contact with each other is less than 2%, and there exists no regular hexahedrons in the packing result. It is confirmed from the result that 2 or 3 spheres are usually in contact with each other, but 4 spheres contact is rare and that of 5 spheres is not observed even in high packing fraction.

Comparison with the experimental results is presented in Sec. II.3.2.4.1.

Next two dimensional RDF (2d-RDF) is introduced as follows: The 2d-RDF gives the information as to how the cross section circles of the spheres appearing in a certain cross section of the container, in which spheres are distributed irregularly, are distributed. This is a newly defined quantity in order to compare the calculated spatial distribution of spheres by MCRDF with the experimental result. The definition is the average number of sphere centers in a cylindrical shell of which the height is  $2r_0$ , where  $r_0$  is the radius of the sphere. The conceptual arrangement of 2d-RDF is illustrated in Fig. 2.21. Practically,

$$2d-RDF(r) = \frac{\left[ \begin{array}{c} \text{The number of spheres contained} \\ \text{in a cylindrical shell, } N \end{array} \right]}{2\pi r dr} \quad [n/cm^3] \quad (2.61)$$

If necessary, this is deformed into the next equation:

$$2d-RDF_p(r) = \frac{N \cdot V_0}{2\pi r dr} \quad [\text{Packing fraction}] \quad (2.62)$$

where  $V_0$  is the volume of the sphere. Also this equation can be transformed into the next

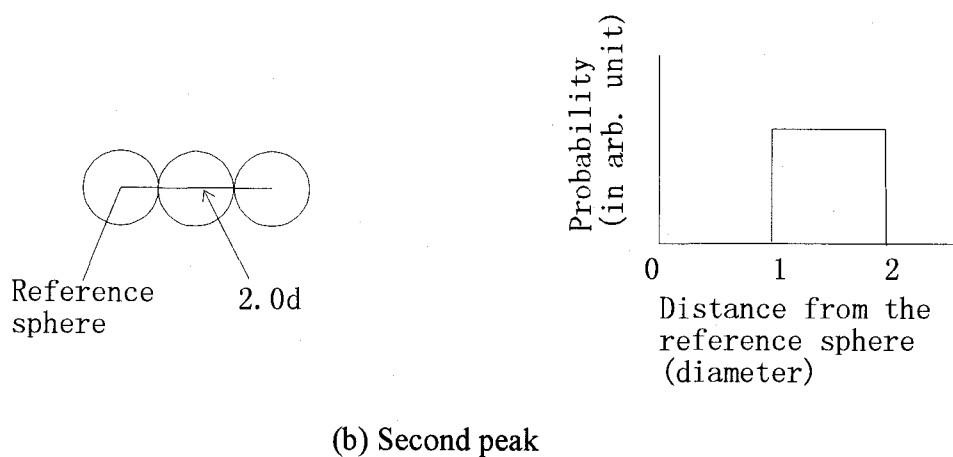
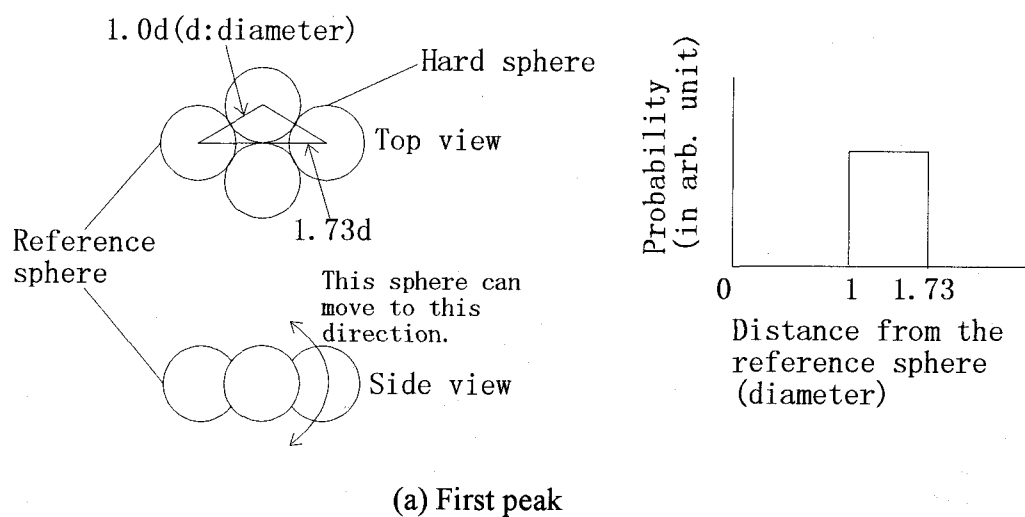


Fig. 2.19 Considerations of peak positions in RDF.

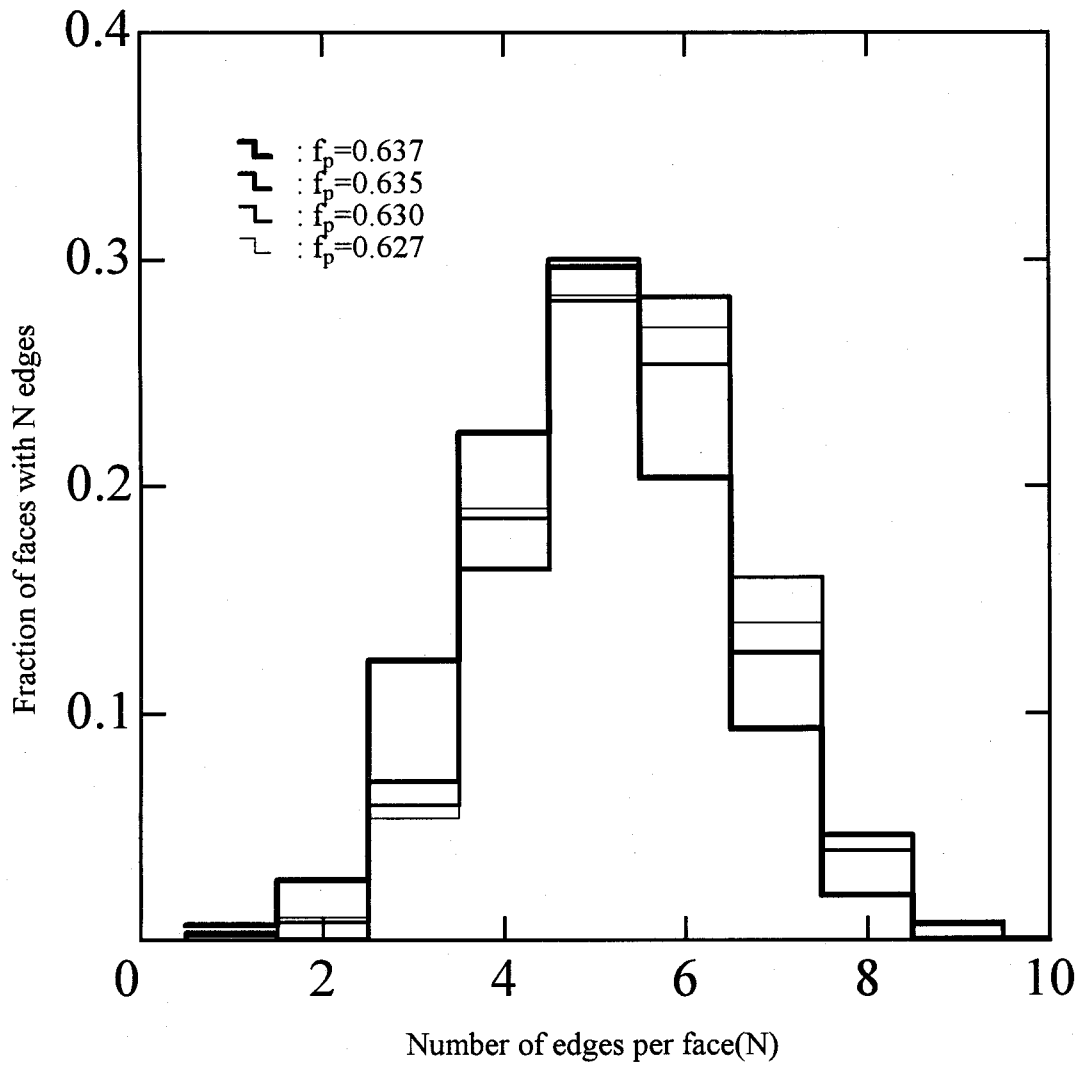
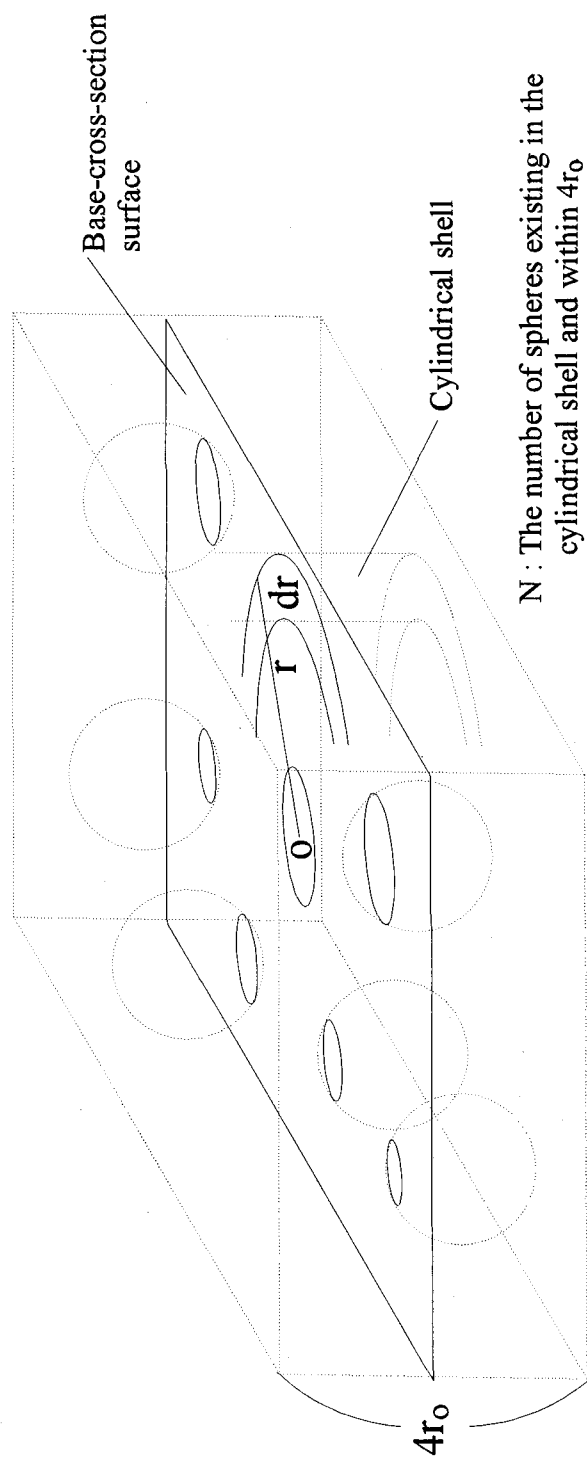


Fig 2.20 Distribution of faces with N edges for near-RCP.



$$2d-RDF = \frac{N}{\text{Volume of the cylindrical shell within } 4r_0} \quad [n/cm^3]$$

Fig. 2.21 Schematic definition of 2-dimensional RDF.

equation:

$$2d-RDF_r(r) = \frac{N \cdot V_0}{2\pi r dr \cdot f_p} \quad [\text{Relative packing fraction}] \quad (2.63)$$

where  $f_p$  is the packing fraction.

In MCRDF, the cubic container used for packing simulation is divided into several slab regions in which each one is  $4 r_0$  in thickness. On each base-cross-section surface, spheres interfering with the surface are regarded as reference spheres. According to the definition above, the number of spheres meeting the criteria is counted. An example of 2d-RDF is shown in Fig. 2.22. The broken line is the 2d-RDF for the packing fraction of 0.3. The maximum peak is located at 1-diameter, and this means that spheres in contact with others are dominant in the packing. The solid line similarly corresponds to the packing fraction of 0.3, which is made by decreasing the radii of the packed spheres to adjust the packing fraction to 0.3, after packing spheres in the RCP state by MCRDF. In this case, there is no spheres in contact with others, therefore, the strong peak can be observed at a little more distant location than the previous case. The peak location is easily given by  $(f'/f)^{1/3}$  in diameter unit, as is detailed in Sec. IV.2.1, where  $f'$  and  $f$  are the packing fractions before and after decreasing the radii, respectively.

The packing of spheres with this procedure can well reproduce the packing of CFPs in a fuel compact used as HTGR fuel element. The details about this matter is presented in Sec. IV.2.1. Also, the comparison result with the real cross section of fuel compact is shown in Sec. II.3.2.4.2.

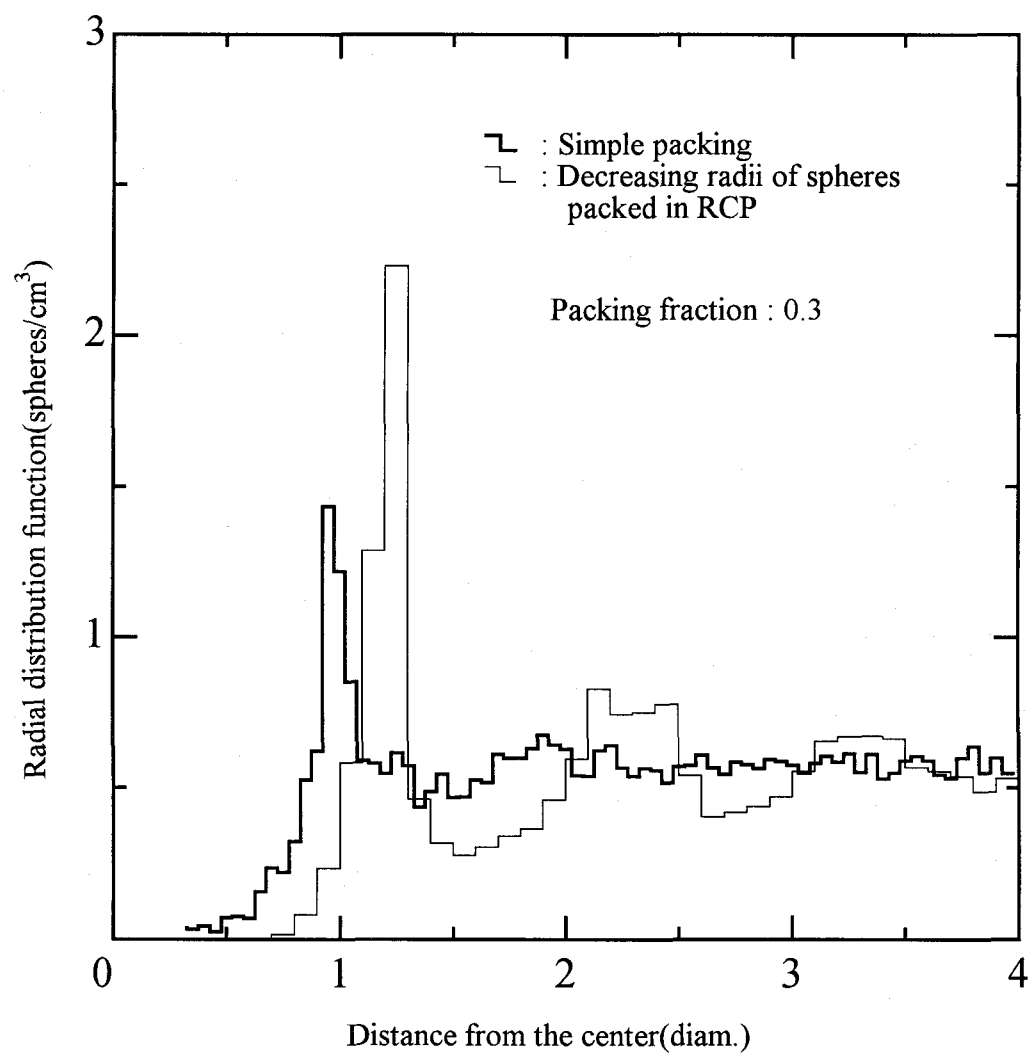


Fig. 2.22 Calculated 2-dimensional RDF by MCRDF.



### II.3.2.3.3 NND

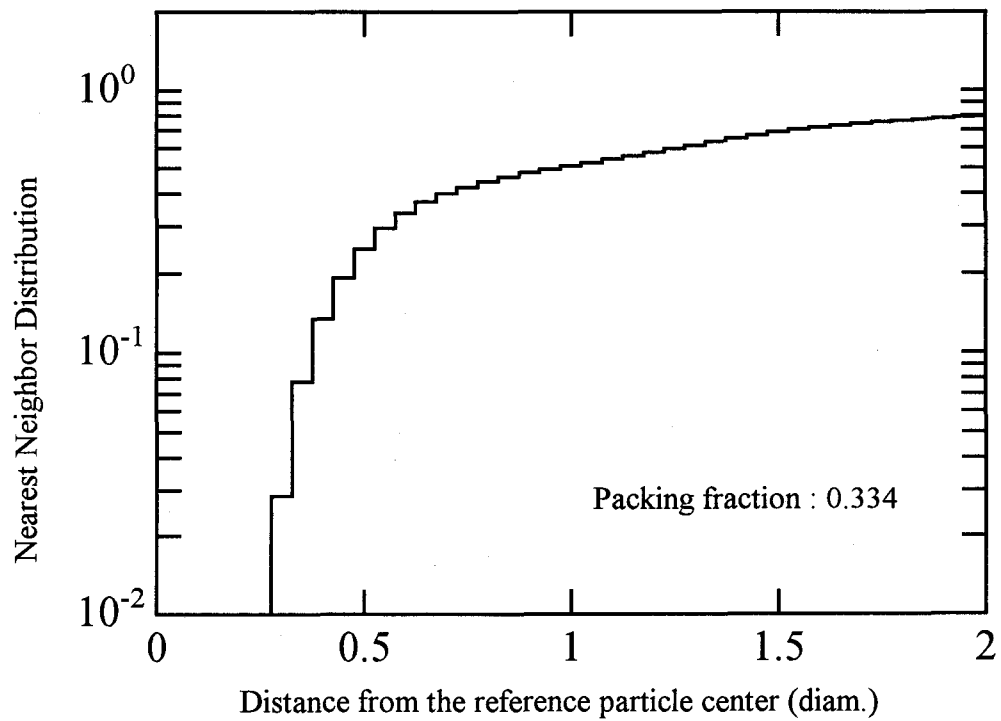
The main purpose of MCRDF in the present study is to evaluate the NND, which is defined as the probability of finding the nearest neighbor spherical geometry in a spherical shell at distance  $r$  from the reference point, as already introduced in Sec. II.3.1 and in Fig. 2.9. The NND is expressed as a matter of form:

$$NND(r) = 1 - \frac{S}{4\pi r^2} \quad (2.64)$$

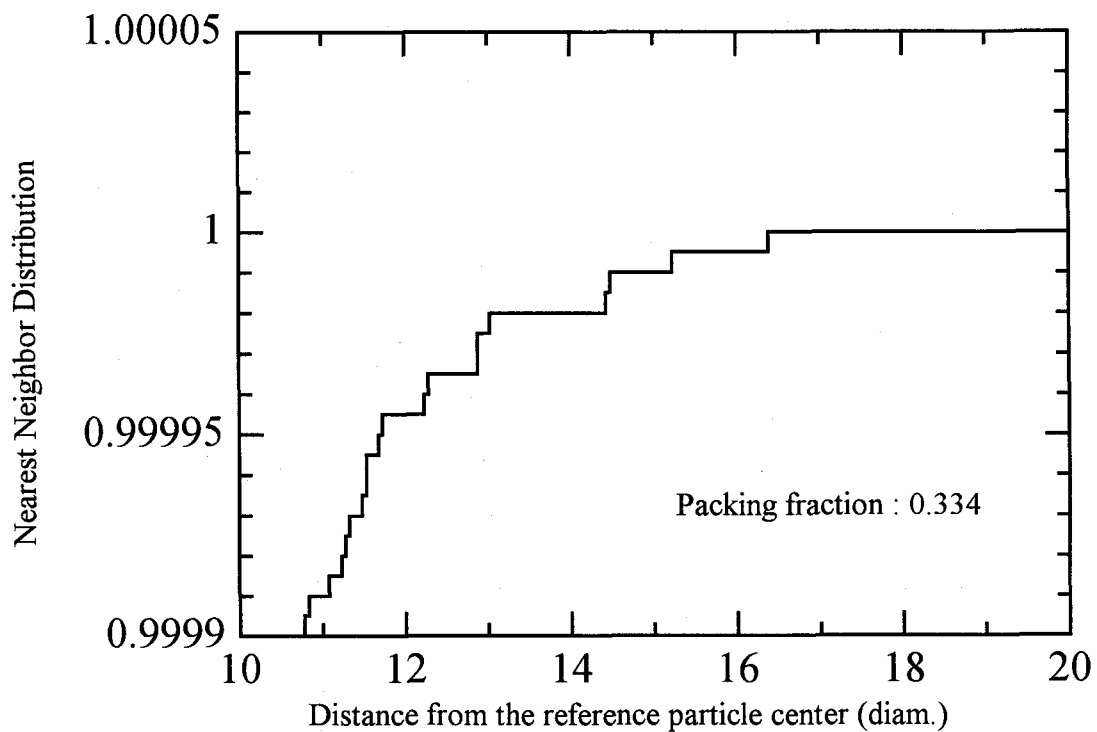
where  $S$  is the area of the spherical shell surface which the reference center point can view without being not obstructed by the spheres existing around the reference.

In MCRDF, NND can be calculated by a ray-trace method after finishing a packing of equal hard spheres. The NND is evaluated by  $10^5$  ray-traces calculation for a system having 1000 spheres. The NND is a cumulative probability distribution realizing a direct sampling from it with a random number. Thus it must have data from 0 up to unity. An example of NND is shown in Fig. 2.23. By the MCRDF calculation, the cumulative probability approaches unity at 15 to 20 diameters from the reference point. However, MCRDF can deal with only 1000 spheres at the maximum because of the limitation of the computer performance. As a result, it seemed that we could obtain NND ranging up to several diameters at most. To solve this problem, the rays getting out of the cubic container are reentered at any place between CFPs except for the calculation for ordered packed geometries such as FCC, BCC and so on. In case of the ordered packed geometries the rays escaping from the container are moved to the position inside the container which is determined so that the relation of the positions of the ray and the spheres after the move, becomes the same as that when escaping. Of course, the direction of the ray is not changed. The packing and ray-trace calculations are finished in  $\sim 10$  and several minutes, respectively.

Table 2.4 summarizes the options to calculate NNDs by MCRDF. The options available are classified by the start positions, i.e., surface of sphere, between spheres, boundary surface of the container and in the sphere. As mentioned in detail in Sec. II.4.1.2, in a practical Monte Carlo transport simulation, three kinds of NNDs calculated by assuming that the start positions are sphere surface, between spheres (in matrix material) and boundary surface of the container are required, corresponding to NND1, option 1 of NND2 and option 5 of NND3 in the



(a) Around the reference particle



(b) Near NND=1.0

Fig. 2.23 An example of NND for packing fraction of 0.334 to be used for VHTRC core calculation.

Table 2.4 Calculation options of MCRDF.

Subroutine	Option	Initial condition of ray-trace			Treatment when escaping <sup>1)</sup>	Employed in this work
		Starting position	Starting angle			
NND1	—	Sphere surface	Cosine		Yes	○(NND1)
NND2	1	In matrix, uniformly	Isotropic		Yes	
	2	In matrix, first collision place	Isotropic		Yes	○(NND2)
NND3	1	Container surface	Normal vector direction		Yes	
	2	In the container <sup>2)</sup>	Isotropic		Yes	
	3	In matrix <sup>2)</sup>	Isotropic		Yes	
	4	In the container	Isotropic		Yes	
	5	(The same as NND2, option 1)				○(NND3)
CRCP	—	Sphere surface	Cosine		No	
CRCP2	—	Sphere center	Isotropic		No	

1) If a ray gets out of the container, MCRDF continues tracking after moving it to any place in the matrix region.

2) At the start position, when making a plane normal to the vector of a ray, if the distance between the plane and the first entering sphere is below the radius of the sphere, the sphere is neglected. Except for options 2 and 3 of NND3, the sphere is not neglected.

table, respectively. It is an interesting result that the option 2 of NND2 corresponds to NND for the start from the boundary surface of the container, namely option 5 of NND3. This means that two kinds of ray-traces in Fig. 2.24 are exactly equivalent.

From the MCRDF calculations, it is found that there is a correlation between packing fraction and maximum free path of a ray in the ray-trace calculation. The maximum free path is defined as the maximum length beyond which a ray can not track without entering a spherical geometry. Figure 2.25 shows the relation of them for  $10^5$  ray-traces. From the calculation results in the figure, it is confirmed that NNDs for a lower packing fraction require a larger amount of data.

To discuss it theoretically, the maximum free path;  $r_{\max}$ , that is defined as the length beyond which the NND is zero, is expressed as the maximum length that meets the next equation.

$$1 - \text{NND}(r) > \frac{1}{N}, \quad (2.65)$$

where  $N$  is the number of ray-traces. Introducing Eq. (2.50) as  $\text{NND}(r)$ , The Eq. (2.65) is rewritten as

$$r < \frac{2(1-f_p)}{3f_p} \ln N, \quad (2.66)$$

where  $f_p$  is packing fraction. Thus we obtain  $r_{\max}$ ,

$$r_{\max} = \frac{2(1-f_p)}{3f_p} \ln N. \quad (2.67)$$

It will be shown in Sec. II.3.3 that Eq.(2.50) could not reproduce an actual arrangement especially near the reference point, however, it could predict the tendency of NND for the distance  $r$  over several diameters. It is confirmed that the tendency of the maximum free path for the packing fraction can be well reproduced by the theoretical curve calculated with Eq. (2.67). In conclusion, with Eq.(2.67), we can obtain  $r_{\max}$  from the given information about the packing fraction of spherical geometries and the dimensions of the system in practical applications. Using the value, we can know beforehand the appropriate number of ray-traces and the necessary

amount of memory occupied by NND data.

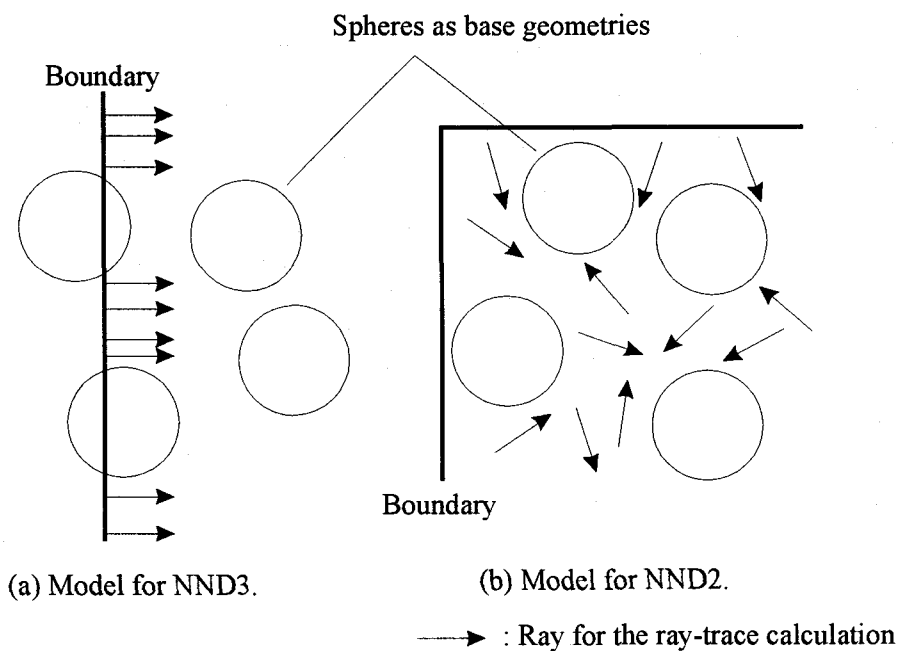


Fig. 2.24 Difference of the models in NND2 and NND3 calculations.  
These two samplings are exactly the same if the starting position of rays are chosen uniformly in the matrix and the vectors are isotropic especially in the right side case.

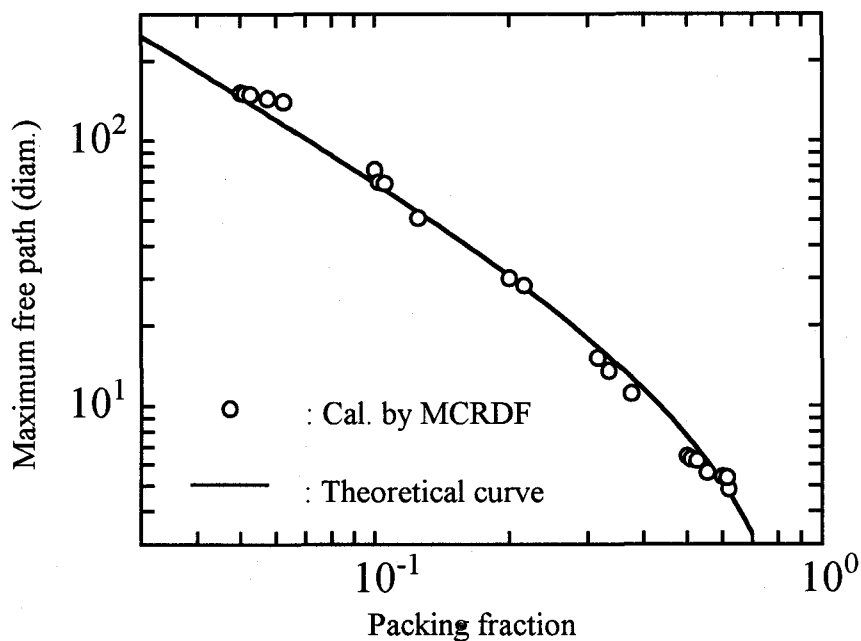


Fig. 2.25 Maximum free path of rays without entering any sphere.

### II.3.2.3.4 Entering angle distribution into sphere

The angular distribution of the particle entering one of the irregularly distributed spheres is required, together with NND, for a Monte Carlo transport calculation of a system having irregularly distributed spherical geometries. The entering angle distribution is evaluated at the same time when calculating NNDs by the ray trace method. In Sec. II.3, it was shown that the angular distribution can be expressed by cosine distribution based on a simple physical consideration, if the spheres are arranged randomly. Figure 2.26 shows the entering distribution for packing fraction of 0.635 when calculating NND1 in Table 2.4. From the figure, it is found that up to 1.5-diameter the distribution is slightly shifted from cosine distribution. The reason is that existence of the reference sphere affects the arrangement of spheres around it, resulting in the distortion of the angular distribution. Of course, in lower packing fractions, the number of contact between the reference and others decreases, as shown therefore in Fig. 2.27, at a low packing fraction of 0.3 the distortion is not seen. However, it is not found out the reason why the distributions fairly fluctuate depending on the distance in Fig. 2.26.

Because even in high packing fractions like RCP, the discrepancy from the cosine distribution is not so large, cosine distribution is assumed for all practical Monte Carlo calculations in this study. Of course, we can consider the precise angular distribution by preparing the data base in the future, if necessary.

### II.3.2.3.5 Distribution of faces with N edges

The number of spheres in contact with a reference sphere is called the number of edges per face, which is known as one of the Voronoi-cell statistics. This is valuable for discussion of amorphous metal characteristics, because the packing of hard spheres seems to be an excellent approximation to the atomic structure of amorphous metals composed of similar sized atoms<sup>(14)</sup>. In MCRDF, if the distance between the reference sphere and another one decreases below 1% of the diameter of sphere, it is regarded as a neighboring sphere of the reference. We count the number of neighboring spheres for the reference sphere to evaluate the number of edges per face. Examples of the distribution of faces with N edges for near-RCP packings calculated by MCRDF are described in Fig. 2.20. Almost the same results are seen for different packing fractions. For high packing fractions, the number of edges per face is around 5~6. It seems that the number of

edges per face tends to decrease with increasing the packing fraction. Actually, it was found from Clarke's result<sup>(14)</sup> that for the packing fraction of  $0.637 \sim 0.645$  spheres having 5 edges per face becomes dominant.

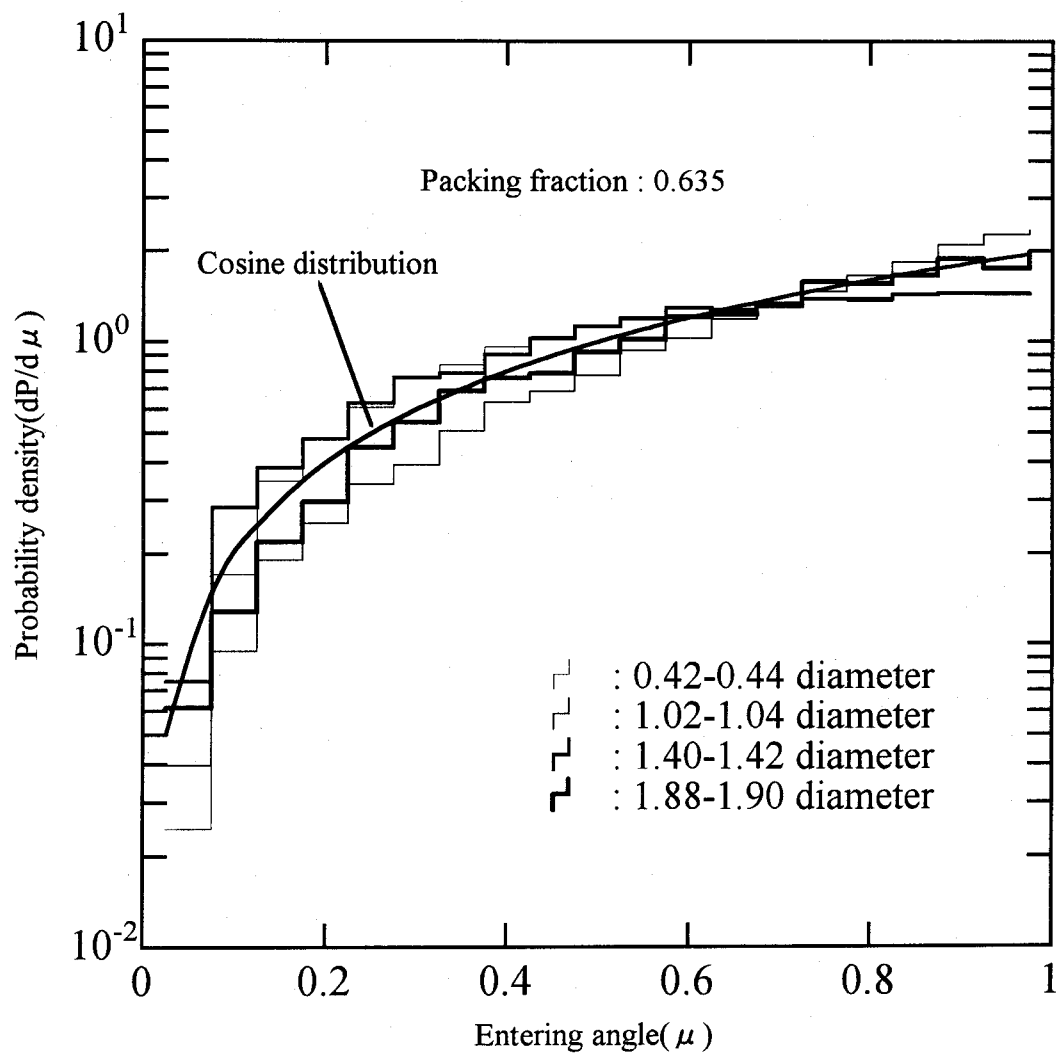


Fig. 2.26 Entering angle distribution into sphere in a high packing fraction.

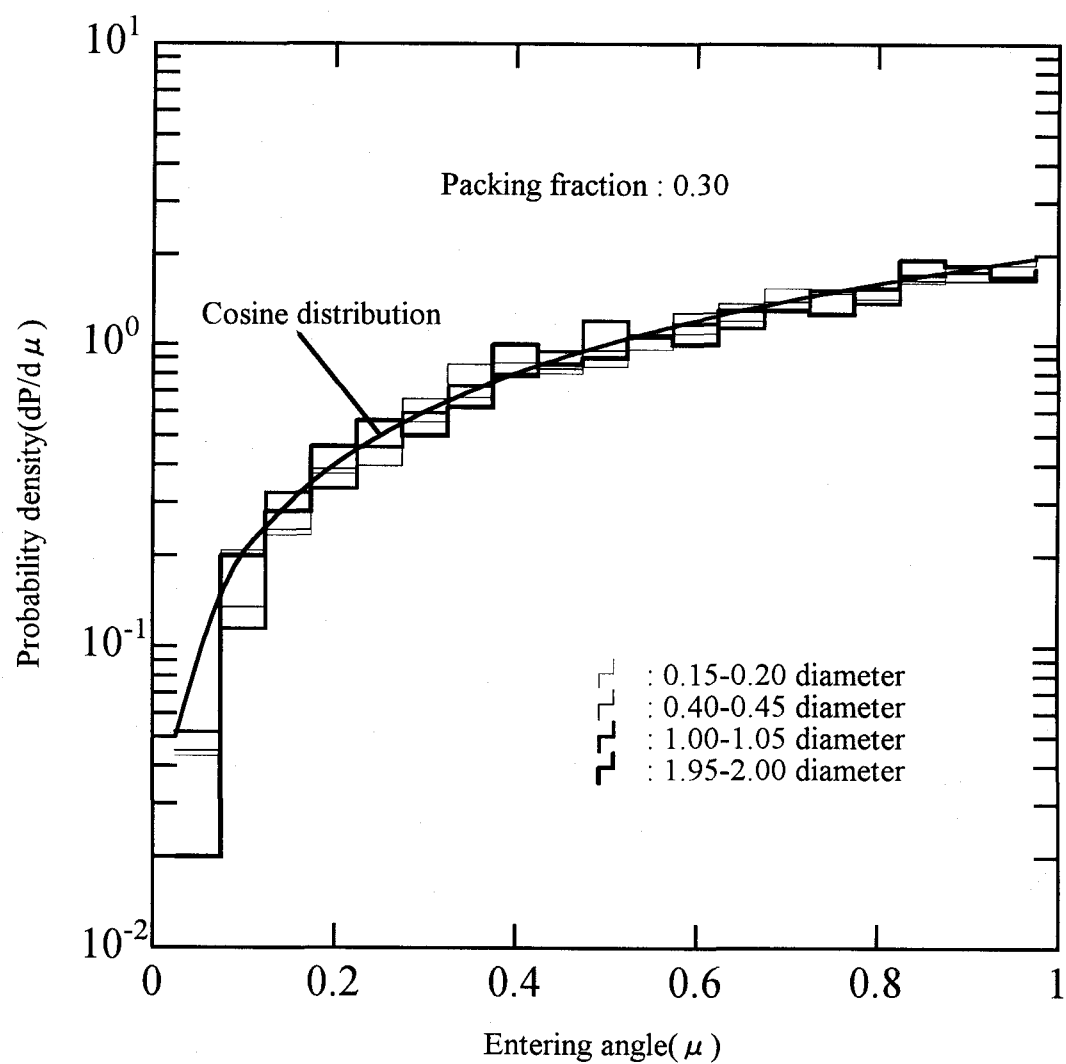


Fig. 2.27 Entering angle distribution into sphere in a low packing fraction.



### II.3.2.4 Validation of MCRDF

The validation of the developed method including the MCRDF code is carried out in Chap. 3. In this section, the validation of MCRDF is done through the comparison of the calculated RDF for RCP with the experimental result. Also, the cross-checking of the code with other calculated results is presented.

As an experimental result to be compared, the investigation result of the structure of noncrystalline electrodeposited Ni-P alloys by X-ray scattering<sup>(42)</sup> was used. The X-ray diffraction analysis method was well applied to investigation of characteristics for metallic solids. Diffraction patterns observed for noncrystalline metallic solids consist of only a few broad overlapping peaks, because noncrystalline solids lack the long-range structural periodicity which is characteristics of crystalline solids. The interference function,  $I(k)$ , is closely related to the corrected X-ray diffraction pattern as shown in the next equation<sup>(43)</sup>:

$$I(k) = \frac{[I_{\text{cu}}^{\text{coh}}(k) - c_{\text{Ni}}c_{\text{P}}(f_{\text{Ni}} - f_{\text{P}})^2]}{(c_{\text{Ni}}f_{\text{Ni}} + c_{\text{P}}f_{\text{P}})^2}, \quad (2.68)$$

where  $I_{\text{cu}}^{\text{coh}}(k)$  is the coherent intensity obtained by correcting the measured intensity for background, polarization and Compton modified scattering,  $k = 4\pi \sin \theta / \lambda$ ,  $f_{\text{Ni}}(k)$  and  $f_{\text{P}}(k)$  are the dispersion corrected atomic scattering factors for nickel and phosphorus based on Cromer<sup>(44)</sup> and Cromer and Waber<sup>(45)</sup>, and  $c_{\text{Ni}}$  and  $c_{\text{P}}$  are the atomic concentrations of nickel and phosphorus, respectively. The interference function can be related to an atomic radial distribution function  $\text{RDF}(r)$  which is characteristics of the atomic arrangement in the isotropically diffracting material. This relation is given by

$$\text{RDF}(r) = \frac{\rho(r)}{\rho_0} = 1 + \frac{1}{2\pi^2 r \rho_0} \int_0^\infty k(I(k) - 1) \sin(kr) dk, \quad (2.69)$$

where  $\rho_0$  is the average atomic density. Details about the experiment are given in Refs.(42) and (43). Figure 2.28 shows the experimentally obtained RDF of Ni-P alloy compared with the calculation by MCRDF. For the positions of peaks in the distribution, both results agree excellently. However, an opposite tendency is found with respect to the absolute intensities of the first and second peaks. In the figure, simulation results by Bennett<sup>(10)</sup> and Jodrey<sup>(12)</sup> are shown for

the cross-checking, and theirs are in good agreement with ours for both the peak positions and intensities. The packing fractions except for the experimental result are around that of RCP, while the packing fraction estimated from the Ni-P diffraction investigation is a little higher packing fraction, 0.669<sup>(42)</sup>. This is the reason that the discrepancy of peak intensities between MCRDF and the experimental result appears, considering the fact that the intensities of the first and second peaks vary sensitively in accordance with the packing fraction<sup>(11)</sup>.

It can be confirmed from the comparison that MCRDF can reproduce the RDF of an actual packing within a sufficient accuracy.

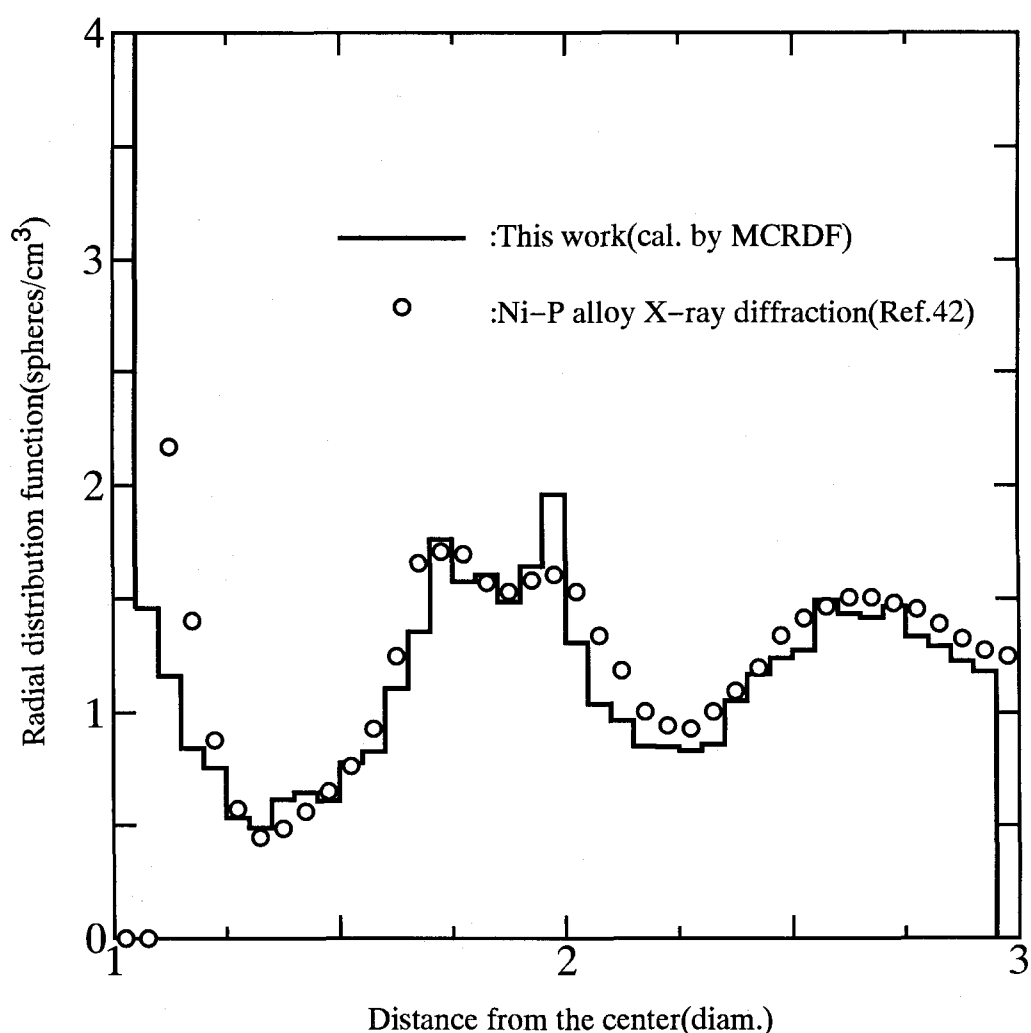


Fig. 2.28 Comparison of radial distribution function between the experimental result made from Ni-P alloy X-ray diffraction analysis and MCRDF calculation.

### II.3.3 Determination of method to calculate NNDs

In Sec. II.3, probability distribution, NND, necessary for Monte Carlo sampling of geometry in a system having irregularly distributed spherical geometries was introduced and its evaluation method was described. It was already shown that we decided to select the numerical packing simulation of hard spheres and the ray-trace method to evaluate NND among three candidates, i.e., (1) numerical packing simulation, (2) equation of state for liquids (P-Y equation) and (3) theoretical calculation based on a statistical assumption. Here, we present the reason why development of the MCRDF code was chosen for the present study.

From the first, it was recognized that the candidate (1) is the most powerful method of the three candidates to obtain a near-exact solution of packing of irregularly distributed spherical geometries, however the candidate (1) requires a new packing simulation code to precisely reproduce packing of them. We hoped that an application of the P-Y equation to Monte Carlo transport simulation becomes a promising route to solve the present problem of treatment of them, because it has been already solved in an analytical expression to facilitate practical sampling<sup>(15,30)</sup>, and it has been already applied to a practical problem of the study of effective resonance absorption of irregularly distributed CFPs in a fuel compact used in HTGRs with the RDF derived from the P-Y equation<sup>(9)</sup>. However, there is an issue that the P-Y equation can consider the inter-molecular forces. In fact, Fig. 2.29 indicates that the RDF derived from the P-Y equation fairly disagrees with the experimental result and other simulation calculation results. We were obliged to withdraw the P-Y equation from the candidate. As for an NND distribution made by the method (3), the curve is also expressed as an analytical form as in Eq. (2.50), therefore the Monte Carlo sampling may become quite simple. Also, the assumption in derivation of the NND is more reasonable than the case of the P-Y equation. Figure 2.30 shows the differentiation of NNDs obtained by MCRDF and the method (3). From the results for packing fractions of 0.5 and 0.6, the theoretical curve reproduces the simulation results evaluated by MCRDF in any region except very close to the reference sphere. However, the theoretical NND for the packing of 0.3 does not agree with the result obtained by decreasing the radii of spheres packed in an RCP state calculated by MCRDF, which is a special treatment for HTGR fuel, for example, introduced in Sec IV.2.1. These results mean that the discrepancy enlarges with decreasing the distance from the reference sphere and with decrease of the packing fraction. The reason is that so many spheres does not exist in the neighborhood of the reference, namely there is a local arrangement composed

of several spheres near the reference in a real configuration, and therefore statistical treatment may not be available. In other words, since we employed the assumption of a uniform distribution of point particles, the RDF became constant. The above discussion is very serious and may include a fatal issue for the candidate (3), because in a real transport behavior in an HTGR core, most transport particles get into the spherical fuels (CFPs) near the reference after getting out from it. The NND near the reference is thus very important. We had to conclude that especially for an analysis of a low-packing-fraction system such as a compact type fuel in HTGRs, the NND calculated by Eq. (2.50) cannot be utilized even as an approximation.

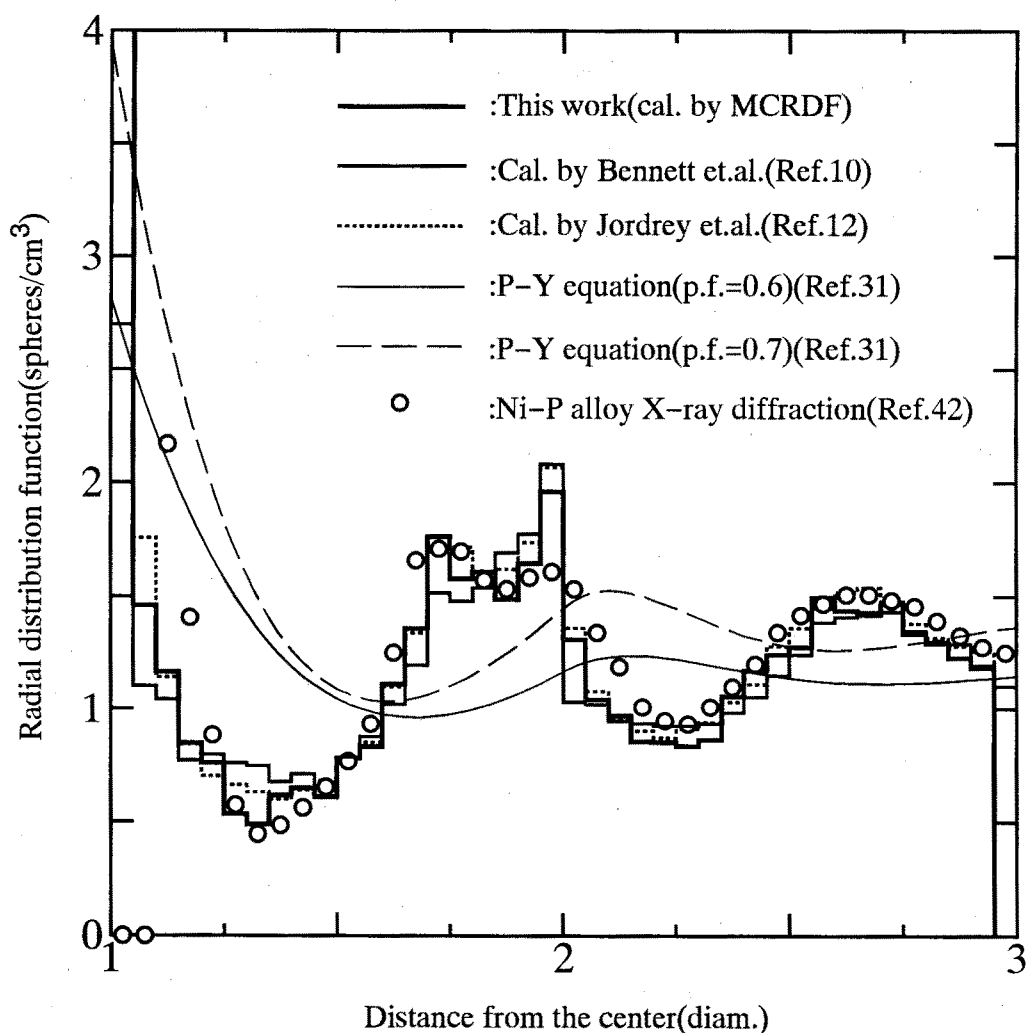


Fig. 2.29 Comparison of radial distribution functions for RCP: Simulated results by Bennet, Jodrey and MCRDF, theoretical results by P-Y equation and experimental result of Ni-P alloy X-ray diffraction analysis.

From the discussions above, the candidate (1), numerical packing simulation was finally chosen for preparing NNDs, by considering our essential purpose of aiming at reference solution of transport calculation of HTGR cores by Monte Carlo code in order to realize more rational nuclear reactor design. As for the method (3), for higher packing fractions It is thought that there is the possibility left of applying the method to the present purpose as an approximated NND evaluation method at higher packing fractions.

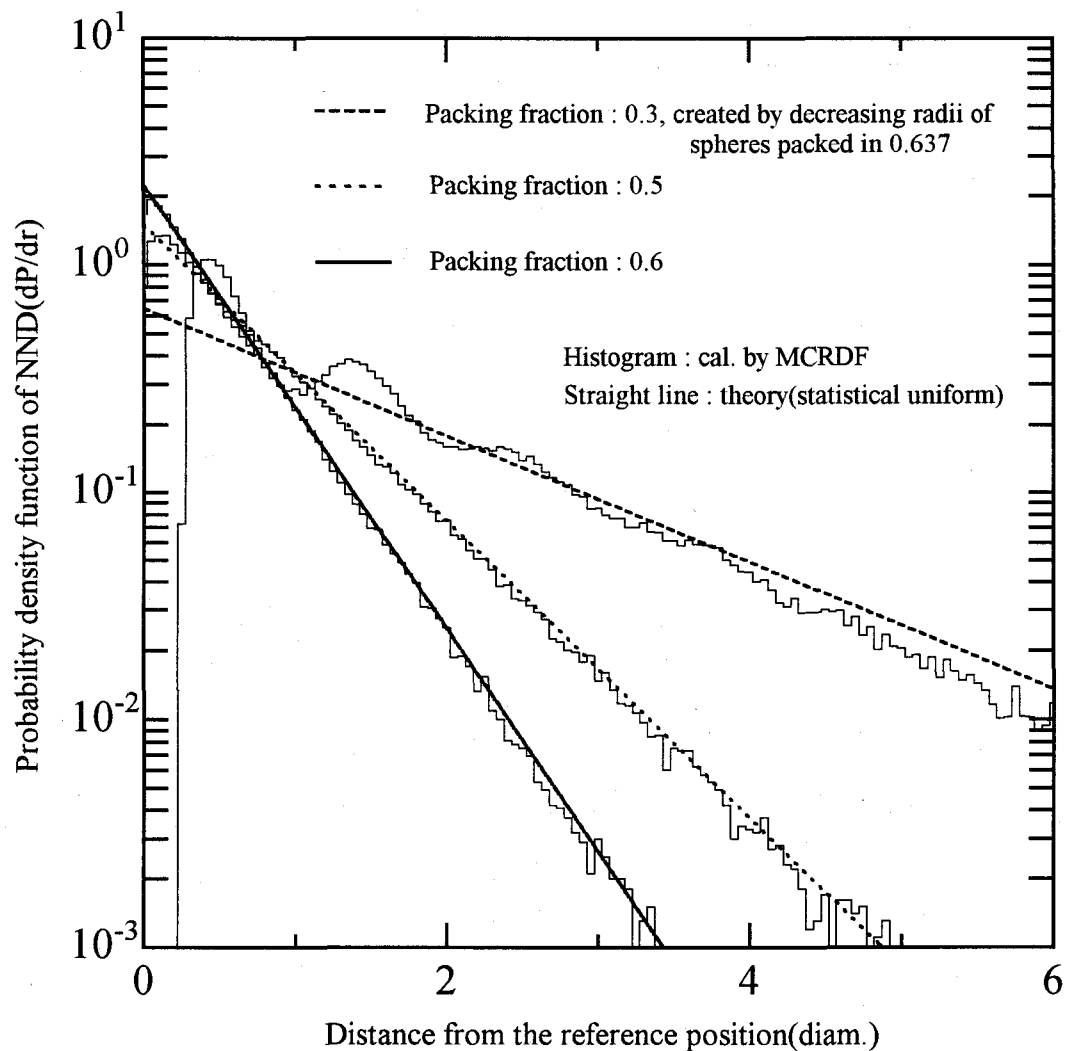


Fig. 2.30 Comparison of probability density function of NND between MCRDF calculation and theoretical analysis result.

## **II.4 Application to Monte Carlo code**

In the following sections, details about application of the developed method to Monte Carlo code are interpreted. The essential sampling method developed and necessary probability distribution are explained precisely in Secs. II.2 and II.3, respectively. They are essential and very important. However, even in realizing a practical use, unexpectedly there exist various important key points to be examined. In the following, the practical sampling concept and method in Monte Carlo simulation algorithm are given. Finally, it is understood that we have to develop two kinds of Monte Carlo codes including the new method depending upon the packing fraction.

### **II.4.1 Sampling method of irregularly distributed geometries**

#### **II.4.1.1 Basic principle of sampling**

Supposing that as an example of spherical geometries utilization, a pebble bed type HTGR is selected for an object which we treat strictly by Monte Carlo method. In this case, there are many fuel pebbles, loaded irregularly in the reactor core, in which a lot of CFPs are packed also irregularly. In general they are contained in a container, therefore they never interfere with the boundary surface of the container. Our objective is to treat such a geometry exactly, that is, to model it as it is. This is, in other words, equivalent to giving the reference solution. In a Monte Carlo transport calculation, to simulate a packing of them exactly, spherical fuel elements should be arranged, so as not to interfere with the boundary surface, just within the region where they exist. And to reproduce the prescribed packing fraction after sampling them, a generalized sampling method properly coping with any sampling event at any location in a container having any shape should be established. Consequently, in case of simulating a packing of spherical fuel elements in a practical transport calculation, if a spherical fuel element to be arranged is likely to interfere with the boundary surface, it should be removed and the next spherical fuel element should be re-sampled (This is called "Low packing fraction mode". Details including the sampling treatment near the boundary are given in Sec. II.4.1.3.). Therefore, the total volume fraction of spherical fuel elements arranged shows slightly smaller than the prescribed packing fraction, i.e., that of NND, because the number of spherical fuel elements arranged near the boundary surface becomes smaller as shown in Fig. 2.31. From a physical consideration, it was found that the total

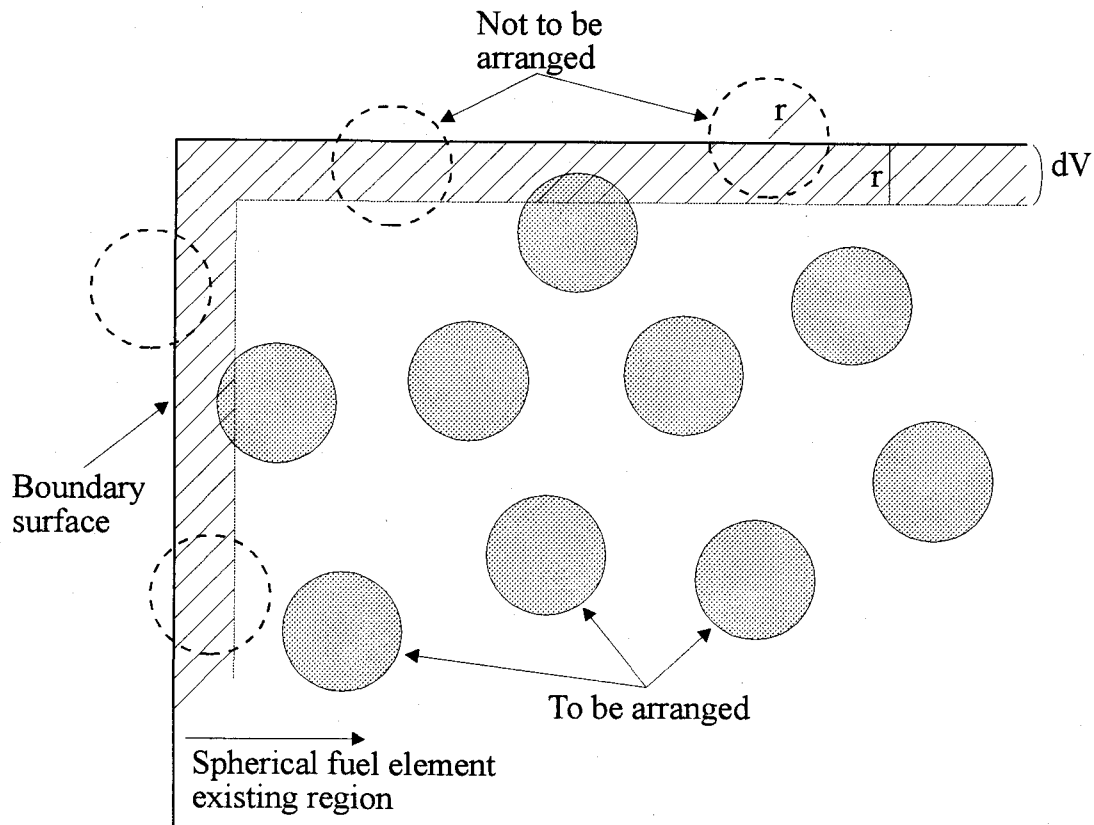


Fig. 2.31 Schematic sampling description in Monte Carlo simulation.

volume of the arranged spherical fuel elements was equal to the prescribed packing fraction multiplied by the container's volume excluding surface layer (See Fig. 2.31). It means that an appropriate correction is required to achieve the inventory of spherical fuel elements corresponding to the prescribed packing fraction. As a result, to realize the sampling of spherical fuel element so as to reproduce the prescribed packing fraction excluding ones interfering with the boundary surface, we have to use the NND for a slightly higher packing fraction determined by

$$f' = f \frac{V}{V - dV} \quad (2.70)$$

where  $f$  is the real packing fraction,  $f'$  the packing fraction of the NND required,  $V$  the volume of the region where spherical fuel elements exist, and  $dV$  the volume of layer  $r$  (sphere radius) in depth from the surface of the region, as shown in Fig. 2.31.

On the other hand, there is a possibility of doing an individual calculation of NND by MCRDF for each problem considering its peculiar modeling and packing fraction in order to simulate the individual problem precisely. But this is of course not a practical means. The packing simulation procedure in MCRDF, in order to develop a general purpose program, is idealized, as if an infinite container including an infinite number of hard spheres is used, by using a finite container and periodic boundary conditions (See Fig. 2.14). In this model, the volume, occupied by all the spheres, which is exactly the same as the total volume multiplied by the packing fraction, always corresponds to the summation of the volumes of the spheres interfering with the boundary as well as not interfering with it. This is a very important fact and therefore using the NND made with this model and removing the interfered spheres when sampling in a practical Monte Carlo transport calculation, as is expected, the packing fraction estimated from the number of arranged spheres underestimates the prescribed packing fraction; that of the NND used. This conclusion is similar to the requirement in the previous discussion from the stand point of the sampling: The NND is prepared, the packing fraction of which should be modified by Eq.(2.70), and in case of sampling a sphere, an interfered sphere should be removed and then a sphere should be re-sampled.

However, as well known, the packing fraction of packing of hard equal spheres has the upper limit<sup>(46)</sup>. As described in Sec. II.3.2.3, the experimentally obtained packing fraction limits of the three dimensional random packing show almost the same value of 0.636 to 0.637<sup>(26,36)</sup>. Recently, it was believed that the RCP could occur for the packing fraction of  $0.64 \pm 0.02$ <sup>(12,39)</sup>. With MCRDF, the packing fraction of RCP is estimated to be 0.6386 by extrapolating the calculated packing fractions to eliminate finite computer time effects as shown in Fig. 2.17. The predicted packing fraction of RCP by MCRDF is a little smaller than Berryman's expectation. However MCRDF was confirmed in Sec. II.3.2.3.1 to be reliable by comparing with the experimental result. From the result of the above-mentioned discussion, it can be assumed that the packing fraction of RCP does not exceed this packing fraction limit;  $f_{RCP}$ . Consequently, depending on the packing fraction and the dimensions of the modeled geometry, the available upper packing fraction is limited by

$$f < f_{RCP} \cdot \frac{V - dV}{V} \quad (2.71)$$

The specific example which does not meet the limitation is the pebble bed reactor such



as AVR and PROTEUS. In these reactor cores, especially for irregularly packing cores, spherical fuel elements (fuel pebbles) are just damped without shaking. The packing fraction is, therefore, about 0.62 being less than RCP's, the packing state of which is called random loose packing (RLP)<sup>(29)</sup> as already introduced in Sec. II.3.2.1. Since the right hand term in Eq. (2.71), which can be estimated by considering the dimensions of these reactors, is not beyond the packing fraction of RLP, they could not be treated with the present sampling method (Low packing fraction mode). Consequently, the sampling method should be divided into two processes corresponding to higher packing fractions of  $\sim$ RLP or over, and lower packing fractions below several tens %. The difference between these two methods is to arrange or not to arrange the interfered spherical elements as clearly understood by the following description. Therefore, the sampling simulated by the method for lower packing fractions is nearer to an actual packing. However, the method requires the packing fraction correction by Eq. (2.70) for each problem caused by the wall effect.

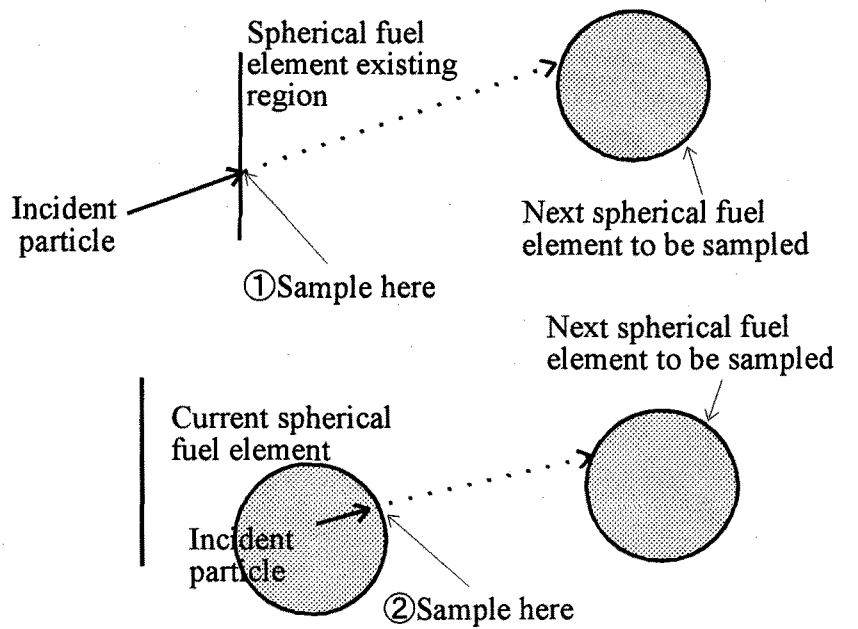
For higher packing fractions, the difficulty in sampling is overcome by the following procedure (This is called "High packing fraction mode"): A new method, which allows sampled spheres to interfere with the boundary surface, was developed. In this method, when arranging a spherical fuel element, even if the spherical fuel element is likely to interfere with the boundary, it is not removed. The intersection region of the spherical fuel element and the spherical-fuel-existing region, which is separated by the boundary surface, is regarded as an available fuel region. Namely, successive Monte Carlo samplings of spherical fuel elements at the boundary make a lot of partial spherical fuel elements interfering with the boundary surface of the spherical-fuel-existing region. This means that, strictly speaking, this method does not reproduce perfectly a real packing compared with Low packing fraction mode because of allowing use of intersection regions. However, the summation of the volumes of arranged spherical fuel elements only in the spherical-fuel-existing region, including the partial regions of interfered ones, exactly corresponds to the prescribed packing fraction of spherical fuel elements. In the Low packing fraction mode, due to neglecting partial regions, correction of packing fraction for NND was required. Using the new method, troublesome problem-dependent calculations of NND for a corrected higher packing fraction depending on dimensions, are not necessary. Moreover, the same NND can be utilized for the systems having the same packing fraction irrespective of their shape or dimensions, resulting in saving troubles especially in parameter survey calculations. Also it is very important that this method enables to simulate a packing with an enough high packing fraction up to the physically achievable upper limit;  $f_{RCP}$ .

### II.4.1.2 Essential sampling timing and necessary NNDs

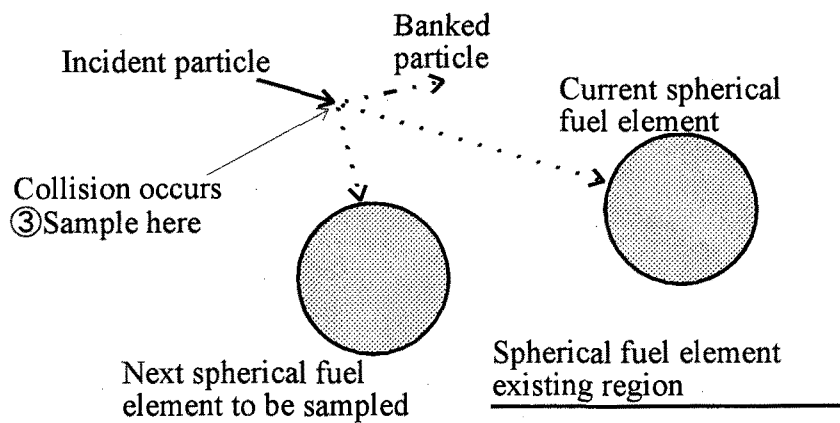
At the beginning, the essential procedure of sampling a base geometry in Monte Carlo transport simulation of a system having a lot of base geometries distributed irregularly is reviewed once again: If a particle enters the system, a base geometry is arranged probabilistically along the particle flight path one after another according to the NND. The location to enter a base geometry is determined by sampling from the NND, and then the entering angle is sampled from a cosine distribution (See Fig. 2.7). By using these values, the location of the base geometry is finally determined and is fixed until the next sampling is carried out.

According to the procedure above, the sampling of a base geometry is done when a particle enters the system. However, the sampling procedure strongly depends on the current particle location. In this section, when a particle is in the system, the practical timing of sampling and the NNDs used depending on the sampling place are presented.

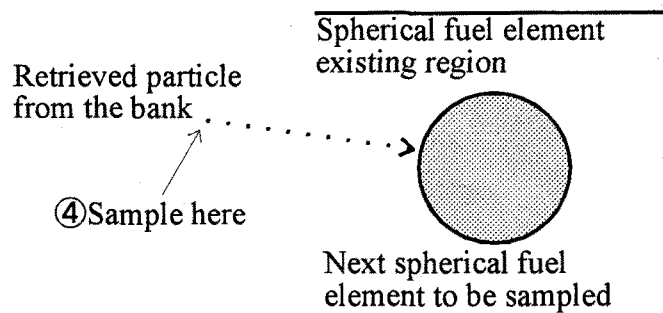
Similar to the previous section, let us start with a pebble bed type HTGR having two kinds of spherical fuel elements, i.e., fuel pebbles loaded irregularly in the core and CFPs packed in a fuel pebble. In a transport calculation with the developed method, sampling of a spherical fuel element is carried out at a timing described in Fig. 2.32. As in Sec. II.4.2.2, the logic of sampling procedure does not change for both the sampling of a fuel pebble in the core and the sampling of a CFP in the fuel pebble, though the pebble bed type HTGR has a double heterogeneity due to fuel pebbles and CFPs. A spherical fuel element should be sampled ①when a particle reaches a region where spherical fuel element exists, ②when it gets out of spherical fuel element, ③when it collides a material atom and the secondary particle is banked (In this case, for example, a neutron may create some particles by  $(n, Xn)$  reaction. The excessive particles information is stored in the array temporarily. After the current neutron transport calculation is finished, retrieving their information and their tracking starts. The excessive particles are called "bank particles" and "bank" means their temporary storing array.) and ④when a banked particle is retrieved from the bank, respectively. Especially for the high packing fraction mode, because interference of spherical fuel element with boundary surface is allowed, in case of ①, the current particle may directly enter a spherical fuel element interfering with the boundary surface. Similarly, after entering it, the particle can directly get back to the region where spherical fuel element does not exist. Among the four cases, ③ and ④ are regarded as the same process from the standpoint of spherical fuel element sampling. Consequently, the following three NNDs are to be prepared as shown in Fig. 2.33.



(a) In case that a particle just reaches the region in which spherical fuel element exists



(b) In case of banking the secondary particle



(c) In case of retrieving a particle from the bank

Fig. 2.32 Sampling timing of spherical fuel element.

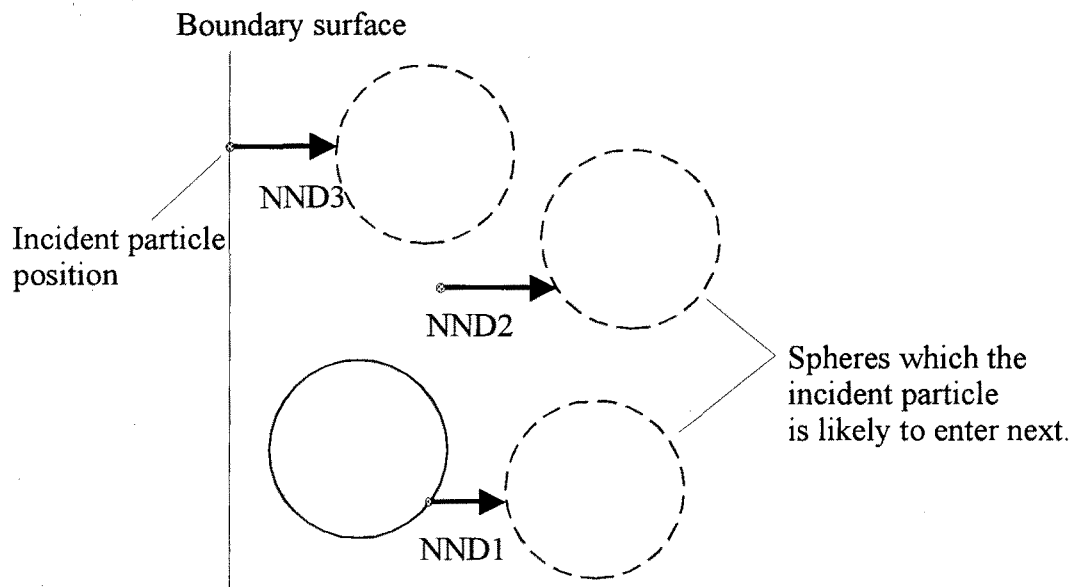
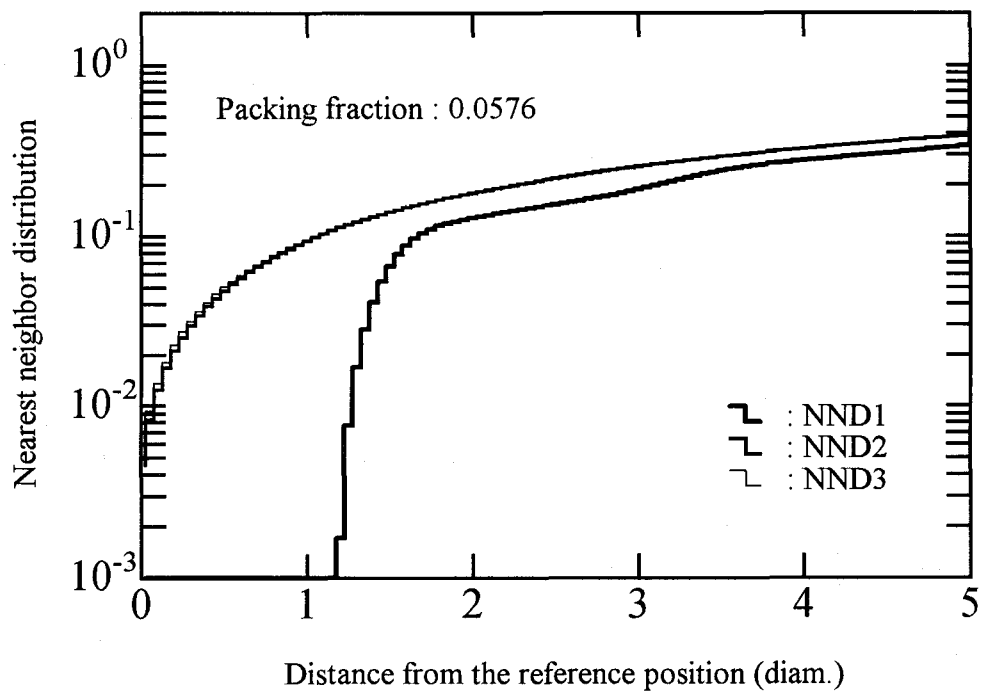


Fig. 2.33 Descriptive arrangement of the starting position in the ray-trace calculation for necessary three NNDs.

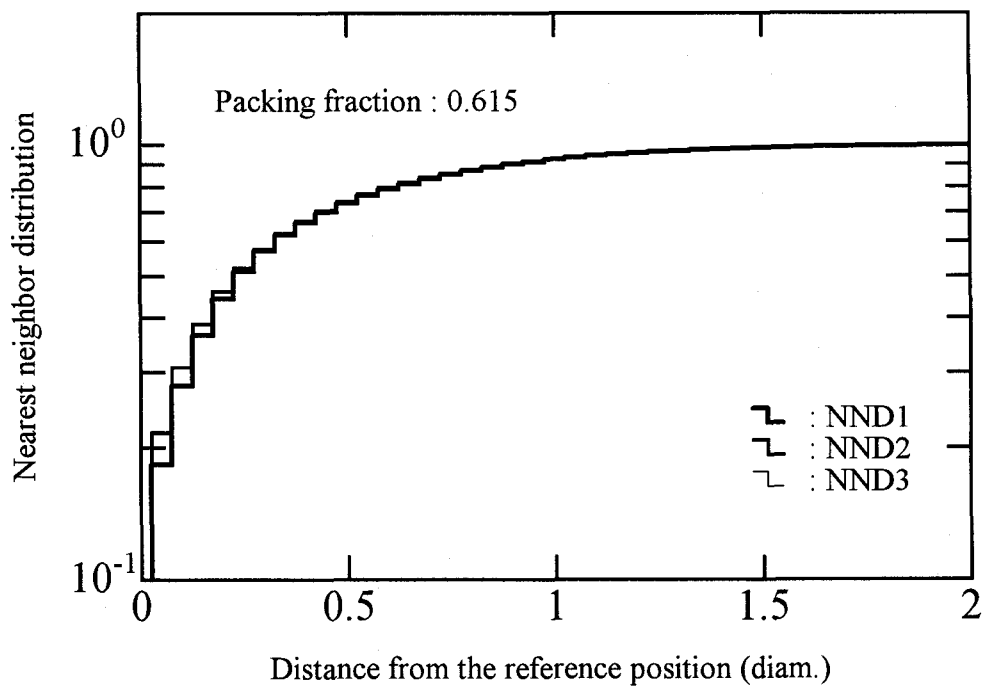
- (1)NND1: A ray-trace starts on the surface of a spherical fuel element in the direction sampled from a cosine distribution, because when a particle enters a sphere from a random direction and get out of a sphere randomly, their angular distribution is exactly cosine of the angle between the normal vector on the start point of the sphere and the particle direction vector.
- (2)NND2: A ray-trace starts in the matrix. However, strictly speaking, the starting point distribution is not uniform in the matrix but depends on the collision density in the matrix. A ray starts from the position where a real particle, starting from sphere surface with the same condition as NND1 calculation, first collides a matrix atom. Therefore the NND2 is dependent of the total cross section of the matrix material.
- (3)NND3: A ray-trace starts on the boundary surface of the region where spherical fuel elements exist. As we can understand in Sec. II.4.1.3, spheres interfering with the boundary of the container should be taken into consideration in making the NND3, to conserve the total inventory of spheres. In a Monte Carlo transport calculation, sampling of a base geometry at the boundary inside and outside the interfered spheres should be simulated separately. As an NND3, it is necessary to exclude samplings in the inside

of the interfered spheres. Consequently, this is exactly equivalent to the ray-trace sampling from the matrix uniformly. The above description is hard to understand. We can clarify it a little later.

Specific examples of NNDs are shown in Fig. 2.34. These are corresponding to the NNDs for CFPs in a fuel pebble and fuel pebbles (These were actually prepared for the pebble bed type HTGR, PROTEUS). Also, Fig. 2.35 shows the NNDs for VHTRC. In HTGRs, CFPs are packed usually in a low packing fraction because matrix material such as graphite exists between CFPs to suppress the rapid temperature rise in a fuel compact or fuel pebble, while fuel pebbles in near-RLP. Figs. 2.34 and 2.35 show, as a result, that their distributions vary considerably. However, in general, it is found from the figure that the NND2 and NND3 are almost the same. The reason is as follows: The NND2 depends on mainly the first collision density of the particle getting out of a spherical fuel element as described earlier. The first collision density tends to become uniform as decreasing the macroscopic cross section of the matrix material and as increasing the packing fraction of the spherical fuel elements. On the other hand, the NND3 can be made by the ray-trace calculation from the matrix uniformly as shown in Sec. II.3.2.3.3. The NND3 becomes strictly equivalent to the NND2, if the NND2 is calculated by assuming that the collision density is constant in the matrix region. In normal applications, mostly the macroscopic total cross section is not so large. Hence, even if the packing fraction is low, the NND2 and NND3 become equal in many cases. It can be found from Figs. 2.34 and 2.35 that they become almost the same distribution irrespective of the packing fraction if matrix material is graphite. In conclusion, it is generally confirmed that the NND2 becomes almost the same as the NND3, as far as the total macroscopic cross section of the matrix is not beyond  $1(\text{cm}^{-1})$ .



(a)NNDs for CFPs in a fuel pebble.



(b)NNDs for fuel pebbles.

Fig. 2.34 Specific examples of NNDs for a pebble bed reactor.

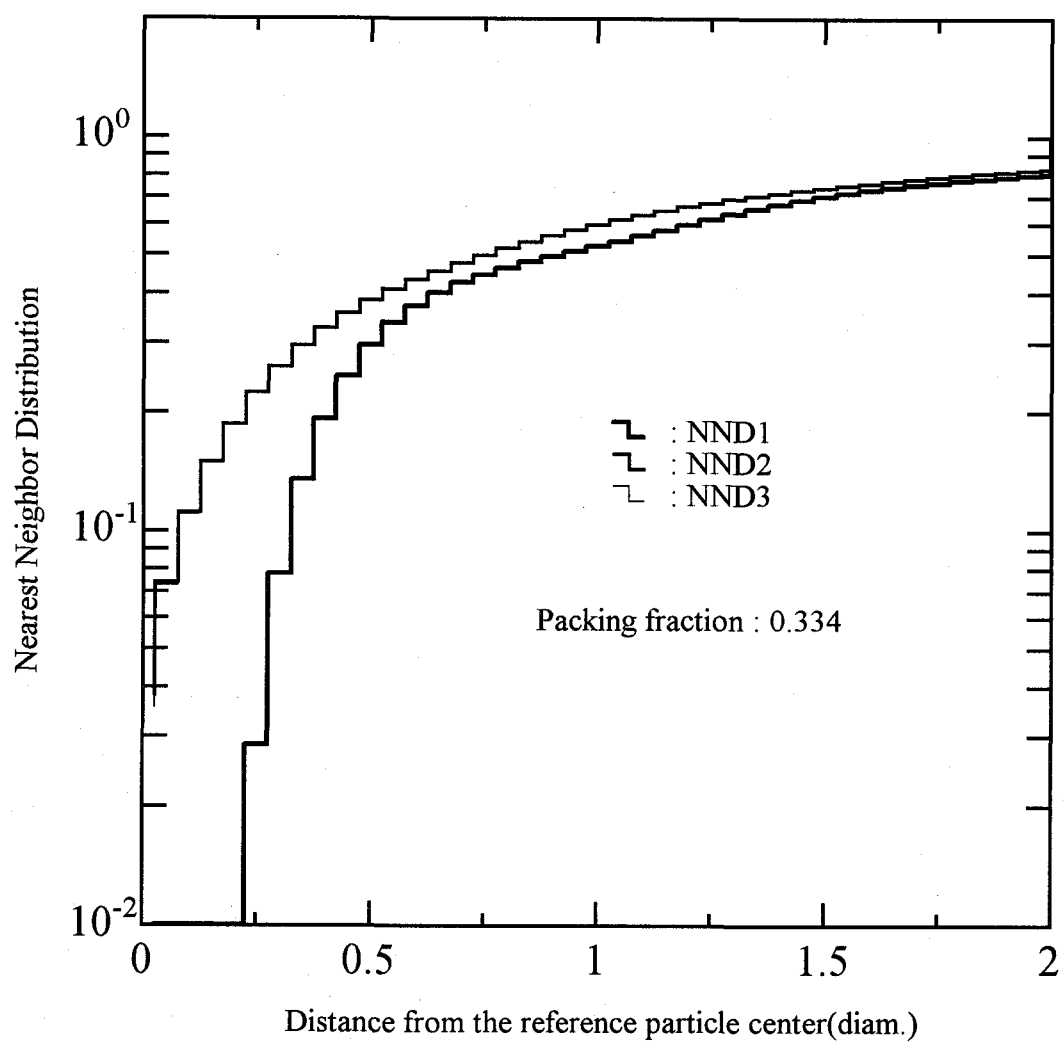


Fig. 2.35 NNDs necessary for VHTRC core calculation.

### II.4.1.3 Sampling method at boundary surface

The most important thing in the present method is how to deal with the sampling near the boundary surface of the container. In the Low packing fraction mode, arrangement of a base geometry interfering with the boundary is prohibited, while in the High packing fraction mode the interference is allowed. For both cases, their respective sampling procedures to reproduce the prescribed packing fraction (inventory of arranged base geometries) were required. In the following two sections, the developed sampling procedures for the two modes around the boundary are precisely described. These procedures are generalized and essential methods to reproduce the real arrangement, which can keep the inventory, i.e., the packing fraction, of the base geometries, in case of sampling a base geometry in a Monte Carlo transport calculation.

#### II.4.1.3.1 Low packing fraction mode

There are two problems to be clarified in the sampling near the boundary as shown in Fig. 2.36. One is how we deal with the sampling when a base geometry to be arranged is likely to interfere with the boundary. And the other is how to sample a base geometry when a particle reaches the boundary of the container. First the former is discussed. Figure 2.37 summarizes the treatment of an interfered geometry with the boundary. Case (a) is a normal case that a base geometry intended to be arranged in accordance with the sampling results from the NND and cosine distribution is likely to interfere with the boundary. In this case, simply a countermeasure is that the base geometry is just not arranged and the transport continues, because the low packing fraction mode aims to reproduce the real configuration. Case (b) is a little complicated problem. In this case, also the base geometry to be interfered with the boundary is not arranged (This is called the virtual base geometry in the following.). However, as shown in Fig. 2.37, there is a path available to track behind the virtual base geometry. And none can know that there is another base geometry behind the virtual base geometry. If the virtual base geometry is just removed this time, at the next sampling from the transport kernel, the particle may transport even behind the virtual base geometry. In such a case the sampling should be completed by taking into account the whole path to the boundary: The base geometry  $\alpha$  is not arranged. There is a possibility of existence of a base geometry behind the location Q. A re-sampling is required at the point Q. If a base geometry is successfully arranged like  $\beta$  in Fig. 2.37, the transport simulation progresses



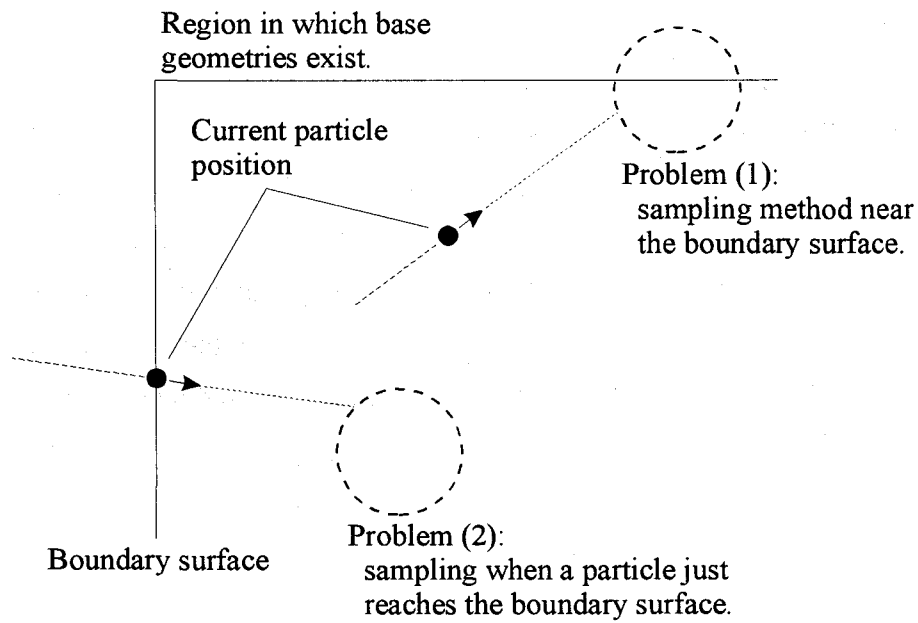


Fig. 2.36 Main problems to be clarified at the sampling.

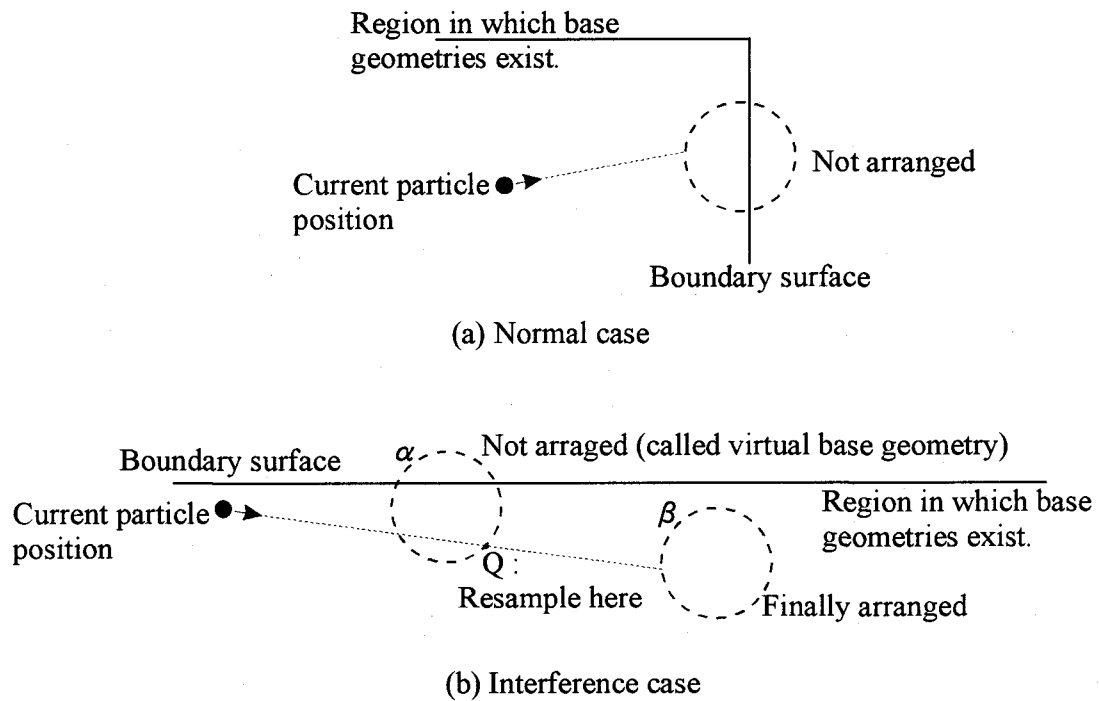


Fig. 2.37 Treatment of interfered geometries with the boundary at the sampling.

to the next step of sampling of the transport kernel. If another interference occurs, re-sampling process is repeated.

Next we discuss the latter case introduced at the beginning of this section. In case that an incident particle reaches the boundary into the base geometry existing region, the method to sample and arrange a base geometry is as follows: The basic concept of sampling at the boundary surface is shown in Fig. 2.38. As shown in the figure, there are two sampling procedures, A and B. Case A is a normal sampling. Case B occurs when the incident particle starts inside the base geometry interfering with the boundary surface. This event is seemingly unnecessary, but quite important to reproduce the packing fraction exactly in a practical Monte Carlo transport simulation. Of course, this is consistent with production process of NND3, because MCRDF calculates the NND3 by excluding the interfered spheres. Actually, CFPs expressed as (b) in the figure are excluded in a transport calculation with the present sampling method because all base geometries exist completely inside a fuel compact. However, when sampling a base geometry at the boundary, they must be considered though they will not be arranged. Why do we need to consider a sampling process for the case B? Clearly in the present study we intend to develop a generalized purpose sampling method applying any kinds of geometries. This means that the ideal packing state we aim at is apparently an example as shown in Fig. 2.39, as a result of transport calculation. We have to remove the interfered base geometries which we can see the cross sections (circles in the case of Fig. 2.39) to reproduce a real configuration. Of course, the packing fraction therefore has to be corrected appropriately to consider this effect as pointed out in Sec. II.4.1.1. If all the samplings at the boundary are done by the method for case A, Fig. 2.39 cannot be reproduced and the packing fraction correction is impossible because it depends on the geometry. Considering these facts, the sampling of a base geometry is performed as the following procedure.

When a particle reaches a boundary surface of a region in which base geometries exist, cases B and A occur with the probability of the same as packing fraction and the probability of the rest, respectively, because the ideal packing state is like an example in Fig. 2.39 and the area ratio of base geometries appearing on the surface in Fig. 2.39 can be estimated to be equal to the packing fraction of them in the container, from a physical consideration that surface is integral element to calculate volume. Therefore, each case should be selected with each probability at first. In case A the sampling of a base geometry is done with an NND3 at the boundary surface, while in case B the sampling of a base geometry is done with an NND1 at the place 0.75 radius inside from the boundary surface. More detail description about case B is given as follows: It is found

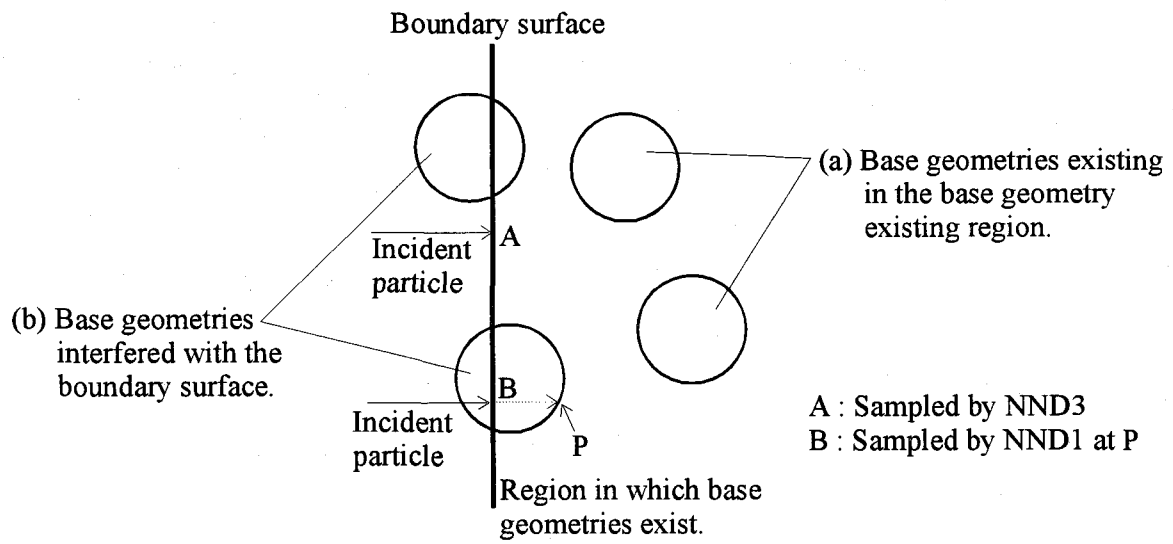


Fig. 2.38 Basic concept in sampling at the boundary surface.

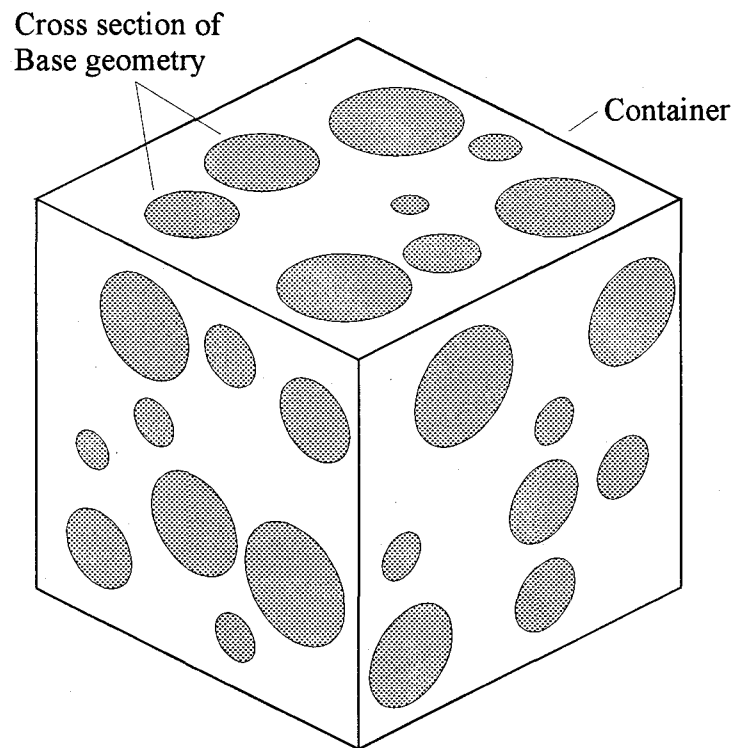


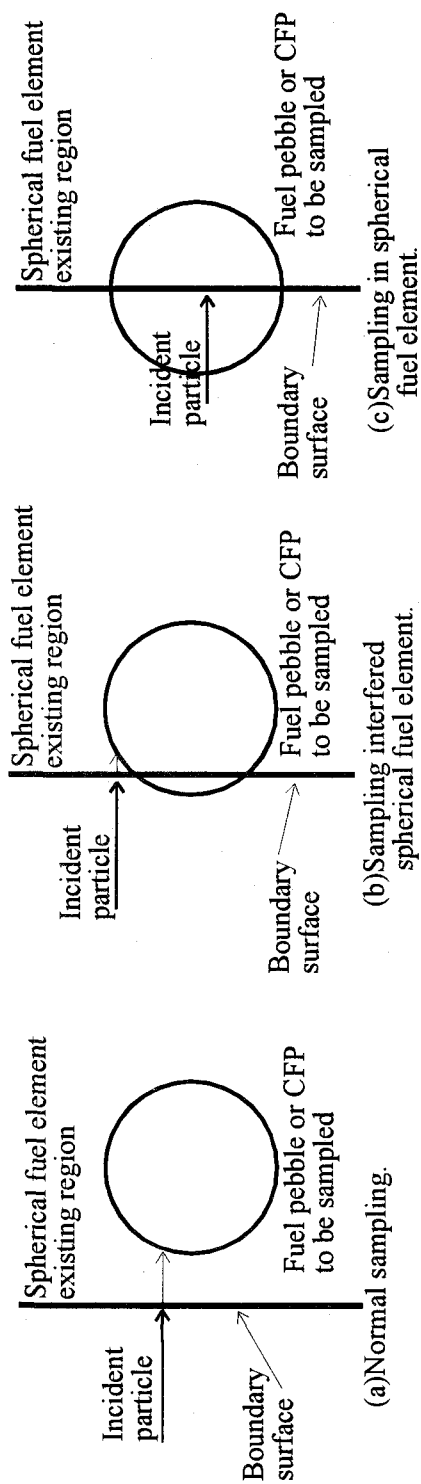
Fig. 2.39 Ideal packing state.

from Fig. 2.38 that there is no base geometries up to the point P in case B. Similar to the discussion at the beginning of this section, we have to re-sample at the point P (actually not re-sample in this case). This requires one to use NND1 for the re-sampling, because the point P is on a base geometry. Also, as for the location of P, it varies depending on the place of the cross section of base geometry cut by the boundary surface. Hence, the average depth from the boundary should be estimated. From the Fig. 2.39, the division of base geometries are made completely at random, and the cutting place is also random. The average depth is evaluated as the average penetrating length to the boundary surface of a base geometry from any point in the base geometry with Monte Carlo method, and obtained to be 0.75 radius<sup>(1)</sup>. In case B, the sampling should be conducted at 0.75 radius inside from the boundary with NND1.

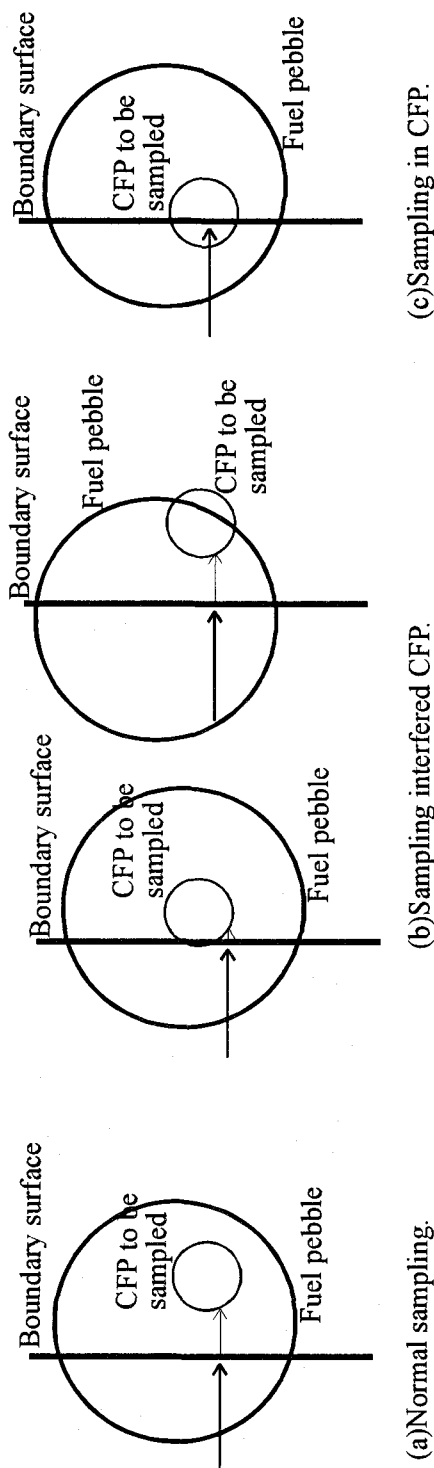
### **II.4.1.3.2 High packing fraction mode**

There are also two problems similar to the Low packing fraction mode in the sampling near the boundary, i.e., how we deal with the sampling when a base geometry to be arranged is likely to interfere with the boundary, and how to sample a base geometry when a particle reaches the boundary of the container. For the former problem, since in the High packing fraction mode the interference is allowed, once a base geometry is arranged with sampling results from the NND and cosine distribution, even if the base geometry is interfered with the boundary, only the inside portion of the base geometry divided by the boundary is regarded as an available region.

In Sec. IV.2.2, the High packing fraction mode is applied to the pebble bed reactor analysis. In the following, therefore the latter problem is treated including the double heterogeneity due to fuel pebbles in the reactor core and CFPs in the fuel pebble. The sampling in the High packing fraction mode, when a particle reaches the boundary of the container (reactor core, or fuel pebble) in which a lot of base geometries (fuel pebbles in the core or CFPs) exist, makes the algorithm in the Monte Carlo code fairly complicated caused by the complexity of its arrangement process. Figure 2.40 shows various sampling patterns allowed in this method. The case (a) is a normal sampling with NND1 or NND3, which corresponds to the case (a) in Fig. 2.32. In the case (1),(a), NND1 not NND3 may be used because the boundary can be the surface of fuel pebble or CFP. In the case (b), re-sampling is required, for the Low packing fraction mode, on the opposite sphere surface. However, in the High packing fraction mode this base geometry is partially valid excluding the portion jutting out the region where base geometries does not exist. Similar to the



- (1) Fuel pebble or CFP is sampled when incident particle reaches the boundary surface into spherical fuel element existing region.
- CFP sampling is done at the boundary if the region where the particle will enter is fuel pebble.
  - Fuel pebble sampling is done there if it is fuel pebble existing region.



- (2) CFP sampling when fuel pebble is sampled by (c) in (1)

Fig. 2.40 Sampling patterns at boundary surface.

case (1),(a), NND1 is used if the boundary is the surface of fuel pebble or CFP. Treatment of the case (c) is a little complicated. This is a case that can occur in the case (a), ① in Fig. 2.32, and also that a particle directly enters a spherical fuel element; therefore the base geometry to be arranged interferes with the boundary surface. The Low packing fraction mode processes it by the same procedure as the case (b), that is re-sampling. However, in the high packing fraction mode this base geometry is arranged. Thus, the probability that the case (c) occurs and how to determine the coordinates of a base geometry to be arranged must be discussed next. Also in cases (a) and (b) in Fig. 2.40(1), it is noticed that when a fuel ball is sampled, the cell, where the particle existed previously, may be the cell in which fuel ball does not exist, fuel ball itself or CFP.

As for the probability of the case (c), from a physical consideration, the area ratio of base geometries appearing in any cross section of base-geometry-existing region can be equal to the packing fraction of them, as shown in the previous section (See Fig. 2.39), if they are distributed sufficiently at random in that region. Therefore, when an incident particle is going to enter the base-geometry-existing region at the boundary surface, the particles in the percentage of packing fraction induce the case (c). While cases (a) and (b) are induced by the rest particles.

We discuss next where base geometry should be arranged in the case (c). As recognized easily, it is a very important feature in this method that the boundary surface is equivalent to any cross section of base-geometry-existing region (See Fig. 2.39). This means that the number of cross section circles per unit  $\mu$  appearing on the cross section is constant, where the  $\mu$  value is calculated from the radius  $r$  of cross section circle using the condition in Fig. 2.41. Also, the number of incident particles inserting the cross section circle per unit area is constant. These facts seemed to lead to the next sampling method: First a  $\mu$  value is sampled uniformly to make a cross section circle, then coordinates to enter a base geometry are sampled uniformly in the circle, finally a unit vector is sampled isotropically. Consequently, the sphere is arranged as a base geometry such that the coordinates and the vector get equal to those of the incident particle on the boundary surface (See Fig. 2.7). This method was expected to reproduce the actual behavior. However, since the area of a cross section circle varies depending on the  $\mu$  value, the sampling number per unit area in the circle varies also depending on the  $\mu$  value. This means that it is required at the sampling that the weight of a tracking particle should be adjusted, as shown in the later. This adjustment arises variance increase because a large difference in particle weight exists with respect to the  $\mu$  value. We, therefore, introduced a very simple method that coordinates in a given sphere and a unit vector are sampled uniformly and isotropically,

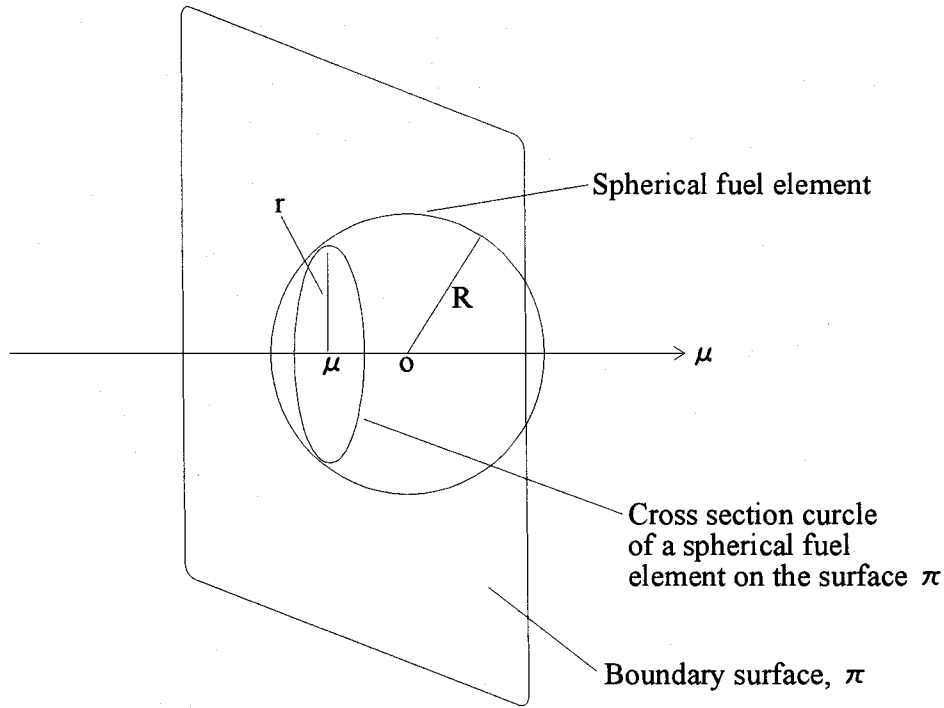


Fig. 2.41 Arrangement of spherical fuel element interfering with boundary surface.

respectively. Then, as described earlier, the sphere is arranged as a base geometry such that the coordinates and the vector get equal to those of the incident particle on the boundary surface. As shown in the following, this sampling method can reproduce the actual behavior of the case (c) in Fig. 2.40.

First, we confirm from the following discussion that uniform sampling of  $\mu$ , which determine coordinates in the cross section circle, is equivalent to sampling uniformly in a sphere, adopted in this study. The former sampling method indicates an actual situation, that is equivalent to selecting any cross section in base-geometry-existing region. As described earlier, the number of the cross section circles per unit  $\mu$  is constant. And sampling is done uniformly on the boundary surface, that means the number of sampling in the cross section circle is proportional to the area of it. Consequently, the sampling number density function,  $F(\mu)d\mu$ , is written as

$$F(\mu)d\mu = C\pi r^2 d\mu, \quad (2.72)$$

where C is the proportional constant. The  $\mu$  meets the relation,  $r^2 + \mu^2 = R^2$ , where r is the radius of cross section circle, R the radius of base geometry (spherical fuel element in this section). Finally

we obtained

$$F(\mu)d\mu = C\pi(R^2 - \mu^2)d\mu. \quad (2.73)$$

As  $\pi(R^2 - \mu^2)d\mu$  is volume element of sphere,  $F(\mu)d\mu$  is confirmed to be proportional to the volume of base geometries between  $\mu \sim \mu + d\mu$  and therefore to be uniform in a base geometry.

Next we discuss the direction of a sampled unit vector. It is a very important key point to check whether or not the average transmitting length in the arranged base geometry from the sampled position becomes equal to the actual transmitting length. In case of sampling coordinates uniformly in a sphere and transmitting vector isotropically, which is the method employed in this study, the average transmitting length is  $0.750R$  as calculated with a Monte Carlo method<sup>(1)</sup>. We check that the average transmitting length in an actual case, evaluated here by the following procedure, becomes  $0.750R$ .

- (1) To make a cross section circle on the plane  $\pi$ , sample a position uniformly with respect to the  $\mu$  axis.
- (2) Sample incident particle coordinates uniformly within the cross section circle on the plane  $\pi$ .
- (3) Give the incident particle the weight of  $W(\mu); 3/2 \cdot (1 - \mu^2)$ .
- (4) Sample a unit vector isotropically.
- (5) Calculate the length to the boundary surface from the incident particle position along the unit vector, and tally the length multiplied by the weight of the particle.

Where the weight  $W(\mu)$  is given as  $S(\mu)/S_{ave}$ ;  $S(\mu)$  is the cross section circle area at  $\mu$ ,  $S_{ave}$  is the effective cross section area of the sphere with respect to  $\mu$ ;  $2/3 \cdot \pi R^2$ . As described earlier, the weight,  $S(\mu)/S_{ave}$ , can be used as a correction factor to adjust the effect of cross section circle area. From the Monte Carlo calculation, the average transmitting length for an actual case is estimated to be  $0.750R$ , which is confirmed to be equal to that of the method adopted in this study.

In a practical transport simulation, the incident angle distribution of the particle at the boundary surface cannot be known and may not be isotropic. Thus, using a broad parallel beam as another extreme condition, the average transmitting length is similarly calculated, and  $0.752R$  is obtained. From the results, it is concluded that this method is applicable for almost all practical situations.



## II.4.2 Developed codes

The new method developed in this study was implemented in the general purpose Monte Carlo code MCNP-3B<sup>(47)</sup>. MCNP was developed at Los Alamos Scientific Laboratory (LASL), USA, for neutron, photon, or coupled neutron-photon transport, including the capability to calculate eigenvalues for critical systems. The first version of MCNP was released in June, 1977. The current version, MCNP-4B<sup>(48)</sup>, includes electron transport. MCNP has various features as follows: The code treats an arbitrary three-dimensional configuration of materials in geometric cells bounded by first- and second-degree surfaces and some special fourth-degree surfaces. Pointwise cross section data are used. Especially for neutrons, all reactions given in a particular cross section evaluation are accounted for. Variance reduction techniques which are available to improve computational efficiency include geometry splitting and Russian roulette, weight window, correlated sampling, and so on.

Two modified codes MCNP-CFP and MCNP-BALL for the Low and High packing fraction modes, respectively, were developed based on MCNP-3B. New subroutines and modification of the original routines with respect to arranging a base geometry were added to MCNP-3B. For MCNP-BALL, moreover, some main routines in MCNP-3B had to be modified. For this reason, though having aimed at preparation of modular routines of the method at the beginning of the development, we gave up the idea of generalized development and did the exclusive modification for MCNP-3B. Some extra efforts are required for implementation of the method into other general Monte Carlo codes. The details are given in Ref. (3).

### II.4.2.1 MCNP-CFP code

MCNP-CFP can realize a transport simulation of a system having a lot of base geometries distributed irregularly, and employs an exact model prohibiting samplings of spherical elements interfering with the boundary surface of the container. Spherical elements with several layers are available as base geometries. However, just one kind of spherical element can be treated. The algorithm of MCNP-CFP is shown in Fig. 2.42. The main transport routine HSTORY is modified with a program of arrangement process of spherical element. In SOURCK and COLIDK subroutines, a routine was added that the location of spherical element to be entered by a generated neutron accompanying fission reaction is stored. Also other excess particles created by

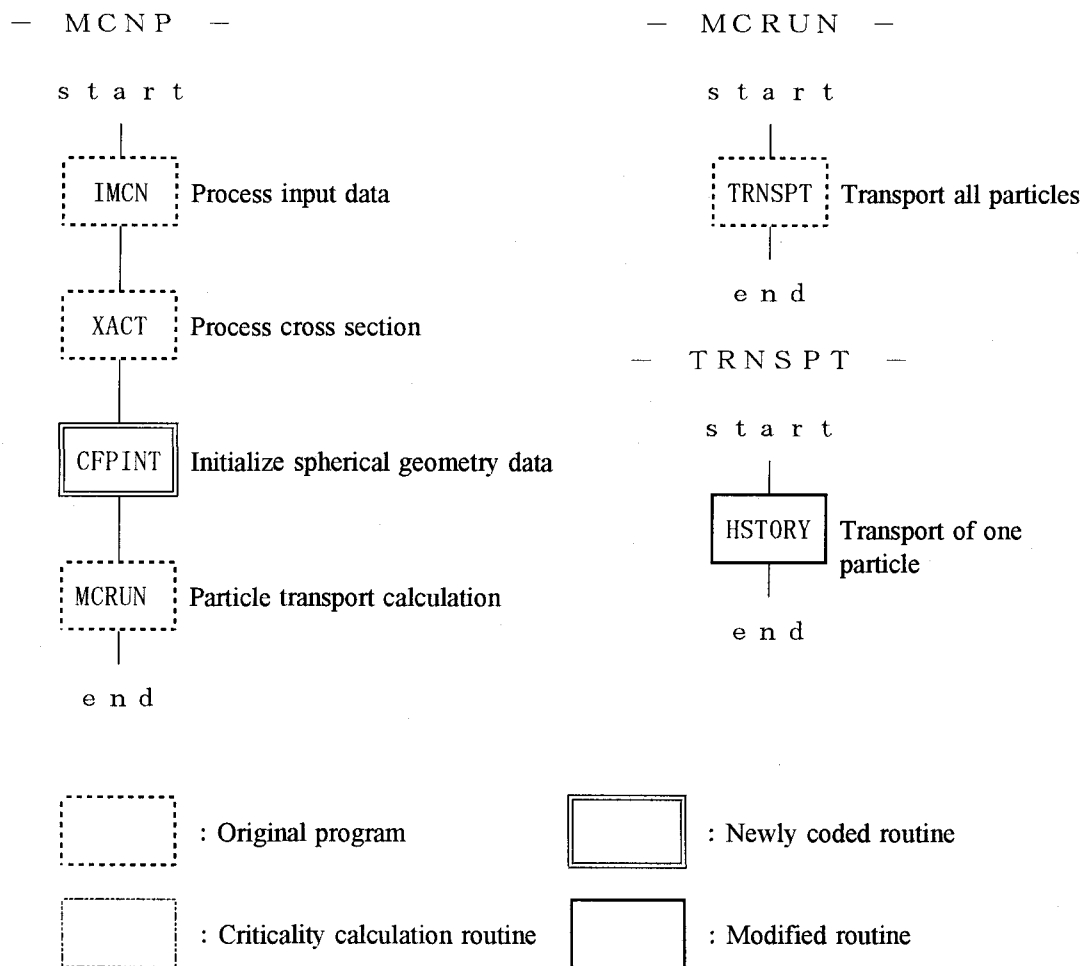


Fig. 2.42 Flow of particle transport in MCNP-CFP (1/2).

- HISTORY -

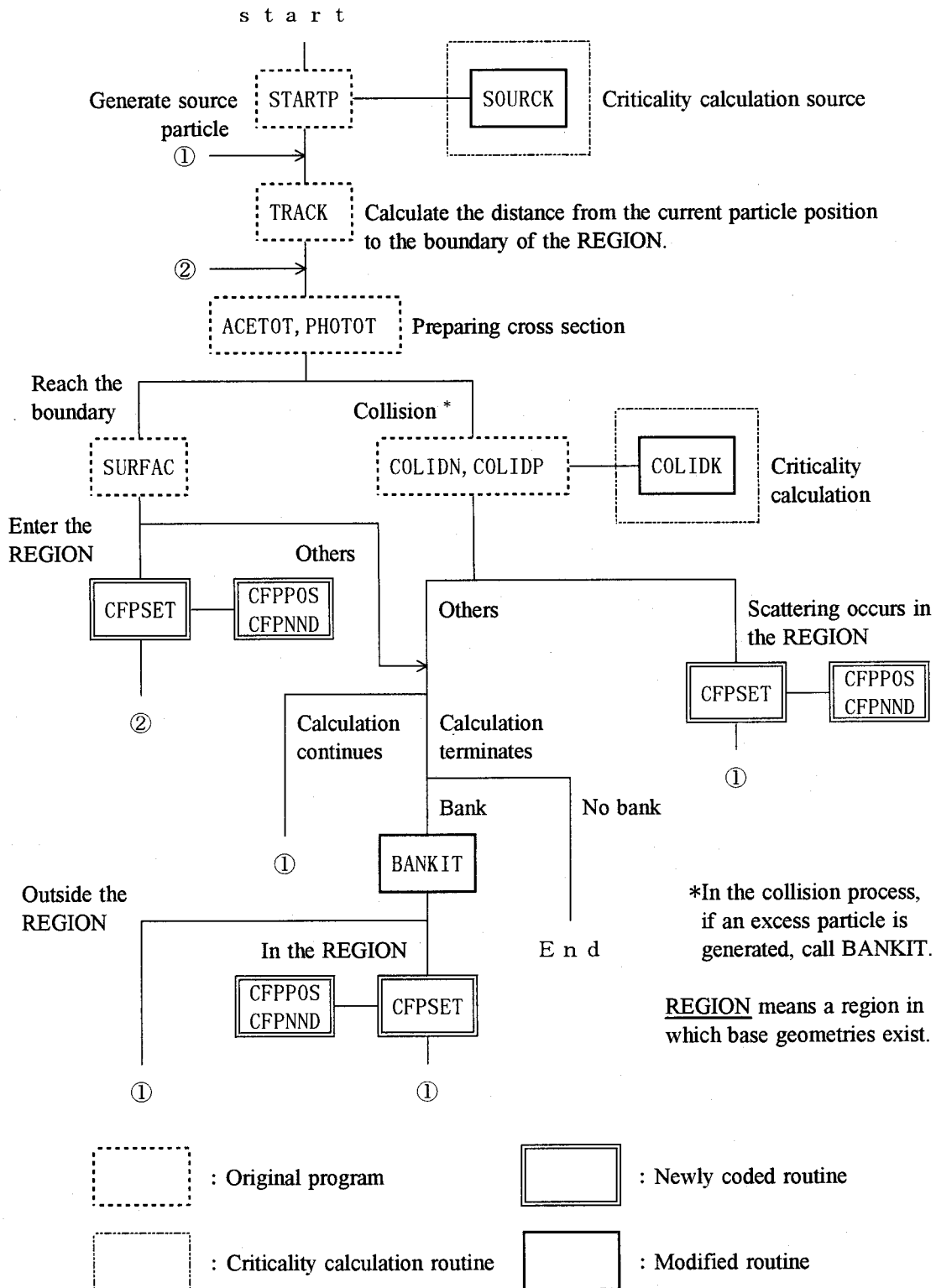


Fig. 2.42 Flow of particle transport in MCNP-CFP (2/2).

(n,xn) reaction, Russian roulette process and so on are banked by BANKIT, in which the location of the spherical element is stored until the information is retrieved from the bank. The arrangement of a spherical element is done at timings illustrated in Fig. 2.32 by calling subroutine CFPSET. In CFPSET, CFPPOS of determining the position of spherical element to be arranged and CFPNND to confirm the interference of spherical element to be arranged with the boundary surface, are included. CFPNND calculates the minimum length from the center of arranged spherical element to the boundary surfaces. In order to avoid the interference between the spherical element arranged and the boundary surface, the following checks are carried out when a spherical element is just arranged (See Fig. 2.43).

(1) Check the relation of  $DI < DLS$ ,

where  $DI$  is the distance from the current particle coordinates to the entering location on the spherical element and  $DLS$  is the distance along the flight direction to the boundary surface from the current particle coordinates.

(2) Check the relation of  $DMN > RAD$ ,

where  $DMN$  is the minimum distance from the center of the spherical element to the surfaces of which the spherical-element-existing region is composed and  $RAD$  is the maximum radius of the sphere surfaces constituting a spherical element.

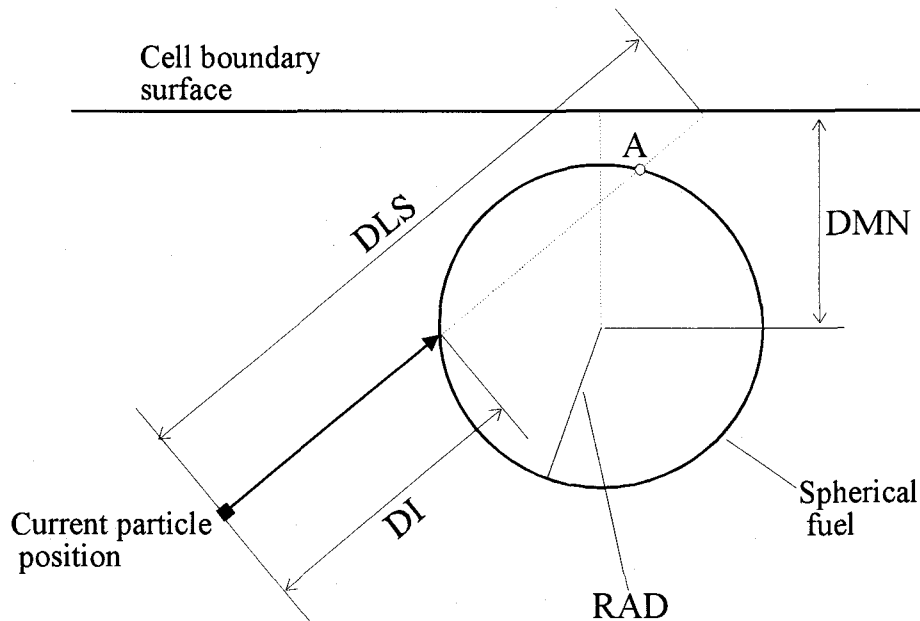


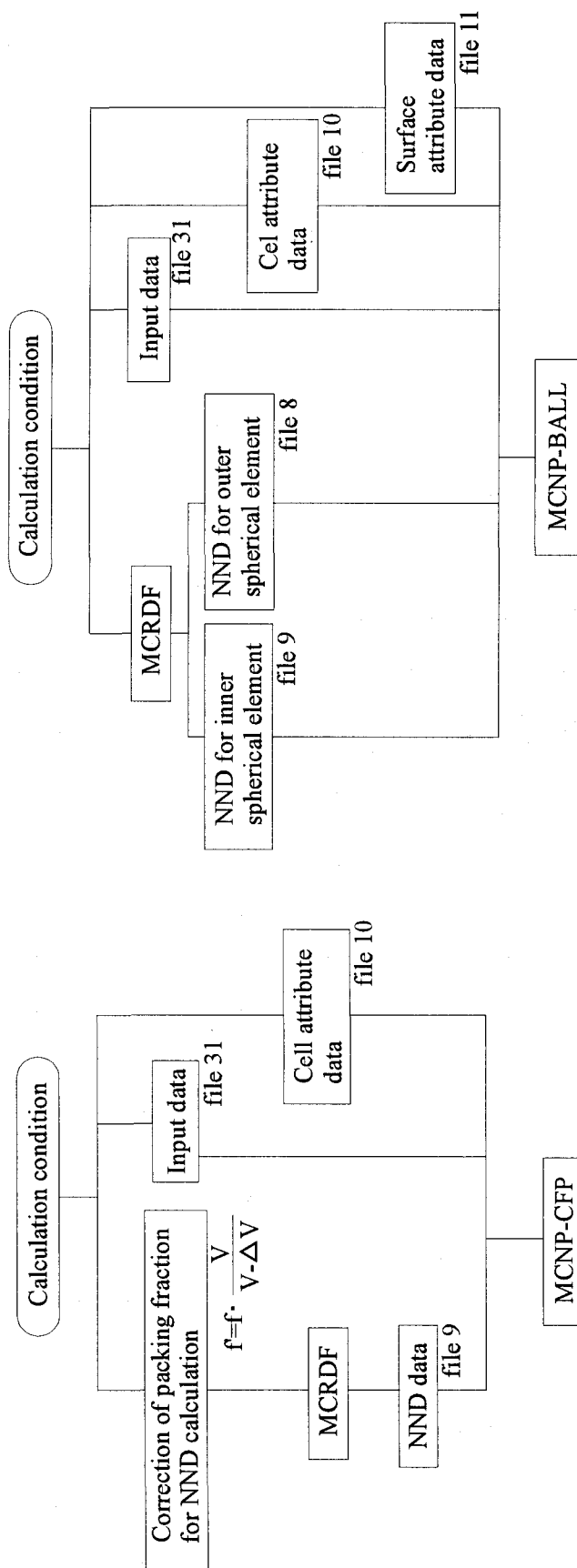
Fig. 2.43 Relation of spherical element to be arranged and boundary surface.

In case of violating (1), spherical element is not arranged. In case of violating (2), the re-sampling of a spherical element is necessary at the exit boundary surface of the spherical element (point A in Fig. 2.43), if the point A is in the spherical-element-existing region. Using the present sampling method, the prescribed packing fraction of the region having any complicated boundary surfaces can be conserved by using the boundary surface correction introduced in Sec. II.4.1.1. The location of a spherical element to be arranged is finally determined from the sampling result using NNDs and a cosine distribution for entering angle. Also the flow of the calculation procedure with MCNP-CFP is described in Fig. 2.44. Before the calculation, the packing fraction correction has to be done with the shape and dimensions of the system, i.e., the container of the spherical elements. The NNDs for the corrected packing fraction are prepared with MCRDF. As the input data, the attribute data indicating which cell is spherical element or a cell in which a lot of spherical elements exist is required in addition to the standard input data for MCNP-3B. The details are given in Ref. (3).

## II.4.2.2 MCNP-BALL code

MCNP-BALL can simulate a particle transport of a system with irregularly distributed spherical elements, allowing samplings of spherical elements which interfere with the boundary. But generally no applications exist which possess the interference structure. Strictly speaking, the code thus cannot realize exact reproduction of the same packing configuration as the real one. Because MCNP-BALL was developed mainly for the analysis of a pebble bed type reactor such as PROTEUS, as shown in Sec. II.4.1.3.2, the code can deal with two kinds of spherical elements such as fuel pebble and CFP at the same time. This means that the code can cope with two kinds of spherical elements constituting a double heterogeneous structure, and it can be analyzed as exactly as possible with the improved algorithm. Of course, for this reason, a spherical element having coated layers and a system with fuel pebbles and moderator pebbles can be also precisely modeled. It is easily realized by some further modification to increase the number of kinds of pebbles or layers.

The algorithm of MCNP-BALL is shown in Fig. 2.45. Similar to MCNP-CFP, the main transport routine HSTORY was modified in the same way. In addition, TRACK and SURFAC subroutines had to be revised taking into account the interference process. In subroutines SOURCK and COLIDK, modification due to banking process of fission neutrons as is introduced in the

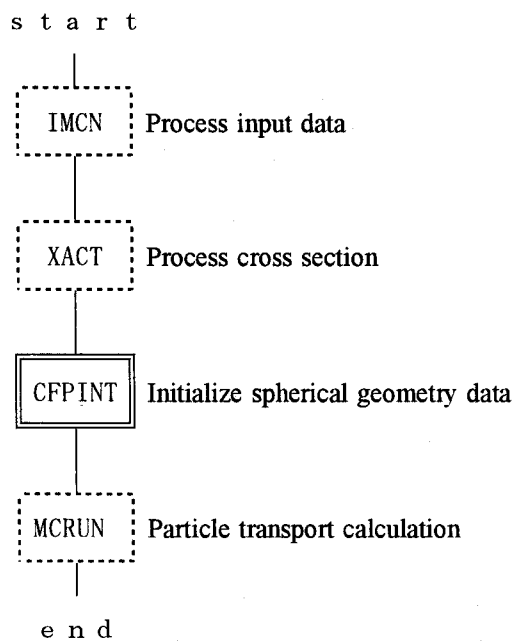


(a) MCNP-CFP

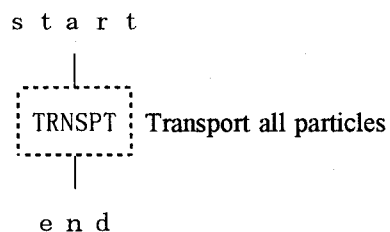
(b) MCNP-BALL

Fig. 2.44 Calculation flow of MCNP-CFP and MCNP-BALL.

— MCNP —



— MCRUN —



— TRNSPT —

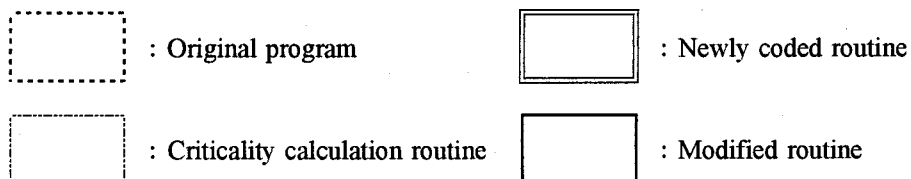
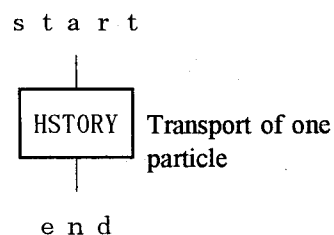
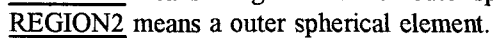


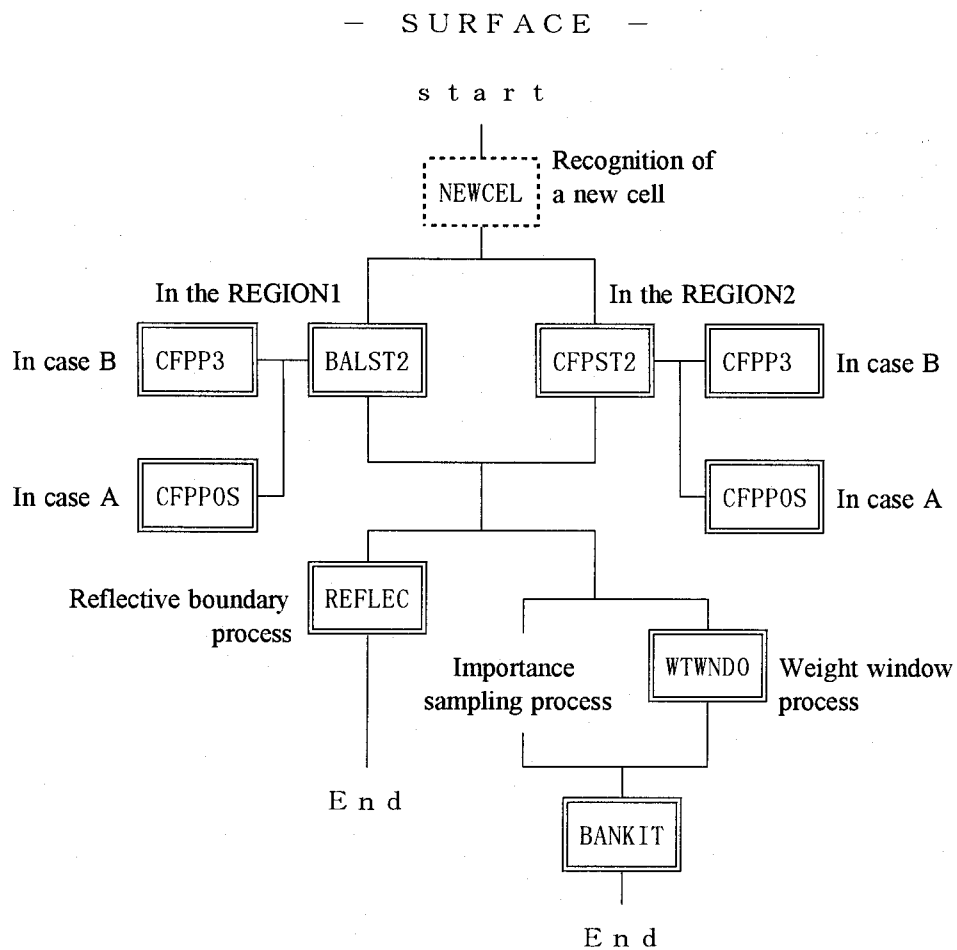
Fig. 2.45 Flow of particle transport in MCNP-BALL (1/3).

s t a r t



- 121 -





Note: Cases A and B mean sampling patterns A and B in Fig. 2.38, respectively.

Fig. 2.45 Flow of particle transport in MCNP-BALL code (3/3).

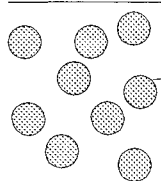
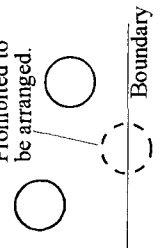
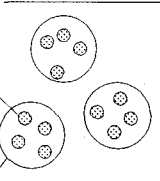
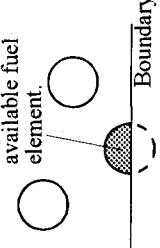
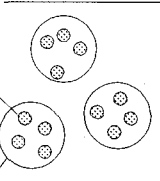
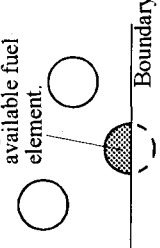
previous section was similarly carried out. Also in BANKIT, the same revision was done. The arrangement of a spherical element is done in two subroutines. One is BALSET coded for the arrangement process for "outer spherical element" corresponding to fuel pebble. The other is CFPSET for "inner spherical element" corresponding to CFP in a fuel pebble. Although MCNP-CFP needs a troublesome check of the coordinates of spherical element arranged because the interference with the boundary surface is prohibited, MCNP-BALL needs to confirm only whether or not the location to enter a spherical element determined by sampling is in the spherical-element-existing region, since MCNP-BALL allows the interference of spherical element with the boundary. MCNP-BALL, therefore, arranges a spherical element in CFPPOS and do not need a check subroutine corresponding to CFPNND in MCNP-CFP. However, when an incident particle enters the spherical element existing region from the outside, a particular case occurs that the particle enters directly a fuel ball or a CFP in it. Hence one of the most important main routines in MCNP-3B, the SURFAC subroutine, had to be modified to change the cell identification number from that of the spherical-element-existing region to that of the spherical element itself after entering the spherical-element-existing region. Also due to this modification, the following input cell card is required, which indicates that a spherical fuel element is existing also in the cell where it exits (In MCNP, the input cell card of a cell of a sphere is just an expression indicating that the cell is existing in the inside region of the sphere). Moreover if the spherical fuel element is a CFP, the additional input data, indicating that the CFP is existing in a fuel ball and also existing in the cell where the fuel ball exists, must be required. After perceiving a new cell in NEWCEL when the incident particle reaches a boundary of a cell, if the cell is the region where outer spherical elements exist, BALST2 is called, and if the cell is the region where inner spherical elements exist, CFPST2 is called. In each subroutine, the sampling at B in Fig. 2.38 is carried out with the probability that is the same as the packing fraction, and the sampling at A is done with the rest as shown in Sec. II.4.1.3. The former is done at CFPP3, while the latter at CFPPOS.

The flow of the calculation procedure with MCNP-BALL is described in Fig. 2.44. Before a MCNP-BALL calculation, two sets of NNDs have to be prepared for the outer and inner spherical elements. However, the packing fraction correction is not necessary. As for the input data in addition to the standard input data for MCNP-3B, the cell attribute data indicating which cell is a spherical element or a cell in which a lot of spherical elements exist is required. Moreover, the surface attribute data of indicating which surfaces constitute the spherical element used for the calculation.

## II.5 Summary

In this chapter, the essential and general method to deal with Monte Carlo particle transport in a system having a number of base geometries was presented. Practically, it is to arrange a base geometry one after another along an incident particle flight path at a certain place determined probabilistically with the NNDs during a random walk of the particle, resulting in exact reproduction of the packing fraction of the base geometry inventory. The method can simulate the real configuration much better than the conventional ones. The practical simulation by the method was realized by developing two codes of MCNP-CFP and MCNP-BALL, as summarized in Table 2.5. The most conspicuous feature of MCNP-CFP is realization of approximation-free simulation, while it has an upper limit packing fraction available. To supplement this defect MCNP-BALL was developed to cover higher packing fraction up to the physically achievable packing fraction of  $f_{RCP}$ . However, strictly speaking the exactness of the simulation of base-geometry sampling near the boundary is slightly inferior to MCNP-CFP. This restriction is unavoidable if we intend to treat such a system. This means that the developed method is exactly a general and universal procedure of random sampling of geometries in Monte Carlo transport simulation. At first the present method was developed for analysis of HTGRs as shown in Chap. 4, however because of its generality, it can be applied to various practical uses as introduced in Chap. 1. Also, a base geometry available is not only sphere but also other geometry. We think that further investigation is very important and will be indispensable for the future applications.

Table 2.5 Summary of features of MCNP-CFP and MCNP-BALL.

Code	Main target reactor			Treatment of interference with the boundary	Available packing fraction
	Reactor type	Fuel lattice configuration	Packing fraction		
MCNP-CFP	Compact type HTGR (VHTRC, HTTR,...)	Fuel compact, for example.			$^1) \ ^2) < \eta \cdot f_{RCP}$
		Fuel pebble			$^2) < f_{RCP}$
MCNP-BALL	Pebble bed type HTGR (PROTEUS, AVR,...)	Pebble bed core, for example.			$^2) < f_{RCP}$

- 1) Correction factor to adjust the effect of lack of spherical elements near the boundary.  
2) Physically achievable packing fraction;  $f_{RCP}$

## REFERENCES

- (1) I. Murata, T. Mori and M. Nakagawa, *Nucl. Sci. Eng.* **123**, 96 (1996).
- (2) I. Murata, A. Takahashi, T. Mori and M. Nakagawa, *J. Nucl. Sci. Technol.* **34**, 734 (1997).
- (3) I. Murata, T. Mori, M. Nakagawa and H. Itakura, "Continuous Energy Monte Carlo Calculations of Randomly Distributed Spherical Fuels Based on Statistical Geometry Model," *JAERI-Research 96-015*, Japan Atomic Energy Research Institute (1996).
- (4) I. Murata, T. Mori, M. Nakagawa and H. Shirai, "Packing Simulation Code to Calculate Distribution Function of Hard Spheres by Monte Carlo Method : MCRDF," *JAERI-Data/Code 96-016*, Japan Atomic Energy Research Institute (1996).
- (5) J. Spanier and E. M. Gelbard, "Monte Carlo Principles and Neutron Transport Problems," Addison-Wesley Publishing Company.
- (6) D. C. Irving, *Nucl. Sci. Eng.*, **15**, 273 (1971).
- (7) D. C. Irving, "The Adjoint Boltzmann Equation and Its Simulation by Monte Carlo," *ORNL-TM-2879*, Oak Ridge National Laboratory (1970).
- (8) E. A. Straker et al., "The MORSE Code - A Multigroup Neutron and Gamma-ray Monte Carlo Transport Code," ORNL-4585, Oak Ridge National Laboratory (1970).
- (9) K. Tsuchihashi and Y. Gotoh, *Nucl. Sci. Eng.*, **58**, 213 (1975).
- (10) C. H. Bennet, *J. Appl. Phys.*, **43**, 2727 (1972).
- (11) J. L. Finney, *Mater. Sci. Eng.*, **23**, 199 (1976).
- (12) W. S. Jodrey and E. M. Tory, *Powder Technol.*, **30**, 111 (1981).
- (13) W. S. Jodrey and E. M. Tory, *Phys. Rev. A*, **32**, 2347 (1985).
- (14) A. S. Clarke and J. D. Wiley, *Phys. Rev. B*, **35**, 7350 (1987).
- (15) E. Thiele, *J. Chem. Phys.*, **39**, 474 (1963).
- (16) J. L. Finney, *Proc. R. Soc. (London), Ser. A* **319**, 479 (1970).
- (17) J. L. Finney, *Proc. R. Soc. (London), Ser. A* **319**, 495 (1970).
- (18) W. R. Smith and D. Henderson, *Mol. Phys.*, **19**, 411 (1970).
- (19) M. F. Wehner and W. G. Wolfer, *J. Stat. Phys.*, **42**, 493 (1986).
- (20) J. D. Bernal, *Proc. R. Soc. (London), Ser. A* **280**, 299 (1964).
- (21) J. L. Finney, *Nature (London)*, **266**, 309 (1977).
- (22) J. M. Gordon, et al., *J. Chem. Phys.*, **65**, 2771 (1976).
- (23) M. Shahinpoor, *Powder Technol.*, **25**, 163 (1980).

- (24) D. P. Haughey and G. S. G. Beveridge, *Chem. Eng. Sci.*, **21**, 905 (1966).
- (25) H. L. Weissberg and S. Prager, *Phys. Fluids*, **5**, 1390 (1962).
- (26) G. D. Scott, *Nature*, **194**, 956 (1962).
- (27) G. Mason, *Nature*, **217**, 733 (1968).
- (28) J. K. Percus and G. Y. Yevick, *Phys. Rev.*, **110**, 1 (1958).
- (29) J. G. Berryman, *Phys. Rev. A*, **27**, 1053 (1983).
- (30) M. S. Wertheim, *Phys. Rev. Lett.*, **10**, 321 (1963).
- (31) G. J. Throop and R. J. Bearman, *J. Chem. Phys.*, **42**, 2408 (1965).
- (32) J. H. Conway and N. J. A. Sloane, "Sphere Packings, Lattices and Groups," Springer Verlag, New York(1988).
- (33) C. A. Rogers, "Packing and Covering," Cambridge University Press, Cambridge(1964).
- (34) C. A. Rogers, "The packing of equal spheres," *Proc. London Math. Soc.*, **8**, 609(1958).
- (35) J. H. Lindsey II, *Mathematika*, **33**, 137 (1986).
- (36) G. D. Scott and D. M. Kilgour, *Brit. J. Appl. Phys.*, **2**, 863 (1969).
- (37) E. J. LeFevre, *Nature (London)*, **235**, 20 (1972).
- (38) K. Gotoh and J. L. Fenney, *Nature (London)*, **252**, 202 (1974).
- (39) L. V. Woodcock, *Chem. Soc., Faraday Trans. II*, **72**, 1667 (1976).
- (40) L. V. Woodcock and C. A. Angell, *Phys. Rev. Lett.*, **47**, 1129 (1981).
- (41) V. C. Aguilera-Navarro et al., *J. Chem. Phys.*, **76**, 749 (1982).
- (42) G. S. Cargill III, *J. Appl. Phys.*, **41**, 2248 (1970).
- (43) G. S. Cargill III, *J. Appl. Phys.*, **41**, 12 (1970).
- (44) D. T. Cromer, *Acta Cryst.*, **18**, 17 (1965).
- (45) D. T. Cromer and J. T. Waber, *Acta Cryst.*, **18**, 104 (1965).
- (46) "What is Random Packing?," *Nature*, **239**, 488 (1972).
- (47) J. F. Briesmeister, "MCNP-3B Newsletter," Los Alamos National Laboratory (1988).
- (48) "MCNP -A General Monte Carlo N-Particle Transport Code, Version 4B," *LA-12625*, J. F. Briesmeister, Ed., Los Alamos National Laboratory (1997).

## III. VALIDATION OF THE METHOD

### III.1 Introduction

The developed method has to be examined by comparing with experimental results to confirm its applicability to practical uses. Some results for the comparisons are presented in Chap. IV. On the other hand, during the developing phase, validations with respect to more basic aspects are to be done, because it is easier to remove faults of the method. In Sec. II.3.2.4, MCRDF has been validated through the comparison of RDF of RCP with the experimental result as well as other numerical evaluation. In this chapter<sup>(1-3)</sup>, the basic functions of the developed system including the NNDs made by MCRDF and algorithms of MCNP-CFP and MCNP-BALL were validated through the two comparisons of the results obtained by the method with the reference calculations: (1) Calculations of inventory of base geometries in the container by both track length estimator and direct evaluation method mainly to confirm an accuracy of the NND, and (2) Criticality calculations for ordered packed geometries mainly to examine the sampling algorithm of a base geometry.

### III.2 Inventory calculations of irregularly distributed geometries

#### III.2.1 Inventory evaluation method

With the Monte Carlo method, the volume of each cell can be estimated easily using broad parallel beam as a source and track length estimator under condition that all cells are void. Using this method, the total volume occupied by successively arranged base geometries by sampling during a particle transport calculation can be obtained. However, it can be recognized from the following discussion about the volume calculation that the track length estimator is not so efficient: The volume of the cell of interest,  $\kappa$ , as shown in Fig. 3.1 is estimated by the following procedure. From the definition of the track length estimator,

$$TLE = \frac{1}{V} \frac{\sum_{i=1}^N x_i \cdot WGT}{N_0} \quad (1/cm^2/incident \text{ particle}) \quad (3.1)$$

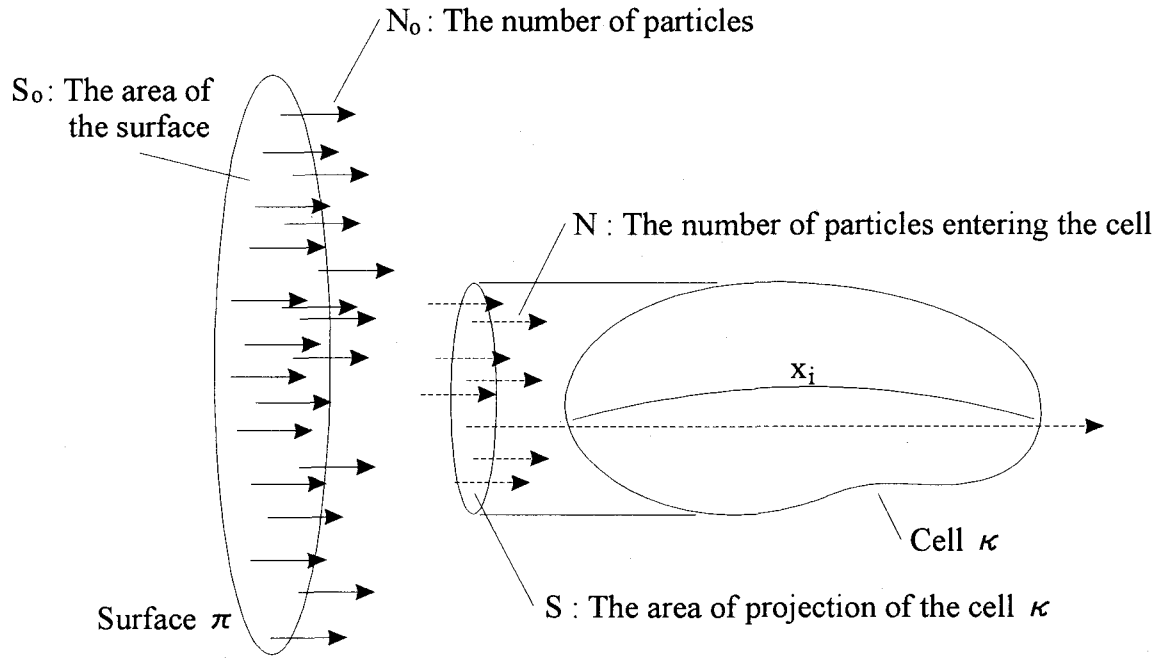


Fig. 3.1 Principle of volume estimation by track length estimator.

where  $V$  is the volume of the cell  $\kappa$ ,  $N_0$  the number of incident particles from the surface  $\pi$ ,  $N$  the number of particles entering the cell,  $x_i$  the transmitting length of the particle in the cell, and WGT the particle weight. Since  $V$  is unknown, normally set  $V=1$ . Also, the area of the surface  $\pi$  is  $S_0$  and the area of the projection of the cell on the surface is  $S$ . Now we set  $\text{WGT}=S_0$  to obtain

$$TLE = \frac{\sum_{i=1}^N x_i \cdot S_0}{N_0} \quad (3.2)$$

And

$$\bar{x} = \frac{\sum_{i=1}^N x_i}{N} \quad (3.3)$$

Also



$$\frac{N_0}{S_0} = \frac{N}{S} \quad (3.4)$$

Then

$$TLE = S \cdot \bar{x} = V(\text{Volume of the cell}) \quad (3.5)$$

From Eq. (3.5), it is found that the track length estimator calculates the effective transmitting length through the cell. Next similar to the above, the volume occupied by the base geometries arranged,  $V_b$ , as shown in Fig. 3.2, is

$$V_b = \frac{\sum_{i=1}^N \sum_j \lambda_{ij} \cdot WGT}{N_0} \quad (3.6)$$

where  $\lambda_{ij}$  is the transmitting length of the particle through j-th arranged base geometry during i-th history.

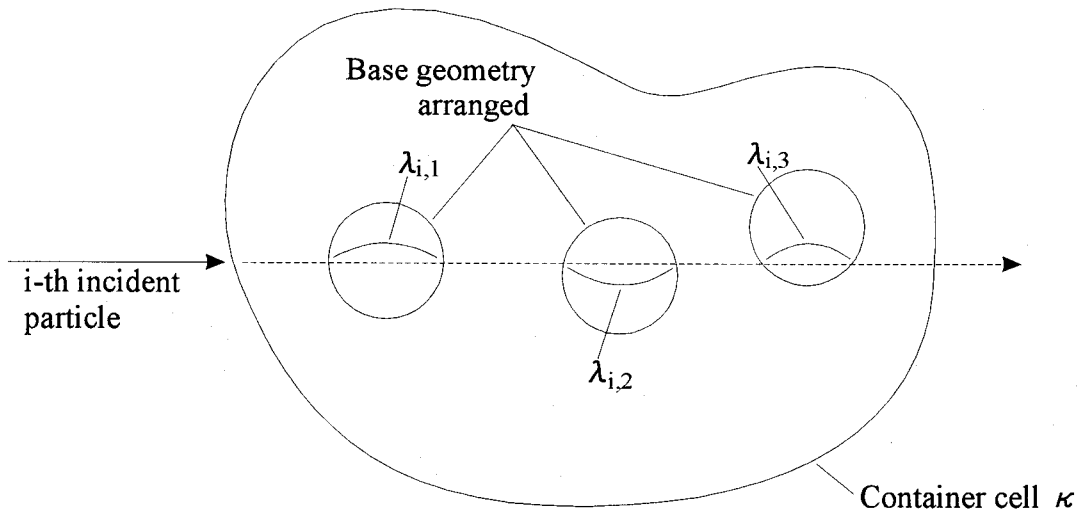


Fig. 3.2 Application of track length estimator to estimation of base geometries volume.

With the same transformation procedure,

$$V_b = \frac{S}{N} \sum_i \sum_j \lambda_{ij} \quad (3.7)$$

Now we use

$$y_i = \sum_j \lambda_{ij} \quad (3.8)$$

where  $y_i$  is the cumulative transmitting length of base geometries arranged during history  $i$ . Then

$$\bar{y} = \frac{\sum_i y_i}{N} \quad (3.9)$$

is the effective transmitting length through all base geometries arranged in a complete history. This means that

$$V_b = S \cdot \bar{y} \quad (3.10)$$

is equivalent to the volume occupied by base geometries arranged. Obviously, Eq.(3.7) shows the summation of the transmitting lengths through base geometries corresponds to the volume occupied. It can be expected therefore that the statistical fluctuation of the summation strongly affects the accuracy of the estimate. Actually, the CPU time necessary for the calculation is unexpectedly long even though the model is simple and there is no interaction between the incident particle and the material atom because all cells are void. As a counterplan, a direct evaluation from not the transmitting length but the number of base geometries arranged is employed. Instead of each transmitting length, the average of it, e.g.,  $4r/3$  for sphere, is used to suppress statistical fluctuation effectively. The volume fraction, i.e., packing fraction, of the base geometries is obtained by

$$f = \frac{\frac{2}{3} d_{base} \cdot N_{ent}}{N_{pop} \cdot L_{ave}} \quad (3.11)$$

where  $d_{\text{base}}$  is the diameter of base geometry,  $N_{\text{ent}}$  the number of entering a base geometry (the number of arrangement),  $N_{\text{pop}}$  the number of entering the region in which base geometries exist, and  $L_{\text{ave}}$  the average transmitting length in the region having base geometries ( $= (\text{Volume of the container cell}) / (\text{Area of the projection of the container cell on the source surface})$ ).

The practical procedure is as follows: The dimensions of a simple geometry chosen for inventory checking calculation were determined such that their representative lengths, e.g., diameter of sphere, side of cube and so on, become about 10 times larger than that of the base geometry, because the interference effect induced by the boundary surface, affecting the calculation result, is getting small with increase of the ratio, while there are few applications for the ratio less than 10. For instance, those of HTTR and VHTRC, which cannot be determined strictly because their dimensions are a little complicated, are about 10 or more (They are regarded as the ratio of the effective neutron transmitting length through the fuel compact to the diameter of CFP.). At the same time, when the ratio is not so large, the correction of the packing fraction cannot be neglected, and it means that such a model is very suitable for confirming the validity of the sampling method. An example of the calculation model is shown in Fig. 3.3. There is just a simple geometry to be checked in phase space, and a base geometry is modeled in the geometry. A circular and broad parallel beam which can bombard the whole of the geometry is placed.

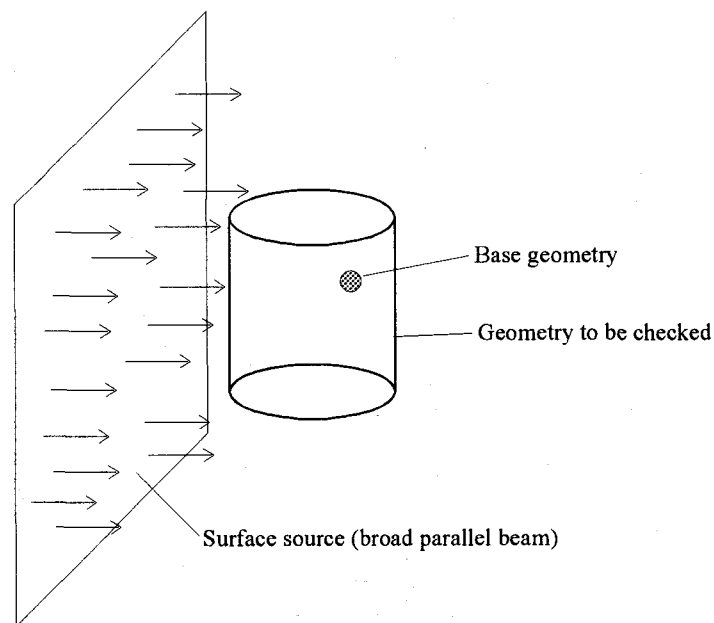


Fig. 3.3 Inventory check calculation model for MCNP-CFP.  
This is a cylindrical model.

By this method, the inventory of the base geometries actually arranged can be estimated to compare the ideal packing fraction. From the comparison result, we can confirm that the evaluated NNDs can reproduce the prescribed packing fraction. In the present study, the track length estimator was used as a supplementary method, because it was found from the comparison of both results that the direct evaluation method is superior to the track length estimator from the stand point of the calculation accuracy.

### **III.2.2 Inventory checking for MCNP-CFP**

In a transport calculation by MCNP-CFP, to simulate the packing of base geometries precisely the packing fraction available is restricted within a relatively low packing fraction due to correction of interference effect with the boundary surface. For this reason, an inventory checking for a packing fraction of 30 % is done for simple geometries such as cube, sphere, cylinder and so on. This packing fraction is also corresponding to that of CFPs in the fuel compact adopted in VHTRC, taken up for an analysis exercise in Chap. IV. The absolute dimensions of the geometry do not matter, while the ratio of the dimensions between the container geometry and the base geometry is very important for the checking, as shown in the previous section. The ratio of base geometry diameter to the container's representative dimensions is set to be about 10. The calculation model is  $100 \times 100 \times 100 \text{ cm}^3$  cube, in which a base geometry, that is assumed to be 10 cm-diameter sphere, is set. The sphere moves along the particle flight in the container cell during the calculation. Table 3.1 summarizes the results for plane, sphere, cylinder and cone. The NNDs used are for the packing fraction of 30%, however due to the interference effect the resulting packing fractions are smaller than 30%. It can be said that the NNDs are evaluated enough accurately because every calculated packing fraction is in good agreement with the theoretical result within the relative difference of 0.1%. Consequently, we can reproduce the inventory of base geometries properly by MCNP-CFP considering the correction of the packing fraction due to the boundary surface interference effect.

### **III.2.3 Inventory checking for MCNP-BALL code**

Originally MCNP-BALL was developed to analyze a pebble bed type reactor core. The inventory checking is conducted assuming that the CFPs and fuel pebbles exist and they make

Table 3.1 Inventory check of base geometries for MCNP-CFP.

Surface type	Packing fraction		Relative difference (%)	Geometry <sup>4)</sup>
	Exact value <sup>1)</sup>	Calculation		
Plane	0.2187	0.2185 $\pm$ 0.0003 <sup>2)</sup> 0.2185 $\pm$ 0.0003 <sup>3)</sup>	-0.09 -0.09	100 $\times$ 100 $\times$ 100 (cm)
Sphere	0.2187	0.2185 $\pm$ 0.0003 <sup>2)</sup>	-0.05	r = 50 cm
Cylinder	0.2187	0.2185 $\pm$ 0.0003 <sup>2)</sup>	-0.09	r = 50 cm by 100 cm long
Cone	0.1215	0.2185 $\pm$ 0.0003 <sup>2)</sup>	+0.08	r = 32 cm by 50 cm long

1) The value is equal to  $0.3 \times f$ , where  $f$  is a correction factor for the wall interference effect.

2) The NND was calculated for the packing after decreasing the radii of CFPs packed in RCP.

3) The NND was calculated for the packing of CFPs packed in 30 %.

4) The CFP radius is 5 cm.

a heterogeneous structure as in AVR or PROTEUS reactors. In the inventory checking, the inner spherical element volume (CFP volume in a fuel pebble) and the outer spherical element volume (moderator and fuel pebble volumes) in simple geometries such as sphere, plane and cylinder were calculated for the comparison with the ideal values. The packing fractions of 0.3 for the inner spherical element and 0.5 for the outer spherical element were selected to simulate CFP packing fraction in a fuel pebble and that of fuel pebbles in the pebble bed reactor, respectively. As described in Sec. II.4, MCNP-CFP cannot deal with this situation because the corrected packing fraction by Eq. (2.70) shows  $\sim 0.69$  for the outer spherical fuel element, which is beyond the packing fraction of RCP. The ratio of spherical element diameter to its container dimensions is set to be conservatively about 10 similar to the case of MCNP-CFP, because, for instance, the ratios for AVR and PROTEUS reactor cores are about 50 and 30, respectively. The calculation model and results are shown in Fig. 3.4 and Table 3.2, respectively. In the calculation, to check the applicability to a practical geometry, there are several layers added in each spherical element. From the result, calculated packing fraction in each cell and total packing fractions in the regions of fuel pebble, moderator pebble and CFP are in good agreement with the ideal values within a relative error of 0.2%. It was confirmed from the result that the inventory of spherical elements can be reproduced in the simulation calculation with this method in a sufficient accuracy.

### III.3 Criticality calculations of ordered packing models

In an inventory checking calculation, all cells must be void. This restriction indicates that the NND2 cannot be validated, because interactions of the incident particles with material atoms never occur in the inventory calculation model. The complete validation for a irregular arrangement is thought to be difficult, since there exists no other methods to treat such a geometry exactly. We therefore have to turn our eyes on an ordered packing. Among various methods to pack a large number of spherical elements, only ordered close packing, e.g. face centered cubic lattice (FCC), body centered cubic lattice (BCC) and so on, can provide the exact positions of all spheres. This fact enables us to treat these systems precisely by modeling all spherical elements using reflective boundary conditions with a conventional Monte Carlo code (Normally this calculation method requires much labor and perseverance in modeling. Therefore, this is not a practical method especially in a design work. However, there is a rare example of modeling them by assuming spherical elements distributed irregularly are packed in order<sup>(4)</sup>). On the other hand,

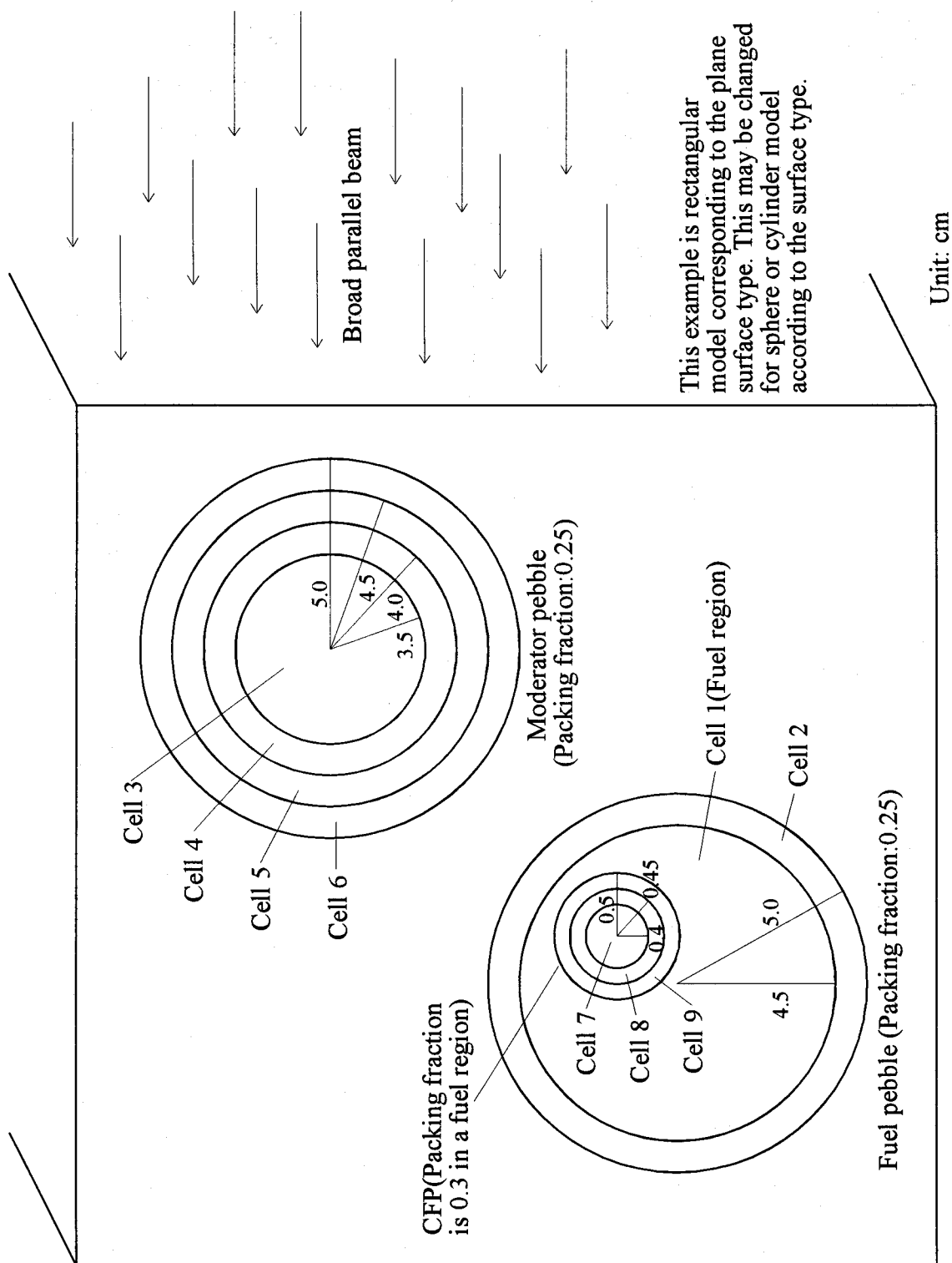


Fig. 3.4 Inventory check calculation model for MCNP-BALL.  
This is a rectangular model.

Table 3.2 Inventory check of base geometries for MCNP-BALL.

Surface type	Region	Absolute ratio			Relative ratio		
		Calculation	Ideal	Difference(%)	Calculation	Ideal	Difference(%)
Sphere	Fuel ball	cell 1	0.1278 ±0.0002	0.1276	-0.16		
		cell 2	0.06774±0.0001	0.06775	-0.015		
	Total(incl. CFP)		0.2503 ±0.0002	0.25	0.12	0.5007±0.0007 <sup>1)</sup>	0.5 0.14
	Moderator ball	cell 3	0.08568±0.0002	0.08575	-0.082		
		cell 4	0.04220±0.00008	0.04225	-0.12		
		cell 5	0.05413±0.00009	0.05425	-0.22		
Total		cell 6	0.06765±0.0001	0.06775	-0.15		
			0.2497 ±0.0002	0.25	-0.12	0.4993±0.0007 <sup>2)</sup>	0.5 -0.14
	CFP	cell 7	0.02802±0.00005	0.02799	0.11		
Plane		cell 8	0.01188±0.00002	0.01186	0.17		
		cell 9	0.01483±0.00003	0.01482	0.068		
	Total		0.05473±0.00006	0.05468	0.091	0.2998±0.0006 <sup>3)</sup>	0.3 -0.067
	Fuel ball		0.2505 ±0.0003	0.25	0.20	0.5010±0.0006 <sup>1)</sup>	0.5 0.20
Cylinder	Moderator ball		0.2495 ±0.0003	0.25	-0.20	0.4990±0.0006 <sup>2)</sup>	0.5 -0.20
	CFP		0.05478±0.00007	0.05468	0.18	0.2999±0.0005 <sup>3)</sup>	0.3 -0.033
	Fuel ball		0.2501 ±0.0003	0.25	0.040	0.5005±0.0008 <sup>1)</sup>	0.5 0.10
Cylinder	Moderator ball		0.2496 ±0.0003	0.25	-0.16	0.4995±0.0008 <sup>2)</sup>	0.5 -0.10
	CFP		0.05468±0.00008	0.05468	0.0	0.2999±0.0007 <sup>3)</sup>	0.3 -0.033

1) Ratio of fuel balls to all balls.

2) Ratio of moderator balls to all balls.

3) Ratio of CFPs to fuel balls.



the developed method can deal with these models using the NNDs. Through the comparison of the two results, the developed method can be validated. In a calculation of an ordered packing lattice, spheres packed were regarded as a fuel element which is 10 % enriched  $\text{UO}_2$  and graphite was assumed to be the matrix material between spheres. And infinite multiplication factors were evaluated with and without the matrix material.

The NNDs used were evaluated with MCRDF. After a packing of an ordered packing lattice (Of course packing simulation is not necessary) was prepared, adjusting the radii of packed spheres to fit the packing fraction because that of ordered packing model is fixed, the NNDs were calculated by a ray-trace method.

### **III.3.1 Criticality calculation by MCNP-CFP**

FCC and simple cubic lattice were employed for the criticality calculation. The calculation models of the original MCNP and MCNP-CFP are illustrated in Figs. 3.5 and 3.6, respectively. A unit lattice for each case was used with reflective boundary conditions to simulate an infinite system for the original MCNP calculation. Therefore, it seems that there exist innumerable fuel pebbles in the system. In the MCNP-CFP calculation, an enough large cube having just one spherical fuel element was modeled. It also has reflective boundary conditions to realize an infinite system. This equal model can be used for other test calculations by MCNP-CFP irrespective of the packing state (shape of the container, packing fraction and so on), because the difference of how to pack spherical fuel elements only appears in the NNDs explicitly. The packing fraction of spherical fuel elements is set to be 30%. In both calculations by MCNP and MCNP-CFP, the 100-cycle calculation was conducted, the batch size of which was 2000 particles. The calculation results are shown in Table 3.3. Good agreement is obtained for the multiplication factors between two codes in any case. The validity of the developed method including MCNP-CFP was thus confirmed.

### **III.3.2 Criticality calculation by MCNP-BALL**

The calculation model with MCNP-3B as a conventional Monte Carlo code is shown in Fig. 3.7. A fuel pebble (outer spherical element) is placed at the center of a cubic with reflective boundary conditions, in which CFPs (inner spherical elements) are distributed in a cubic lattice.

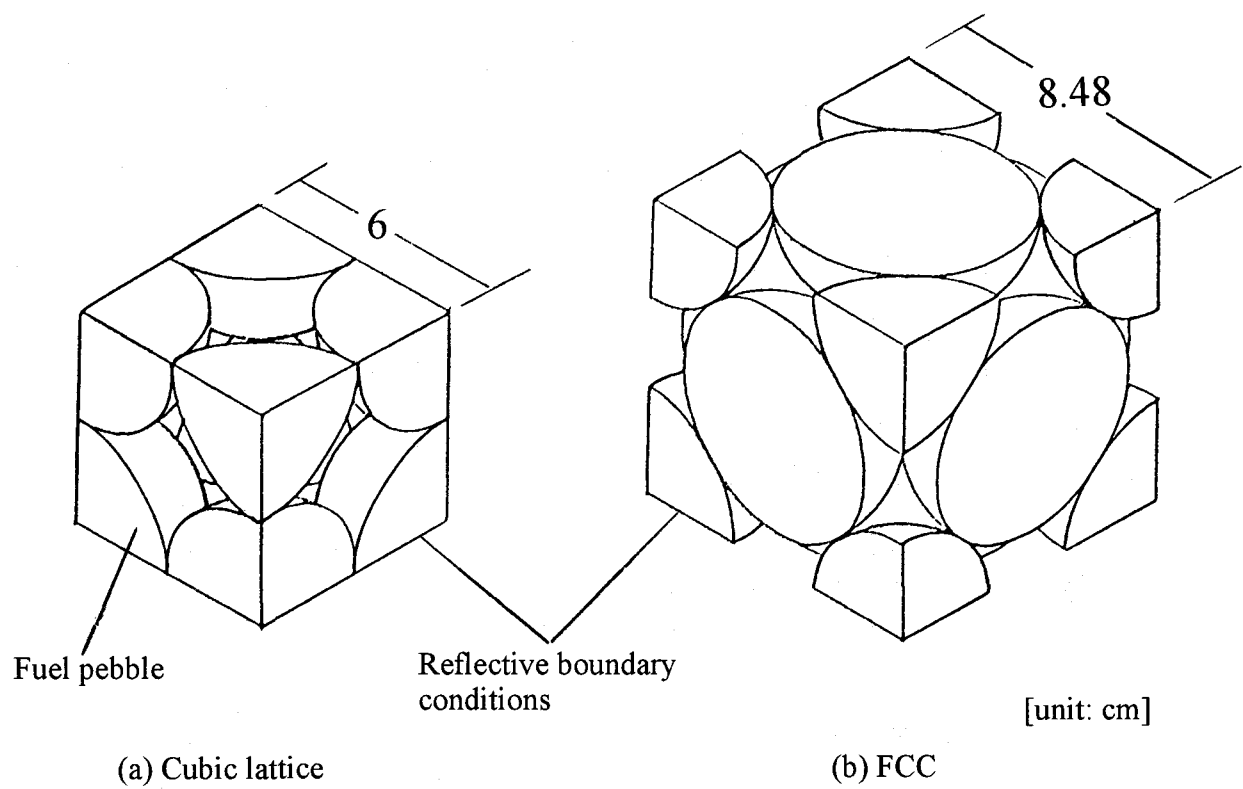


Fig. 3.5 Criticality calculation models for ordered packing lattices with MCNP.

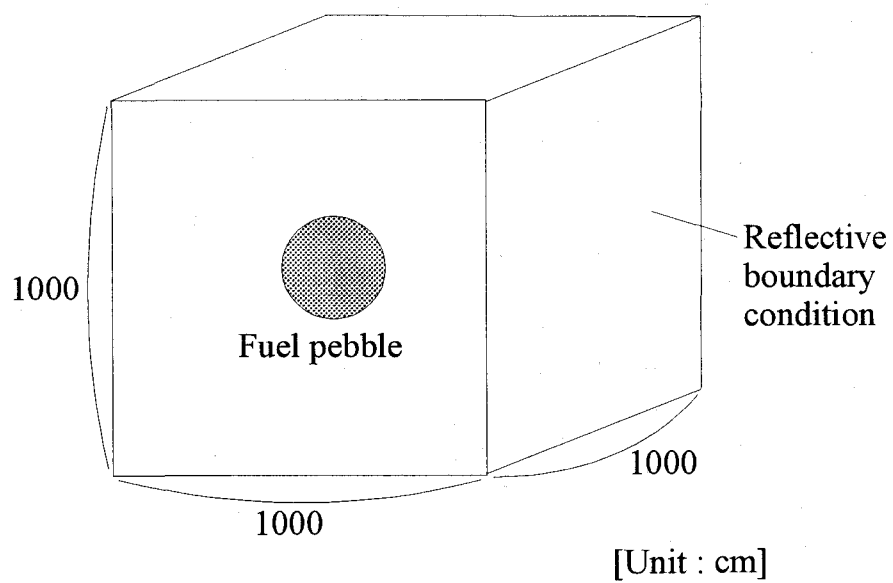


Fig. 3.6 Criticality calculation model for MCNP-CFP.

Table 3.3 Comparison of infinite multiplication factors for ordered packing lattices between MCNP-CFP and a conventional Monte Carlo code.

Lattice <sup>1)</sup>	Unit cell dimension	Matrix material	Infinite multiplication factor ( $k_{\infty}$ )		Difference ( $\Delta k$ )
			Conventional(MCNP-3B)	MCNP-CFP	
Cubic	6	Graphite	1.146 $\pm$ 0.002	1.148 $\pm$ 0.002	-0.002
			1.105 $\pm$ 0.001	1.107 $\pm$ 0.002	+0.002
Face centered cubic	8.48	Graphite	1.140 $\pm$ 0.002	1.141 $\pm$ 0.002	-0.001
			1.102 $\pm$ 0.002	1.105 $\pm$ 0.003	+0.003

1) Calculation conditions are as follows:

- a) The packing fraction is adjusted to 0.3 by reducing the radii of spherical fuels packed in face centered cubic or cubic lattice.  
b) The fuel contains 10 % enriched  $UO_2$ .

Table 3.4 Comparison of infinite multiplication factors for simple cubic geometry between MCNP-BALL and a conventional Monte Carlo code.

Case <sup>1)</sup>	Matrix graphite <sup>2)</sup>		Infinite multiplication factor ( $k_{\infty}$ )	
	In fuel ball	Between balls	MCNP-BALL	MCNP-3B
1	×	×	1.118 $\pm$ 0.002	1.121 $\pm$ 0.002
2	○	×	1.019 $\pm$ 0.002	1.019 $\pm$ 0.002
3	○	○	1.159 $\pm$ 0.002	1.162 $\pm$ 0.002

1) Calculation conditions are as follows:

- a) Diameters of fuel pebble and CFP are 10cm and 1cm, respectively.  
b) As fuel material in CFPs, 10% enriched  $UO_2$  is used.

2) ○, × mean cases with and without graphite matrix, respectively.

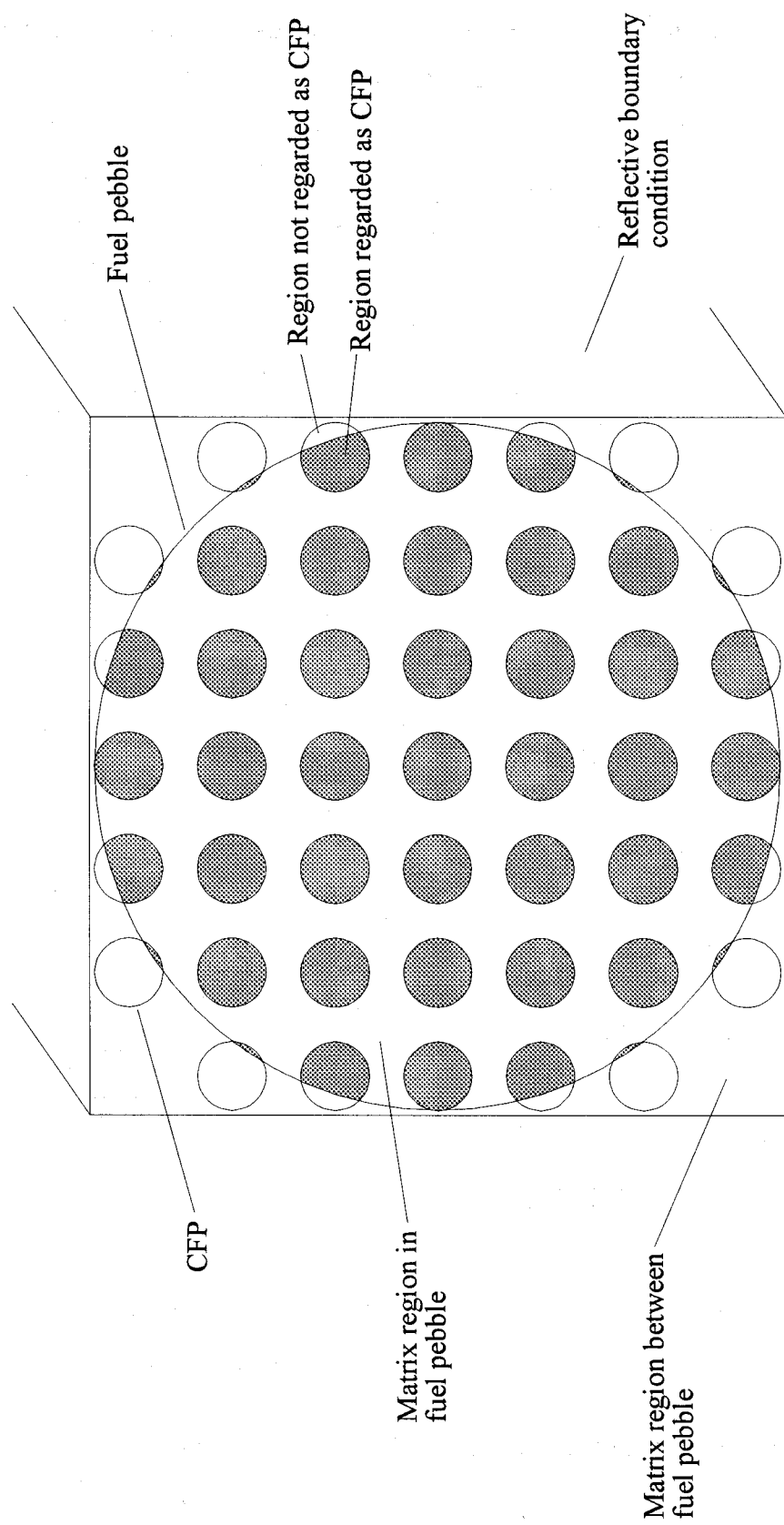


Fig. 3.7 Criticality calculation model for simple cubic geometry with MCNP.

Therefore, it also seems that there are an infinite number of fuel pebbles in the system. Each fuel pebble contains 203 CFPs in which the 80 interfere with the boundary surface of the fuel pebble. This fact means that this calculation can give useful validation information of the algorithm treating interfered spherical fuel element, because MCNP-BALL allows interference of spherical fuel elements with the boundary surface. The packing fractions of fuel pebbles and CFPs are 0.5 and 0.157, respectively. The calculation model with MCNP-BALL is quite simple, that is just an enough large cubic container with reflective boundary conditions, a fuel pebble in it and a CFP in the fuel pebble, as shown in Fig. 3.8. Fuel pebbles and CFPs are to be arranged successively and irregularly with the NNDs during the transport calculation. The MCNP-BALL and MCNP-3B calculations were done in criticality source mode with 100 cycles, the batch size of which is 2000 particles. Table 3.4 shows the multiplication factors of criticality calculations with and without matrix graphite between spherical fuel elements. The results with the two codes gave good agreement within the statistical errors. Also, Fig. 3.9 shows the comparison of the neutron spectrum, corresponding to each case in Table 3.4, averaged within the matrix region in fuel pebbles. Excellent agreement was obtained for all cases over the whole energy range. Results obtained by the comparisons suggest MCNP-BALL can be used for the analysis of HTGRs having pebble bed type cores such as PROTEUS.

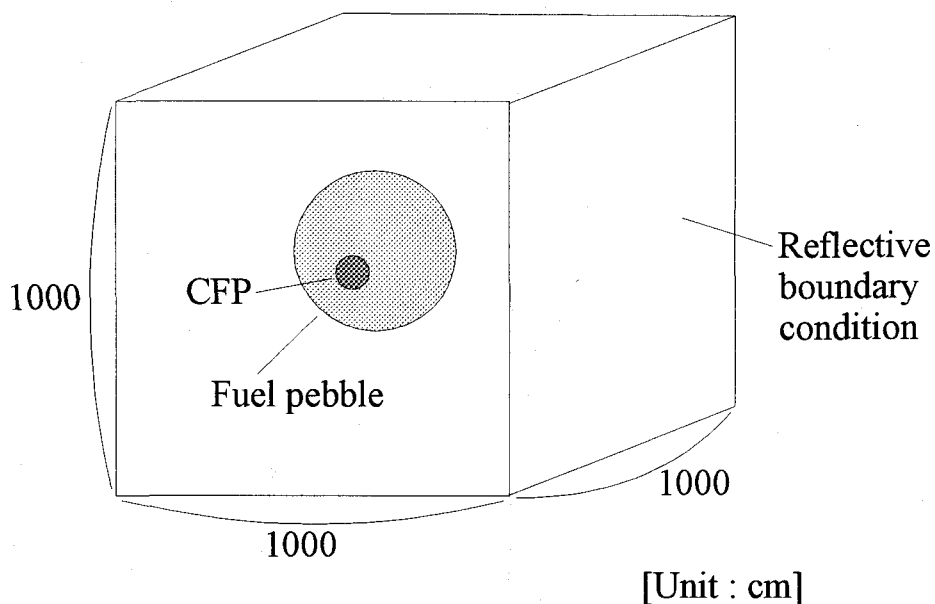


Fig. 3.8 Criticality calculation model for MCNP-BALL.

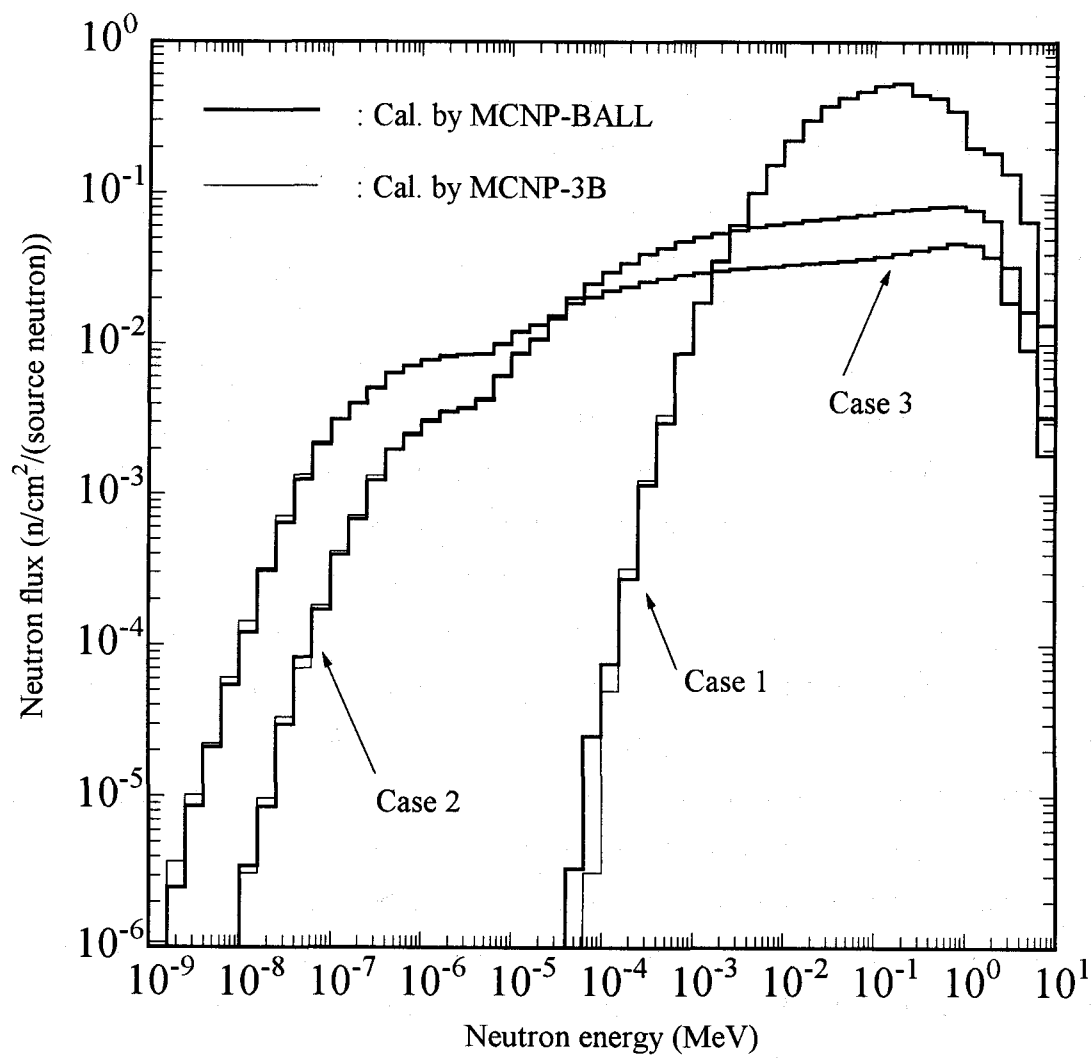


Fig. 3.9 Comparison of neutron spectra in matrix of fuel pebble for simple cubic geometry.

### **III.4 Summarized discussion of the validation**

The most important issue is whether the developed code can reproduce the inventory of base geometries or not. The reproduction ability strongly and only depends upon the NNDs and the algorithm of sampling. In the development phase, therefore, much effort and trial and error were required to complete MCRDF and the sampling method, because a small mistake in NND or the sampling algorithm enhances a large discrepancy in the final result by the repeated samplings. However, once the development of the method is successfully completed, it gives almost a perfect reference solution as described in this chapter, leading to our recognition that this is the essential and universal method of sampling a base geometry in a system where a lot of base geometries exist, by Monte Carlo method. From these experiences, it was also found that the inventory checking is the most essential and most important validation means in the present development. After the confirmation of the inventory reproduction, we were able to expect that the criticality calculation of ordered packing lattice perfectly agrees with the ideal result obtained by the conventional Monte Carlo code. Actually, the agreement was excellent. What surprised us exceedingly is not only to reproduce the irregular arrangement of base geometries by this method but also to include even the streaming effect of ordered packing lattice into the NNDs perfectly.

The validity study introduced in this chapter is not equivalent to the confirmation through the comparison with the experimental results. As is well known, in a transport calculation by the Monte Carlo method if the modeling is done perfectly, it can give a reference solution naturally. It is not always an efficient method to validate the method with experimental results using a large-scaled system, e.g., the critical assembly experiment, because the location of the fault in the method is not easily found from the comparison. Moreover, there may be some mistakes and errors in the experiment. We conclude as follows: The numerical comparison in this chapter is regarded as the very validation work. We are, as a result, confident that the validated method can be applied firmly to any geometry having an irregular configuration. In Chap. 4, the applicability, not validation, of the method is introduced.

## REFERENCES

- (1) I. Murata, T. Mori and M. Nakagawa, *Nucl. Sci. Eng.*, **123**, 96 (1996).
- (2) I. Murata, A. Takahashi, T. Mori and M. Nakagawa, *J. Nucl. Sci. Technol.*, **34**, 734 (1997).
- (3) I. Murata, T. Mori, M. Nakagawa and H. Itakura, "Continuous Energy Monte Carlo Calculations of Randomly Distributed Spherical Fuels Based on Statistical Geometry Model," *JAERI-Research 96-015*, Japan Atomic Energy Research Institute (1996).
- (4) F. C. Difilippo, "Applications of Monte Carlo Methods for the Analysis of MHTGR Case of the VHTRC Benchmark," *ORNL/TM-12698*, Oak Ridge National Laboratory (1994).



## IV. APPLICATIONS

### IV.1 Introduction

In the previous chapter, the validation result just by the numerical results without the experimental results was presented. In this chapter the analyses of three experimental results are described<sup>(1-4)</sup>. This is not a supplementary analyses to cover Chap. 3. The validation study is completed in Chap. 3, and the applicability of the method through the analyses for some experiments is examined in this chapter.

For confirming the applicability, criticality experiments at VHTRC<sup>(5)</sup> and PROTEUS<sup>(6)</sup> were utilized for MCNP-CFP and MCNP-BALL, respectively. VHTRC is the only operating HTGR type critical assembly except for HTTR soon achieving its first criticality. PROTEUS is also the only available critical assembly having a pebble bed type core. There are only two examples<sup>(7,8)</sup> of the analysis for VHTRC using a Monte Carlo code with approximate procedures as shown in Sec. I.5.2. Normally, the analysis was conducted with a diffusion method<sup>(9,10)</sup>. We can compare our result with the diffusion calculation result. However, it should be noticed that at PROTEUS various criticality experiments for the basic study of HTGR are now being performed, and therefore most experimental data are not finalized. Thus the cross checking cannot be done. Our result is still valuable for a benchmark calculation data in the future. Both analysis results will show that the developed method enables us to do a precise core analysis of HTGR by Monte Carlo method, including the criticality estimation as well as the shielding analysis.

Next, the heterogeneity effect of heavy concrete due to heavy aggregates contained was analyzed with the developed method. The heavy concrete is expected to be used as a fusion reactor shield. The experimental heterogeneity effect was obtained using some heavy concrete samples at a DT neutron source facility. In a design work, usually the heavy concrete shielding effect is evaluated conservatively by assuming that the heavy concrete is regarded as ordinary concrete. This applicability analysis is the first trial of confirming whether or not the developed method can evaluate it so precisely and accurately that a rational shielding design will be realized. The analysis result will indicate that the developed method can simulate particle transport in heavy concrete exactly and it has a large heterogeneity effect so that the conventional method cannot treat it accurately.

## IV.2 Analyses of critical assembly experiments

In HTGRs, spherical fuel elements, CFPs, are employed to utilize high-temperature coolant gas, namely to suppress the maximum fuel temperature as low as possible. It means practically that FP release from CFP and damage of it due to the extreme fuel temperature rise can be prevented by ceramic coating layers. However, if CFPs are just poured into a container to form fuel compact or fuel pebble, CFPs are in contact with each other resulting in the temperature rise locally. To avoid it, generally CFPs overcoated with carbon are packed in a container, and they are pressed and formed, then the fuel compact or fuel pebble is manufactured by sintering them. By this production process, the local temperature rise can be effectively prevented. However, it is fairly difficult to simulate this process in a Monte Carlo transport calculation by the present developed method. A specific method of making NNDs to reproduce this situation as accurately as possible is presented in the next section. After that, analyses results for VHTRC and PROTEUS with the respective NNDs prepared by the special procedure are described in Sec. IV.2.2 and IV.2.3, respectively.

### IV.2.1 NND evaluation for CFP

The packing fraction of CFPs in the HTGR fuel element is set to be low, normally below 30 %, in order to keep the intactness of the fuel element during the operation. Now we discuss how to prepare the NNDs reproducing the packing of such CFPs in the fuel compact used in VHTRC or HTTR. Of course, the same discussion can be applied to the case of fuel pebble in a pebble bed reactor such as AVR, PROTEUS and so on. It is very easy to simulate a simple packing of 30 %. However, we have to confirm whether or not the NNDs can reproduce the real spatial distribution of CFPs in the fuel compact, because the production process of the fuel compact is generally complicated and is not taken into account in the NNDs. For that purpose, the cross section photographs<sup>(11)</sup> of the fuel compacts used for an irradiation test of the HTTR's at Oarai Gas Loop (OGL-1)<sup>(12)</sup> in JAERI are utilized for the comparison of the cross section of the fuel compact and the 2-dimensional RDF made from the photograph. Figure 4.1 shows the cross section photograph of the irradiated fuel compact in OGL-1(Case (c)) and two calculated results. Case (a) is obtained from the packing in packing fraction of 0.3 and in case (b) the packing fraction is adjusted by decreasing the radii of CFPs packed in RCP as detailed in the later. From

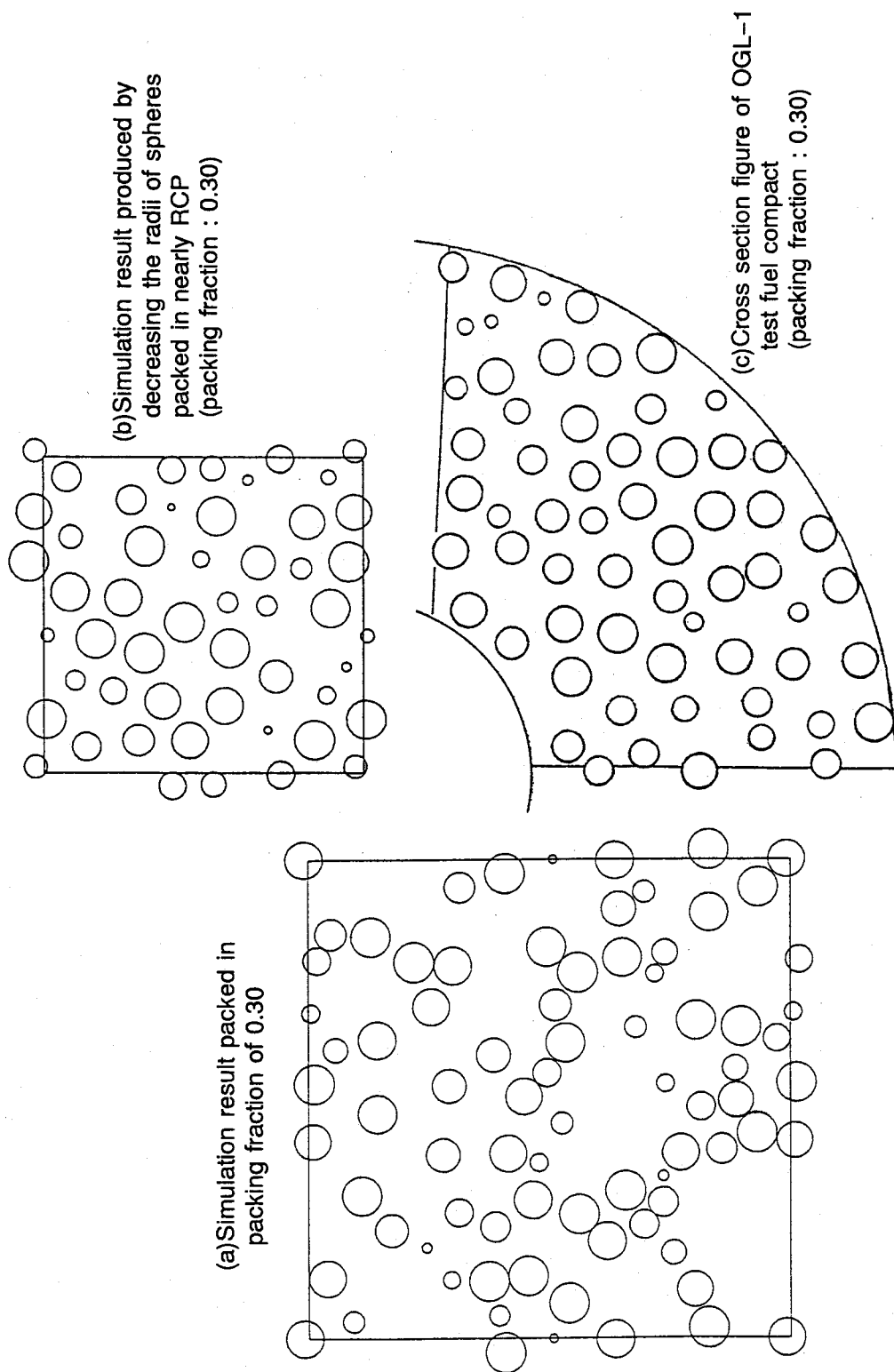


Fig. 4.1 Cross sections of hard sphere packings calculated by MCRDF compared with the cross section of the OGL-1 test fuel compact.

the figure, a large discrepancy between cases (a) and (c) is seen: There are gaps between CFPs in case (c), while many CFPs are in contact with others in case (a). We cannot avoid the packing of case (a) if packing is done by a usual collective rearrangement procedure employed normally in many packing simulation codes as well as MCRDF. Figure 4.2 shows the comparison of 2-dimensional RDFs introduced newly between the calculations (histograms) and the experimental result. The 2-dimensional RDF is defined as the average number of sphere centers in a cylindrical shell of which height is  $2r_0$  ( $r_0$  is the radius of a sphere) as detailed in Sec. II.3.2.3.2, and the experimental one was evaluated from the cross section photographs. The practical method to obtain the experimental 2-dimensional RDF is described in Appendix A. Although the accuracy of an experimental result is not high due to a small number of data, it can be said that the simple packing method with the collective rearrangement cannot reproduce the spatial distribution of CFPs in a fuel compact because of the disagreement of both peak locations observed in the figure as well as the discrepancy of the configuration of cross section circles of CFPs in Fig. 4.1.

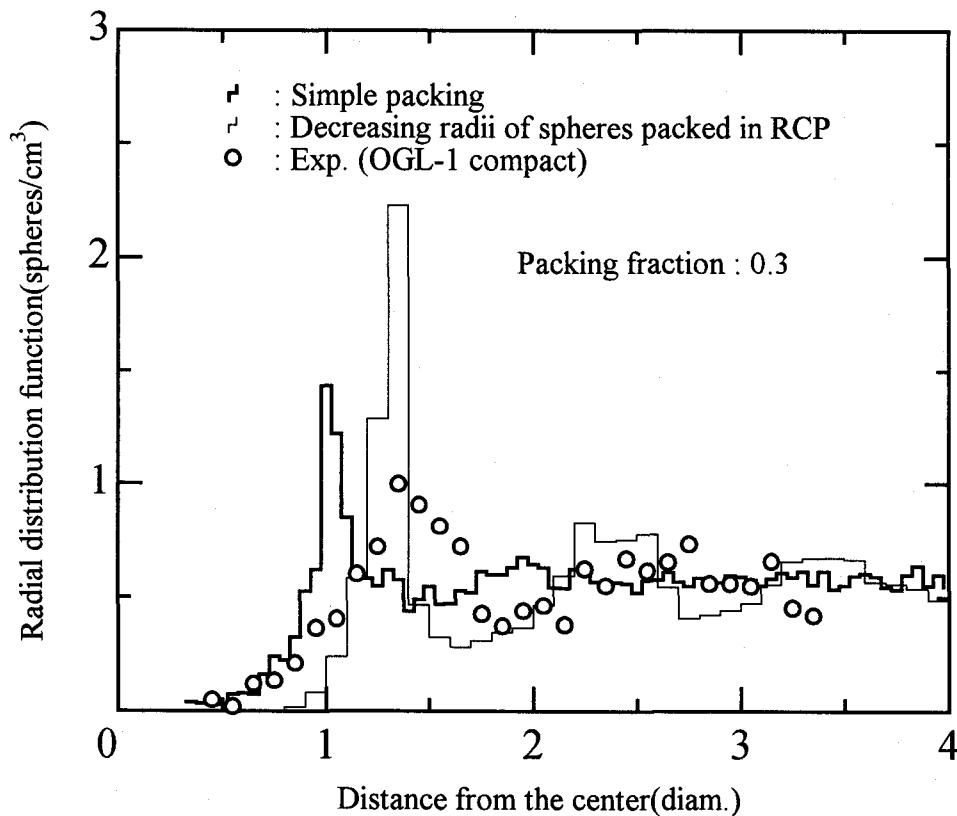


Fig. 4.2 Comparison of 2-dimensional RDFs between calculated results by MCRDF and experimental result obtained from the cross section photographs of the OGL-1 test fuel compacts.

From the above discussion, to remove the observed discrepancy the simple method of just packing CFPs was modified so as to reproduce the spatial distribution of CFPs as well as its packing fraction by taking into account the production process of the fuel compact. The fuel compact employed in HTGR is produced by the following procedure<sup>(13)</sup>: CFPs over-coated with carbon are packed in the container, then pressed and formed. After that, the fuel compacts are manufactured by sintering them. Hence the next procedure was developed to simulate the production process.

(1) Random close packing (RCP) calculation

(to simulate packing of over-coated CFPs in a container before press)

(2) Adjustment of the packing fraction of spheres in the container by reducing the radii of them

(to simulate pressing and forming CFPs in the compact)

By this simulation procedure, the discrepancy in Fig. 4.2, i.e., the first peak appears at 1.35-diameter in the experiment and 1-diameter in the calculation result by MCRDF packing in a packing fraction of 0.3, is interpreted as follows: The radii and packing fraction in both steps are related by

$$d_1 = d_0 \cdot \left( \frac{f'}{f} \right)^{1/3}, \quad (4.1)$$

where  $d_0$  and  $f$  are the reference CFP diameter and packing fraction after adjustment in the step (2), and  $d_1$  and  $f'$  are those in the step (1), respectively. The first peak appears at 1-diameter in the step (1). Therefore, the first peak position after the step (2) can be calculated as  $d_1/d_0$  in the unit of CFP diameter  $d_0$ . It is found from the above equation that the higher the packing fraction becomes in the step (1), the larger the distance between CFPs becomes in the step (2). The RCP state ( $f \approx 0.636$ ) in the step (1) consequently results in  $d_1 \approx 1.3d_0$ . This fact means that the nearly RCP state is required to represent the real packing state of CFPs in a fuel compact. As discussed in Chap. II, for this reason, we have developed the packing simulation code MCRDF having a high performance of calculating the packing of CFPs in as high packing fraction as possible, i.e., that of the RCP state. Figure 4.1(b) shows the cross section of the packing made with the above procedure. From the comparison, it is confirmed that the cross sectional view (b) clearly resembles the real cross section (c) much better than (a). Similarly the comparison of the 2-dimensional RDF made by the procedure with the experimental result is described in Fig. 4.2.

The figure shows the first peak location of the 2-dimension RDF created by reducing the radii of CFPs(case (b) in Fig. 4.1) well fits the experimental result. From the discussion above, it is concluded that the packing for case (b) is preferable for reproducing a real packing of CFPs in a fuel compact. Consequently, in order to treat HTGR fuel elements such as a fuel compact or fuel pebble, in which a large amount of CFPs are packed, at first CFPs should be packed in as high packing fraction as possible with MCRDF, then the NND is evaluated from the packing state after decreasing the radii of the spheres packed.

## IV.2.2 Analysis of critical assembly experiment at VHTRC

### IV.2.2.1 VHTRC experiment

A critical assembly named Very High Temperature Reactor Critical Assembly (VHTRC)<sup>(5)</sup> was constructed in 1985 at JAERI for the purpose of examining the neutronic design accuracy of the HTTR core. The VHTRC is a low-enriched-uranium (LEU) fueled and graphite moderated split-type critical assembly which consists of two halves, i.e., one fixed and one movable. The movable half is conveyed toward the fixed half to make the system critical. The description of the assembly is presented precisely in Ref.(5). The conceptual figure of VHTRC and the major specifications of VHTRC are shown in Fig. 4.3 and Table 4.1, respectively. The assembly has a shape of hexagonal prism (2.4 m across the flats and 2.4 m long). Fuel and reflector blocks are loaded in a hexagonal steel frame to form the whole assembly. The fuel block has 19 holes into which fuel rods, graphite rods and so on can be inserted. The fuel rod is a stack of 20 fuel compacts packed in a cylindrical graphite sheath. In this study, the results of the criticality experiment for the core, named VHTRC-1, were used. In the core, fuel compacts, named B-4 type, which contains BISO-type CFPs using 4 wt% enriched  $\text{UO}_2$  kernels, are loaded. The detailed description of the fuel element is shown in Figs. 4.4 and 4.5 and listed in Table 4.2. The details about the criticality experiment are described in Ref.(10). In the analysis, the results on the VHTRC-1-3 and VHTRC-1-4 cores were used, which have 264 and 278 B-4 type fuel rods, respectively. Their cross sectional views are shown in Figs. 4.6 and 4.7.

Table 4.1 Major specifications of VHTRC.

Maximum thermal power (W)	10
Maximum core height (m)	2.4
Maximum core diameter (m)	1.75
Fuel element	Prismatic, CFP
Fuel compact	
Outer diameter (mm)	36
Inner diameter (mm)	18
Height (mm)	36
Fuel	$\text{UO}_2$
$^{235}\text{U}$ enrichment (wt%)	2,4 or 6
Fuel kernel diameter ( $\mu\text{ m}$ )	599
Moderator	Prismatic graphite

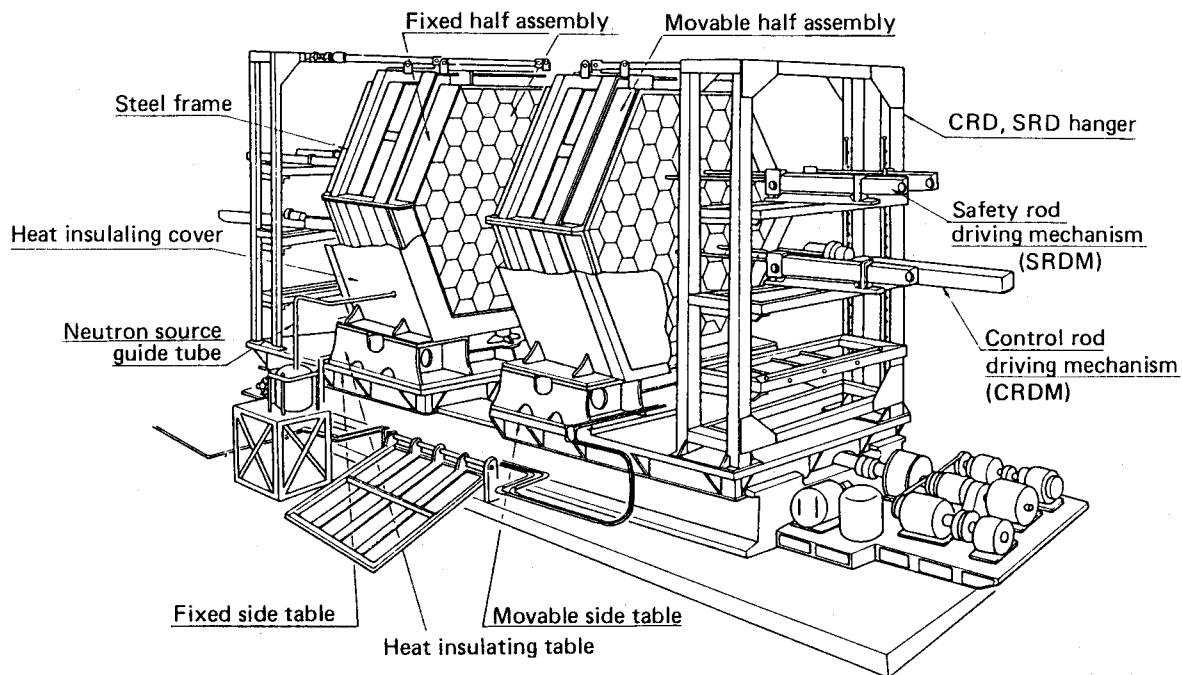


Fig. 4.3 Conceptual figure of VHTRC.

Table 4.2 Description of B-4 type fuel element.

Item		Unit	Measured value
Fuel kernel	Enrichment	(wt%)	$4.000 \pm 0.006$
	Diameter	( $\mu$ m)	$599 \pm 4$
	UO <sub>2</sub> density	(g/cm <sup>3</sup> )	$10.35 \pm 0.08$
	Boron equivalent impurity	(ppm)	<0.3
Coated fuel particle	Layer 1 Thickness	( $\mu$ m)	$79 \pm 4$
	Carbon density	(g/cm <sup>3</sup> )	$1.18 \pm 0.03$
	Layer 2 Thickness	( $\mu$ m)	$78 \pm 4$
	Carbon density	(g/cm <sup>3</sup> )	$1.87 \pm 0.02$
Fuel compact	Diameter	( $\mu$ m)	$913 \pm 10$
	Uranium inventory	(g)	$20.950 \pm 0.044$
	Outer diameter	(mm)	$35.98 \pm 0.05$
	Inner diameter	(mm)	$17.96 \pm 0.02$
	Height	(mm)	$36.01 \pm 0.06$
	Matrix density	(g/cm <sup>3</sup> )	$1.69 \pm 0.02$
	Heavy metal impurity		$(1.1 \pm 1.2) \times 10^{-4}$



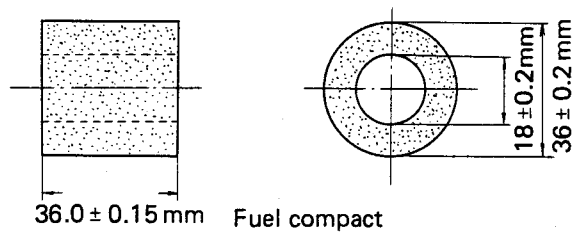
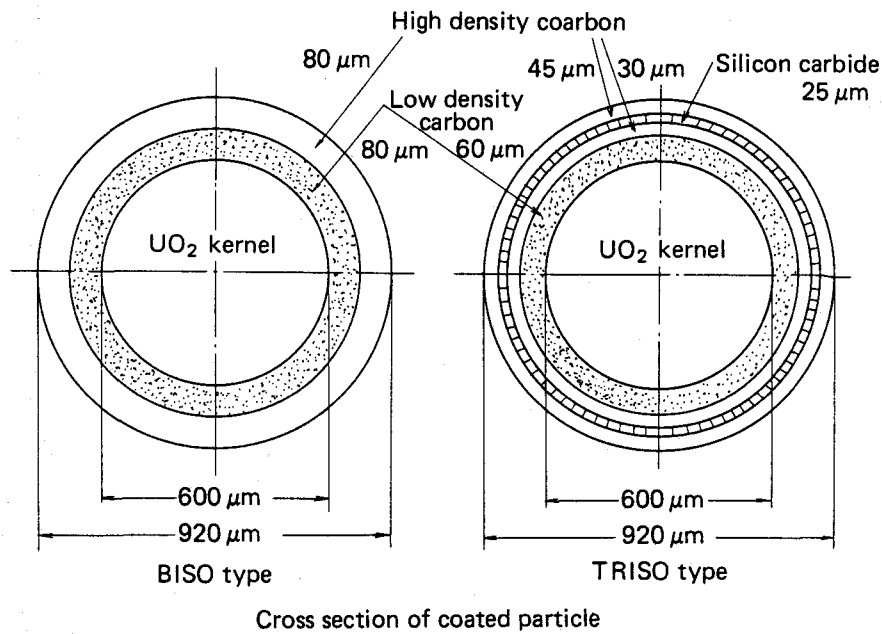


Fig. 4.4 Coated fuel particle and fuel compact for VHTRC.

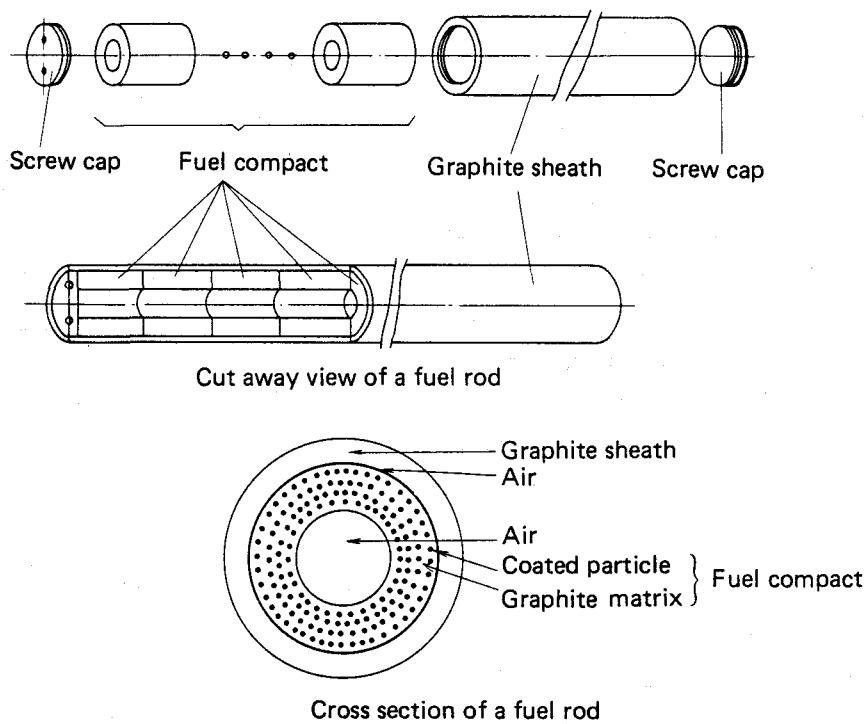


Fig. 4.5 Structure of VHTRC fuel rod.

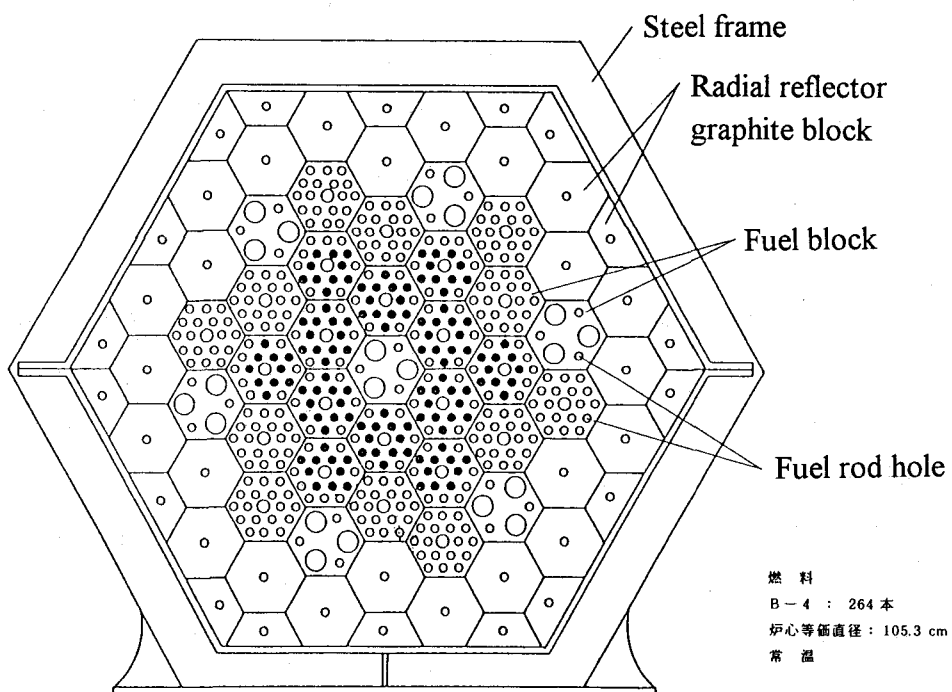


Fig. 4.6 Cross sectional view of VHTRC-1-3 core (264 B-4 fuel rods are loaded).

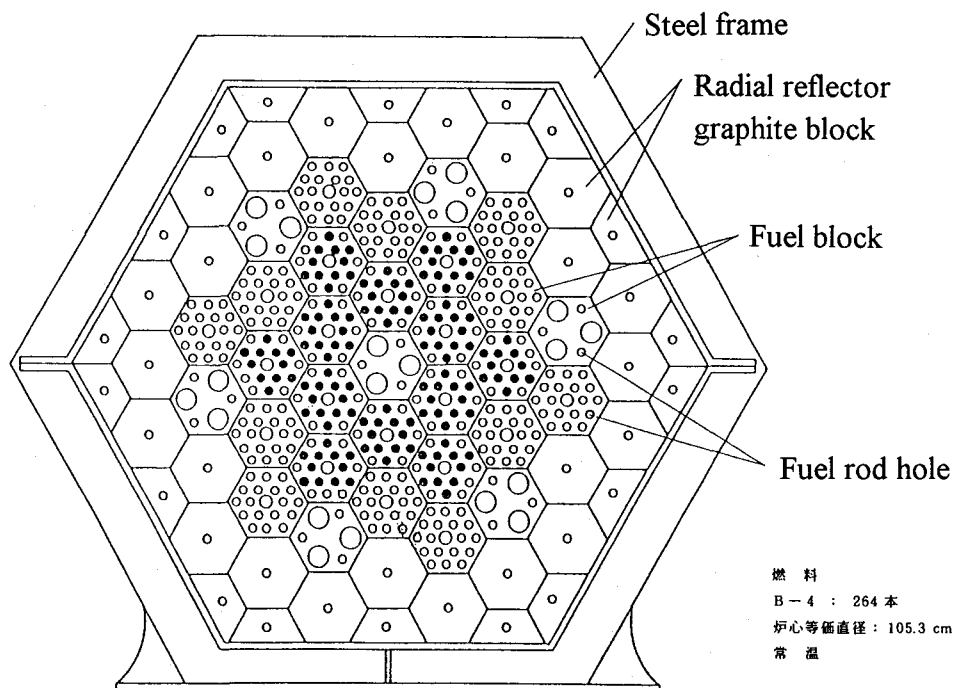


Fig. 4.7 Cross sectional view of VHTRC-1-4 core (278 B-4 fuel rods are loaded).

#### IV.2.2.2 Analysis method and conditions

In the calculation, the structure of compact, graphite sheath, as well as CFP, were precisely modeled. As a CFP model, only one sphere having several coated layers was placed in a certain fuel compact. The spherical model can, therefore, move in the core according to the particle flight. Figure 4.8 shows the calculation model compared with the real geometry. The NNDs used in the analysis were prepared with MCRDF. In order to reproduce the actual packing state of CFPs in a fuel compact as precisely as possible, the production procedure was precisely taken into account in the evaluation of the NNDs as shown in Sec. IV.2.1. The important point is that overcoated carbon finally becomes the matrix graphite between CFPs in the production process and therefore neighboring CFPs never contact with each other. In the evaluation of the NNDs, after the packing was simulated in a packing fraction of  $\sim 0.635$ , which is nearly that of RCP, the radii were decreased to adjust the packing fraction to the packing fraction of CFPs, that is 0.334. The real packing fraction of CFPs is actually 0.3. By adjusting the packing fraction for the NNDs to 0.334 in accordance with the wall effect correction introduced in Sec. II.4.1, the resulting packing fraction of CFPs arranged shows exactly the same as 0.30. The NNDs of VHTRC are shown in Fig. 2.35.

As for other conditions, because graphite was used as a moderator, the free-gas model was used for the material within the neutron energy range down to 4 eV, while the  $S(\alpha, \beta)$  treatment was taken below 4 eV. The calculation with MCNP-CFP was conducted with 120 cycles, the batch size of which is 1000 particles. The CPU time consumed in one run was about 3 hours on the FACOM VP-2600 vector processor at JAERI. Three cross section libraries were used for one model, which were produced from ENDF/B-IV<sup>(14)</sup>, JENDL-3.1<sup>(15)</sup> and JENDL-3.2<sup>(16)</sup>, respectively.

In this study, some analyses were also performed using a nuclear design code system for HTTR<sup>(17)</sup> for the comparison of our results with those of the conventional analysis method. This system was developed specifically for the HTTR neutronic design at JAERI. The system consists of a 1-dimensional cell burnup calculation code DELIGHT, which can deal with the compact type fuel element for HTGR containing irregularly distributed CFPs, the 2-dimensional transport calculation code TWOTRAN-2 to provide the average group constants of graphite blocks where control rods are inserted, and the 3-dimensional diffusion code CITATION-1000VP<sup>(18)</sup>. This code was developed from CITATION so that nuclear characteristics analyses

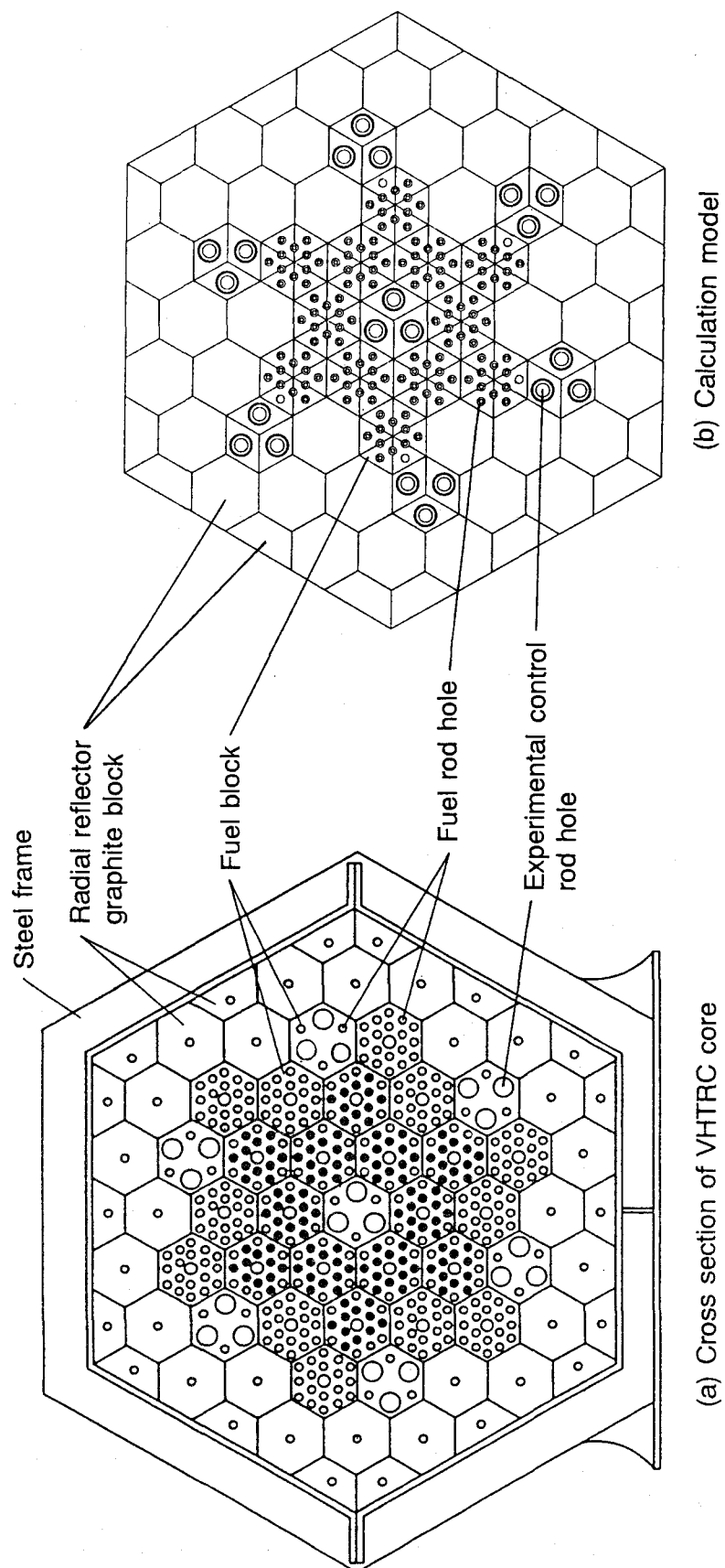


Fig. 4.8 Example of calculation model for VHTRC core compared with the cross section of the real geometry.

could be carried out with a three dimensional whole core model of HTTR in an acceptable short computation time. The details about the calculation using this system are given in Refs. (17) and (19).

#### IV.2.2.3 Results and discussion

The calculated effective multiplication factors with MCNP-CFP are summarized in Table 4.3 compared with the experimental and other calculated results. The results with MCNP-CFP are found to be in fairly good agreement with the experiment especially in case of using ENDF/B-IV and JENDL-3.1. However, significant discrepancy beyond the statistical error was seen for the VHTRC-1-3 core using JENDL-3.2. Obviously the reason is not due to the cross section of graphite, though it is used as neutron moderator which occupies the large volume of the core, because the equal thermal neutron scattering kernel is used in all cases. It is thus presumed from the result that there exist some problems in the cross section data of uranium in JENDL-3.2.

Table 4.3 also shows the calculation results with the diffusion code CITATION-1000VP with the group constants made by DELIGHT. We can see the tendency that the MCNP-CFP calculation results show a little higher values than the experimental ones, while the CITATION's results show an opposite tendency. The possible reasons of their discrepancy are as follows: One is the modeling. The CITATION employs a 3-dimensional triangular mesh. And in the calculation model, one block is divided into 24 triangular meshes in the radial direction, while in the axial direction, a relatively coarse mesh was used because there exists no heterogeneity in the direction. It was pointed out in Ref. (9) that by using an enough fine mesh model the effective multiplication factor increased by  $\sim 0.5\% \Delta k$ . The other reason is attributed to the fact that the used library is partially based on ENDF/B-III especially for FP cross sections in the CITATION calculation, although mainly it is based on ENDF/B-IV.

The reactivity effect due to heterogeneity by CFPs in a fuel compact was evaluated from the calculation result with the CFP smeared model in which the atomic number density in the fuel compact is conserved. The results are shown in Tables 4.3 and 4.4. In Table 4.4, the comparison with the reactivity effects evaluated by other conventional methods, i.e., cell calculations<sup>(20)</sup> and a core calculation<sup>(21)</sup> by a diffusion code is described. All the results agree with each other within  $\pm 15\%$ . Although the statistical uncertainty is still not small, we are convinced

from the above results and discussion that this method can essentially be applied to a real compact type HTGR core such as VHTRC.

Table 4.3 Comparison of effective multiplication factors for VHTRC-1 core.

Case	Nuclear data library	Effective multiplication factor		Difference ( $\Delta$ k)		Code
		VHTRC-1-4	VHTRC-1-3	VHTRC-1-4	VHTRC-1-3	
Present work	ENDF/B-IV	1.0098 $\pm$ 0.0033	0.9941 $\pm$ 0.0027	0.0045	-0.0029	MCNP-CFP
	JENDL-3.1	1.0110 $\pm$ 0.0030	0.9984 $\pm$ 0.0030	0.0057	0.0014	
	JENDL-3.2	1.0121 $\pm$ 0.0032	1.0097 $\pm$ 0.0030	0.0068	0.0127	
Diffusion	ENDF/B-IV	1.001	0.992	-0.004	-0.005	CITATION
Monte Carlo <sup>1)</sup>	ENDF/B-IV	0.9993 $\pm$ 0.0024	—	-0.0105 <sup>2)</sup>	—	MCNP-3A
Experiment	—	1.0053	0.9970	—	—	—

1) Exact 3-dimensional calculation except smearing the number density in a fuel compact.

2) Difference from the present result with ENDF/B-IV.

Table 4.4 Comparison of reactivity effect of CFPs in a fuel compact of VHTRC.

Case	Heterogeneity effect (% $\Delta$ k/k)	Description
Present work	1.0	Calculated by MCNP-CFP
Infinite cell calculation <sup>(20)</sup>	0.84 $\sim$ 1.08	Predicted by 4 different approximation methods
Core calculation <sup>(21)</sup>	0.90	Calculated by SRAC <sup>(22)</sup>

## **IV.2.3 Analysis of critical assembly experiment at PROTEUS**

### **IV.2.3.1 PROTEUS Experiment<sup>(23,24)</sup>**

The PROTEUS is a low-enriched, pebble-bed type reactor critical assembly, which was designed to investigate the physics of pebble-bed system and became the first criticality in 1992 in PSI, Switzerland. Experiments with an ordered close packed geometry (packing fraction of about 0.74) were performed after the first criticality, then those of a irregularly packed geometry (packing fraction of about 0.62) were done. Plans of other various experiments are now in progress. The general layout and descriptions of PROTEUS are shown in Fig. 4.9<sup>(23,24)</sup> and Table 4.5. The available core radius and height of PROTEUS are about 60 cm and up to about 170 cm, respectively. The core height is changeable to adjust the criticality. The fuel pebble contains CFPs whose outer diameter is about 0.9 mm and  $^{235}\text{U}$  of about 1.0 gram (enrichment of about 17% in CFP) in its inner fueled zone, the radius of which is 2.5 cm. The outer radius of fuel pebble is 3.0 cm, therefore the thickness of outer unfueled zone is 0.5cm. Matrix material of the shell and moderator pebble and that between CFPs are graphite. The schematic description of the fuel elements of PROTEUS is shown in Fig. 4.10.

Three irregularly packed lattice experiments were used for the analyses. In these criticality experiments, to examine how to make a complete irregular packing, the loading of pebbles was carried out with two methods<sup>(23)</sup>. One is just clamping the fuel and moderator pebble delivery tubes together in parallel, and each pebble is allowed to fall under gravity into the core from its respective tube. The Core 4.1 was made by this method. And the other is that the fuel and moderator channels are combined by means of a simple funnel-type arrangement to avoid unwanted ordering effects with the former method. The Core 4.2 and 4.3 were made by this method. After criticality, the most important parameter of the core height was measured by flattening the upper surface of the pebble bed gently to achieve an optically even upper surface. Conditions at criticality for each core are listed in Table 4.6.

### **IV.2.3.2 Analysis method and conditions**

The calculation was performed with MCNP-BALL by modeling the reactor precisely except in the core. In the core, one fuel and one moderator pebble were modeled at a certain place



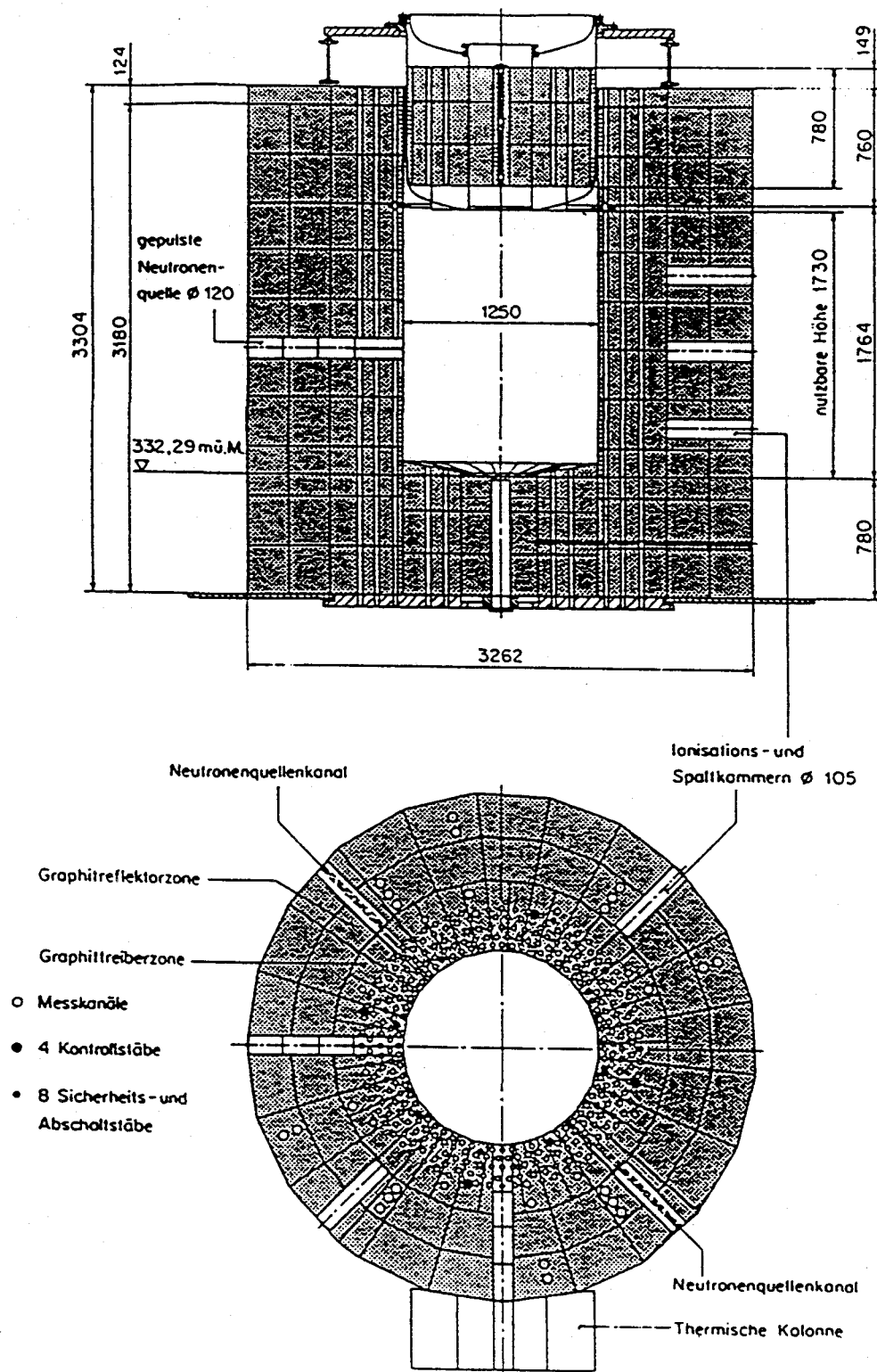


Fig. 4.9 General layout of PROTEUS.

Table 4.5 Description of PROTEUS reactor.

Item	Description
Reactor type	Pebble bed type critical assembly
core type	Ordered close packing (packing fraction is $\sim 0.7405$ )
Fuel element	Random loose packing (packing fraction is $\sim 0.62$ )
	Fuel pebble (including CFPs), Moderator pebble (graphite)
	6cm (5cm in fueled zone)
CFP	6 g/pebble ( $\sim 17\%$ enriched)
	$\sim 4000$ at criticality
	Coated particle fuel
	0.9 mm
Core diameter	9400 CFPs/pebble
Core height	120 cm
Reflector	$< 170$ cm
Criticality	Graphite 1992

Table 4.6 Experimental conditions at criticality of PROTEUS.

Conditions at criticality	Core 4.1	Core 4.2	Core 4.3
Critical height (m)	$1.58 \pm 0.01$	$1.52 \pm 0.01$	$1.50 \pm 0.01$
Critical loading	5020	4940	4900
	5020	4940	4900
Packing fraction (%)	60.0	61.5	61.8
Temperature ( $^{\circ}\text{C}$ )	20	19.2	21
Air pressure (mbar)	975	980	980
Humidity (%)	44	50	50
Date	March 31, 94	April 15, 94	June 22, 94

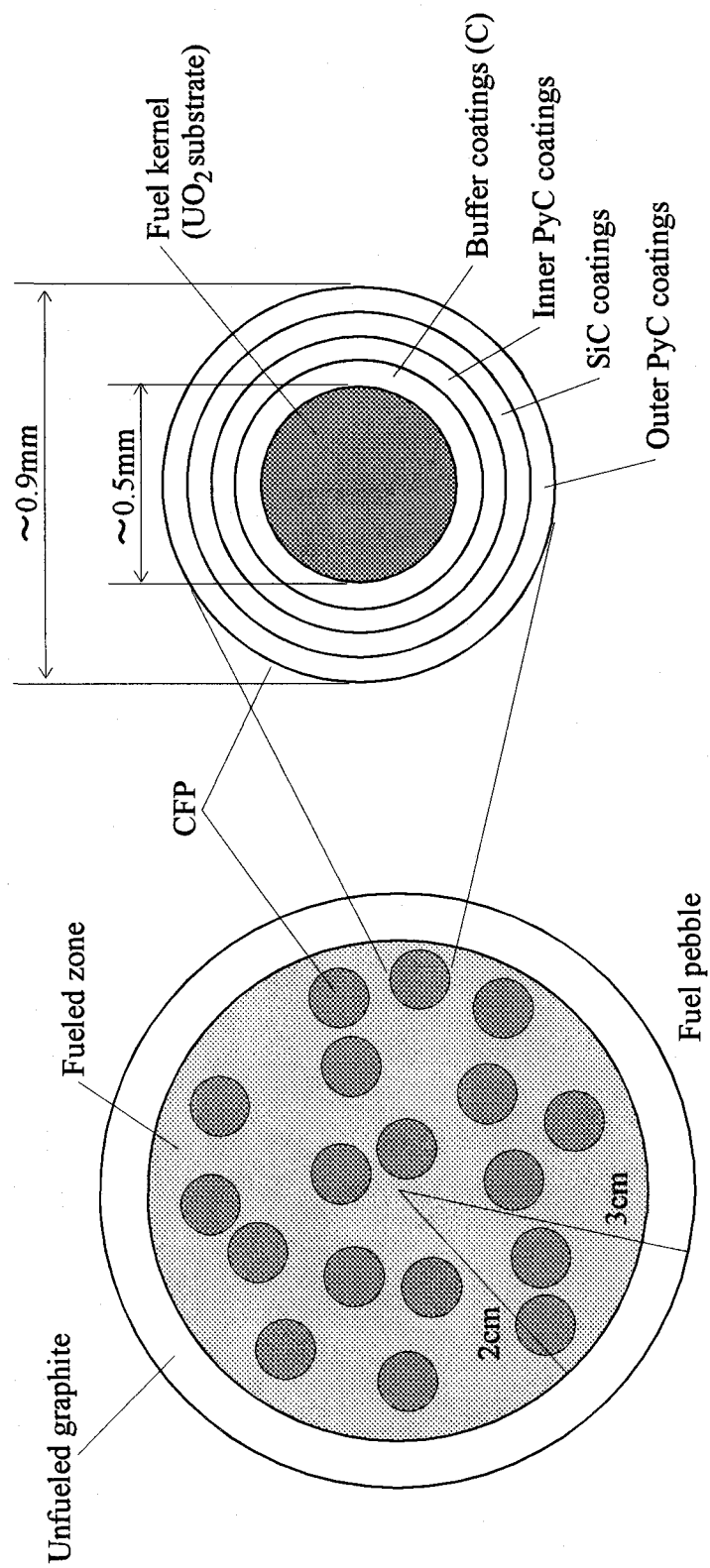


Fig. 4.10 Schematic description of fuel element of PROTEUS.

in the void, while one CFP was arranged in the fuel pebble. The calculation model is illustrated in Fig. 4.11. The necessary NNDs were prepared with MCRDF. The packing fraction of the NNDs for the CFP in the fuel pebble was 0.0576. NNDs for the fuel pebble were prepared for each core, the packing fraction of which is shown in Table 4.6. The examples of NNDs made by MCRDF for PROTEUS are shown in Fig. 2.34. As for other conditions, because graphite was used as a moderator, the free-gas model and the  $S(\alpha, \beta)$  treatment were adopted similar to the analysis of VHTRC. The number of cycles in the calculation was 400, the batch size of which is 2000 particles. Consequently, the 50 hours computation time was required with the IBM work station of RISC System/6000 with Power PC 601 micro processor.

#### IV.2.3.3 Results and discussion

The analyses were carried out for the irregularly packing cores of Core 4.1, 4.2 and 4.3 of PROTEUS. The criticality calculation results are summarized in Table 4.7. The preliminary experimental results are supplied by PSI<sup>(23)</sup> and JAERI.<sup>(24)</sup> The calculation conditions were essentially based on the benchmark problem<sup>(24)</sup> of the PROTEUS core. The analysis results are in fairly good agreement with the measurements though the systematic overestimation is still observed. As for Core 4.1, the discrepancy is slightly larger than Core 4.2 and Core 4.3. Taking the fact into account that the loading method of Core 4.1 was different from the others as described earlier, the overestimation is consistent with this fact, because the analysis was done assuming the pebbles were distributed irregularly.

To investigate the discrepancy of the effective multiplication factors between experiments and calculations, some sensitivity analyses were performed as follows: Generally it is very important to precisely estimate the impurity boron content when calculating the effective multiplication factor. In the reflector graphite of PROTEUS, some amount of boron was added artificially to stabilize its quality. However, the current boron content supplied by PSI<sup>(23,24)</sup> was still preliminary. We therefore examined the boron content sensitivity on effective multiplication factor using MCNP-BALL. The sensitivity was estimated to be  $-1.6\% \Delta k/k / \text{ppm-B}$  as shown in Table 4.8. From the result, this effect is fairly large and it means that it is significant in the core calculation of PROTEUS to estimate the impurity boron content in the graphite reflector. We think this effect can explain the overestimation of the analysis results in Table 4.7 in the future.

As for the measurement of the critical core height, the configuration of the upper

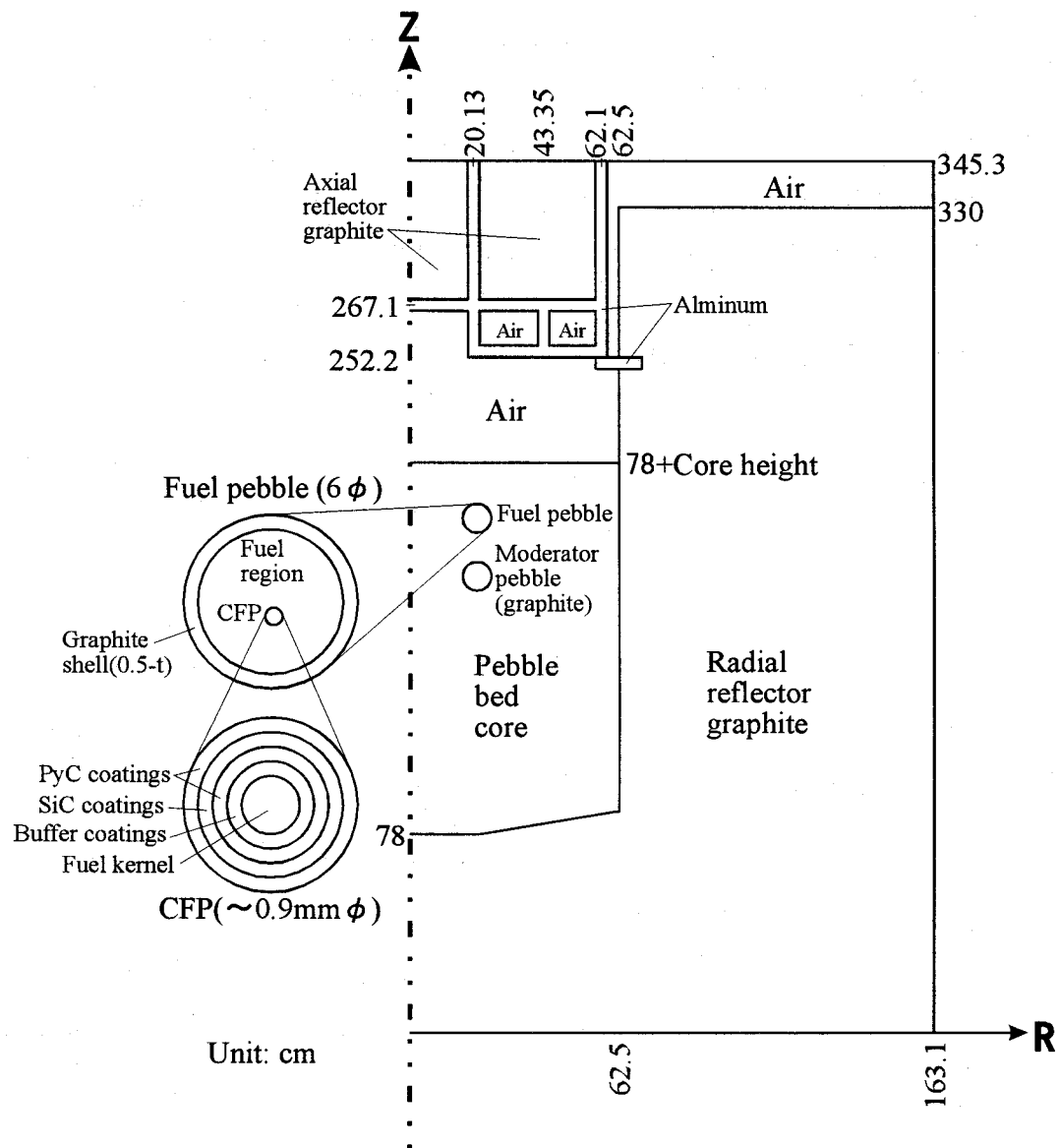


Fig. 4.11 Calculation model of PROTEUS reactor core with MCNP-BALL.

Table 4.7 Criticality calculation results of PROTEUS by MCNP-BALL.

Core	Effective multiplication factor (keff) Experiment	Calculation	History
Core 4.1	1.0134 ± 0.0011	1.0206 ± 0.0011	800000
Core 4.2	1.0129 ± 0.0011	1.0168 ± 0.0011	800000
Core 4.3	1.0132 ± 0.0011	1.0172 ± 0.0011	800000

Table 4.8 Sensitivity analysis results.

Item	Sensitivity
Impurity boron concentration	-1.6 %Δ k/k/ppm-boron
Geometry of upper surface of the core	< 0.05 %Δ k/k
Uncertainty in core height measurement	-0.12 %Δ k/k/cm-core height

surface of the pebble-bed core at criticality differs from that at the measurement, because it was done after flattening the upper surface. This can affect the calculated criticality. The real configuration before flattening is like a pile, namely, it is high around the core center axis, because of using pebble delivery tubes or a funnel-type loader. A cone geometry was assumed as a model of the upper surface of the core as shown in Fig. 4.12, and the sensitivity calculations were done for possible cone heights up to 20 cm. From the result, this effect was found to be very small, that is not beyond  $0.05\% \Delta k/k$  as shown in Table 4.8. It was confirmed that the correction of the effective multiplication factor due to this effect is not necessary and the method to measure the core height employed in this experiment was validated.

Next we discuss the effect of the uncertainty in the measurement of the core height. This effect may cause an error in the final calculation result of multiplication factor, because it can change the packing fraction of fuel pebbles. In the core height measurement, the absolute error is estimated to be 1 cm.<sup>(23,24)</sup> However, because the upper surface of the pebble-bed core is flattened optically to determine the average core height, we think that it would be better to consider the error conservatively as large as the length of the fuel pebble radius. The effect of the core height was thus evaluated under the condition of conserving the inventory of fuel pebbles. From the analysis, the sensitivity was estimated to be  $-0.12\% \Delta k/k/\text{cm}$  (core height) as shown in Fig. 4.13 and Table 4.8. From the result, the error induced by this uncertainty is comparable to the measurement error of effective multiplication factor or the statistical error in Monte Carlo calculations, if considering the 1cm uncertainty, while in case of considering the uncertainty of pebble radius, it is found that the difference becomes fairly large. It is confirmed from the comparison that the measurement uncertainty being as large as the length of the fuel pebble radius can be tolerated. However, we suggest that careful measurement of the critical core height is very important.

Also from the discussions above, parameters measured and used in the analysis, such as core heights, inventory of pebbles, packing fraction of pebbles are different among three cores. Nevertheless, the analyzed results of Core 4.2 and Core 4.3 agree well with each other within an acceptable error. From the calculated results of these different experiments, we concluded that they could be regarded as an equivalent experiment of a reference critical core which was packed in the packing fraction of RLP. And it was confirmed from the above-mentioned results that MCNP-BALL can predict neutronic characteristics accurately for pebble-bed type reactors such as PROTEUS.

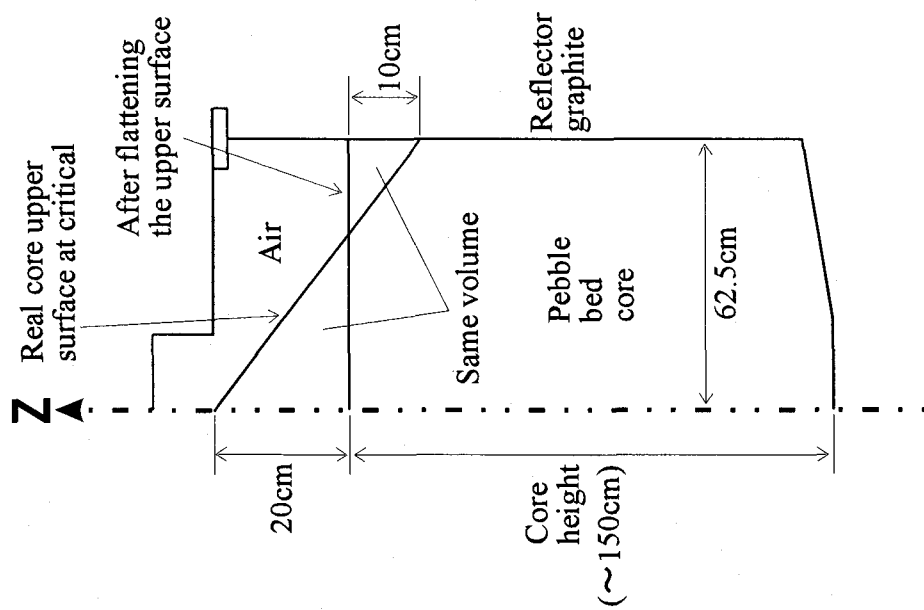


Fig. 4.12 Analysis model for the reactivity effect of configuration of the upper surface in PROTEUS.

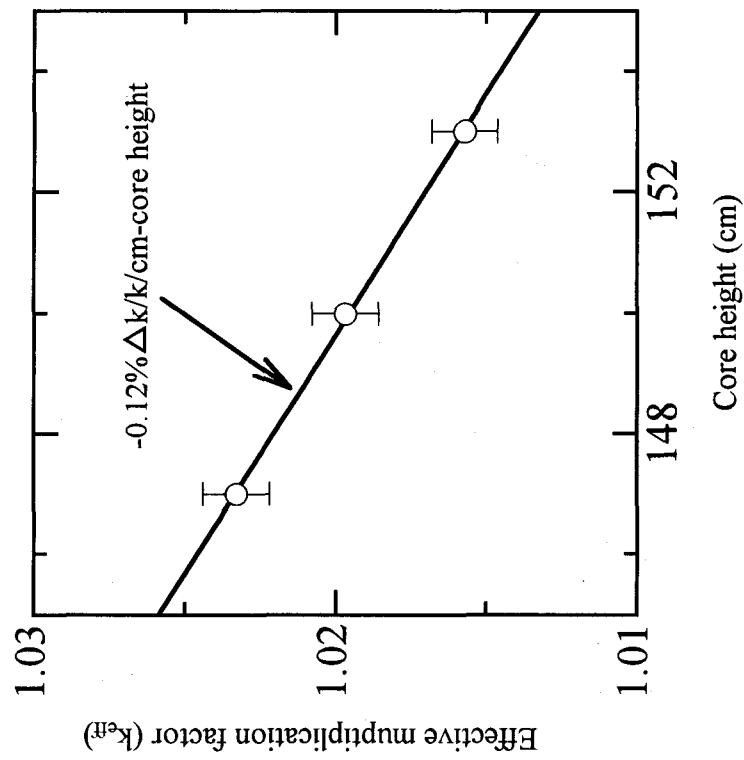


Fig. 4.13 Reactivity effect of core height in PROTEUS.



### IV.3 Heterogeneity effect of heavy concrete by fusion neutrons

As introduced in Sec. I.4.4, heavy concrete is usually utilized in nuclear reactor especially in the case that there exists a particular region requiring a strong shield locally, for example, to attenuate streaming radiation. In fusion reactor, it is expected that heavy concrete will be employed as a strong bulk shield in order to effectively attenuate high energy neutrons and gamma-rays leaking from the first wall region, because it is one of the most effective, reliable and cheap shields.

Heavy concrete is generally made by mixing aggregates, i.e., high density ores, iron punchings and so on, with cement and other materials. It provides strong shielding performance in various applications, though it is obliged to have heterogeneous structure due to the irregular arrangement of the aggregates. There have been various investigations of the shielding potential of heavy concrete in recent years: Spectrum and relaxation property measurements have been carried out using neutrons from thermal reactors<sup>(25,26)</sup>, spontaneous fission neutrons from  $^{252}\text{Cf}$ <sup>(27,28,29)</sup> and DT neutrons<sup>(30,31)</sup>. Also, analyses with a smeared model have been performed for higher energies up to 400 MeV<sup>(32)</sup>.

In the present experiment and analysis, we focused on fusion neutrons under the following consideration. In fusion reactor, neutron anisotropic scattering becomes dominant compared with thermal reactor because the neutron energy is high enough to distort the angular distribution of the emitted neutrons. Neutrons, as a result, strongly flow outward in the blanket or the biological shield, and the local neutron spectrum varies, depending on the neutron penetration length in the shield. Consequently, in such a neutron field, heterogeneous structure caused by the irregular arrangement of aggregates contained in heavy concrete can affect its shielding performance because reaction cross sections of the aggregates differ from those of the concrete as a matrix material. Moreover, in some cases, to strengthen the shielding performance, the amount of heavy aggregates must be increased. And also, to reduce the cost, large aggregates may be required. Such situations, consequently, enlarge the heterogeneity effect and may require a precise investigation about the shielding performance for the design of the fusion reactor shield. However, accurate estimation of the performance of shield concrete is difficult, especially when using a conventional  $S_N$  or diffusion calculation method because it is generally very hard to evaluate the group constants in view of the heterogeneous structure and the local variations of the neutron spectrum in the shield. Actually, only few previous experiments for DT neutrons using

heavy concrete can be cited<sup>(30,31)</sup>, although precise studies for ordinary concrete exist using a pulsed DT neutron source<sup>(33,34)</sup>. Moreover, the former reports did not mention the heterogeneity effect. At present, we cannot, therefore, predict in advance how the heterogeneity affects the shielding performance of heavy concrete. For the future fusion reactor shield design, the precise influence of heavy concrete on shielding performance must be found by experiment. At the same time an appropriate calculation method should be developed, taking into account the dimensions and arrangement of the aggregates, so as to predict the heterogeneity effect for an appropriate reactor design.

In view of the above discussion, in order to investigate how much of the heterogeneity effect heavy concrete is caused by the heavy aggregates, a DT neutron irradiation experiment using various heavy concrete samples created to simulate typical manufactured heavy concrete has been carried out. It employed a pulsed neutron source with the time of flight(TOF) method, foil activation method and so on. Analysis of the experimental results was carried out by using MCNP-CFP which can deal with heavy aggregates in heavy concrete as irregularly distributed spherical elements contained in a homogeneous matrix. Through the analysis of these results, the applicability of MCNP-CFP, especially when used for the heterogeneous system (in which neutrons strongly flow outward and the spectrum varies depending on the neutron penetration distance) has been verified for precise estimations of the heterogeneity effect of heavy concrete in the design of a fusion reactor shield. In addition, the mechanism of the observed heterogeneity effect is studied through Monte Carlo analyses using the general purpose code MCNP-4A<sup>(35)</sup>.

### **IV.3.1 Experimental**

#### **IV.3.1.1 Heavy concrete sample**

For the irradiation experiment, two kinds of heavy concrete samples, having an equal amount of aggregates, were prepared by mixing spherical or cylindrical iron as aggregate with portland cement, fine sand and so on. One is a heterogeneous heavy concrete including cylindrical large iron aggregates, while the other is also a heavy concrete, regarded as a homogeneous model, which contains enough small spherical iron aggregates so that the heterogeneity effect can be neglected. The packing fraction of the aggregates is set to be 0.2~0.4 so as to maintain high densities of 3~4.5 g/cm<sup>3</sup> recommended by the literature<sup>(36)</sup>. Grains of the iron aggregates for

homo- and heterogeneous samples are 0.47 cm  $\phi$  sphere and cylinders of 2.8 cm  $\phi$  by 2.8cm long and 6 cm  $\phi$  by 6 cm long, respectively. Dimensions of a base shield sample are 40x40x20 cm<sup>3</sup>. Thick samples of 20~60 cm can be made by piling them up. Composition of heavy concrete samples is determined by recording the combination ratio of mixed materials when manufacturing them and by assuming that the change in weight after forming the sample is equivalent to evaporation of the contained water. Description of the heavy concrete samples prepared is shown in Tables 4.9 and 4.10 and Fig. 4.14.

Table 4.9 Description of heavy concrete used in the experiment.

Sample I.D.	Iron aggregates		Packing fraction	Weight (kg)
	Shape	Dimensions (mm)		
D0 $\rho$ 20S#1	Sphere	4.76 $\phi$	0.202	101.0
D3 $\rho$ 20C#1	Cylinder	28 $\phi$ x 27.2	0.202	99.6
D6 $\rho$ 20C#1	Cylinder	60 $\phi$ x 60	0.202	99.2
D0 $\rho$ 30S#1,#2,#3	Sphere	4.76 $\phi$	0.302	120.6 <sup>1)</sup>
D3 $\rho$ 30C#1,#2	Cylinder	28 $\phi$ x 27.2	0.302	124.0 <sup>1)</sup>
D6 $\rho$ 30C#1,#2,#3	Cylinder	60 $\phi$ x 60	0.302	124.8 <sup>1)</sup>
D0 $\rho$ 40S#1	Sphere	4.76 $\phi$	0.400	135.8
D3 $\rho$ 40C#1	Cylinder	28 $\phi$ x 27.2	0.400	139.1

1) Averaged within equal type heavy concrete samples.

Table 4.11 Methods for the measurement of various energy neutrons.

Method	Neutron energy group to be measured		
	Thermal neutron	MeV neutron (1 ~ 10MeV)	14 MeV (Elastic peak)
Detector	BF <sub>3</sub>	NE213(TOF)	NE213(TOF)
Foil activation	<sup>115</sup> In(n, $\gamma$ )	<sup>115</sup> In(n,n') <sup>115m</sup> In	<sup>63</sup> Cu(n,2n)
$\gamma$ -ray energy (keV)	1293.5	336	511
Half life	54.4m	4.49h	9.74m

Table 4.10 Typical relative atomic abundance ratio of the heavy concrete.

(a) Packing fraction is 0.2.

Isotope	Heterogeneous heavy concrete (D3 $\rho$ 20C#1, D6 $\rho$ 20C#1)		Homogeneous heavy concrete (D0 $\rho$ 20S#1)
	Iron aggregates	Concrete	
H		1.836E-1	1.402E-1
O		5.521E-1	4.216E-1
Si		2.027E-1	1.548E-1
Al		5.324E-3	4.066E-3
Fe	1.000E+0	1.000E-2	2.439E-1
Ca		4.136E-2	3.159E-2
Mg		1.354E-3	1.034E-3
Na		1.958E-3	1.496E-3
K		1.536E-3	1.173E-3
S		1.126E-4	8.603E-5

(b) Packing fraction is 0.3.

Isotope	Heterogeneous heavy concrete (D3 $\rho$ 30C#1,#2, D6 $\rho$ 30C#1,#2,#3)		Homogeneous heavy concrete (D0 $\rho$ 30S#1,#2,#3)
	Iron aggregates	Concrete	
H		1.735E-1	1.127E-1
O		5.520E-1	3.585E-1
Si		1.965E-1	1.277E-1
Al		6.460E-3	4.196E-3
Fe	1.000E+0	1.050E-2	3.573E-1
Ca		5.576E-2	3.622E-2
Mg		1.824E-3	1.184E-3
Na		1.846E-3	1.199E-3
K		1.448E-3	9.404E-4
S		1.521E-4	9.878E-5

(c) Packing fraction is 0.4.

Isotope	Heterogeneous heavy concrete (D3 $\rho$ 40C#1)		Homogeneous heavy concrete (D0 $\rho$ 40S#1)
	Iron aggregates	Concrete	
H		1.925E-1	1.028E-1
O		5.445E-1	2.907E-1
Si		1.943E-1	1.037E-1
Al		5.581E-3	2.980E-3
Fe	1.000E+0	1.280E-2	4.729E-1
Ca		4.541E-2	2.425E-2
Mg		1.486E-3	7.934E-4
Na		1.858E-3	9.919E-4
K		1.457E-3	7.781E-4
S		1.238E-4	6.608E-5

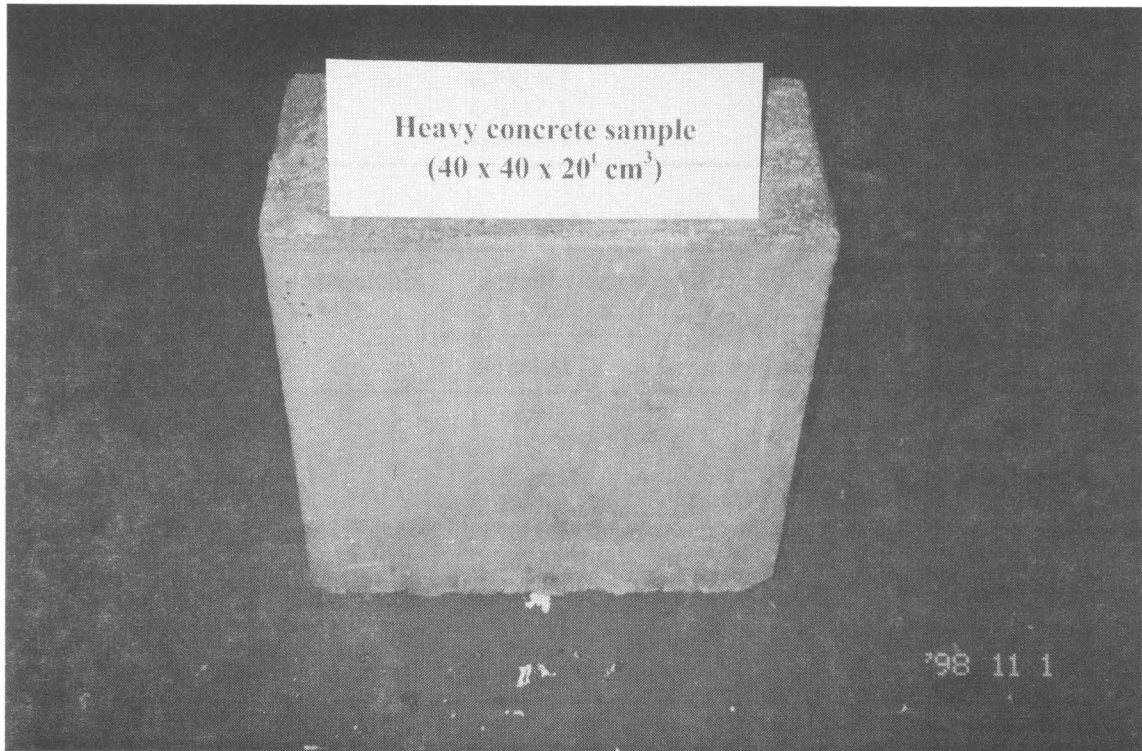


Fig. 4.14 Heavy concrete sample used in the present experiment.

### IV.3.1.2 Method to measure heterogeneity effect

Measurement methods of energy dependent neutrons are summarized in Table 4.11. The experiment consists of two simultaneous measurements of neutron spectrum by NE213 and  $\text{BF}_3$  detectors and reaction rate with activation foils. Measured neutron energy is divided into three ranges of thermal region ( $E_n < 1\text{eV}$ ), MeV region ( $1\text{MeV} < E_n < 10\text{MeV}$ ) and 14MeV region ( $E_n > 10\text{MeV}$ ). The experimental arrangement is shown in Fig. 4.15. A heavy concrete sample is located at 6 cm from the target, the surface of which is perpendicular to 85 degree axis with respect to the deuteron beam line. Therefore, the average energy of neutrons bombarding the sample is estimated to be 14.1 MeV. The collimator, which was specifically made for the neutron DDX measurement<sup>(37)</sup> to reduce background neutron and gamma-ray, is placed between sample and detector. Hence the detector can view only the sample completely. At 8 m from the target on the 85 degree axis, a 10"  $\phi$  by 10 cm thick large NE213 scintillation detector, which is shown in Fig. 4.16, is set up, surrounded by strong shields with ordinary concrete, polyethylene and so on. A  $\text{BF}_3$  (1"  $\phi$  x 4" long) detector in Fig. 4.17 used for measuring thermal neutron is also located at about 50 cm from the sample so that it can view only the sample by collimating with thin  $\text{B}_4\text{C}$  and Cd shield wound around it to suppress low energy neutron background. The activation foils are uniformly put on the sample surface opposite to the target side.

Data acquisition was carried out by the following process. Above MeV region, the neutron spectrum was measured by the TOF method with the NE213 detector. Details of the data reduction are described in Refs.(34) and (38). To refine the energy resolution, the flight path was set to be enough long ( $\sim 8\text{m}$ ) so as to realize precise time analysis by time-to-amplitude converter (TAC). Figure 4.18 shows the block diagram of the measuring system for the present TOF experiment. In order to attain wide dynamic range by the neutron-gamma pulse shape discrimination technique, two parallel pulse shape discrimination circuits were employed. The gain ratio of two delay line amplifiers (DLA) was set to be 1:10 so as to cover wide energy range of 0.7~15 MeV. Measured raw TOF data were converted into the neutron energy spectrum by correcting them with the detector efficiency and the neutron mean emission time after subtracting the background pulse height spectrum (PHS) from the foreground PHS. For the determination of energy-dependent detector efficiency, the following methods were adopted; DT neutron source spectrum measurement,  $^{252}\text{Cf}$  TOF experiment, measurement of leakage neutron spectrum from a small graphite slab and SCINFUL<sup>(39)</sup> calculation. The efficiency curve used in the data reduction

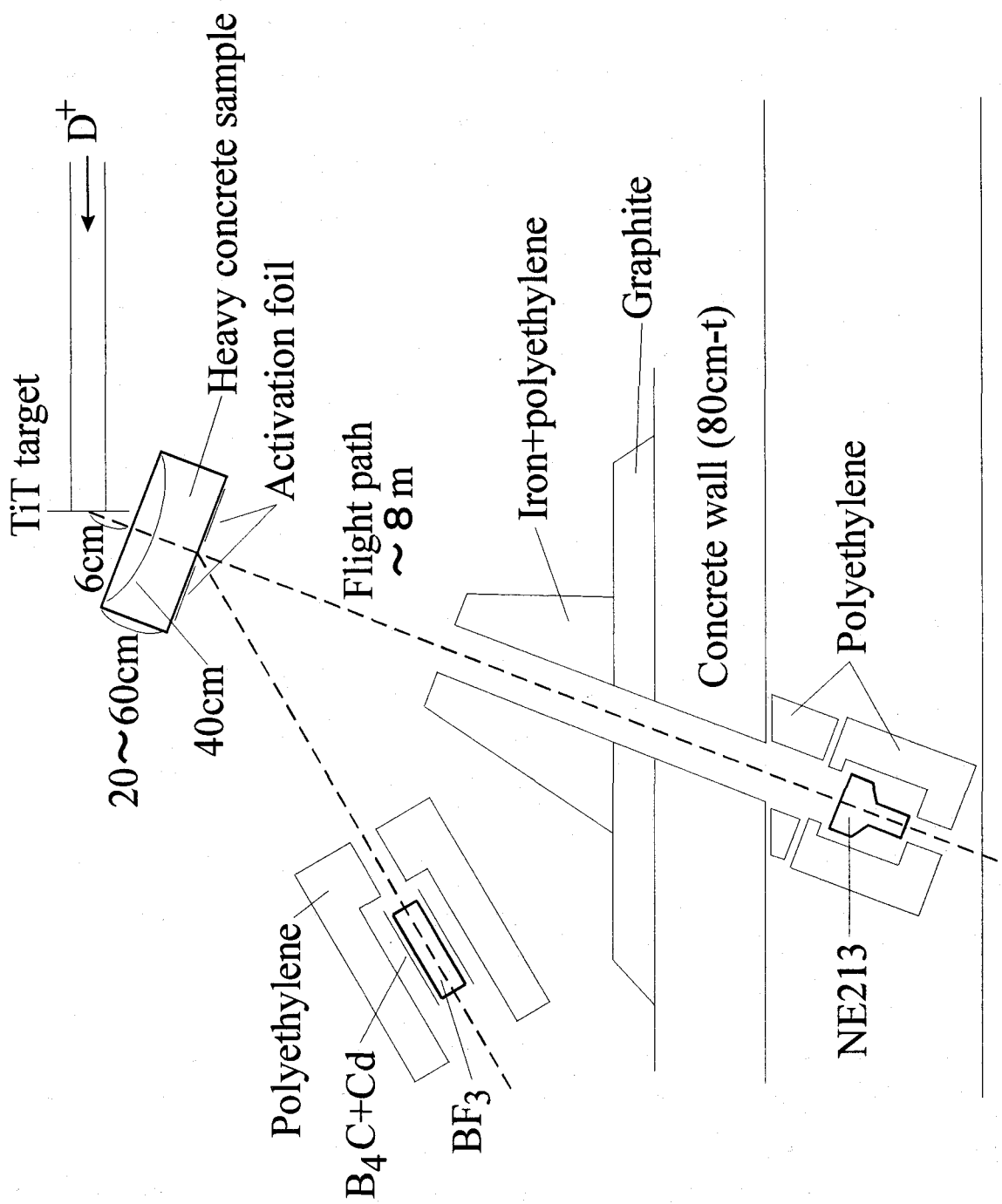


Fig. 4.15 Schematic arrangement of heavy concrete irradiation experiment.



Fig. 4.16 Large NE213 detector (10"  $\phi$  x 10 cm) used to measure high energy neutron spectrum with TOF method in the present experiment.

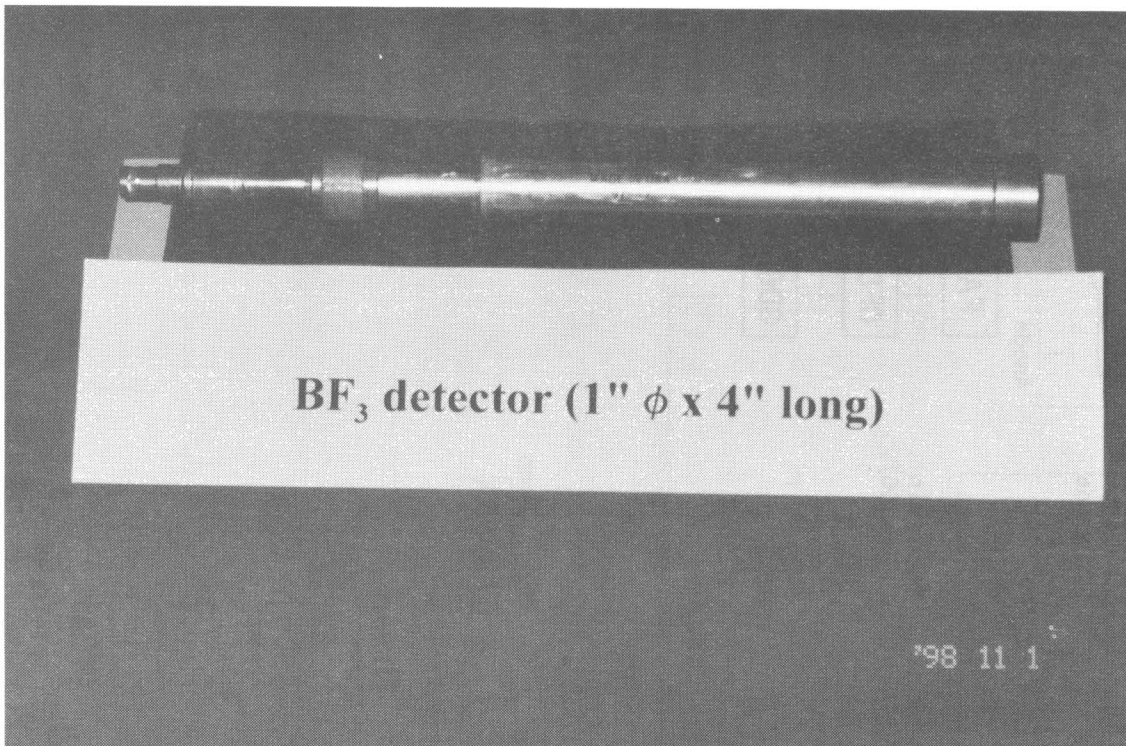


Fig. 4.17  $\text{BF}_3$  detector for measuring thermal neutron flux in the present experiment.



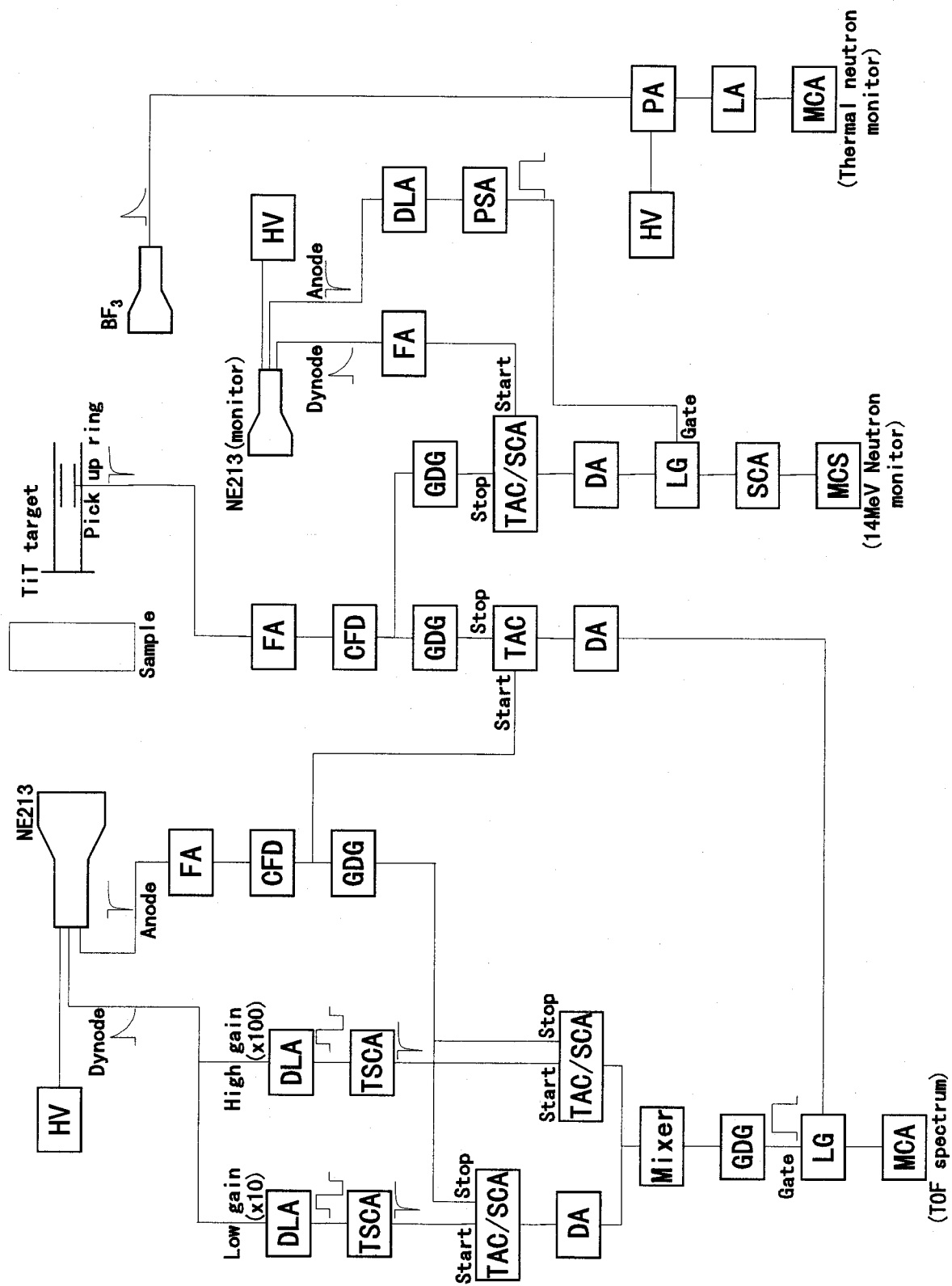


Fig. 4.18 Block diagram of neutron measuring system with the TOF method.

is shown in Fig. 4.19. As for the neutron flux measurement with the  $\text{BF}_3$  detector, a discrimination level was set at the valley between neutron signal and noise including gamma-ray signals. The integral counts above the discrimination level were recorded as the thermal neutron flux data.

For the reaction rate measurement in MeV region,  $^{115}\text{In}(n,n')$  reaction was utilized because its cross sections drew excitation function in the energy region of 1~10 MeV.  $^{65}\text{Cu}(n,2n)$  reaction was used to cover an elastic peak at 14 MeV, since the threshold energy of the reaction is as high as 12 MeV. In this energy region, neutrons produced by elastic scattering or uncollided neutrons were dominant. The transmission rate of neutron therefore changed caused by local arrangement of the aggregates. To avoid this place-dependent effect, a thin disc on which several number of foils were fixed was rotated in 4 r.p.m. during the irradiation experiment. As a thermal neutron monitor  $^{115}\text{In}$  was selected again, because it was convenient for it to be used simultaneously as a MeV region monitor. Besides it, there are three important reasons: Thin foil is not necessary as shown in the later. The (n,g) reaction cross section of  $^{115}\text{In}$  is sufficiently large like Au foil. And the half life is appropriately short to eliminate the counting time. In the irradiation of  $^{115}\text{In}$ , foils with and without Cd filter were simultaneously used to remove the contribution of resonance reaction in epi-thermal region.

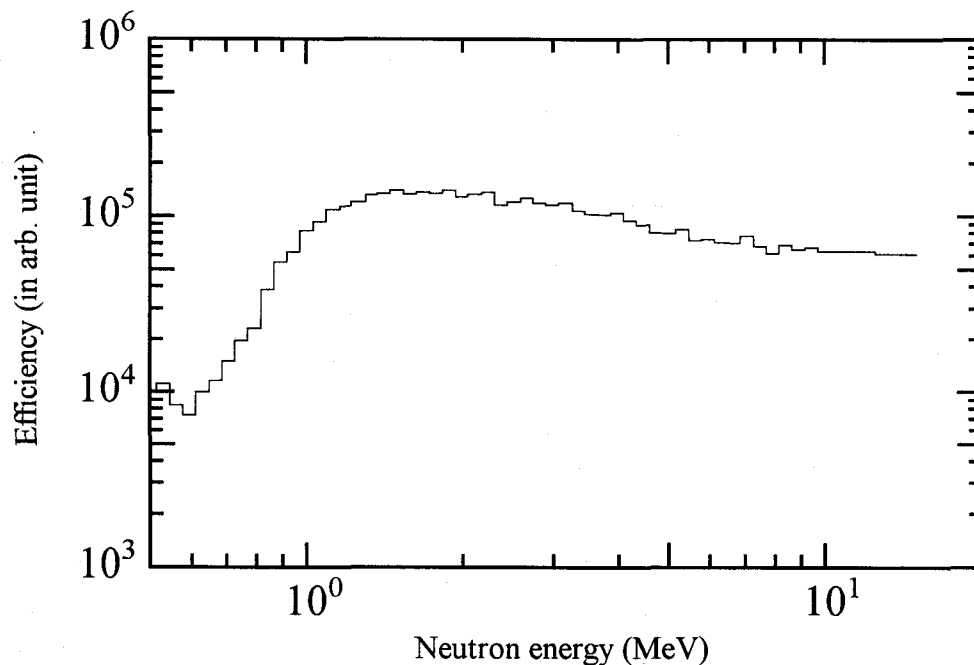


Fig. 4.19 NE213 detector efficiency used in the present experiment.

In one measurement, two sequential experiments were performed with a heterogeneous heavy concrete and the corresponding homogeneous one made of the same amount of iron absorber and matrix materials. We have introduced the ratio of the two results, i.e., hetero- and homogeneous samples, with respect to neutron spectrum, reaction rate and so on, because to examine the ratio was a reasonable way to discuss the heterogeneity effect of heavy concrete. For a practical examination of the heterogeneity effect, the results obtained by the NE213 and BF<sub>3</sub> detectors were mainly used, while those of activation foils as supplementary results were utilized for cross-checking of the measured values.

#### **IV.3.1.3 14 MeV neutron source**

As a neutron source, the Intense 14 MeV Neutron Source Facility OKTAVIAN<sup>(40)</sup> at Osaka University, Japan was used. The OKTAVIAN can generate  $\sim 10^9$  neutrons/sec by bombarding a 10 Ci TiT target with pulsed deuteron beams with about 2 nsec pulse width and 2 MHz repetition frequency. This narrow pulse width could realize measurement of precise neutron spectrum by the TOF method with good energy resolution. The neutron fluence was determined by Al foil and a neutron yield monitor; NE213(1"  $\phi$   $\times$  1" long) scintillator located at about 3 m from the target. Only 14 MeV neutrons were counted by the neutron-gamma pulse shape discrimination and extraction of 14 MeV-isolated peak from the TOF spectrum. In the present experiment, the average neutron intensity was about  $5 \times 10^8$  neutrons/sec.

#### **IV.3.2 Analysis method**

The experimental results were analyzed by a general purpose Monte Carlo code MCNP and the modified version MCNP-CFP, which was particularly used for the analysis of heterogeneous heavy concrete model. Calculations for the homogeneous one were done with MCNP-4A.

The MCNP-CFP has already been applied to the analyses of VHTRC and PROTEUS critical assembly experiments as described in Sec. IV.2. In the analysis, MCNP-CFP simulated the arrangement of coated fuel particles (CFPs) packed irregularly in a fuel compact or fuel pebble. It means that the applicability of the code for the use in an isotropic neutron field was confirmed. In the present analysis, MCNP-CFP is applied to the analysis of the shielding performance of

heavy concrete in a DT neutron field. This means that we can examine the validity of neutron transport estimation of heavy concrete in a field that neutrons strongly flow outward and the spectrum continuously changes depending upon the neutron penetration length, for example, in such as blanket, biological shield in fusion reactor facility.

As for the calculation condition, a three dimensional exact model was adopted, and an isotropic neutron source, considering the measured energy spectrum, was used as shown in Fig. 4.20. JENDL-3.2 was selected as cross section library for the calculation. The ratio was evaluated in the same way as the data reduction of the experiment with hetero- and homogeneous model calculation results. In the analysis, two kinds of ratios were evaluated as follows: One was for the direct comparison between experiment and calculation to verify MCNP-CFP, as shown in the next equation.

$$[\text{Ratio}(1)] = \frac{[\text{Neutron spectrum in heterogeneous heavy concrete}]}{[\text{Neutron spectrum in homogeneous heavy concrete}]} \quad (4.2)$$

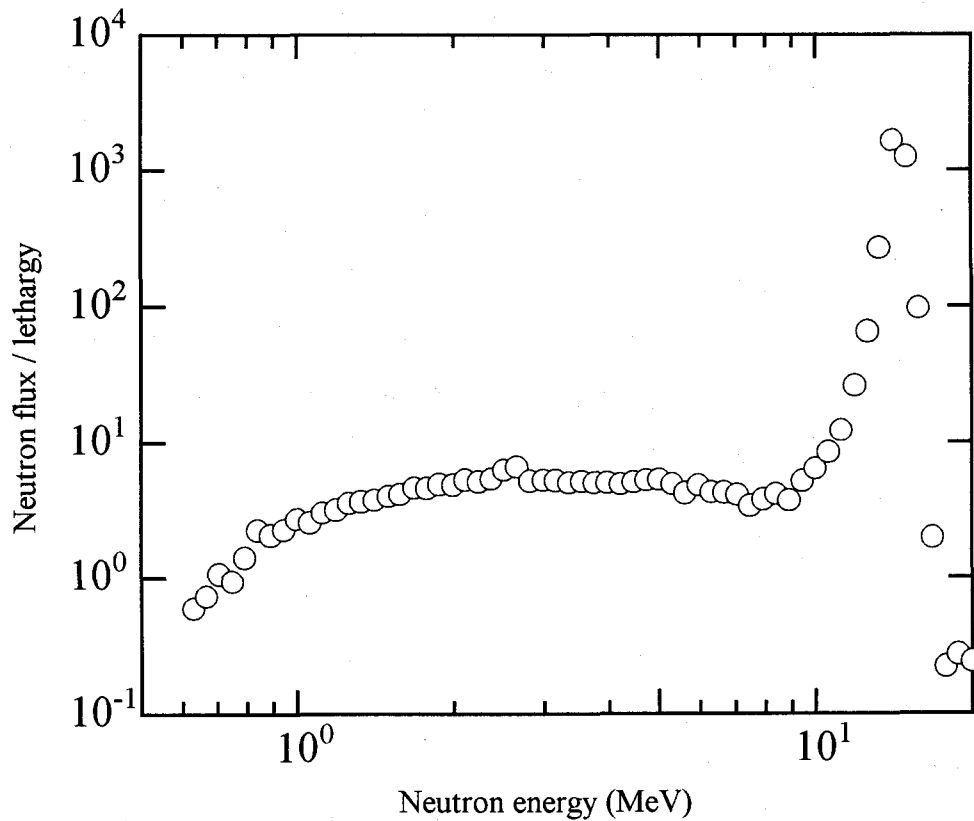


Fig. 4.20 Source neutron spectrum.

Since it is, in principle, difficult to manufacture hetero- and homogeneous heavy concretes having exactly an equal composition and weight, even if their production process is taken into account, the Ratio(1) may include a significant effect due to the small discrepancy of the composition and the weight in addition to the genuine heterogeneity effect. For this reason, the other ratio was evaluated as the "real" heterogeneity effect by using the verified code:

$$[\text{Ratio}(2)] = \frac{[\text{Neutron spectrum in heterogeneous heavy concrete}]}{[\text{Neutron spectrum in homogenized model of heterogeneous heavy concrete}]} \quad (4.3)$$

where the homogenized model has exactly the same composition as the heterogeneous one. This model calculation was done by MCNP-4A with the same cross section library.

### IV.3.3 Results and discussion

#### IV.3.3.1 Comparison of measured and calculated heterogeneity effects

Figures 4.21-4.25 show the measured and calculated ratios of the neutron flux obtained by BF<sub>3</sub> and NE213 detectors and of the reaction rates with Cu and In foils. In Figs. 4.21-4.23, the dependencies of the ratio at the packing fraction of 30% as a function of shield thickness are shown for 14 MeV, MeV and thermal regions, respectively, while Figs. 4.24 and 4.25 show the dependencies for the 20 cm thick shield as a function of packing fraction for 14 MeV and MeV regions, respectively. In this section, we discuss the experimental results and the analysis results of them. The "real" heterogeneity effect will be discussed in the next section. Possibly, the ratios contain small but significant effect arising from the discrepancy between the compositions of hetero- and homogeneous samples as mentioned in the previous section. However, mostly we can discuss the heterogeneity effect using these results. The significant effect above is made clear a little later. Some features that can be seen from these experimental heterogeneity effects are as follows:

- (1) As a whole, the ratio is below unity.
- (2) The intensity of the heterogeneity effect becomes weaker in MeV region compared with 14 MeV region.
- (3) Especially in MeV and 14 MeV regions, the effect becomes strong with increase of the sample thickness, the aggregate dimensions and the packing fraction of the aggregates.
- (4) The ratios determined by the measured neutron spectrum and the measured activity of

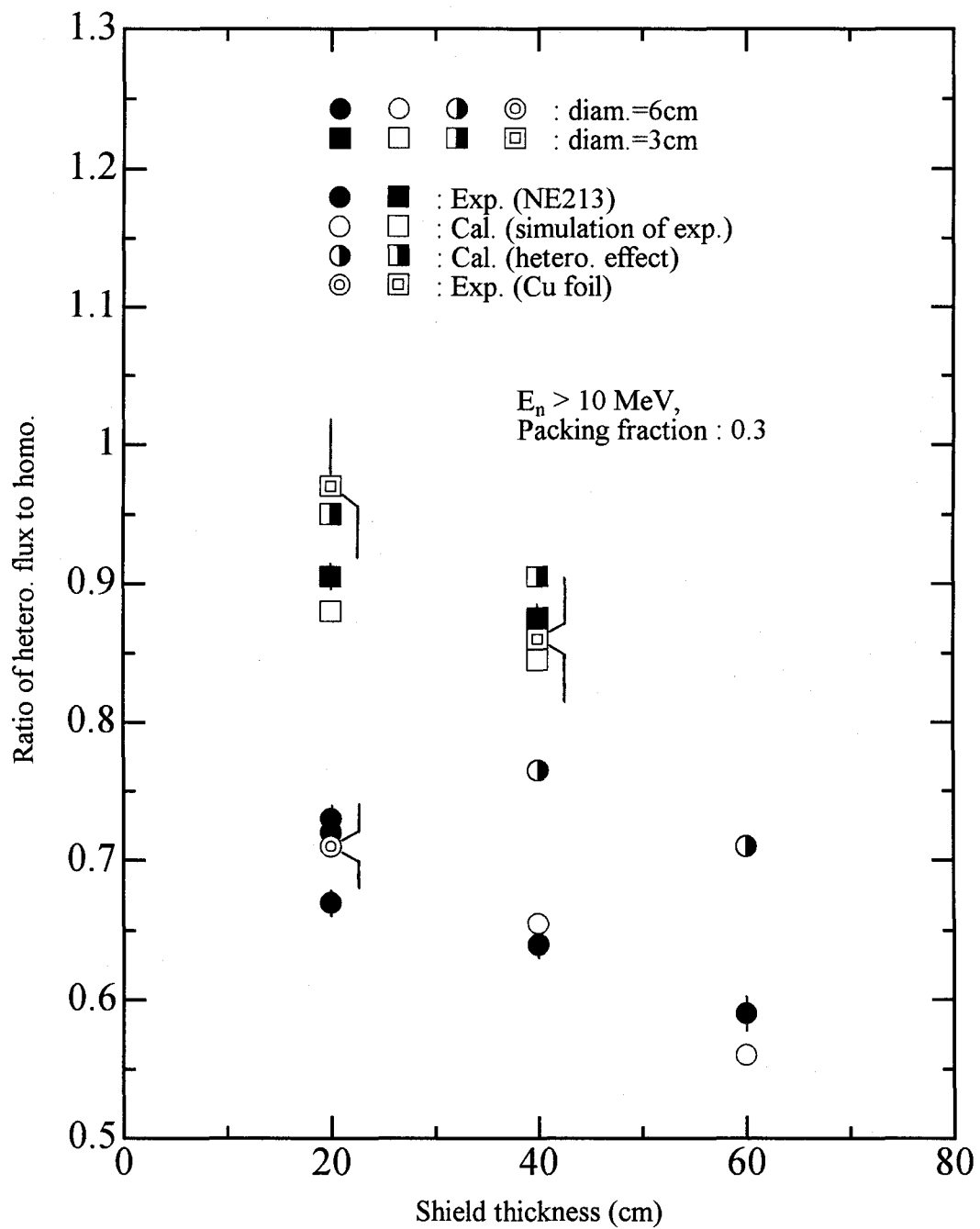


Fig. 4.21 Dependency of neutron flux ratio between heterogeneous and homogeneous samples as a function of shield thickness for 14 MeV region.

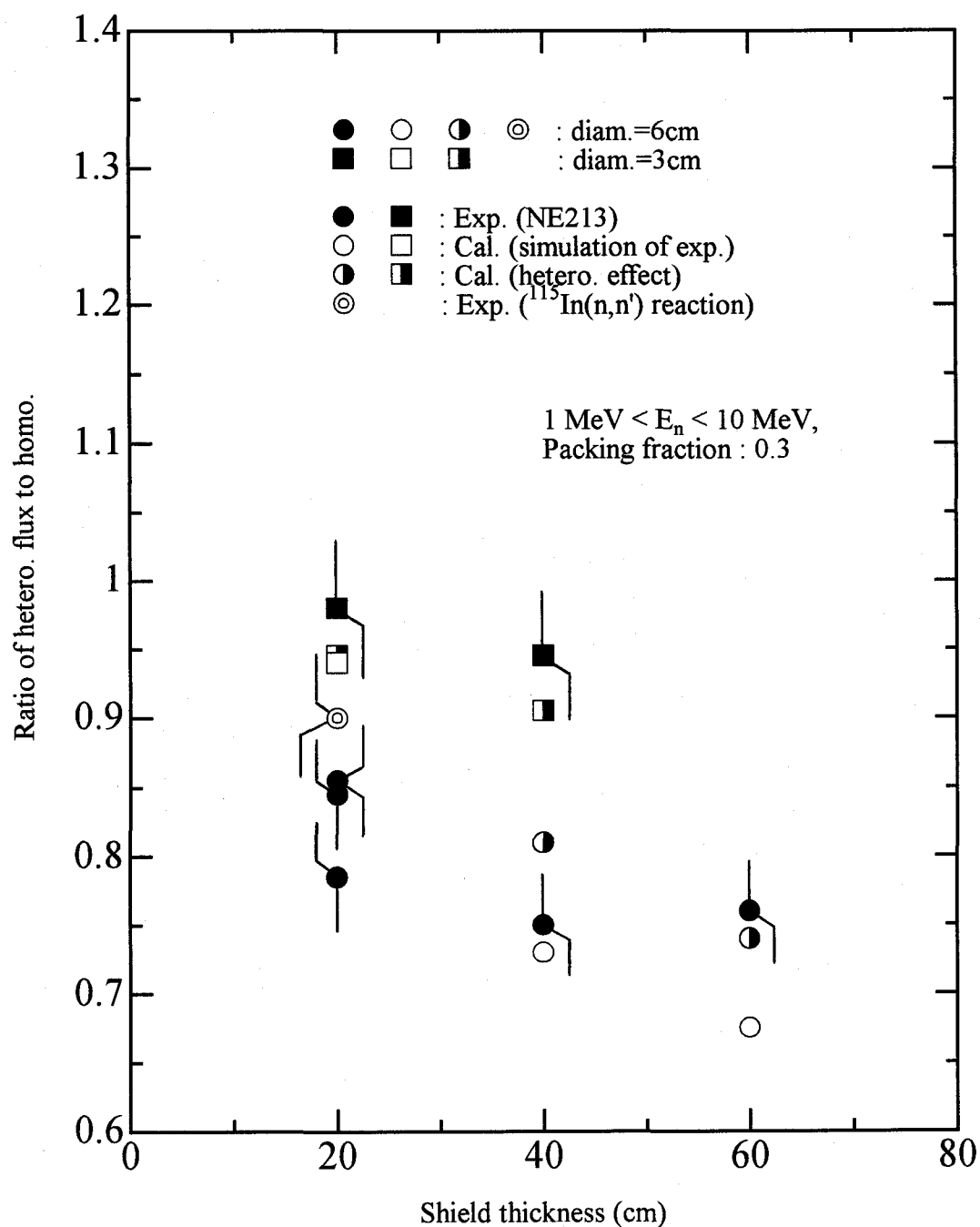


Fig. 4.22 Dependency of neutron flux ratio between heterogeneous and homogeneous samples as a function of shield thickness for MeV region.

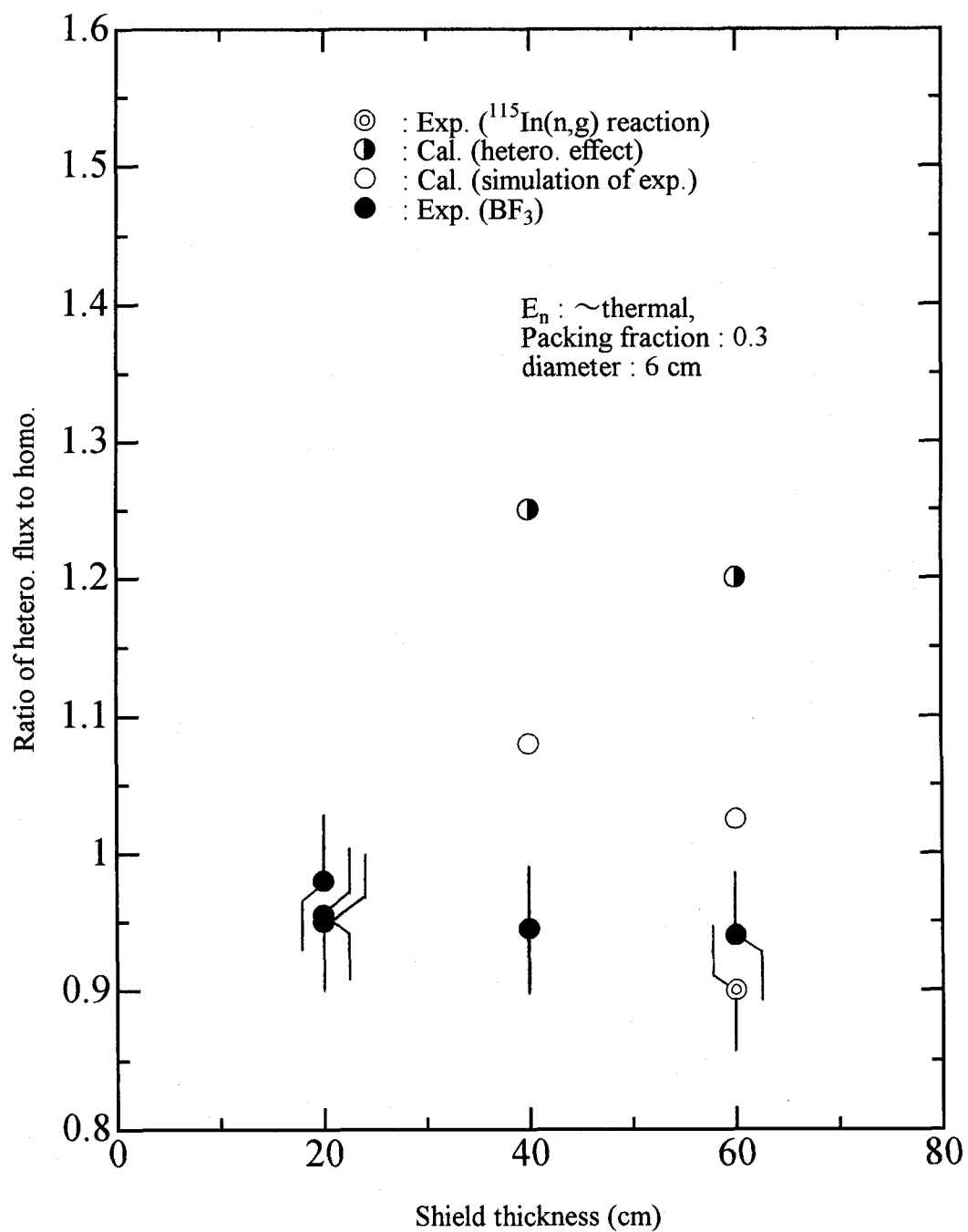


Fig. 4.23 Dependency of neutron flux ratio between heterogeneous and homogeneous samples as a function of shield thickness for thermal region.



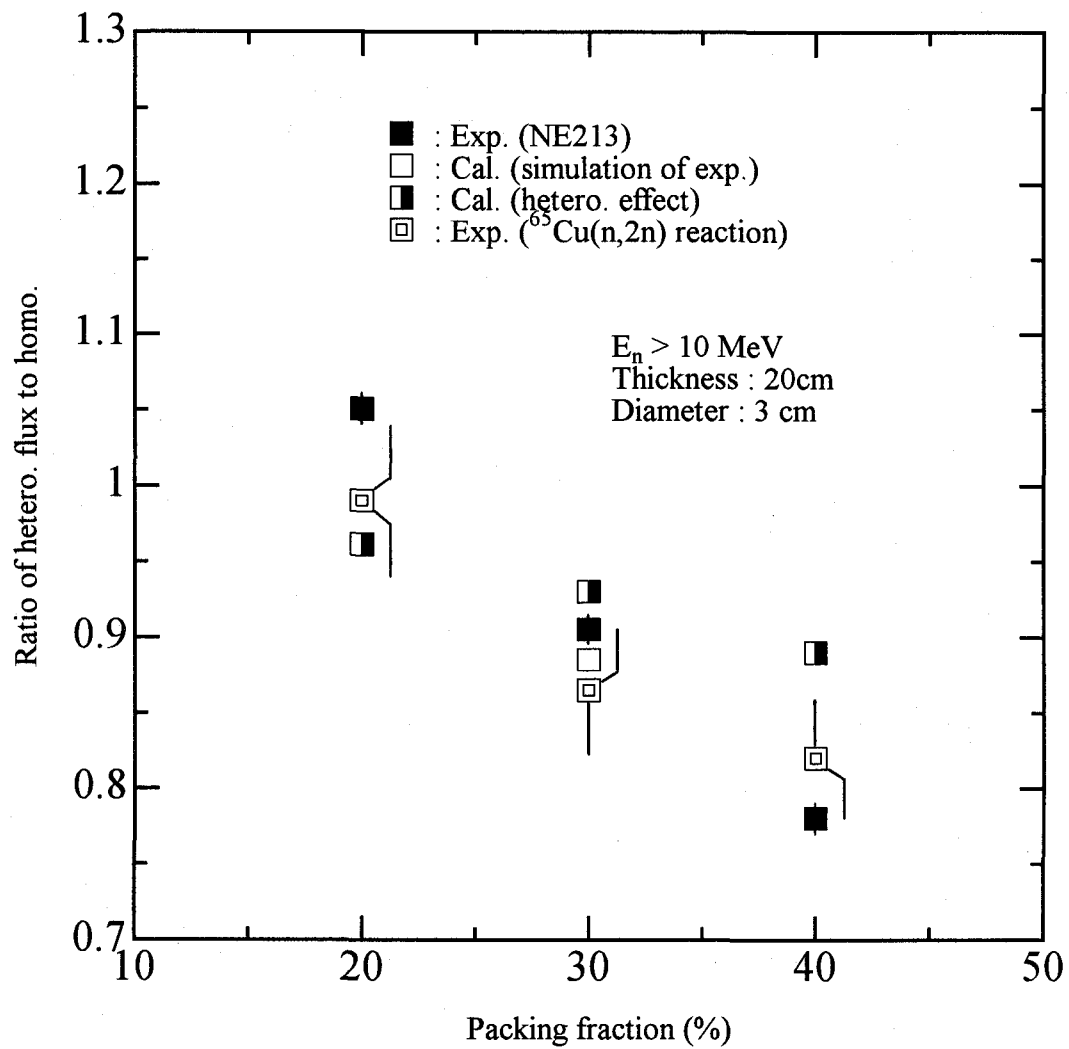


Fig. 4.24 Dependency of neutron flux ratio between heterogeneous and homogeneous samples as a function of packing fraction for 14 MeV region.

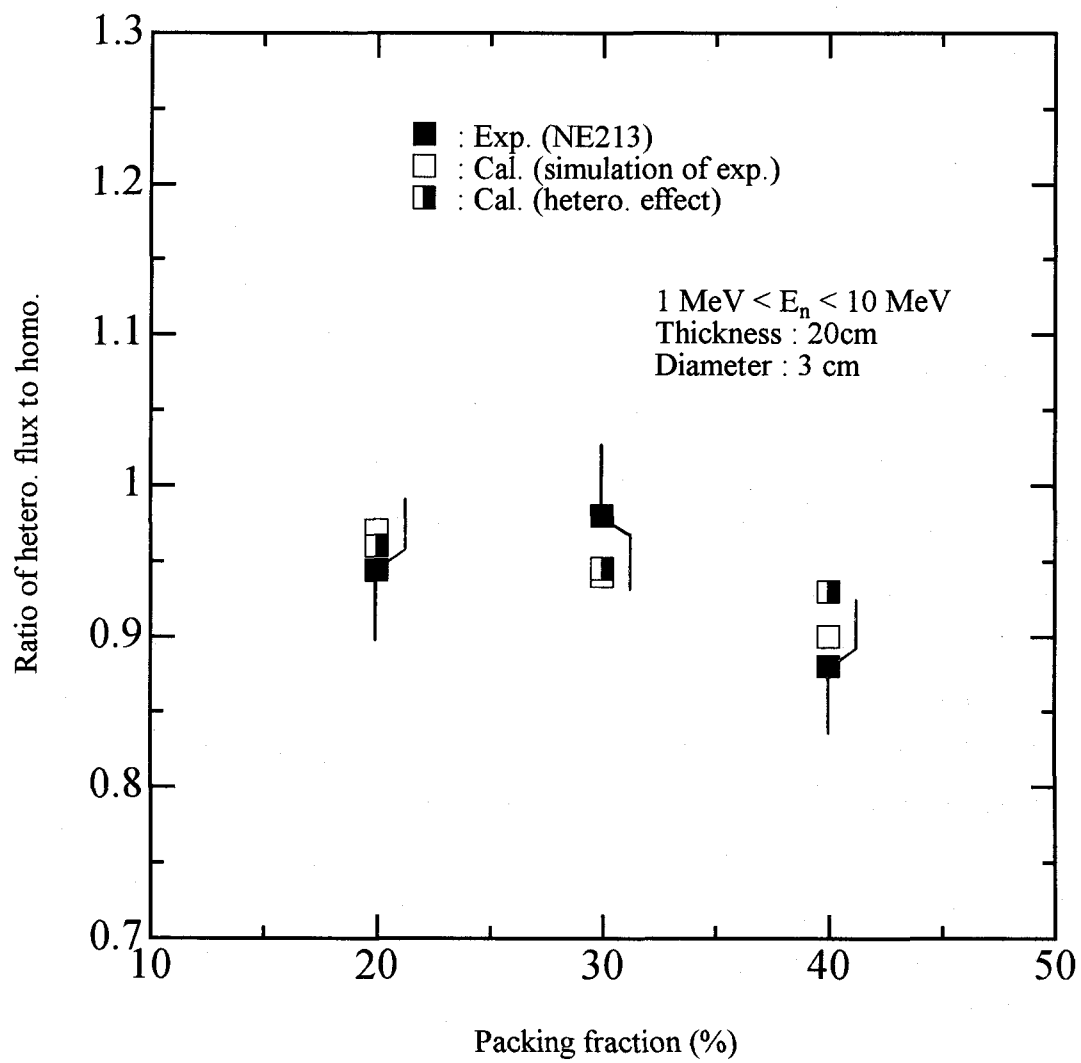


Fig. 4.25 Dependency of neutron flux ratio between heterogeneous and homogeneous samples as a function of packing fraction for MeV region.

activation foil agree fairly well with each other. The validity of the experiment itself is confirmed.

From the comparison of experimental and calculated heterogeneity effects, the following remarks are obtained:

- (1) Good agreement is obtained except thermal region.
- (2) In thermal region, the experimental result shows a little smaller than the calculation.

From the physical consideration, the disagreement is thought to be mainly due to the following reason: In case of using concrete sample, uncertainty in the determination of the composition is inevitable because of the escape of water by evaporation procedure. The small difference of the macroscopic cross section can generally give only a small effect for one scattering of a particle. The effect is amplified extremely by a large number of scatterings resulting in the large discrepancy of the final results.

Figure 4.26 shows the measured neutron spectrum ranging from 0.7 to 15 MeV obtained by the TOF method, compared with the calculation. The measured spectrum in Fig. 4.26 well reproduces the cross section structure of oxygen in Fig. 4.27<sup>(41)</sup>: A large resonance at 1 MeV makes a deep valley, while a deep dip around 2.5 MeV in the cross section curve makes a peak in the spectrum. On the other hand, as for iron contained in 30 vol-% in the sample, explicitly no significant structure due to the reaction cross section exists in the neutron spectrum, as it was reported that no conspicuous peaks in the leakage neutron spectrum from iron slab by DT neutrons are seen in MeV region<sup>(42)</sup>. Excellent agreement is found between the spectra obtained by the experiment and the calculation except a slight discrepancy in about 5-6 MeV. Because MCNP-CFP cannot deal with a point detector, the calculation for heterogeneous sample cannot be compared directly with the experiment in Fig. 4.26. Figure 4.28 describes the comparison of the calculated leakage neutron spectra from hetero- and homogeneous samples at the surface of them. Examining the shapes of the calculated spectra in Figs. 4.26 and 4.28, in higher energies above 0.8 MeV, the difference between the two samples is getting larger in Fig. 4.26 as is similarly seen in Fig. 4.28. Also it can be found that the spectra at the detector position (Fig. 4.26) are relatively larger around 4-10 MeV than that of the sample surface (Fig. 4.28), because forward scattered neutrons are dominant at the detector position compared with those of the sample surface. In the present study, the calculated heterogeneity effect is defined as the ratio made from the calculated spectra at the sample surface, not at the detector position. This may give unanticipated effect to the calculated ratio. Fortunately, this unanticipated effect is expected to be

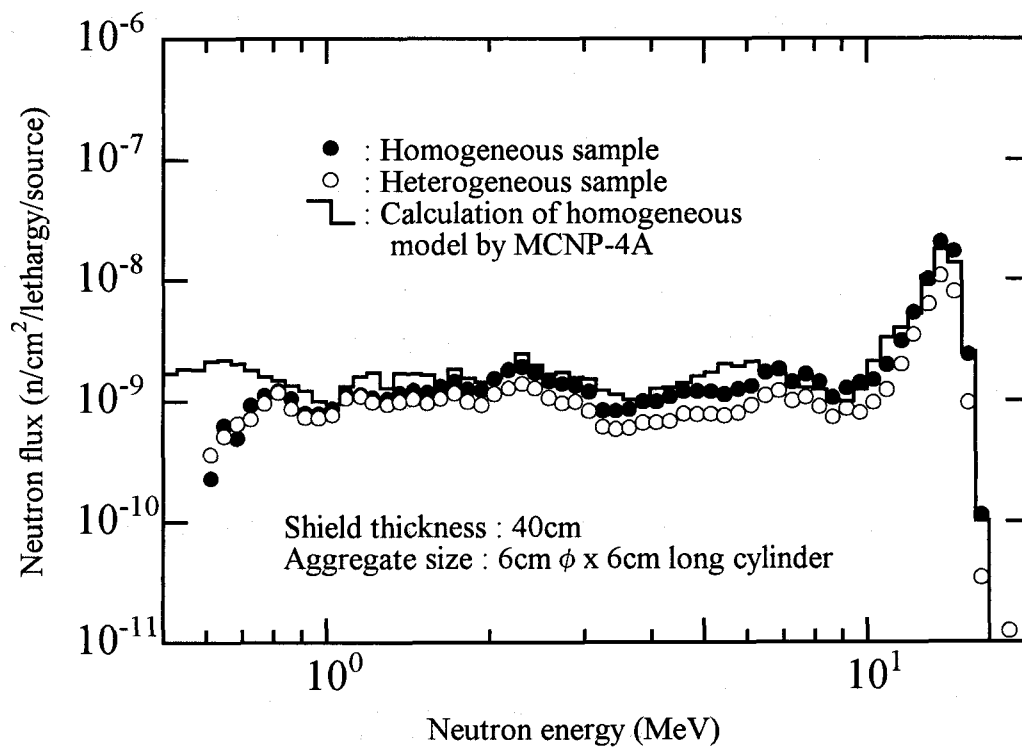


Fig. 4.26 Comparison of measured and calculated neutron spectra at the detector position.

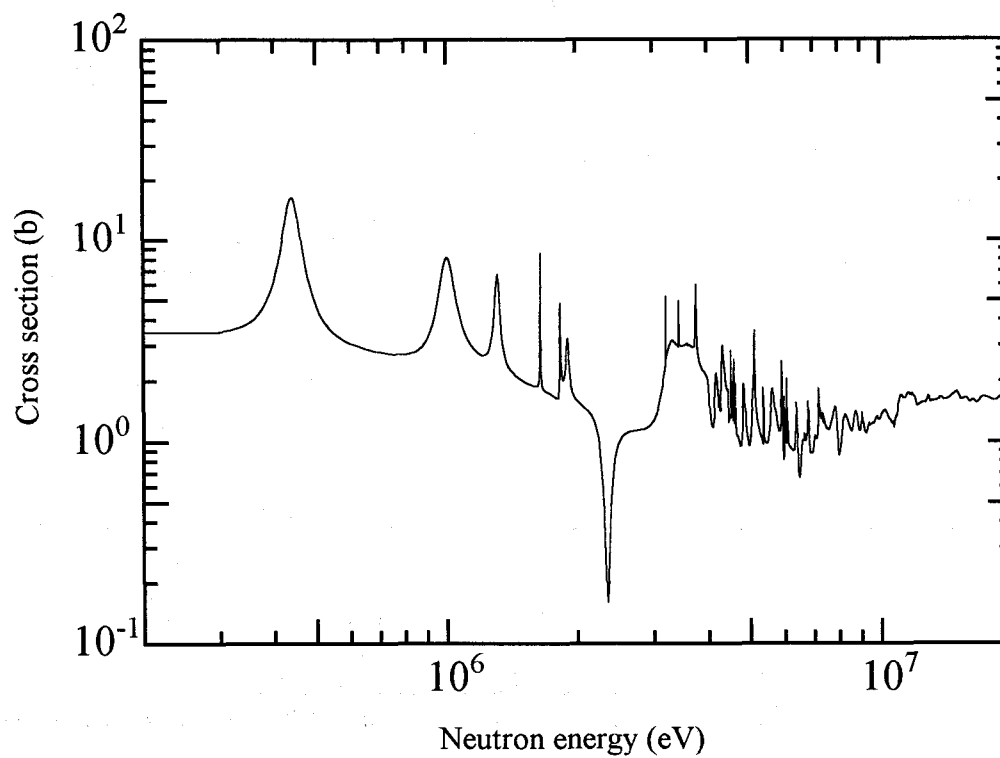


Fig. 4.27 Total reaction cross section of  $^{16}\text{O}$  in JENDL-3.2.

cancelled out because of using ratio of hetero- and homogeneous model calculation results. It is confirmed, as a result, that the heterogeneity effects estimated with the MCNP-CFP calculations can well reproduce the experimental results.

Consequently, though there is a slight disagreement in thermal region, MCNP-CFP can evaluate heterogeneity effect of heavy concrete having absorber aggregates, even if an environment has to be considered that neutrons strongly flow outward in the shield and therefore the spectrum continuously changes depending upon the neutron penetration length.

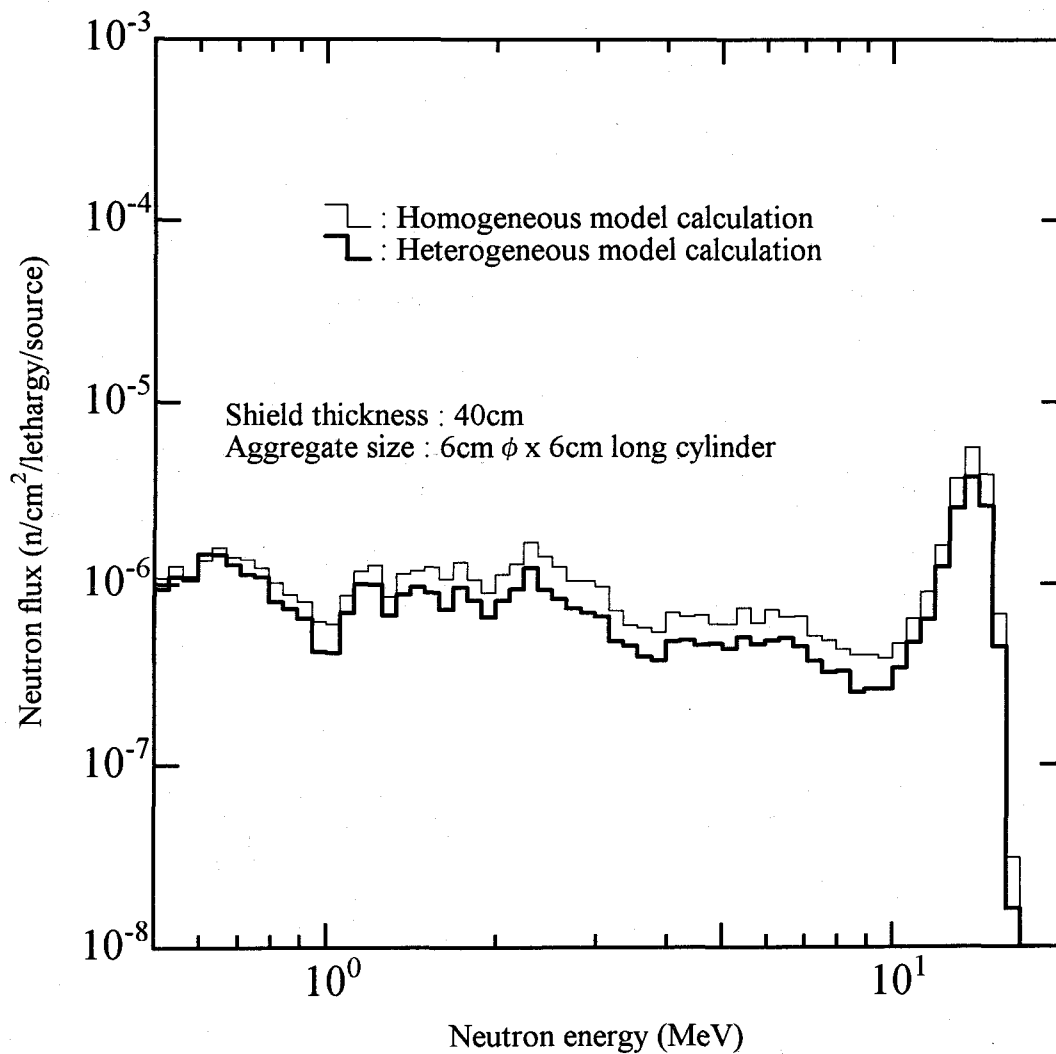


Fig. 4.28 Comparison of calculated neutron spectrum between heterogeneous and homogeneous models at the sample surface.

### IV.3.3.2 Heterogeneity effect of heavy concrete

The "real" heterogeneity effects, i.e., Ratio(2) introduced in Sec. IV.3.2, are described in Figs. 4.21-4.25. From the comparison with the experimental results shown in the previous section, though mostly agreed results can be found among the Ratio(1), (2) and the experimental result, some striking points are seen as follows: The "real" heterogeneity effect for the sample containing 6 cm  $\phi$  aggregates shows a little larger than the measured value. And in thermal region an opposite trend to the experiment is observed; the heterogeneity effect is beyond unity. This was expected before the experiment. It is presumed that these results are mainly caused by a slight difference in the composition and dimensions of the two samples used in one experiment. Practically, we think it is due to the fact that the difference, i.e., shortage, of the total weight and the iron aggregates weight of the homogeneous sample is not negligible.

Summarizing the obtained results so far, from the stand point of shielding performance, heterogeneous shield is of advantage in 14 MeV region, while in thermal region homogeneous shield is sufficient. In MeV region, the tendency similar to that of 14 MeV region can be seen, however, the effect is weak. If estimating the effect as dose equivalent, the heterogeneity effect can be eliminated because contributions of low and high energy neutrons are cancelled out. Above result is completely beyond our expectation that we had before the experiment: We thought that the effect for 14 MeV region would not be so strong, and therefore the ratio should show a little higher value than unity, because it was generally believed that the shielding performance with the homogeneous system was superior to the heterogeneous one. As a result of the discussion above, homogeneous shield is better from the stand point of shielding performance. However, both the experiment and the calculation have emphasized an opposite trend to our expectation except the fact that in thermal region the homogeneous system looked advantageous. The reason why in MeV and 14 MeV regions the heterogeneous shield is of great advantage is presented in the following.

For high energy neutrons such as DT neutrons, obviously iron has more excellent shielding potential than concrete shield. It means that homogeneous heavy concrete is superior to heterogeneous one when focusing on the attenuation of only the high energy source neutrons. As mentioned above, the present experiment has indicated an opposite phenomenon. The MCNP-CFP calculation, however, has supported the experimental result. The calculation model is illustrated in Fig. 4.29. In the model, interference with the boundary surface is prohibited to precisely

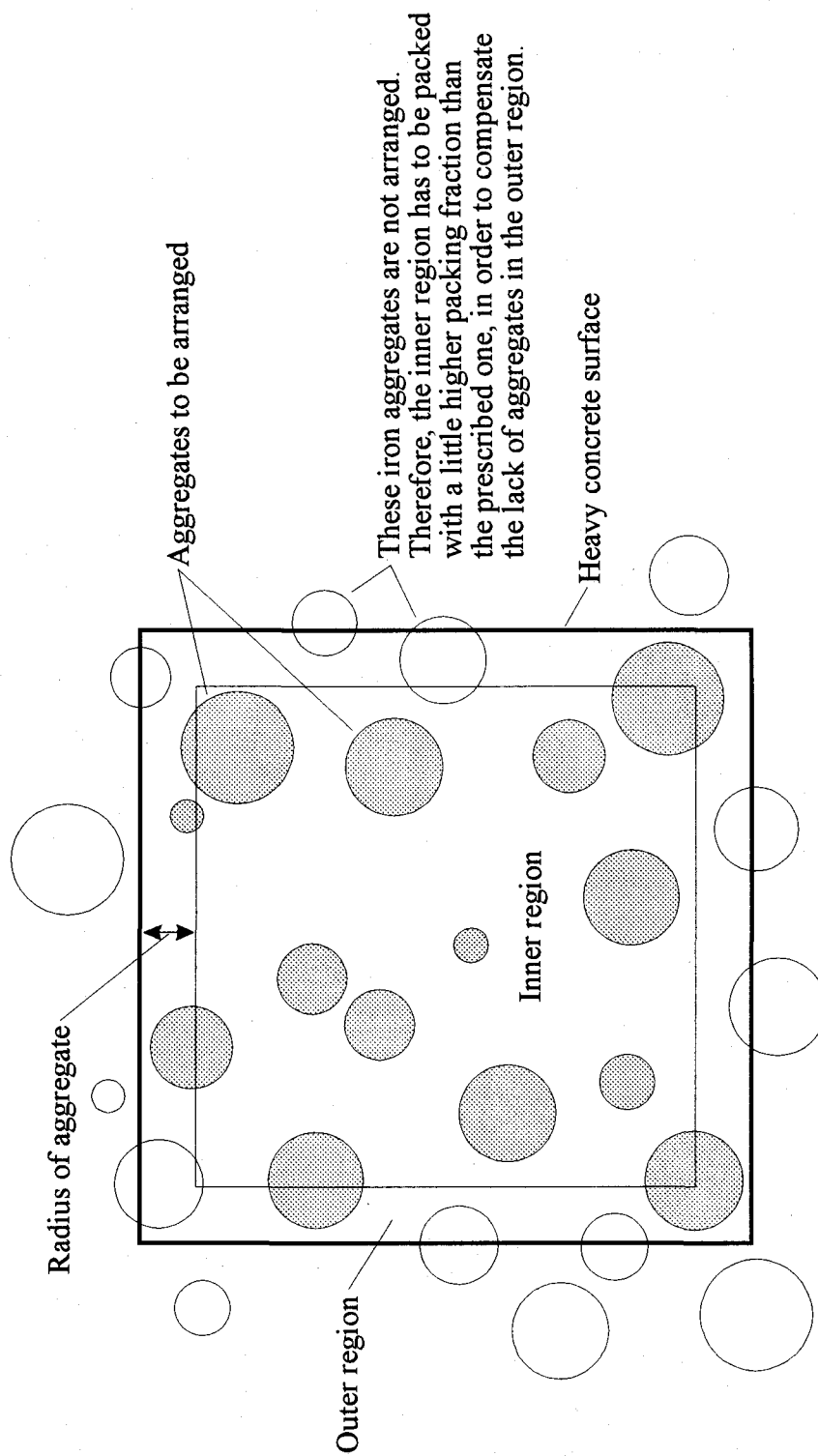


Fig.4.29 Cross sectional view of MCNP-CFP calculation model used for the analysis of heavy concrete.

simulate an actual structure. Consequently the packing fraction around the center of the model is obliged to be rather increasing. Seemingly this model can attenuate high energy neutrons effectively. In order to confirm the hypothesis, the following two analyses have been conducted as shown in Fig. 4.30. They are based on a model allowing interference (interference model) and the other prohibiting it (no-interference model). All iron aggregates contained in the heavy concretes have been modeled to avoid unknown effect of the statistical geometry model adopted in MCNP-CFP. Hence a conventional Monte Carlo code MCNP-4A was used. The most important calculation condition considered is preservation of the inventory of the aggregates. The calculation results are given in Table 4.12. The composition of the heavy concrete used for the present calculation is set to be almost the same as that of the heavy concrete used for the experiment. We can instantly see that the calculation result with the developed method clearly shows the same result as that of no-interference model, resulting in a conclusion that no-interference model should be preferred for understanding the result of the experiment. From the result, the present heavy concretes have a similar structure to the calculation model of MCNP-CFP, and high energy neutrons can be shielded more effectively. In fact, considering the manufacturing process of heavy concrete, it is thought that produced heavy concretes generally have such structure more or less. It means that MCNP-CFP can become a powerful tool to be applied to precise shielding analyses of such heavy concretes. Also it is found that appearance of this kind of heterogeneity effect which is apparently unexpected is rather adequate phenomenon. Consequently, it is understood that the heterogeneity effect we confirmed in the experimental results remarkably occurs with increase of the packing fraction of the aggregates and with increase of the size of the aggregate, in other words, with decrease of the shield dimensions, especially perpendicular to the neutron flow direction.

Figure 4.31 shows the calculated neutron spectra of the hetero- and homogeneous systems for the whole energy range from thermal to 14 MeV. As mentioned earlier, dose equivalent can be cancelled out by taking flux-to-dose conversion factor into consideration. There exists a boundary energy of about 1 MeV to separate interpretation of the heterogeneity effect. The heterogeneity effect below the boundary is a well known effect which is caused by a heterogeneous mixture of two materials having different reaction cross sections. And therefore it is generally easy to predict how much effectiveness it has. However, above the boundary the effect strongly depends on the dimensions of the shield and the aggregates in it. In design work, it is thus suggested to prepare heavy concrete shield so as to eliminate the latter effect. From the present study, for a point neutron source, the next equation has to be met to neglect the



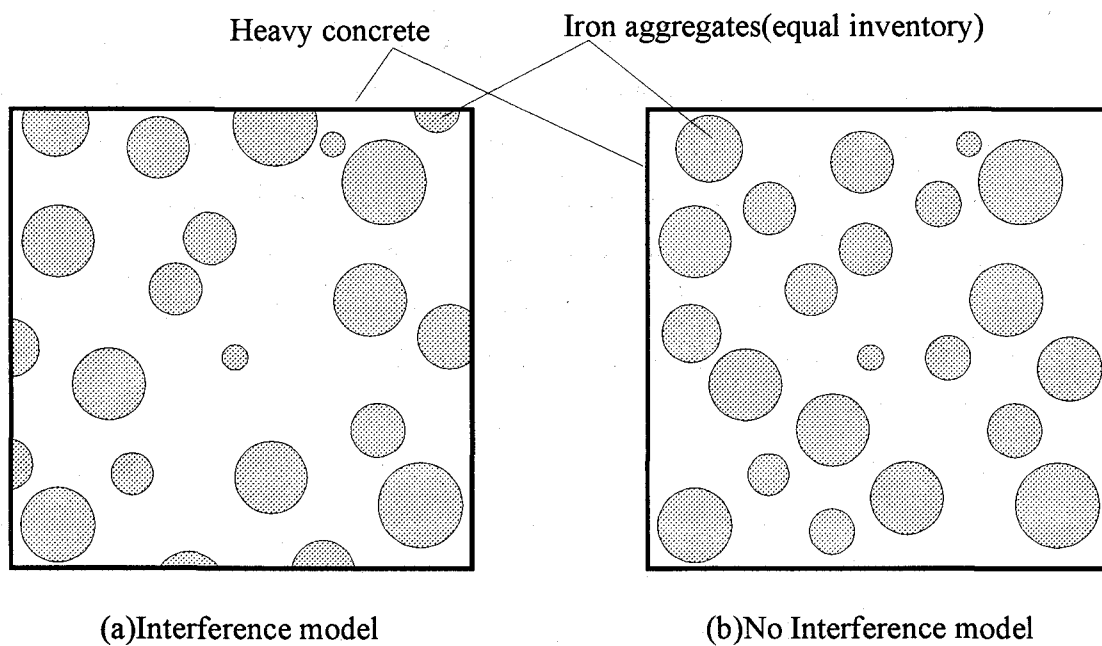


Fig.4.30 Cross sections of calculation models for MCNP-4A.

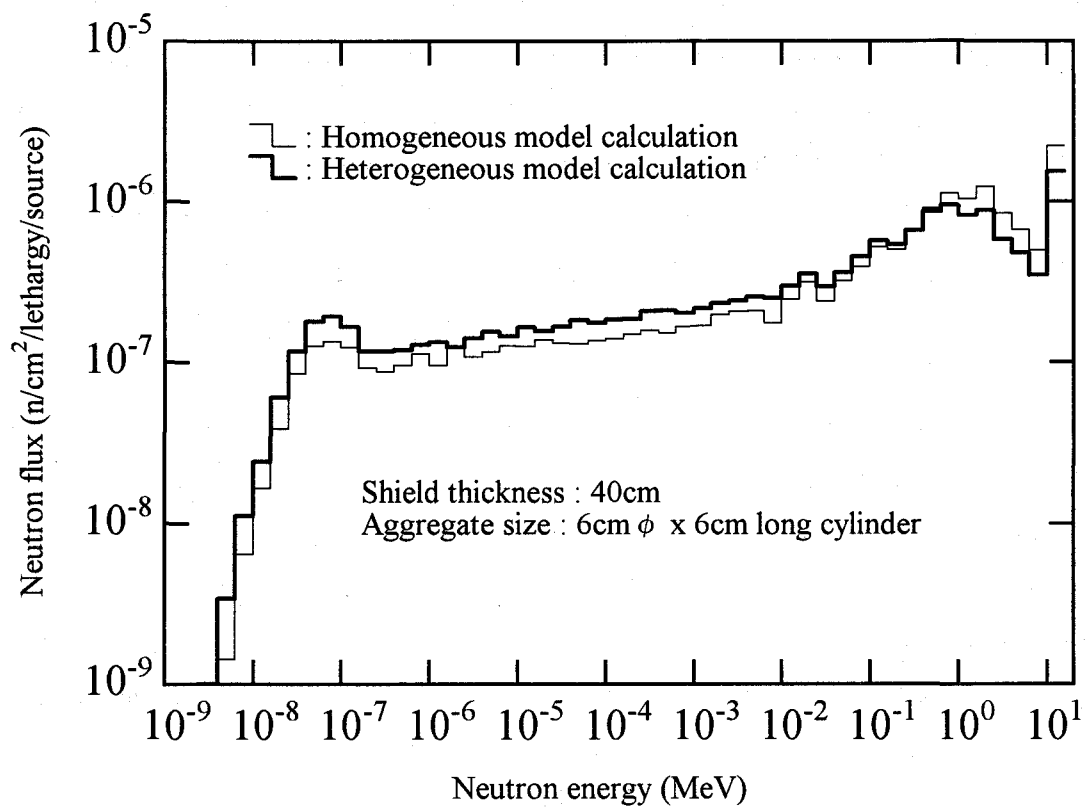


Fig. 4.31 Comparison of calculated neutron spectrum for the whole energy range.

heterogeneity effect above the boundary:

$$\frac{[\text{Shield thickness perpendicular to neutron flow direction}]}{[\text{Absorber aggregate diameter}]} \gg 10 \quad (4.4)$$

If this condition is not satisfied, use of MCNP-CFP for the analysis is recommended. In this case, shielding performance for the forward direction, i.e., neutron flow direction, becomes excellent for source neutrons. On the other side, leakage of neutrons from the side surface increases especially in case of single use. If many heavy concretes are used at the same time, interference in heterogeneity effect between adjacent shields may arise. In this case, a precise analysis by MCNP-CFP is required. In addition, this heavy concrete has the advantage of dose equivalent cancellation. This is convenient in a design work of neutron shield when using a conventional calculation method. If the condition is satisfied, the shielding performance of the heavy concrete deteriorates only below the boundary energy compared with the homogeneous shield. Therefore, it is allowed to analyze with a conventional calculation method except thermal region. Also cancellation of the shielding performance can not be expected. However, a heterogeneity effect, that neutrons are well shielded only for the forward direction, is suppressed.

Table 4.12 Calculation result of boundary interference effect.

Calculation model		Code	Neutron flux at the surface (n/cm <sup>2</sup> /source neutron)		
			E <sub>n</sub> >10MeV	1<E <sub>n</sub> <10MeV	E <sub>n</sub> =thermal
Homo.		MCNP-4A	8.9E-7	2.5E-6	5.6E-6
Hetero.	Interference model	MCNP-4A	9.7E-7	2.7E-6	5.7E-6
	No-interference model	MCNP-4A	6.8E-7	2.0E-6	6.3E-6
	Statistical geometry model	MCNP-CFP	6.7E-7	2.0E-6	6.1E-6

## IV.4 Summary

In this chapter, the applicability of the developed method was confirmed through the analyses of two criticality experiments and DT neutron transmission experiment with heavy concrete. The analyses of criticality experiments were done for those of VHTRC and PROTEUS corresponding to the applicabilities of MCNP-CFP and MCNP-BALL, respectively. The cross-checking of the results with other method can be done only for VHTRC, because the experimental results of PROTEUS supplied by PSI is still preliminary. For VHTRC, the comparison was done with the result calculated by the nuclear design code system for HTTR. As a result, they agreed fairly well with each other and the experimental result. Also, the reactivity effect of irregularly distributed CFPs was first evaluated exactly. The result was also in good agreement with other theoretical results, showing also for the first time that the other methods were sufficiently acceptable for practical use, since our method is based on a strict and rigorous calculation method with the continuous energy Monte Carlo process. Consequently, it can be concluded that the simulation with the developed method can exactly reproduce the experimental result in HTGR.

As for the heavy concrete irradiation experiment using DT neutrons, although the VHTRC experiment means the confirmation of the applicability of the method in an isotropic neutron field, the present experiment enable us to examine the validity of neutron transport estimation of heavy concrete in a field that neutrons strongly flow outward in it and the spectrum continuously changed depending on the neutron penetration length. From the result, a little discrepancy was seen in thermal region, however, in higher energy region the heterogeneity effect was well reproduced by MCNP-CFP calculation. Also, it was found that the heterogeneity effect itself is unexpectedly large, the shielding performance of heterogeneous shield is greater than the homogeneous one especially in higher energy region, and the effect strongly depends on the dimensions of the shielding sample. These results are important and quite valuable for shielding design works of well rationalized fusion reactor as well as high energy radiation / particle-accelerator facilities in the future.

The above experiments and analyses indicate that an accurate transport simulation, i.e., reference solution, can be realized by, not a conventional approximate method, but the Monte Carlo method for a practical application adopting irregular arrangement of base geometries.

## REFERENCES

- (1) I. Murata, T. Mori and M. Nakagawa, *Nucl. Sci. Eng.*, **123**, 96 (1996).
- (2) I. Murata, T. Mori, M. Nakagawa and H. Itakura, "Continuous Energy Monte Carlo Calculations of Randomly Distributed Spherical Fuels Based on Statistical Geometry Model," *JAERI-Research 96-015*, Japan Atomic Energy Research Institute (1996).
- (3) I. Murata and A. Takahashi, "Analysis of Critical Assembly Experiments by Continuous Energy Monte Carlo Method with Statistical Geometry Model," *Technol. Repts. Osaka Univ.*, **48**, 19 (1998).
- (4) I. Murata, S. Yoshida and A. Takahashi, "Effect of Heterogeneity for Heavy Concrete on Shielding of Fusion Neutrons," *Fusion Technology* (1999). in press.
- (5) H. Yasuda, et al., "Construction of VHTRC (Very High Temperature Reactor Critical Assembly)," *JAERI-1305*, Japan Atomic Energy Research Institute (1986).
- (6) R. Brogli, et al., *Energy, Oxford* **16**, 507 (1991).
- (7) F.C.Difilippo, "Applications of Monte Carlo Methods for the Analysis of MHTGR Case of the VHTRC Benchmark," *ORNL/TM-12698*, Oak Ridge National Laboratory (1994).
- (8) N. Nojiri et al., "Evaluation of Accuracy of Monte Carlo Code MVP with VHTRC Experiments - Multiplication Factor at Criticality, Burnable Poison Worth and Void Worth-," *JAERI-Tech 97-060*, Japan Atomic Energy Research Institute (1997).
- (9) K. Yamashita et al., "Accuracy Investigation of Nuclear Design Method for High Temperature Engineering Test Reactor (HTTR) Based on VHTRC Experimental Data," *JAERI-M 88-245*, Japan Atomic Energy Research Institute (1988).
- (10) F.Akino et al., "Critical Experiment on Initial Loading Core of Very High Temperature Reactor Critical Assembly (VHTRC)," *J. Atomic Energy Soc. Japan*, **31**, 682 (1989).
- (11) K. Fukuda et al., "Irradiation Experiments of 3rd, 4th and 5th Fuel Assemblies by an In-Pile Gas Loop, OGL-1," *JAERI-M 86-092*, Japan Atomic Energy Research Institute (1986).
- (12) S.Matsunaga, et al., "Construction and Performance Test of OGL-1," *J. Atomic Energy Soc. Japan*, **21**, 245 (1979).
- (13) K.Fukuda et al., "Research and Development of HTGR Fuels," *JAERI-M 89-007*, Japan Atomic Energy Research Institute (1989).
- (14) D. Garber et al., "ENDF-102 Data Formats and Procedures for the Evaluated Nuclear Data File, ENDF," *BNL-NCS-50496* (1975).

- (15) K. Shibata et al., "Japanese Evaluated Nuclear Data Library, Version-3 - JENDL-3," *JAERI-1319*, Japan Atomic Energy Research Institute (1990).
- (16) T. Nakagawa et al., "Japanese Evaluated Nuclear Data Library Version 3 Revision-2: JENDL-3.2," *J. Nucl. Sci. Technol.*, **32**, 1259 (1995).
- (17) K. Yamashita et al., "Nuclear Design of a High-Temperature Engineering Test Reactor (HTTR)," *Nucl. Sci. Eng.*, **122**, 212 (1996).
- (18) H. Harada and K. Yamashita, "The Reactor Core Analysis Code CITATION-1000VP for High Temperature Engineering Test Reactor," *JAERI-M 89-135*, Japan Atomic Energy Research Institute (1989).
- (19) S. Saito, et al., "Design of High Temperature Engineering Test Reactor," *JAERI-1332*, Japan Atomic Energy Research Institute (1994).
- (20) K. Tsuchihashi et al., *J. Nucl. Sci. Technol.*, **22**, 16 (1985).
- (21) F. Akino, Japan Atomic Energy Research Institute, private communication (1994).
- (22) K. Tsuchihashi, et al., "Revised SRAC code system," *JAERI-1302*, Japan Atomic Energy Research Institute (1986).
- (23) T. Williams, Paul Scherrer Institute, private communication (1995).
- (24) T. Yamane and H. Yasuda, Japan Atomic Energy Research Institute, private communication (1995).
- (25) I. I. Bashter, "Neutron Relaxation Lengths in Light and Heavy Concrete Shields," *Nucl. Engineer*, **34**, 142 (1993).
- (26) A. S. Makarios et al., "On the Utilization of Heavy Concrete for Radiation Shielding," *Ann. Nucl. Energy*, **23**, 195 (1996).
- (27) K. Shin et al., "Measurement of Fission Neutron Spectra Transmitted through Iron, Heavy Concrete, Polyethylene and Graphite Slabs," *Mem. Fac. Eng. Kyoto Univ.*, **43**, 331 (1981).
- (28) B. S. Seshadri and R. Venkatesan, "Transmission Characteristics of  $^{252}\text{Cf}$  Neutrons Passing through Rare Earth and Boron Loaded Concrete Slab Shields," *Nucl. Eng. Des.*, **117**, 325 (1989).
- (29) A. S. Mollah et al., "Measurements of Neutron Shielding Properties of Heavy Concretes Using a Cf-252 Source," *Nucl. Eng. Des.*, **135**, 321 (1992).
- (30) B. S. Seshadri et al., "Spectra of D-T Neutrons Transmitted through Rare Earth Mixed Concretes," *Nucl. Eng. Des.*, **97**, 223 (1986).
- (31) B. S. Seshadri, "Transmission Measurements of D-T Neutrons through Gadolinium Loaded

- Concrete and Polypropylene," *J. Nucl. Sci. Technol.*, **26**, 881 (1989).
- (32) N. Nakanishi et al., "Calculated Shielding Characteristics of Eight Materials for Neutrons and Secondary Photons Produced by Monoenergetic Source Neutrons with Energies Less Than 400 MeV," *Nucl. Technol.*, **112**, 132 (1995).
- (33) K. Oishi et al., "Experiment and Analysis of Neutron Spectra in a Concrete Assembly Bombarded by 14-MeV Neutrons," *Nucl. Sci. Eng.*, **103**, 46 (1989).
- (34) J. Yamamoto et al., "Measurement and Analysis of Leakage Neutron Spectra from SS-316, Concrete, Water and Polyethylene Slabs with D-T Neutron Source," *Proc. 6th. Int. Conf. Radiation Shielding*, Tokyo, 464 (1983).
- (35) "MCNP-A General Monte Carlo N-Particle Transport Code, Version 4A," *LA-12625-M*, J. F. Briesmeister (Ed.), Los Alamos National Laboratory (1993).
- (36) T. Rockwell III (Ed.), "Reactor Shielding Design Manual," D. Van Nostrand Company, Inc. (1956).
- (37) A. Takahashi et al., "Measurement of Double Differential Neutron Emission Cross Sections for Incident Neutrons of 14 MeV," *J. Nucl. Sci. Technol.*, **25**, 215 (1988).
- (38) A. Takahashi et al., "Measurements of Double Differential Neutron Emission Cross Sections for Fusion Reactor Candidate Elements," *J. Nucl. Sci. Technol.*, **21**, 577 (1984).
- (39) J. K. Dickens, "SCINFUL: A Monte Carlo Based Computer Program to Determine a Scintillator Full Energy Response to Neutron Detection for En Between 0.1 and 80 MeV: User's Manual and Fortran Program Listing," *ORNL-6462*, Oak Ridge National Laboratory (1988).
- (40) K. Sumita et al., "Osaka University 14 MeV Intense Neutron Source and Its Utilization for Fusion Studies," *Proc. 12th Symp. Fusion Technology*, Julich, **1**, 681 (1982).
- (41) T. Nakagawa et al., "Japanese Evaluated Nuclear Data Library Version 3 Revision-2: JENDL-3.2," *J. Nucl. Sci. Technol.*, **32**, 1259 (1995).
- (42) Y. Oyama et al., "Measurement and Calculations of Angular Neutron Flux Spectra from Iron Slabs Bombarded with 14.8-MeV Neutrons," *Nucl. Sci. Eng.*, **115**, 24 (1993).

## V. CONCLUSIONS

### V.1 Summary of the study

The present study has started when the design activity of HTTR was in progress at JAERI. At that time we could analyze a particle transport phenomenon in an HTGR core approximately. However, achievement of a more rational design became one of the most important purposes of the design activity in HTTR. We had to realize a calculation of the most probable solution for the particle transport, though actually it was very hard for us as well as design staffs of LWRs. The prescribed goal was to establish a calculation method to simulate a real system as precisely as possible to obtain an exact result, i.e., reference solution. The research and development for that purpose was conducted for three years with the special budget for basic research in JAERI. After the R&D program, the developed method was finally completed by the analyses of VHTRC experiments for confirmation of the applicability to a real reactor core. Using this method, the shielding analysis of HTTR was carried out to obtain the reference dose equivalent on the operating floor of HTTR. However, it was not used to evaluate the nuclear characteristics. The evaluation was done by the specifically developed nuclear design code system for HTTR with some conventional methods such as a lattice burnup code with a collision probability method and a diffusion code. Nevertheless, in HTTR, which is going to become its criticality soon, considering the analysis of VHTRC experiments and HTTR's start-up physics tests by the Monte Carlo code MVP with the correction of the reactivity for the effect of spherical fuel elements, CFPs, it is generally thought that the cross-checking of the nuclear design code system had to be done with the reference solution at the design phase. The details about the matter are presented in the next section.

The originality of the present method is not only to realize a precise treatment of the HTGR fuel elements in which a lot of CFPs exist, but also to establish a basic method of calculating a system having irregularly distributed geometries by the Monte Carlo method. The irregular arrangement system possesses many advantages if the base geometry is spherical. The present method is thus expected to be applied to the transport analysis of systems, such as fusion blankets, minor actinide incineration reactors, and so on, for obtaining the reference solution in the future.

The summary of the present study is given in the following by dividing the content into

three subdivisions, i.e., theory and development, validation and applicability.

- Theory of the method and development of the code

To simulate particle transport in irregularly distributed geometries by the Monte Carlo method, sampling of a base geometry itself was preferred as the solution. A base geometry is arranged at a certain forward place being distant from the current particle position. The base geometry arranged is fixed until the next sampling event due to particle scattering, fission and so on, occurs. The sampling of a base geometry is done by the following two steps: (1) Sample a location of an incident particle entering into a base geometry using the NNDs. (2) Sample an incident angle of the particle entering into the base geometry from cosine distribution. The coordinates of a base geometry to be arranged are determined by the two samplings. The NNDs consist of three distributions corresponding to different sampling places of (a) on the surface of base geometry, (b) in the matrix between base geometries, and (c) on the surface of the container in which base geometries exist. The NNDs were made by the ray-trace method for the packing state of base geometries prepared by the three dimensional hard sphere packing simulation code MCRDF developed newly in this study. By this method, in principle any geometry can be dealt with as a base geometry. However, actually a sphere was assumed throughout the present study, because sphere has various advantages compared with others and in most applications spherical element is employed. The method was implemented in the general-purpose Monte Carlo code MCNP to develop two revised codes MCNP-CFP and MCNP-BALL. In MCNP-CFP, to reproduce the packing state precisely, the interfered spherical fuel element was prohibited to be arranged. As a result, the available packing fraction was limited to be relatively low. On the other hand, In MCNP-BALL, to simulate a higher-packing-fraction state, the interference had to be allowed. Consequently, MCNP-BALL can analyze a packing state in up to a physically achievable packing fraction of  $f_{RCP}$ . In order to precisely reproduce the packing with any packing fraction, the above-mentioned separation of applicable packing fractions into two codes is unavoidable and it is a universal countermeasure in the problem of treatment of irregularly distributed geometries by the Monte Carlo method. Their main functions are summarized in Table 2.5.

- Validation of the method

The validation of the method was performed by several means at each developing phase as shown in Table 5.1. For MCRDF, since the configuration of atoms in noncrystalline alloy



Table 5.1 Validations of the method performed at each developing phase.

Object validated	Validation method
MCRDF	<ul style="list-style-type: none"> <li>• Comparison of RDF calculated by MCRDF with the experimental result made from X-ray diffraction of Ni-P alloy.</li> </ul>
MCNP-CFP, MCNP-BALL	<ul style="list-style-type: none"> <li>• Inventory checking of base geometries arranged in the container. (Track length estimator is utilized for obtaining a reference result.)</li> <li>• Comparison of criticality calculated for ordered packed geometries. (Presice modeling is done with reflective boundary conditions to obtain a reference result.)</li> </ul>
Applicability confirmation	
MCNP-CFP	<ul style="list-style-type: none"> <li>• Analysis of VHTRC criticality experiments.</li> <li>• Measurement of the heterogeneity effect of heavy concrete induced by DT neutrons and its analysis</li> </ul>
MCNP-BALL	<ul style="list-style-type: none"> <li>• Analysis of PROTEUS criticality experiments.</li> </ul>

resembles an irregular packing of hard spheres, the RDF made from the X-ray diffraction pattern of noncrystalline electrodeposited Ni-P alloys was compared with the calculation by MCRDF. The cross-checking of them with other calculated results was also done. The comparison results showed fairly good agreement with each other. Also MCNP-CFP and MCNP-BALL were validated through the two comparisons of the results obtained by the developed method with the theoretical values or reference calculations: (1) Calculations of inventory of base geometries in the container, and (2) Criticality calculations for ordered packed geometries. The former was indebted to the fact that the simple but more efficient method to estimate the volume occupied by the base geometries arranged was found, namely the direct evaluation method as well as the track length estimator in the Monte Carlo code. And the latter was indebted to the following reasons: An ordered close packing could provide the exact positions of all spheres. We therefore treated these systems precisely by modeling all spherical elements with reflective boundary conditions using a conventional Monte Carlo code. These comparison results led to excellently good agreements between the developed method and the reference calculation method, showing that the validity of the present method was firmly confirmed.

- Applicability of the method

The applicability of the developed codes was confirmed through the analyses of two criticality experiments and DT neutron irradiation experiment with heavy concrete. The former was done with the criticality experiments at VHTRC and PROTEUS which correspond to the applicability confirmation of MCNP-CFP and MCNP-BALL, respectively. The cross-checking of the results with those of the diffusion method was done for VHTRC. As a result, the calculated results agreed fairly well with each other and the experimental result. Also, the reactivity effect of irregularly distributed CFPs was first evaluated exactly. The result was also in good agreement with other theoretical results, showing also for the first time that the other methods were sufficiently acceptable for practical use, because our method is based on a strict and rigorous calculation procedure. Consequently, it can be concluded that the simulation with the developed method can exactly reproduce the experimental result in HTGR. Next the heavy concrete irradiation experiment using DT neutrons and its analysis were conducted. The experiment enables us to examine the validity of neutron transport estimation of heavy concrete in a field that neutrons strongly flow outward in it and the spectrum continuously changes depending on the neutron penetration length. From the result, a little discrepancy was seen in thermal region, however, in

higher energy region the heterogeneity effect was well reproduced by the presently developed MCNP-CFP. Also, it was found that the heterogeneity effect itself is unexpectedly large, the shielding performance of heterogeneous shield is greater than the homogeneous one especially in higher energy region, and the effect strongly depends on the dimensions of the shielding sample. These results are important and quite valuable for shielding design works of well rationalized fusion reactors as well as high energy radiation / particle-accelerator facilities in the future.

Finally, the reports published are summarized as follows: The basic theory of the method is given in Refs. (1)-(4), details about MCRDF Ref. (2), MCNP-CFP Refs. (1) and (4), MCNP-BALL Ref. (2), analysis results of VHTRC experiments Refs. (1),(4) and (5), those of PROTEUS Ref. (5), heavy concrete irradiation experiments and analyses Ref. (6), and abstract of the present study Ref. (7), respectively.

## **V.2 Proposal of the future work**

As described in the present thesis, the developed method is superior to other conventional methods in respect of precise treatment of irregularly distributed geometries. However, it was pointed out from the analysis results of the VHTRC experiments that the results obtained by the present method agreed with the experimental ones as accurately as those of the nuclear design code system for HTTR including DELIGHT (collision probability method) and CITATION-1000VP (vectorized diffusion code). The issue is which method is of advantage? or can the present method be really of advantage? The result of VHTRC analysis cannot give a sufficient conclusion, however, of course it is quite clear that the present method can supply the most probable answer in any calculation methods, because the development has been progressed aiming at the reference solution, and it has been completed through the validation activity described in Chap. III. The only thing we can conclude so far is that the recent MVP analyses for VHTRC experiments and HTTR start-up tests indicate that the more the core configuration becomes complicated the less the agreement between the nuclear design code system and the experiment or the reference solution by MVP is sufficient: Practically, the VHTRC experimental results can be pretty well reproduced through the Monte Carlo analysis with MVP by adding the reactivity effect of CFPs evaluated by other method (SRAC code system). An example of the result is shown in Tables 1.1 and 1.2. Also, it is found from the preliminary analyses for HTTR's

start-up physics tests using the nuclear design code system for HTTR and the reference Monte Carlo code MVP that various corrections such as calculation mesh effect, radiation streaming and so on cannot be avoided to obtain acceptable results by using the nuclear design code system for the start-up tests. The comparison result of burnable poison reactivity used in HTTR is shown in Tables 1.3 and 1.4. From the results, the agreement between the present method and the conventional method is presumed to be caused by the reason that the core is quite simple or not large. We have to make clear the final conclusion in the future by much effort of analyses for the new experimental results with our and other methods, if the experimental data at HTTR and PROTEUS will be open to us.

There are two problems to be investigated from the standpoint of accurate reproduction of a real packing of base geometries. One is packing simulation near the boundary of the container. The developed method warrants the inventory reproduction of base geometries in the container. Also, in the Low packing fraction mode, an ideal packing excluding interfered base geometries with the boundary is realized. However, in a real system there may be a local region near the boundary in which base geometries are not packed irregularly. We should find out the local effect on the final calculation result. Fortunately, the effect tends to decrease with increasing of the ratio between the dimensions of base geometry and that of the container. The ratio is around 10 or more for many applications. And the agreement of the analysis and measurement for the VHTRC criticality experiment (the ratio is  $\sim 10$ ) is excellent. Hence, the effect is expected to be negligibly small, however, it depends on the ratio. It should be concluded that it is necessary to evaluate the effect accurately in the future. The other problem is "Is packing of interest in the present study random or irregular". The term used in this thesis is "irregular", because strictly speaking packings in usual applications are not random, but irregular. On the other hand, the packing made by MCRDF can be regarded to be random taking into account the packing algorithm. We should examine how much influence the discrepancy between them gives. It is expected that a fuel compact containing a lot of CFPs is a typical example, the packing of which is the farthest from the random state, because in other applications base geometries are just poured into the container. Even in the fuel compact, the packing of CFPs is done almost randomly considering the cross section photograph and the comparison of 2-dimensional RDF. In fact, confirming the randomness of CFPs in the cross section photograph, it was decided that the fuel compact could be adopted for a practical use in HTGRs. Consequently, all the packings in practical applications show irregular state, but actually almost equal to random one. The influence

is, as a result, fairly less than the preceding effect for the packing simulation near the boundary of the container. However, the qualitative discussion should be done for the completion of the developed method in the future.

The issue with respect to the developed codes to open to users is as follows: The newly developed MCNP-CFP and MCNP-BALL codes were based on the general Monte Carlo code MCNP. We are obliged to spend much time in a case that a complicated or large geometry is analyzed by MCNP. In JAERI, it is therefore planning to implement the present method in MVP. MVP is a general purpose vectorized continuous energy Monte Carlo code which was developed in JAERI. The computation speed is therefore much faster than MCNP. The revised MVP including the present method will be used as a core monitor code at HTTR in the future. In addition, some companies indicate their intention of use of MCNP-CFP or MCNP-BALL for HTGR research and development. We have to complete the final version for such users in the near future.

Another problem for the future is expansion of the function for MCNP-CFP and MCNP-BALL. Some new plans not only for criticality calculation of reactors but also for other particle transport problem such as transmission of neutrons through heavy concrete are proposed as follows: One is development of point detector. In a transport calculation with MCNP-CFP or MCNP-BALL, just one base geometry is arranged at each sampling timing in the container cell in which actually a lot of base geometries exist irregularly. Therefore, a general point detector implemented in MCNP cannot work correctly. However, since as described in Sec. II.4.1.3, the ratio of the cross section area of base geometries appearing in any cross section surface of a container including a lot of base geometries distributed irregularly is exactly the same as packing fraction. Similar to this fact, when a ray-trace transmits the container, the ratio of transmitting length in base geometries is clearly the packing fraction. Taking into account this fact as a correction in the contribution calculation of the point detector, the new point detector is realized in MCNP-CFP and MCNP-BALL. The second plan is development of variance reduction in a system including irregularly distributed geometries. The issue is how to efficiently sample a base geometry in a system having base geometries packed in a very low packing fraction. For example, in a pebble bed reactor, generally the packing fraction of CFPs in a fuel pebble is very low, e.g.,  $\sim 6\%$  in PROTEUS, consequently requiring a long computation time to obtain a result with an acceptable good accuracy. If it becomes possible to increase the arranged base geometries by weight adjustment of the particle, the best way is to modify the packing fraction around 50 %.

However, It is easily recognized that it is very difficult to reproduce a real system by such adjustment. Or as a simpler method, we have to investigate the feasibility of conventional variance reduction techniques by weight window (WW), importance sampling and so on. The third one is burnup estimation especially for a pebble bed reactor. The burnup calculation by the Monte Carlo method was basically established. However, during the operation of a pebble bed reactor, because fuel pebbles continuously flow, the burnup cannot be known by calculation. A new sampling method to simulate the flow of each base geometry is required. In other words, we have to simulate the flow path of them considering the conflict force between base geometries. Of course, the sampling of base geometry flow using the result of mock-up experiment of base geometry flow is not so difficult.

It is thought that these are the minimum requirements necessary for practical design works. Further investigation of the developed codes is of importance not only for development of future HTGRs but also for obtaining the reference solution for more rational nuclear facilities in the future. Utilization of sampling of geometries is a unique idea and the developed sampling process is a universal method for the Monte Carlo application. This is the reason why the present study is important, valuable and interesting. We think that we need to and have to continue this promising research strongly for the future.

## REFERENCES

- (1) I. Murata, T. Mori and M. Nakagawa, *Nucl. Sci. Eng.*, **123**, 96 (1996).
- (2) I. Murata, A. Takahashi, T. Mori and M. Nakagawa, *J. Nucl. Sci. Technol.*, **34**, 734 (1997).
- (3) I. Murata, T. Mori, M. Nakagawa and H. Shirai, "Packing Simulation Code to Calculate Distribution Function of Hard Spheres by Monte Carlo Method : MCRDF," *JAERI-Data/Code 96-016*, Japan Atomic Energy Research Institute (1996).
- (4) I. Murata, T. Mori, M. Nakagawa and H. Itakura, "Continuous Energy Monte Carlo Calculations of Randomly Distributed Spherical Fuels Based on Statistical Geometry Model," *JAERI-Research 96-015*, Japan Atomic Energy Research Institute (1996).
- (5) I. Murata and A. Takahashi, "Analysis of Critical Assembly Experiments by Continuous Energy Monte Carlo Method with Statistical Geometry Model," *Technol. Repts. Osaka Univ.*, **48**, 19 (1998).
- (6) I. Murata, S. Yoshida and A. Takahashi, "Effect of Heterogeneity for Heavy Concrete on Shielding of Fusion Neutrons," *Fusion Technology* (1999). in press.
- (7) I. Murata, T. Mori and M. Nakagawa, "Continuous energy Monte Carlo calculations of randomly distributed spherical fuels in HTTR based on statistical geometry model," *JAERI-Review 95-014*, 63 (1995).

# **APPENDIX A EVALUATION METHOD OF 2-DIMENSIONAL RDF FROM THE CROSS SECTION PHOTOGRAPHS OF REAL FUEL COMPACTS**

In Sec. IV.2.1, the calculated 2-dimensional RDF by MCRDF was compared with the experimentally obtained one. The experimental 2-dimensional RDF was evaluated from the cross section photographs of fuel compacts used for an irradiation test of the HTTR's at the Oarai Gas Loop (OGL-1) in JAERI. The evaluation of 2-dimensional RDF was done by reading the distances between CFPs on the photographs. The practical procedure<sup>(1)</sup> is described in the following:

## **A.1 Fuel compacts used**

The 4th and 5th fuel compacts<sup>(2,3)</sup> used for the irradiation test experiments of the HTTR's at OGL-1 were utilized for making the 2-dimensional RDF. The descriptive data of the fuel compacts are listed in Table A.1.

## **A.2 Measurement method**

### **A.2.1 Preparation of the cross section photographs**

An example of a photograph used is shown in Fig. A.1. This is horizontal cross section of an irradiated fuel compact. The actual dimensions of the photograph are small, i.e., 5 cm x 5 cm ~ 10 cm x 10 cm. It is difficult to read the distance directly from the original photographs. Hence, they were enlarged to prepare the base figures for measurement of the distances.

### **A.2.2 Determination of scale**

The scale of each enlarged photograph was determined through the comparison of the measured outer diameter of a real fuel compact with that of the photograph. Considering the deformation caused by enlarging the photograph by a copier, the outer diameter in the photograph was evaluated by averaging four measurements of the outer diameter every 45 degrees, as shown



in Fig. A.2.

### **A.2.3 Determination of base center CFP and sampling circle**

The CFP as base center CFP was determined. The distance was measured between the base center CFP and other one named surrounding CFP. The measurements were conducted within a circle (sampling circle), the center of which is the base center CFP and the radius of which is  $3d$ , where  $d$  is a radius of CFP on the photograph. The value  $d$  was determined by taking into account the measured diameter of real ones and the scale of the photograph. Eight base center CFPs can be selected every 45 degrees in one photograph such that the circles do not overlap with each other as shown in Fig. A.3. The diameters of the cross section circles appearing on the photograph vary because of the difference of cutting position. The base center CFPs were thus randomly determined that their dimensions are not biased.

### **A.2.4 Determination of surrounding CFP**

The surrounding CFPs were selected. CFPs included completely in a sampling circle were chosen as well as those interfering with the circle even if the center is out of the circle. The surrounding CFPs assigned were numbered. The details are shown in Fig. A.4.

### **A.2.5 Determination of CFP center**

The center positions of the base center CFPs and surrounding CFPs were determined. In order to obtain the positions as accurately as possible, using a transparent vinyl sheet in which several concentric circles are described, the most probable CFP center location was found and it was marked by a needle as shown in Fig. A.5.

### **A.2.6 Measurement of the distance**

The distances between the base center CFP and  $\sim 20$  surrounding CFPs were measured. As shown in Fig. A.6, the distance was measured between two holes made by a needle and was read in a unit of 0.2 mm. The error was estimated to be about  $1/20$  diameter because the

apparent diameter of the CFP was 5~6 mm.

### A.3 Results

The frequency distribution of the distance was summarized from the measured results. The unit of the distribution was 1/10 diameter and the maximum distance was 4 diameters. We made the final result using 18 photographs. The number of measured points is 2949. The final result is shown in Table A.2 and Fig. 4.2.

### REFERENCES

- (1) I. Murata, T. Mori, M. Nakagawa and H. Shirai, "Packing Simulation Code to Calculate Distribution Function of Hard Spheres by Monte Carlo Method : MCRDF," *JAERI-Data/Code 96-016*, Japan Atomic Energy Research Institute (1996).
- (2) K. Fukuda et al., Japan Atomic Energy Research Institute, Private Communication (1992).
- (3) K. Fukuda et al., "Irradiation Experiments of 3rd, 4th and 5th Fuel Assemblies by an In-Pile Gas Loop, OGL-1," *JAERI-M 86-092*, Japan Atomic Energy Research Institute (1986).

Table A.1 Descriptive data of compacts used to evaluate 2d-RDF.

Irradiation test	Sample No.		ID	Outer diameter(mm)	Packing fraction (vol%)
5th OGL-1	113	A-3	790PC-38	24.00	30.38
	114	A-10	790PC-31	24.01	30.36
	115	A-15	790PC-26	24.02	29.98
	116	B-3	790PC-58	24.01	29.49
	117	B-10	790PC-51	23.99	30.43
	118	B-15	790PC-46	24.00	30.37
	119	C-3	790PC-18	24.01	30.05
	120	C-10	790PC-11	24.01	30.00
	121	C-15	790PC-6	24.03	29.98
4th OGL-1	132	A-3	780PC-53	23.98	30.10
	133	A-10	780PC-27	23.97	30.55
	134	A-15	780PC-13	24.02	30.01
	135	B-3	780PC-58	23.98	30.11
	136	B-10	780PC-41	23.97	30.69
	137	B-15	780PC-20	24.02	29.99
	138	C-3	780PC-48	23.97	30.11
	139	C-10	780PC-32	24.01	30.62
	140	C-5	780PC-6	24.02	29.98

Table A.2 Frequency distribution of the measured distance for each fuel compact.

Radial direction		Sample No.																		
Group	Diameter	113	114	115	116	117	118	119	120	121	132	133	134	135	136	137	138	139	140	Total
1	0.1																			0
2	0.2																			0
3	0.3																			0
4	0.4																			0
5	0.5										1				1					2
6	0.6								1		0				0					1
7	0.7			1		1		1	1		0		1	2	0					7
8	0.8			2	1	0	2	0	0		0	1	0	2	0				1	9
9	0.9		2	0	1	1	1	0	1	2	1	0	2	2	0	1		1	1	16
10	1	4	2	2	2	1	1	3	2	1	2	2	0	2	1	1	3	1	1	31
11	1.1	0	3	1	2	4	4	1	1	2	3	1	3	3	2	2	3	1	2	38
12	1.2	7	0	5	6	6	2	3	4	5	2	2	1	3	4	2	5	3	2	62
13	1.3	5	4	3	7	5	6	5	7	3	4	3	4	1	4	5	7	2	6	81
14	1.4	7	9	7	6	7	7	5	4	8	6	9	8	3	8	7	5	6	9	121
15	1.5	8	7	4	4	5	5	6	4	7	5	5	4	7	13	7	5	10	12	118
16	1.6	5	4	6	8	7	11	10	9	5	6	5	3	6	7	9	4	4	4	113
17	1.7	1	4	5	4	6	4	8	7	4	10	8	6	7	3	7	9	8	6	107
18	1.8	6	1	2	6	7	8	3	3	4	7	4	2	1	2	4	4	3	0	67
19	1.9	3	4	3	3	6	7	3	3	4	2	2	0	1	6	3	4	4	4	62
20	2	8	4	1	2	3	2	2	9	1	3	4	7	6	4	6	4	3	8	77
21	2.1	10	6	3	8	6	5	6	2	5	3	3	5	8	4	2	2	4	3	85
22	2.2	3	3	3	3	6	3	7	1	8	4	6	3	3	3	1	10	3	3	73
23	2.3	7	4	5	8	11	9	6	8	9	4	3	9	10	12	4	5	7	5	126
24	2.4	9	8	8	9	5	10	10	3	1	7	4	4	5	4	9	7	7	6	116
25	2.5	5	3	9	10	11	9	1	10	11	11	11	4	5	5	14	5	10	13	147
26	2.6	9	3	6	9	7	13	9	7	4	7	9	4	8	11	7	9	7	12	141
27	2.7	8	12	10	10	10	8	6	11	15	8	10	8	9	6	6	9	5	5	156
28	2.8	10	7	13	9	8	7	10	8	14	11	14	13	10	9	11	11	8	8	181
29	2.9	8	6	5	12	6	7	8	6	4	4	9	7	9	15	9	6	12	10	143
30	3	10	4	9	14	12	14	5	10	6	8	8	5	6	7	8	4	8	10	148
31	3.1	7	9	4	4	10	8	11	12	4	14	10	6	5	7	11	12	5	11	150
32	3.2	8	8	7	14	12	10	14	12	13	10	9	6	11	9	7	13	14	9	186
33	3.3	12	2	7	5	11	8	8	5	9	5	5	8	9	6	7	8	10	7	132
34	3.4	7	1	8	3	3	15	9	9	12	4	9	8	9	1	11	7	6	4	126
35	3.5	11		1	2	1	1	6	7	7	4	1	6	9	1	2	4	4	3	70
36	3.6	4					4	6	6	6			1			2	1	3	2	35
37	3.7	1					3	3	5	4	1									17
38	3.8						1	1	3											5
39	3.9																			0
40	4																			0
Total		183	120	140	172	178	195	176	181	178	157	157	138	162	155	165	166	159	167	2949

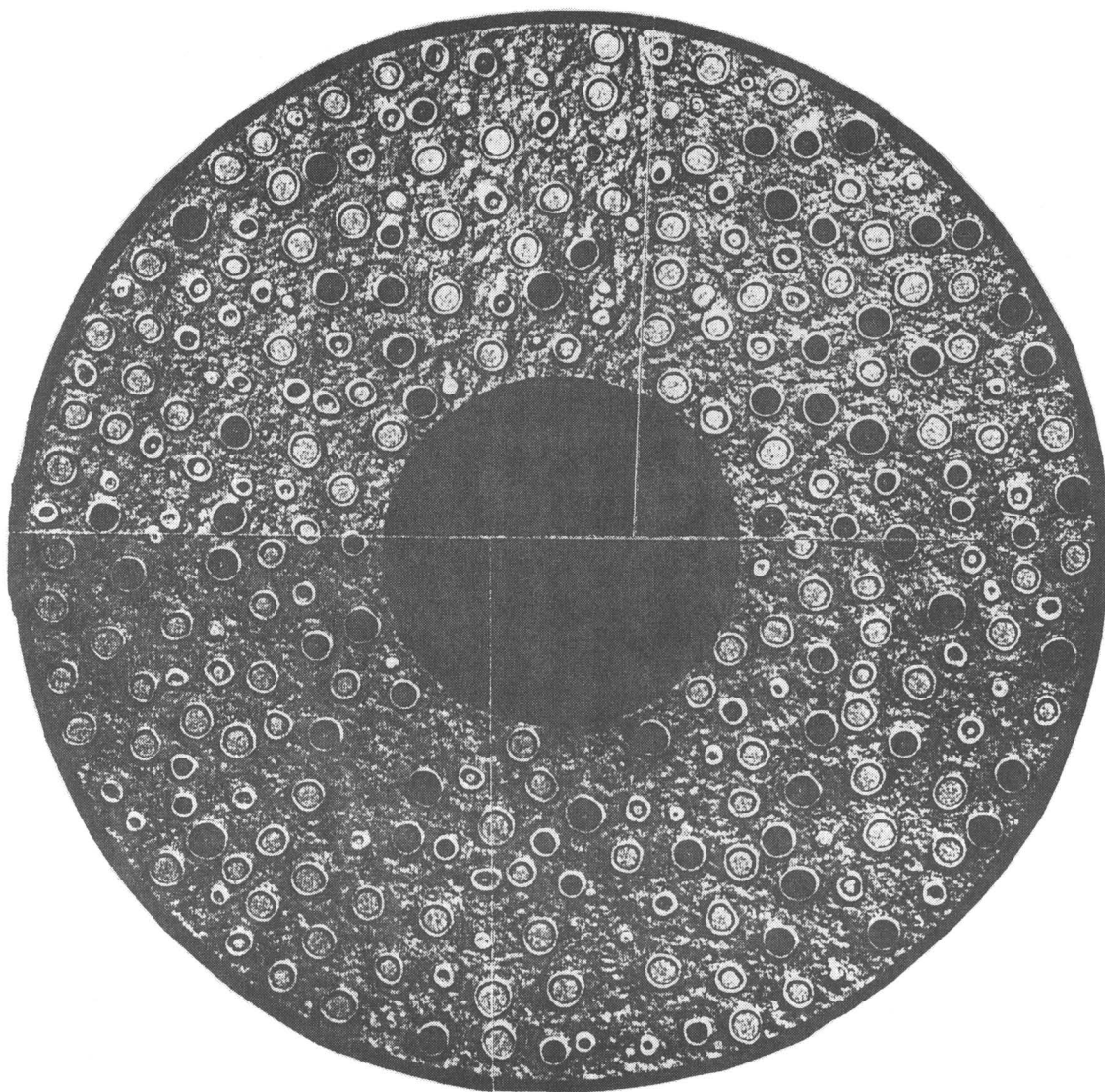
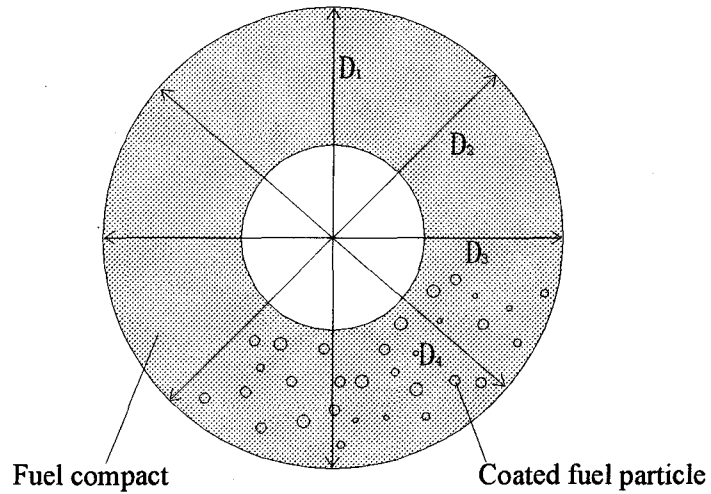


Fig. A.1 Photograph used for distance measurement between CFPs.  
(Sample No. 119 in Table A.1)



$$D = (D_1 + D_2 + D_3 + D_4) / 4$$

$D_1$  : Measured diameter of fuel compact on the photograph.

Fig. A.2 Measurement method of outer diameter of fuel compact from cross section photograph.

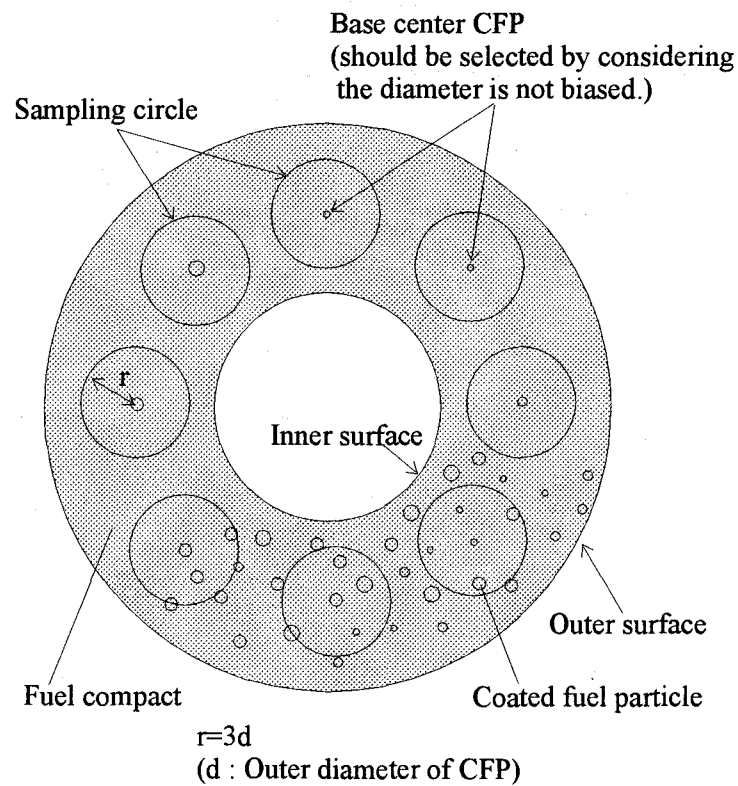


Fig. A.3 Determination of the base center CFP and the sampling circle.

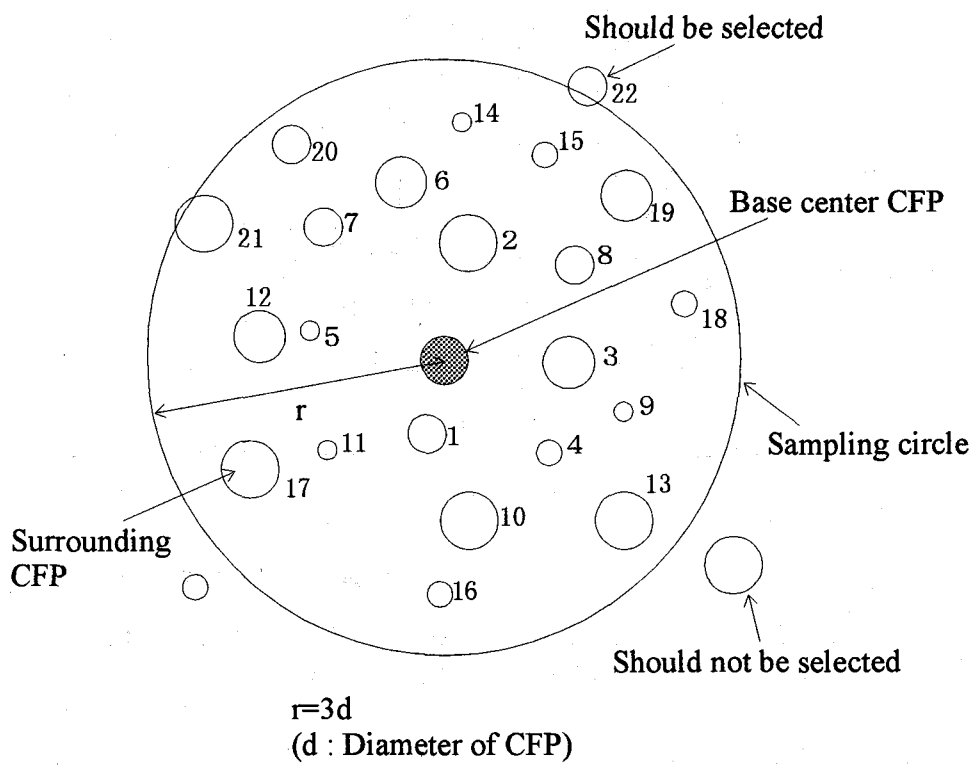


Fig. A.4 Determination of surrounding CFPs in a sampling circle.

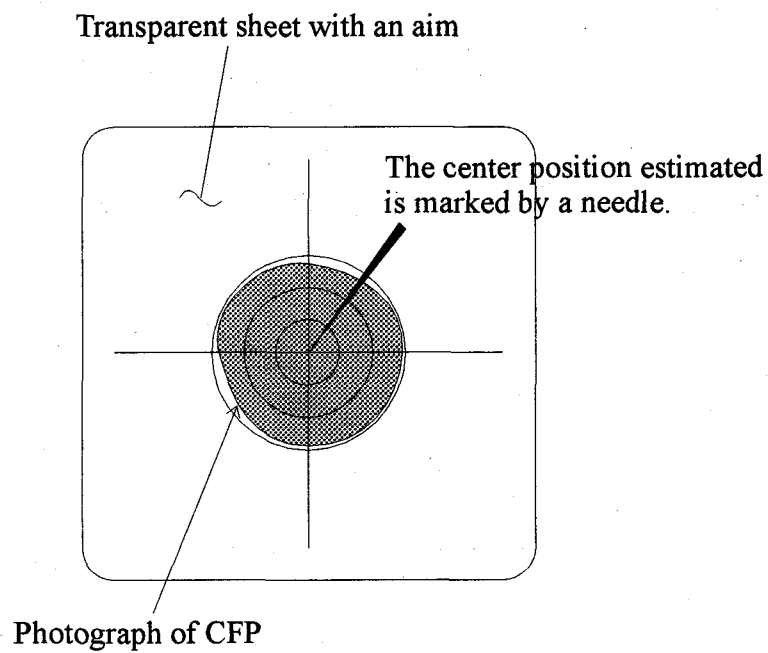


Fig. A.5 Determination of CFP center location.

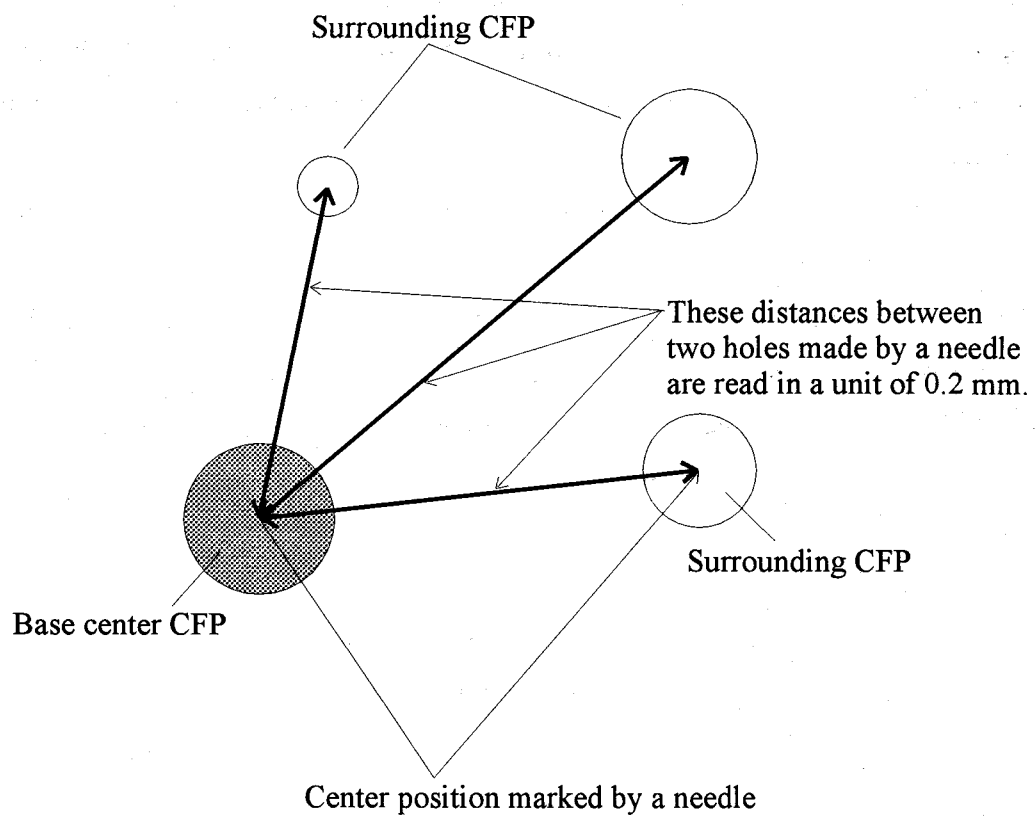


Fig. A.6 Method to measure the distance between centers of CFPs.



## ACKNOWLEDGEMENT

The present thesis includes mainly the works carried out at Department of HTTR Project in Japan Atomic Energy Research Institute (JAERI) and partly the experimental research at Department of Nuclear Engineering, Osaka University.

The author would like to express his greatest appreciation to Professor Akito Takahashi of Osaka University for his excellent direction with critical discussion and patient encouragement. The author also wishes to express his gratitude to Professors Toshikazu Takeda and Toshiyuki Iida of Osaka University for their valuable comments, suggestive discussions and careful reading of the thesis.

The author wishes to show his sincere gratitude to Drs. Masayuki Nakagawa and Takamasa Mori of JAERI who collaborated on the works with the present author, and Dr. Keichiro Tsuchihashi of JAERI who gave me a clue of the present study, Drs. Hideshi Yasuda, Fujiyoshi Akino and Tsuyoshi Yamane of JAERI who supplied the experimental data at VHTRC and PROTEUS critical assemblies, Mr. Hirofumi Itakura of CSK corporation and Hiroshi Shirai of AMP Technology Japan Ltd. who developed the codes and performed a large number of computations, Dr. Kousaku Fukuda who supplied the cross section photographs of fuel compacts irradiated at OGL-1.

Thanks are also due to Drs. Shinzo Saito, Toshiaki Tobioka, Toshiyuki Tanaka, Yukio Sudo of JAERI for their continuous support and encouragement in the present study, Dr. Shusaku Shiozawa of JAERI for his leading the author to become interested in research, Dr. Ryuichi Shindo of JAERI for his valuable discussions on the reactor physics of HTTR, Dr. Kiyonobu Yamashita of JAERI for his help and support in everything about JAERI and HTTR, Messrs. Nozomu Fujimoto and Naoki Nojiri for their preparing the latest calculation results for the neutronic characteristics of HTTR. To Drs. Kazuhiko Kunitomi, Kazuhiro Sawa and Messrs. Soh Maruyama, Shigeaki Nakagawa, Takeshi Takeda, Akio Saikusa and other colleagues in HTTR Reactor Development Division the author gratefully acknowledges their kind support and valuable suggestions of the present work.

The author is indebted to many people in the course of the present study and would like to express his gratitude to them, especially to Messrs. Hisashi Sugimoto and Jun Datemichi for their excellent maintenance and operation at OKTAVIAN, to Mr. Shigeo Yoshida for his devoted support of many-times all-night measurements at heavy concrete irradiation experiment,

to Dr. Hiroyuki Miyamaru for his critical discussions on the theoretical points of the present study, and to post- and under- graduate students in Takahashi Lab., Department of Nuclear Engineering, Osaka University for their cooperation, good-fellowship and support.

In addition, concerning the analytical study of the critical assembly experiments at PROTEUS in Sec. IV, the following is should be noted: The analyses were performed within the frame of the International Atomic Energy Agency's Coordinated Research Programme on Validation of Safety Related Physics Calculations for Low-Enriched Gas-Cooled Reactors. The planning, execution and analysis of the experiments are being carried out by an international team based at the PROTEUS critical experiment facility of the Paul Scherrer Institute, Villigen, Switzerland.

Finally, special thanks are due to my wife Idumi for her love and devoted assistance on everything about our life and health.

# LIST OF PUBLICATIONS

## Publications directly related to the thesis

**I. Murata**, T. Mori and M. Nakagawa, "Continuous Energy Monte Carlo Calculations of Randomly Distributed Spherical Fuels in High-Temperature Gas-Cooled Reactors Based on a Statistical Geometry Model," *Nucl. Sci. Eng.*, **123**, 96 (1996).

**I. Murata**, A. Takahashi, T. Mori and M. Nakagawa, "New Sampling Method in Continuous Energy Monte Carlo Calculations for Pebble Bed Reactors," *J. Nucl. Sci. Technol.*, **34**, 734 (1997).

**I. Murata**, S. Yoshida and A. Takahashi, "Effect of Heterogeneity for Heavy Concrete on Shielding of Fusion Neutrons," *Fusion Technology* (1999). in press.

**I. Murata** and A. Takahashi, "Analysis of Critical Assembly Experiments by Continuous Energy Monte Carlo Method with Statistical Geometry Model," *Technol. Repts. Osaka Univ.*, **48**, 19 (1998).

**I. Murata**, T. Mori and M. Nakagawa, "Continuous Energy Monte Carlo Calculations for Randomly Distributed Spherical Fuels Based on Statistical Geometry Model," *JAERI-Research 96-015* (1996).

**I. Murata**, T. Mori and M. Nakagawa, "Packing Simulation Code to Calculate Distribution Function of Hard Spheres by Monte Carlo Method: MCRDF," *JAERI-Data/Code 96-016* (1996).

**I. Murata**, T. Mori and M. Nakagawa, "Continuous Energy Monte Carlo Calculations of Randomly Distributed Spherical Fuels in HTTR Based on Statistical Geometry Model," *JAERI-Review 95-014*, 63 (1995).

## **Related publications**

**I. Murata**, R. Shindo and S. Shiozawa, "Importance Determination Method for Geometry Splitting with Russian Roulette in Monte Carlo Calculations of Thick and Complicated Core Shielding Structure," *J. Nucl. Sci. Technol.*, **32**, 971 (1995).

K. Yamashita, R. Shindo, **I. Murata**, S. Maruyama, N. Fujimoto and T. Takeda, "Nuclear Design of a High-Temperature Engineering Test Reactor (HTTR)," *Nucl. Sci. Eng.*, **122**, 212 (1996).

K. Yamashita, K. Tokuhara, R. Shindo, **I. Murata** and A. Saikusa, "Destruction of Weapons-Grade Plutonium with Pebble Bed Type HTGRs Using Burner Balls and Breeder Balls," *J. At. Energy Soc. Japan*, **36**, 865 (1994).

S. Saito, **I. Murata**, et al., "Design of High Temperature Engineering Test Reactor (HTTR)," *JAERI-1332* (1994).

K. Yamashita, R. Shindo, **I. Murata** and T. Watanabe, "Accuracy Investigation of Nuclear Design Method for High Temperature Engineering Test Reactor(HTTR) Based on VHTRC Experimental Data," *JAERI-M 88-245* (1988).

**I. Murata**, K. Yamashita, R. Shindo, S. Shiozawa and M. Takemura, "Neutron Response Analysis of Wide Range Detector in High Temperature Engineering Test Reactor (HTTR)," *JAERI-Tech 95-036* (1995).

**I. Murata**, R Shindo, K Tada, K Sasaki and M Yoshida, "Reactor Shielding Design of the High Temperature Engineering Test Reactor -Analysis of Radiation Streaming through the Standpipes by Monte Carlo Code MCNP-," *Proc. 8th Int. Conf. on Radiation Shielding*, Arlington, 359 (1994).

**I. Murata**, R. Shindo and S. Shiozawa, "Reactor Shielding Design of the High Temperature Engineering Test Reactor -Application of 3-dimensional Monte Carlo Code MCNP to Shielding Analysis for Thick and Complicated Structure-," *Proc. 8th Int. Conf. on Radiation Shielding*, Arlington, 365 (1994).

## **Other publications**

### **HTTR design works**

K. Yamashita, **I. Murata** and R. Shindo, "Analysis of Overall Temperature Coefficient of Reactivity of the VHTRC-1 Core with a Nuclear Design Code System for the High-Temperature Engineering Test Reactor," *Nucl. Sci. Eng.*, **110**, 177 (1992).

K. Yamashita, S. Maruyama, **I. Murata**, R. Shindo, N. Fujimoto, Y. Sudo, T. Nakata and K. Tokuhara, "Optimization of Power Distribution to Achieve Outlet Gas-Coolant Temperature of 950°C for HTTR," *J. Nucl. Sci. Technol.*, **29**, 472 (1992).

K. Yamashita, H. Harada, **I. Murata**, R. Shindo and T. Tsuruoka, "Effects of Core Models and Neutron Energy Group Structures on Xenon Oscillation in Large Graphite-Moderated Reactors," *J. Nucl. Sci. Technol.*, **30**, 249 (1993).

S. Maruyama, K. Yamashita, N. Fujimoto, **I. Murata**, Y. Sudo, T. Murakami and S. Fujii, "Evaluation of Hot Spot Factors for Thermal and Hydraulic Design of HTTR," *J. Nucl. Sci. Technol.*, **30**, 1186 (1993).

K. Sawa, **I. Murata**, S. Shiozawa and M. Matsumoto, "A Study of Plateout Fission Product Behavior During a Large-Scale Pipe Rupture Accident in a High-Temperature Gas-Cooled Reactor," *Nucl. Technol.*, **106**, 265 (1994).

**I. Murata**, K. Yamashita, S. Maruyama, R. Shindo, N. Fujimoto, Y. Sudo and T. Nakata, "Evaluation of Local Power Distribution with Fine-mesh Core Model for High Temperature Engineering Test Reactor(HTTR)," *J. Nucl. Sci. Technol.*, **31**, 62 (1994).

K. Yamashita, **I. Murata**, R. Shindo, K. Tokuhara and H. Werner, "Analysis of Control Rod Reactivity Worths for AVR Power Plant at Cold and Hot Conditions," *J. Nucl. Sci. Technol.*, **31**, 470 (1994).

K. Sawa, **I. Murata**, A. Saikusa, R. Shindo, S. Shiozawa and O. Baba, "Prediction of Nongaseous Fission Products Behavior in the Primary Cooling System of High Temperature Gas-Cooled Reactor," *J. Nucl. Sci. Technol.*, **31**, 654 (1994).

S. Maruyama, K. Yamashita, N. Fujimoto, **I. Murata**, R. Shindo and Y. Sudo, "Determination of Hot Spot Factors for Calculation of the Maximum Fuel Temperatures in the Core Thermal and Hydraulic Design of HTTR," *JAERI-M 88-250* (1988).

S. Maruyama, N. Fujimoto, K. Yamashita, **I. Murata**, R. Shindo and Y. Sudo, "Core Thermal and Hydraulic Design of High Temperature Engineering Test Reactor(HTTR)," *JAERI-M 88-255* (1988).

K. Yamashita, R. Shindo, **I. Murata**, S. Maruyama and K. Tokuhara, "Optimization of Uranium Isotope Distribution and Burnable Poison of High Temperature Engineering Test Reactor (HTTR)," *JAERI-M 89-118* (1989).

K. Yamashita, R. Shindo, **I. Murata** and T. Nakata, "Evaluation of Effective Delayed Neutron Fraction and Prompt Neutron Lifetime for High Temperature Engineering Test Reactor(HTTR)," *JAERI-M 89-198* (1989).

K. Yamashita, R. Shindo, **I. Murata**, S. Nakagawa, T. Nakata and K. Tokuhara, "Evaluation of Reactivity Coefficients of for High Temperature Engineering Test Reactor(HTTR)," *JAERI-M 90-008* (1990).

R. Shindo, K. Yamashita and **I. Murata**, "DELIGHT-7: One Dimensional Fuel Cell Burnup Analysis Code for High Temperature Gas-Cooled Reactors(HTGR)," *JAERI-M 90-048* (1990).

**I. Murata**, K. Yamashita, S. Maruyama, N. Fujimoto, R. Shindo and Y. Sudo, "Evaluation of Shut Down Margin in Scram Condition for High Temperature Engineering Test Reactor(HTTR)," *JAERI-M 91-165* (1991).

K. Sawa, **I. Murata**, R. Shindo and S. Shiozawa, "Evaluation of Fission Product Sources for Shielding Design of HTTR," *JAERI-M 91-198* (1991).

S. Maruyama, K. Yamashita, N. Fujimoto, **I. Murata**, R. Shindo and Y. Sudo, "Thermal and Hydraulic Design for High Temperature Engineering Test Reactor(HTTR)," *Proc. Topical Meeting on the Safety, Status and Future of Non-Commercial Reactors and Irradiation Facilities*, Boise, 304 (1990).

K. Yamashita, R. Shindo and **I. Murata**, "Development and Validation of Nuclear Design Code System for High Temperature Engineering Test Reactor(HTTR)," *Proc. Topical Meeting on the Safety, Status and Future of Non-Commercial Reactors and Irradiation Facilities*, Boise, 351 (1990).

K. Yamashita, **I. Murata**, H. Harada and R. Shindo, "Three-dimensional Analysis for Xenon-induced Oscillation in Graphite Moderated Reactor with the Vectorized Reactor Core Analysis Code CITATION-1000VP," *Proc. First Int. Conf. on Supercomputing in Nuclear Applications*, Mito, 133 (1990).

K. Tokuhara, T. Nakata, **I. Murata**, K. Yamashita and R. Shindo, "Determination of the Temperature Coefficients and the Kinetic Parameters for the HTTR Safety Analysis," *Proc. Specialist's Meeting on Uncertainties in Physics Calculations for Gas Cooled Reactor Cores*, Villigen, 45 (1991).

T. Nakata, K. Tokuhara, **I. Murata**, K. Yamashita and R. Shindo, "Calculational Methods of Power Distribution in the HTTR and Verifications," *Proc. Specialist's Meeting on Uncertainties in Physics Calculations for Gas Cooled Reactor Cores*, Villigen, 53 (1991).

R. Shindo, K. Yamashita and **I. Murata**, "Uncertainties in Calculations of Nuclear Design Code System for the High Temperature Engineering Test Reactor(HTTR)," *Proc. Specialist's Meeting on Uncertainties in Physics Calculations for Gas Cooled Reactor Cores*, Villigen, 81 (1991).

K Yamashita, S Maruyama, **I. Murata**, R Shindo, N Fujimoto, Y Sudo, T Nakata and K Tokuhara, "Optimization of Power Distribution to Achieve Outlet Gas-coolant Temperature of 950°C for High Temperature Engineering Test Reactor (HTTR)," *Proc. Int. Conf. on Nucl. Eng.*, Tokyo, 419 (1991).

**I. Murata**, K Yamashita, S Maruyama, R Shindo, N Fujimoto, Y Sudo and T Nakata, "Evaluation of Local Power Distribution with Fine-mesh Core Model for the HTTR," *Proc. Int. Conf. on Nucl. Eng.*, Tokyo, 413 (1991).

R Shindo, **I. Murata**, K Sawa, S Shusaku, M Takemura and T Mohri, "Reactor Shielding Design of the High Temperature Engineering Test Reactor -Design Analysis and Shielding Characteristics-," *Proc. 8th Int. Conf. on Radiation Shielding*, Arlington, 351 (1994).

### **DT neutron related works**

A. Takahashi, **I. Murata** et al., "A Time-of-flight Spectrometer with Pulse-Shape Discrimination for the Measurement of Double-Differential Charged-Particle Emission Cross Sections," *Nucl. Instr. and Meth.*, **A401**, 93 (1997).

**I. Murata**, S. Yoshida, N. Saito and A. Takahashi, "Mechanism of Secondary Gamma-ray Skyshine from Intense 14 MeV Neutron Source Facility with Hp-Ge Detector," *Fusion Technology* (1999). in press.

S. Yoshida, **I. Murata** and A. Takahashi, "Measurement of Biological Half-Life of Tritium in Handling Worker at Fusion Research Facility," *Fusion Technology* (1999). in press.

Kokooo, **I. Murata**, F. Maekawa, D. Nakano, A. Takahashi and Y. Ikeda, "Benchmark Experiment on Vanadium Assembly with D-T Neutrons -Leakage Neutron Spectrum Measurement-," *Fusion Technology* (1999). in press.

F. Maekawa, Y. Kasugai, C. Konno, M. Wada, Y. Oyama, Y. Ikeda, R. Johnson, E. T. Cheng, M. Pillon, **I. Murata**, Kokooo, D. Nakano and A. Takahashi, "Benchmark Experiment on Vanadium-Alloy Assembly with D-T Neutrons -In-situ Measurement-," *Fusion Technology* (1999). in press.

Kokooo, **I. Murata** and A. Takahashi, "Measurements of Double Differential Cross Sections of Charged Particle Emission Reactions For Several Structural Elements of Fusion Power Reactor by 14.1 MeV Incident Neutrons," *Nucl. Sci. Eng.* (1999). in press.



F. Maekawa, Y. Kasugai, C. Konno, **I. Murata**, Kokooo, M. Wada, Y. Oyama, Y. Ikeda and A. Takahashi, "Benchmark Experiment on Vanadium with D-T Neutron for Validation of Evaluated Nuclear Data Libraries," to be published in *J. Nucl. Sci. Technol.* (1998).

J. Yamamoto, **I. Murata**, A. Takahashi and K. Sumita, "Differential Cross Sections for Gamma-Ray Production by 14MeV Neutrons," *JAERI-M 88-065*, 374 (1988).

**I. Murata**, D. Nakano and A. Takahashi, "Measurement of 14 MeV Neutron Cross Section of  $^{129}\text{I}$  with Foil Activation Method," *Proc. First Internet Symposium on Nucl. Data*, Tokai, *JAERI-Conf 97-004*, 177 (1997).

J. Yamamoto, T. Kanaoka, **I. Murata**, A. Takahashi and K. Sumita, "Gamma-Ray Emission Spectra from Spheres with 14 MeV Neutron Source," *JAERI-M 89-026*, 232 (1989).

D. Nakano, I. Murata and A. Takahashi, "Measurement of Reaction Cross Sections of I-129 Induced by DT Neutrons," *Proc. '96 Symposium on Nucl. Data*, Tokai, *JAERI-Conf 97-005*, 216 (1997).

Kokooo, **I. Murata** and A. Takahashi, "Double Differential Charged Particle Emission Cross Sections of Vanadium for 14.1 MeV Incident Neutron," *Proc. '96 Symposium on Nucl. Data*, Tokai, *JAERI-Conf 97-005*, 216 (1997).

F. Maekawa, Y. Kasugai, C. Konno, M. Wada, Y. Oyama, Y. Ikeda, **I. Murata**, Kokooo and A. Takahashi, "Benchmark Experiment on Vanadium Assembly with D-T Neutrons -In-situ Measurement-," *Proc. '97 Symposium on Nucl. Data*, Tokai, *JAERI-Conf 98-003*, 168 (1998).

Kokooo, **I. Murata**, D. Nakano, A. Takahashi, F. Maekawa and Y. Ikeda, "Benchmark Experiment on Vanadium Assembly with D-T Neutrons -Leakage Neutron Spectrum Measurement-," *Proc. '97 Symposium on Nucl. Data*, Tokai, *JAERI-Conf 98-003*, 204 (1998).

D. Nakano, **I. Murata** and A. Takahashi, "Measurement of Reaction Cross Sections of Fission Products Induced by D-T Neutrons," *Proc. '97 Symposium on Nucl. Data*, Tokai, *JAERI-Conf 98-003*, 210 (1998).

**I. Murata**, J. Yamamoto and A. Takahashi, "Differential Cross Sections for Gamma-Ray Production by 14 MeV Neutrons with Several Elements in Structural Materials," *Proc. Int. Conf. on Nucl. Data for Sci. and Technol.*, Mito, 275 (1988).

Y. Makita, **I. Murata** and A. Takahashi, "Benchmark of FENDL-1, JENDL-3.2 and JENDL-Fusion File using Neutron Leakage Spectra from Spherical Beryllium Assemblies," *Proc. IAEA AGM on Completion of FENDL-1 and Start of FENDL-2*, Del Mar (1995). to be published.

Kokooo, **I. Murata** and A. Takahashi, "Measurements of Double Differential Cross Sections of Charged Particle Emission Reactions by 14.1 MeV Incident Neutrons," *Proc. Int. Conf. on Nucl. Data for Sci. and Technol.*, Trieste, 520 (1997).

**I. Murata**, D. Nakano and A. Takahashi, "Measurement of DT Neutron Cross Sections of  $^{129}\text{I}$  with Foil Activation Method," *Proc. Int. Conf. on Nucl. Data for Sci. and Technol.*, Trieste, 1338 (1997).

S. Yoshida, N. Saito, **I. Murata** and A. Takahashi, "Measurement of Secondary Gamma-Ray Skyshine from Intense 14 MeV Neutron Source Facility with Hp-Ge Detector," *Proc. Int. Conf. on Nucl. Data for Sci. and Technol.*, Trieste, 1392 (1997).